

## **ACKNOWLEDGEMENT**

This material is based upon work supported by the Department of Energy under Award Number DE-FE00006821.

## **DISCLAIMER**

This report was prepared as an account of work sponsored by an agency of the United States Government. Neither the United States Government nor any agency thereof, nor any of their employees, makes any warranty, express or implied, or assumes any legal liability or responsibility for the accuracy, completeness, or usefulness of any information, apparatus, product, or process disclosed, or represents that its use would not infringe privately owned rights. Reference herein to any specific commercial product, process, or service by trade name, trademark, manufacturer, or otherwise does not necessarily constitute or imply its endorsement, recommendation, or favoring by the United States Government or any agency thereof. The views and opinions of authors expressed herein do not necessarily state or reflect those of the United States Government or any agency thereof.

**SMALL SCALE FIELD TEST DEMONSTRATING CO<sub>2</sub> SEQUESTRATION IN  
ARBUCKLE SALINE AQUIFER AND BY CO<sub>2</sub>-EOR AT WELLINGTON FIELD,  
SUMNER COUNTY, KANSAS**

**Project Director/Principal Investigator:**

**W. Lynn Watney  
Senior Scientific Fellow  
Kansas Geological Survey  
Ph: 785-864-2184, Fax: 785-864-5317  
[lwatney@kgs.ku.edu](mailto:lwatney@kgs.ku.edu)**

**Joint Principal Investigator:**

**Yevhen 'Eugene' Holubnyak  
[eugene@kgs.ku.edu](mailto:eugene@kgs.ku.edu)  
Ph: 785-864-2070**

Final Report

By

**Prepared by Yevhen Holubnyak, Lynn Watney, Jennifer Hollenbach, Tiraz Birdie, Mina Fazelalavi, Tандis Bidgoli, Drew Schwab, Alex Nolte, George Tsoflias, John Victorine, Brandon Graham, John Doveton, Jason Bruns, Brett Blazer, Dana Wreath**

**Date of Report: December 31, 2017**

**DUNS Number: 076248616**

**Recipient: University of Kansas Center for Research &  
Kansas Geological Survey  
1930 Constant Avenue  
Lawrence, KS 66047**

**Project/Grant Period: 10/1/2011 through 9/30/2017**

**Signature of Submitting Official:**

**Yevhen 'Eugene' Holubnyak**

## Executive Summary

The objectives of this project are to understand the processes that occur when a maximum of 70,000 metric tonnes of CO<sub>2</sub> are injected into two different formations to evaluate the response in different lithofacies and depositional environments. The evaluation will be accomplished through the use of both in situ and indirect MVA (monitoring, verification, and accounting) technologies. The project will optimize for carbon storage accounting for 99% of the CO<sub>2</sub> using lab and field testing and comprehensive characterization and modeling techniques.

Site characterization and CO<sub>2</sub> injection should demonstrate state-of-the-art MVA tools and techniques to monitor and visualize the injected CO<sub>2</sub> plume and to refine geomodels developed using nearly continuous core, exhaustive wireline logs, and well tests and a multi-component 3D seismic survey. Reservoir simulation studies will map the injected CO<sub>2</sub> plume and estimate tonnage of CO<sub>2</sub> stored in solution, as residual gas, and by mineralization and integrate MVA results and reservoir models shall be used to evaluate CO<sub>2</sub> leakage. A rapid-response mitigation plan was developed to minimize CO<sub>2</sub> leakage and provide comprehensive risk management strategy. The CO<sub>2</sub> was supposed to be supplied from a reliable facility and have an adequate delivery and quality of CO<sub>2</sub>. However, several unforeseen circumstances complicated this plan: (1) initially negotiated CO<sub>2</sub> supply facility went offline and contracts associated with CO<sub>2</sub> supply had renegotiated, (2) UIC Class VI permit proved to be difficult to obtain due to experimental nature of the project. Both subjects are detailed in separate deliverables attached to this report.

The CO<sub>2</sub> EOR and geologic storage in Mississippian carbonate reservoir was successfully deployed. Approximately 20,000 metric tons of CO<sub>2</sub> was injected in the upper part of the Mississippian reservoir to verify CO<sub>2</sub> EOR viability in carbonate reservoirs and evaluate a potential of transitioning to geologic CO<sub>2</sub> storage through EOR. Total of 1,101 truckloads, 19,803 metric tons, average of 120 tonnes per day were delivered over the course of injection that lasted from January 9 to June 21, 2016. After cessation of CO<sub>2</sub> injection, KGS 2-32 well was converted to water injector and is currently continues to operate. CO<sub>2</sub> EOR progression in the field was monitored weekly with fluid level, temperature, and production recording, and formation fluid composition sampling.

As a result of CO<sub>2</sub> injection observed incremental average oil production increase is ~68% with only ~18% of injected CO<sub>2</sub> produced back. Simple but robust monitoring technologies proved to be very efficient in detection and locating of CO<sub>2</sub>. High CO<sub>2</sub> reservoir retentions with low yields within actively producing field could help to estimate real-world risks of CO<sub>2</sub> geological storage for future projects. Wellington filed CO<sub>2</sub> EOR was executed in a controlled environment with high efficiency. This case study proves that CO<sub>2</sub> EOR could be successfully applied in Kansas carbonate reservoirs if CO<sub>2</sub> sources and associated infrastructure is available.

Recent developments in unconventional resources developments in Mid-Continent USA and associated large volume disposal of backflow water and resulted seismic activity have brought more focus and attention to the Arbuckle Group in southern Kansas. Despite the commercial interest, essential information about reservoir properties and structural elements is limited that has impeded managing and regulating disposal brought into the forefront by the recent seismicity in and near the areas of large volumes and rates of brine disposal.

The Kansas Geological Survey (KGS) collected, compiled, and analyzed available data, including well logs, core data, step rate tests, drill stem tests, 2D and 3D seismic data, water level measurements, and others types of data. Several exploratory wells were also drilled and core was collected and modern suites of logs were analyzed. Reservoir properties were populated into several site specific geological models. The geological models illustrate the highly heterogeneous nature of the Arbuckle Group. Vertical and horizontal variability results in several distinct hydrostratigraphic units that are the result of both depositional and diagenetic processes.

Also, during the course of this project it has been demonstrated that advanced seismic interpretation methods can be used successfully for characterization of the Mississippian reservoir and Arbuckle saline aquifer. Analysis of post-stack 3D seismic data at the Mississippian reservoir showed the response of a gradational velocity transition. Pre-stack gather analysis showed that porosity zones of the Mississippian and Arbuckle reservoirs exhibit characteristic AVO response. Simultaneous AVO inversion estimated P- and S-Impedances. The 3D survey gather azimuthal anisotropy analysis (AVAZ) provided information on the fault and fracture network and showed good agreement to the regional stress field and well data. Mississippian reservoir porosity and fracture predictions agreed well with the observed mobility of injected CO<sub>2</sub> in KGS well 2-32. Fluid substitution modeling predicted acoustic impedance reduction in the Mississippian carbonate reservoir introduced by the presence of CO<sub>2</sub>.

Seismicity in the United States midcontinent has increased by orders of magnitude over the past decade. Spatiotemporal correlations of seismicity to wastewater injection operations have suggested that injection-related pore fluid pressure increases are inducing the earthquakes. In this investigation, we examine earthquake occurrence in southern Kansas and northern Oklahoma and its relation to the change in pore pressure. The main source of data comes from the Wellington Array in the Wellington oil field, in Sumner County, KS, which has monitored for earthquakes in central Sumner County, KS since early 2015. The seismometer array was established to monitor CO<sub>2</sub> injection operations at Wellington field. Although no seismicity was detected in association with the spring 2016 Mississippian CO<sub>2</sub> injection, the array has recorded over 2,500 earthquakes in the region and is providing valuable understanding to induced seismicity. A catalog of earthquakes was built from this data and was analyzed for spatial and temporal changes, stress information, and anisotropy information. The region of seismic concern has been shown to be expanding through use of the Wellington earthquake catalog, and has revealed a northward progression of earthquake activity reaching the metropolitan area of Wichita. The stress orientation was also calculated from this earthquake catalog through focal mechanism inversion. The calculated stress orientation was confirmed through comparison to other stress measurements from well data and previous earthquake studies in the region. With this knowledge of the stress orientation, the anisotropy in the basement could be understood. This allowed for the anisotropy measurements to be correlated to pore pressure increases. The increase in pore pressure was monitored through time-lapse shear-wave anisotropy analysis. Since the onset of the observation period in 2010, the orientation of the fast shear-wave has rotated 90°, indicating a change

associated with critical pore pressure build up. The time delay between fast and slow shear wave arrivals has increased, indicating a corresponding increase in anisotropy induced by pore pressure rise. In-situ near-basement fluid pressure measurements corroborate the continuous pore pressure increase revealed by the shear-wave anisotropy analysis over the earthquake monitoring period.

This research is the first to identify a change in pore fluid pressure in the basement using seismological data and it was recently published in the AAAS journal *Science Advances* (Nolte et al., 2017). The shear-wave splitting analysis is a novel application of the technique, which can be used in other regions to identify an increase in pore pressure. This increasing pore fluid pressure has become more regionally extensive as earthquakes are occurring in southern Kansas, where they previously were absent. These monitoring techniques and analyses provide new insight into mitigating induced seismicity's impact to society.

## INTRODUCTION

The objectives of this project was to understand the processes that occur when a maximum of 70,000 metric tonnes of CO<sub>2</sub> are injected into two different formations to evaluate the response in different lithofacies and depositional environments. The evaluation will be accomplished through the use of both in situ and indirect MVA (monitoring, verification, and accounting) technologies. The project was optimized for carbon storage accounting for 99% of the CO<sub>2</sub> using lab and field testing and comprehensive characterization and modeling techniques.

CO<sub>2</sub> was be injected under supercritical conditions to demonstrate state-of-the-art MVA tools and techniques to monitor and visualize the injected CO<sub>2</sub> plume and to refine geomodels developed using nearly continuous core, exhaustive wireline logs, and well tests and a multi-component 3D seismic survey. Reservoir simulation studies will map the injected CO<sub>2</sub> plume and estimate tonnage of CO<sub>2</sub> stored in solution, as residual gas, and by mineralization and integrate MVA results and reservoir models shall be used to evaluate CO<sub>2</sub> leakage. A rapid-response mitigation plan was developed to minimize CO<sub>2</sub> leakage and provide comprehensive risk management strategy. A documentation of best practice methodologies for MVA and application for closure of the carbon storage test was completed by the project.

Many Mississippian age reservoirs in Kansas are currently undergoing final stages of secondary recovery and are suitable for CO<sub>2</sub> EOR. It has been previously estimated that recoverable potential for Mississippian Formation reservoirs in Kansas with CO<sub>2</sub> EOR is 250-350 million barrels of oil (REF). Wellington field is situated in South-Central Kansas near town of Wellington, Sumner County and it is a typical carbonate reservoir of Mississippian age that has produced 20 MMBO since discovery in 1929. This field was converted to waterflood after 1957 and is delivering steady secondary production but nearing the end of a cycle with average daily production per well at ~2.6 bbls using 49 active producing wells and 15 injectors out of more than 290 total drilled wells (KGS, 2017).

The Arbuckle Group is a 600-1,000 ft thick and more than 3,500 ft deep carbonate saline aquifer and historically has been a good candidate for various waste disposal operations, such as oil field brine and chemical plant waste disposal. The Arbuckle is currently being considered for commercial scale CO<sub>2</sub> geological storage it is centrally located to multiple major point sources of CO<sub>2</sub> emissions and a large existing pipeline system with established right-of-ways that may be useful for implementing commercial-scale distribution from CO<sub>2</sub> source to sink.

Wellington Field (Fig. 1) located in the South Central Kansas, Sumner County near town of Wellington is a host of this project and has 49 active production wells and 15 active injection wells producing 132 BOPD. Cumulative oil production is over 20 million barrels since discovery in 1927. An extensive characterization of the Mississippian reservoir at Wellington Field has been conducted as part of a DOE-NETL funded study (DE-FE0002056) to evaluate carbon storage in southern Kansas.



**Figure 1. Map showing the location of Wellington Field, key wells drilled in DE-FE0002056 (#1-28 and #1-32), and the Mississippian injection well drilled under DE-FE0006821 (#2-32).**

## **Part I**

### **CO<sub>2</sub> EOR and Geological Storage in Mississippian Carbonate Reservoir**

Many Mississippian age reservoirs in Kansas are currently undergoing final stages of secondary recovery and are suitable for CO<sub>2</sub> EOR. It has been previously estimated that recoverable potential for Mississippian Formation reservoirs in Kansas with CO<sub>2</sub> EOR is 250-350 million barrels of oil (Crabtree & Christensen, 2012). Wellington field is situated in South-Central Kansas near town of Wellington, Sumner County and it is a typical carbonate reservoir of Mississippian age that has produced 20 MMBO since discovery in 1929. This field was converted to waterflood after 1957 and is delivering steady secondary production but nearing the end of a cycle with average daily production per well at ~2.6 bbls using 49 active producing wells and 15 injectors out of more than 290 total drilled wells (KGS, 2017).

The Mississippian group of formations consists of interlayers of limestone and chert that can be divided older, shallow marine limestone, chert, and cherty limestones, with interbeds of shale, and younger marine and nonmarine shales and sandstones with minor limestones (Newell et al., 1987; Watney et al., 2002). The Upper Mississippian sequence is a limestone and dolostone with interbedded sandstone and shale, as well as some deposits of chert (Goebel, 1968; Zeller, 1968). KGS 1-32 core from Upper Mississippian was described as a moderately argillaceous, fine peloidal limestone to micritic lime mudstone with massive chert (Scheffer, 2012). The Upper Mississippian is composed by the underlying Meramecian and overlying Chesterian stages (Goebel, 1968; Zeller, 1968). The unconformity bounds the Chesterian stage and hosts oil reservoirs.

Baseline geologic characterization, geologic model development, studies of oil composition and properties, miscibility pressure estimations, geochemical characterization, reservoir modelling

were performed. In March of 2015 the injection well (class II) KGS 2-32 was drilled, cored, and logged through an entire anticipated injection interval. Whole core samples were obtained and tested for porosity and permeability, relative permeability, and capillary pressure. The Drill Stem Test (DST) was also conducted to estimate injection interval permeability and pore-pressure. After the injection well KGS 2-32 was acidized, Step Rate (SRT) and Interference (IT) tests were conducted and analyzed for permeability, well pattern communication, and fracture closing pressure. Based on geological characterization efforts it was estimated that the average reservoir porosity around KGS 2-32 well is ~25%. And average permeability is 15-25 mD. The reservoir is located in the upper Chesterian stage and high permeability and porosity zones with oil saturations are observed in the upper ~35 m (115 ft). The perforations for the injection well were selected in the upper 16 m (50 ft) of the reservoir and ~7 m (25 ft) were perforated. The Mississippian reservoir pore fluid pressures is estimated to be below hydrostatic (Bradley, 1975; Sorenson, 2005; Nelson and Gianoutsos, 2011). This departure from the hydrostatic pore pressure is explained by the departure between surface elevations and hydraulic head, which is the result of a major hydrodynamic adjustment associated with post-Laramide uplift, erosion, and formation water discharge (Sorenson, 2005; Nelson and Gianoutsos, 2011). Also, due to oil and gas production in the region and local Wellington field oil production the pore fluid pressure of a Mississippian reservoir was measured at ~7 MPa (1015 psi). The average temperature in the reservoir is ~ 43 °C (~110 °F). The minimum miscibility pressure (MMP) was estimated at ~11.4 MPa (~1,650 psi) (Holubnyak, 2017).

### **Reservoir characterization and properties**

The Mississippian reservoir at Wellington Field has been analyzed using a host of data, including continuous core, an exhaustive suite of modern wireline logs, and multi-component 3D seismic data. These data demonstrate that the reservoir has an average thickness of 42 ft. and is moderately fractured at a range of scales, typical of carbonates in general. The reservoir exhibits an upward increasing porosity trend through the midsection of the field, with effective porosity ranging from 5-27%. Permeability from whole core in Wellington #1-32 ranges from 0.13 to 60 md.

The data set for the log analysis consists of 16 wells with complete suites of porosity and resistivity logs drilled from 1956 to 2011. Also, there were are 5 older wells with older completion dates from 1936 to 1948. These wells had one porosity log, usually Neutron logs with no scale, and no resistivity logs. The Neutron logs of the 5 older wells were normalized with the Neutron logs of the new well (1-32), which was drilled and logged specifically for the purposes of the project, and then converted to the equivalent formation porosity. The 16 newer wells were quality controlled and analyzed by Techlog in terms of porosity, water, oil saturation and minerals (Fig. 1). 2 of these 16 wells (1-32 and 1-28) had Nuclear Magnetic Resonance (NMR) log. The NMR logs were analyzed by Techlog to derive Coates permeability and capillary pressure curves (Appendix A-2 – A-4).

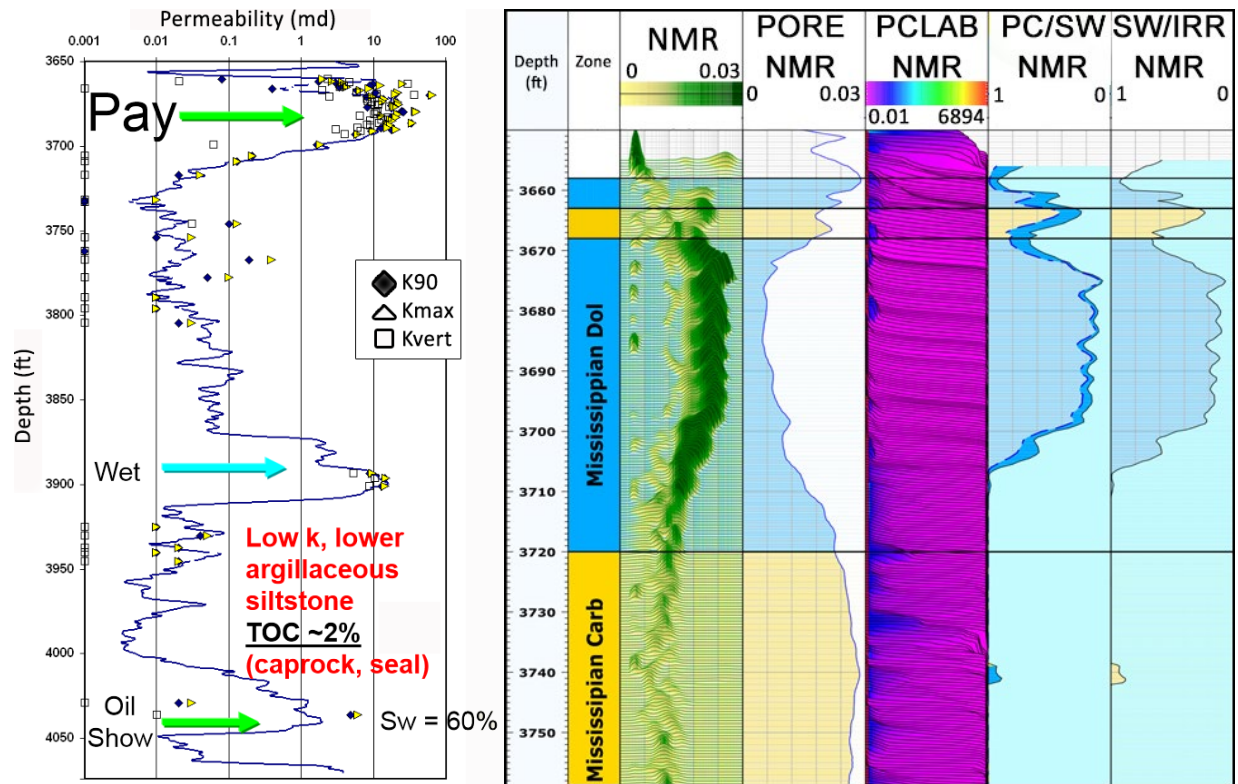


**Figure 2. Well KGS #1-32 estimation of permeability based on magnetic resonance imaging (MRILtm) using porosity and T2 center of gravity versus core permeability (left) and NMR log derived porosity (PORE NMR) and water saturations (PC/SW and SW/IRR NMR).**

Well 1-32 is a new well drilled for the purposes of this project with the comprehensive set of modern logs and core; therefore, it was used as the key well. Routine core data of this well was analyzed by Flow Zone Index (FZI) method and FZI derived values were correlated with log derived porosity and water saturation of this well (NMR irreducible water saturation). Based on irreducible water saturation and porosity, permeability in well 1-32 was estimated, which matched very well with core data and Drill Stem Test (DST) analysis.

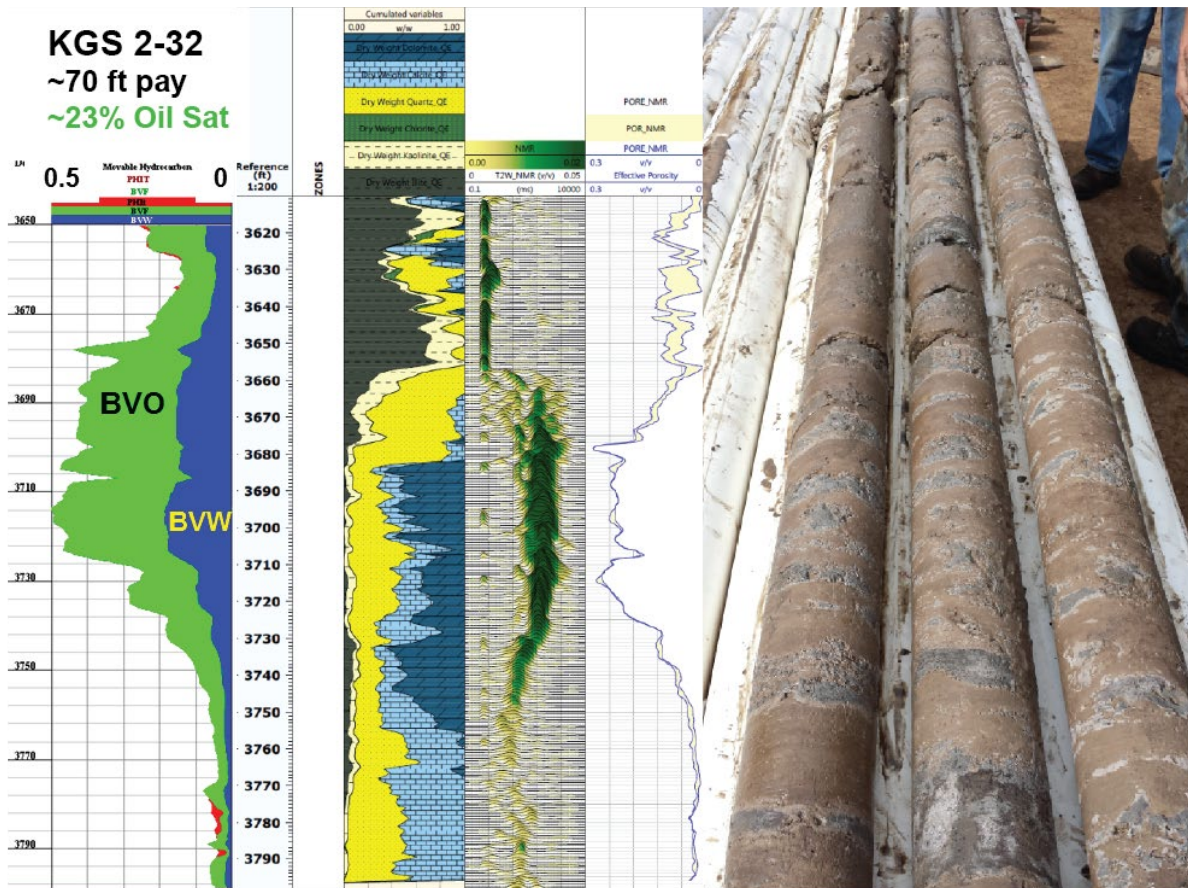


**Figure 3. Well KGS #2-32 estimation of based on magnetic resonance imaging (MRILtm) using porosity and T2 center of gravity versus core permeability (left) and NMR log derived porosity (PORE NMR) and water saturations (PC/SW and SW/IRR NMR).**

The application for Class II EOR well KGS 2-32 was filed by Berexco LLC and permitted by The State Corporation Commission of the State of Kansas (KCC). The permit was obtained to operate a CO<sub>2</sub> EOR well with 2000 bbls/day of water and 225 metric tonnes of CO<sub>2</sub> per day with maximum allowable operational well head injection pressure of 83 bar for water injection phase and 103 bar for CO<sub>2</sub> injection phase.

In addition to characterization, laboratory analyses, geological and reservoir modelling activities Kansas Geological Survey (KGS), Berexco LLC, and other team members: (1) drilled, cored, and logged new injection well KGS 2-32. Core and well logs were analyzed and interpreted. Flow units defined in previous phase of work were confirmed and geologic models were updated. Several core plug samples were collected and relative permeability and capillary pressure curves were derived and correlated with prior estimations to be utilized in reservoir simulation work.

A number of well tests were performed on newly drilled KGS 2-32 well. DST test was completed immediately after drilling commencement and after completion and additional well treatment SRT and interference well tests were performed and analyzed. Log derived permeabilities were correlated with well test derived values. Fracture gradient, operational pressures, and well communication for pilot injection area were confirmed. Measured reservoir

pressure at 5 well locations within pilot area ranged from 50 psi to 70 psi, a departure from initial 114 bar reservoir pressure.

Background geochemical water and oil sampling was deployed. Two different independent labs were used for this survey: Baker Hughes Oilfield Services and KGS internal laboratory. Also, pH and total dissolved solids measurements were analyzed routinely in the field for a background survey and as a part of EOR monitoring program. Inorganic and organic water components concentrations were measured.

Also, an IRIS seismic array that consists of 15 IRIS-PASCAL multicomponent seismometers were installed and placed on a cellular network to record background seismic activity at Wellington Field.

Wellington Field geomodel was updated (Fig. 2) with new data and detailed volumetric analysis and oil-in-place forecast was performed. It was estimated that an area with a radius of 1 km around KGS 2-32 well potentially holds up to 1.7M bbls of potentially recoverable oil and it was estimated that ~10% of this volume would be potentially accessible for performed CO<sub>2</sub> EOR. Forecast reservoir simulations were also performed based on newly updated geomodel.

### **Reservoir structural features**

Based on core observations, Formation Micro Imaging (FMI), dipole-dipole sonic logs, and regional earthquake focal mechanism analysis, the fracture intensity for a selected upper 35 m (115 ft) of Mississippian reservoir was present but estimated as low. Additional well test analysis and 3D seismic analysis reveal at least 12 vertical faults with NNE orientation at Wellington Field reservoir and adjacent Anson Bates field (Bidgoli, Schwab, Bidgoli, & Taylor, 2017). Moreover, using Amplitude Variation with Azimuth (AVAZ) pre-stack method for mapping of subsurface seismic anisotropy which is linked to subsurface stress field helped to map fracture density and orientation in the Mississippian reservoir (Fig. 1) (Graham et al., 2017). The effect of these well studied structural elements and fractures on fluid flow in the reservoir is discussed in this paper.

A field-wide 3D multi-component (converted wave) seismic survey was conducted at the Wellington Field. Both, well-log and seismic data exhibit high variability in porosity distribution throughout the field. Small faults with up to ~80 ft throw and systematic NE- and NW-trending fractures cut the dolomitic carbonate reservoir in Wellington Field. While effects of small faults and fractures have not been recognized by the operator of the decades-old waterflood in the Mississippian reservoir, potential concerns are raised about their impact on the dispersal, containment, and prediction of injected CO<sub>2</sub>.

Preliminary calculations of fault and fracture geometries were performed based on the seismic data in correlation with log analysis. These fault and fractures geometries were included in the existing reservoir model and will play an important role in decision making during the selection process of the suitable 5 spot pattern.

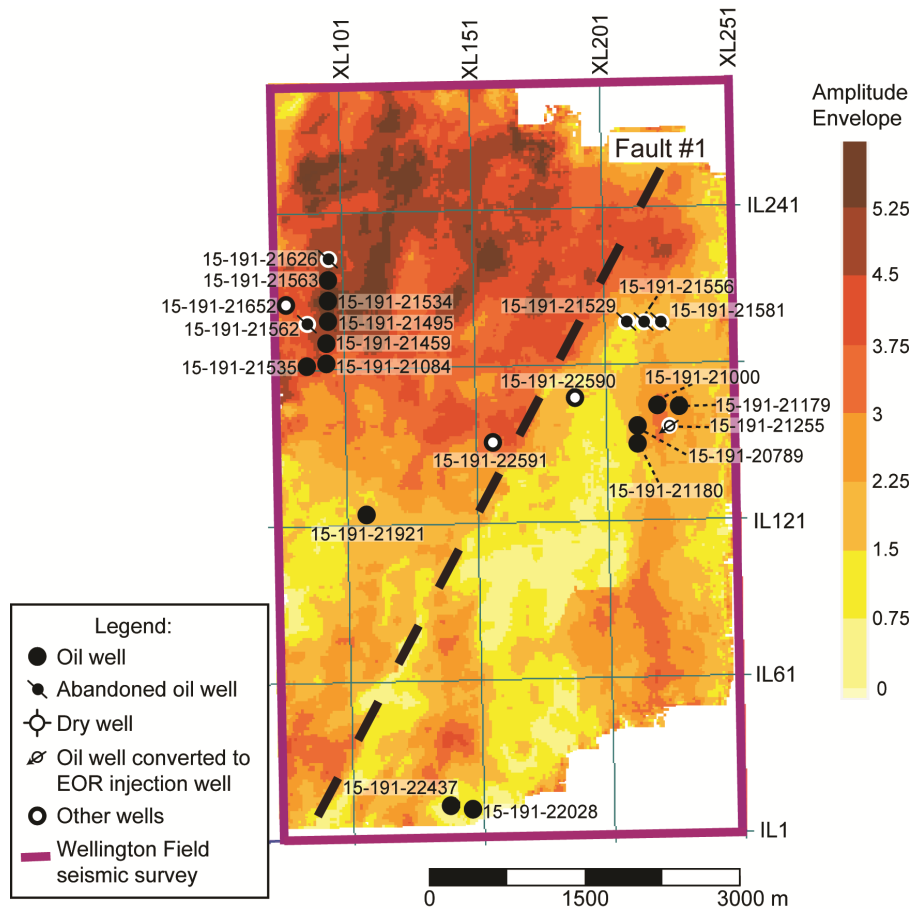


**Figure 4. Amplitude envelope map of the Mississippian reflection (top)**

Slices from a pre-stack depth-migrated seismic amplitude volume in Wellington Field highlighting suspected faults based on termination of seismic reflections. A 5-spot well injection pattern is shown that is impacted by the two faults (bottom).

### **Reservoir model: porosity, permeability, fluid saturations**

Schlumberger Petrel's volume attribute processing (i.e., genetic inversion) was used to derive a porosity attribute from the Pre-Stack Depth Migration (PSDM) volume to generate the porosity model. The seismic volume was created by re-sampling (using the original exact amplitude values) the PSDM 50 feet above the Mississippian and 500 feet below the Mississippian formation (i.e., approximate Mid. Arbuckle formation). The cropped PSDM volume and conditioned porosity logs were used as learning inputs during neural network processing. A correlation threshold of 0.85 was selected and 10,000 iterations were run to provide the best correlation. The resulting porosity attribute was then re-sampled, or upscaled (by averaging), into their corresponding 3-D property grid cell.

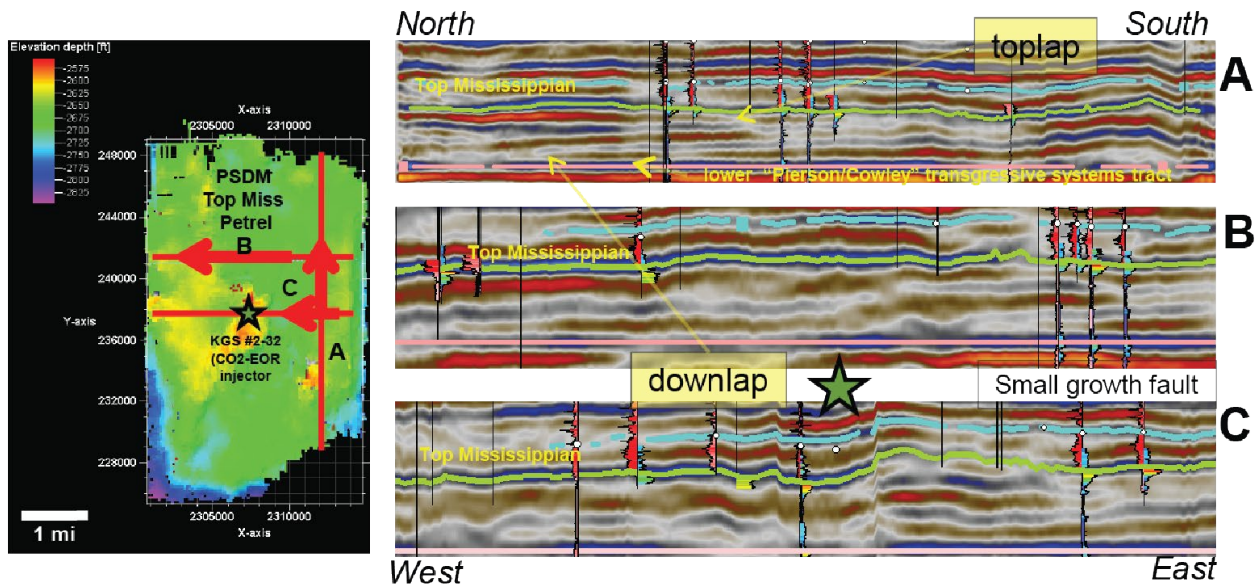


Figure 5. Seismic stratigraphy using PSDM

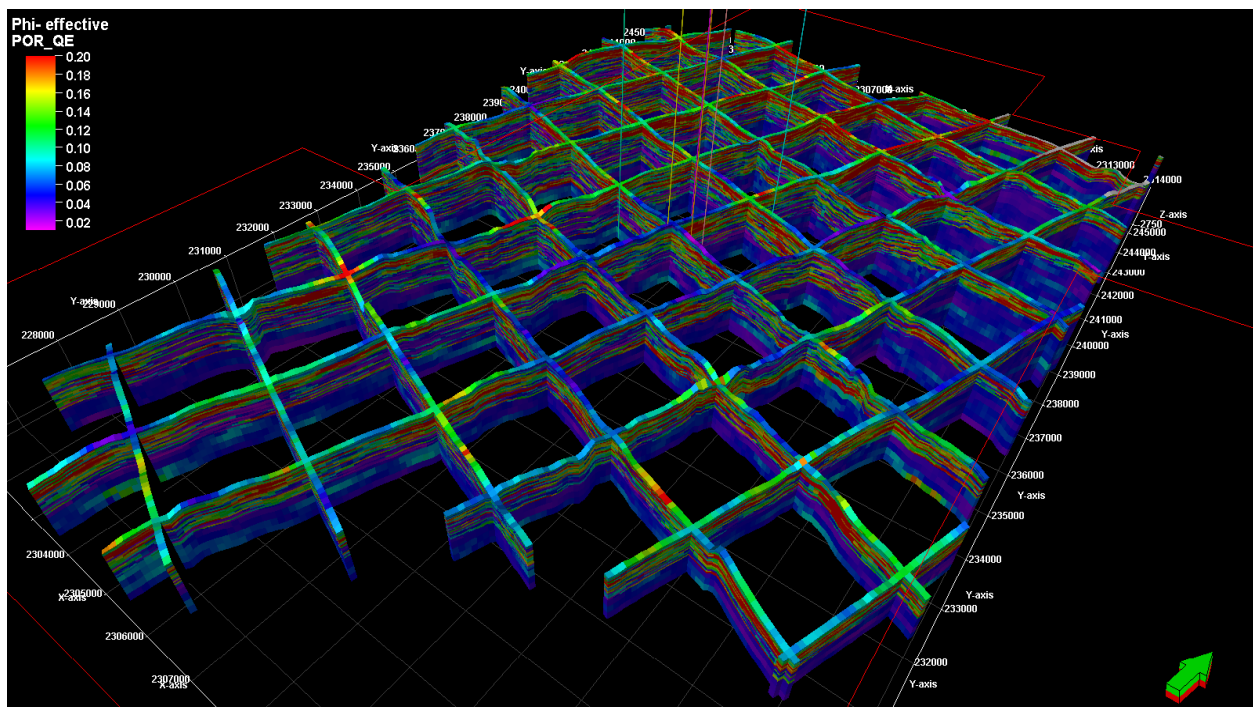


Figure 6. Porosity model

The porosity model was constructed using Sequential Gaussian Simulation (SGS). The porosity logs were upscaled using arithmetic averaging. The raw upscaled porosity histogram was used during SGS. The final porosity model was then smoothed. The following parameters were used as inputs: 1) Variogram type: spherical with nugget: 0.001; 2) Anisotropy range and orientation: lateral range (isotropic): 5000 ft, vertical range: 1-ft, distribution: actual histogram range (0.06–0.11) from upscaled logs; 3) Co-Kriging with secondary 3-D variable: inverted porosity attribute grid and correlation coefficient: 0.75. The porosity model is presented in Fig 3.

The upscaled permeability logs shown in were created using the following controls: geometric averaging method; logs were treated as points; and method was set to simple. The permeability model was constructed using Sequential Gaussian Simulation (SGS). Isotropic semi-variogram ranges were set to 3000-ft horizontally and 1-ft vertically. The permeability was collocated and co-Kriged to the porosity model using the calculated correlation coefficient (~0.70). The resulting SGS based horizontal and vertical permeability distribution (Fig. 7).

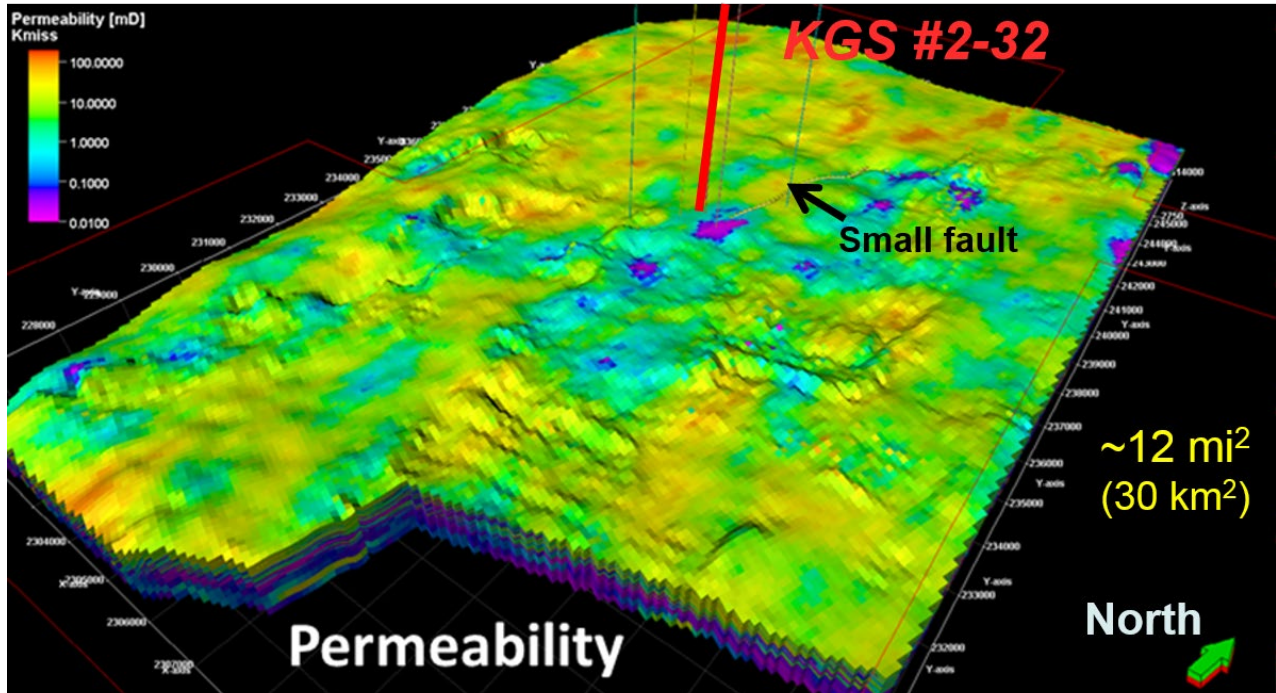
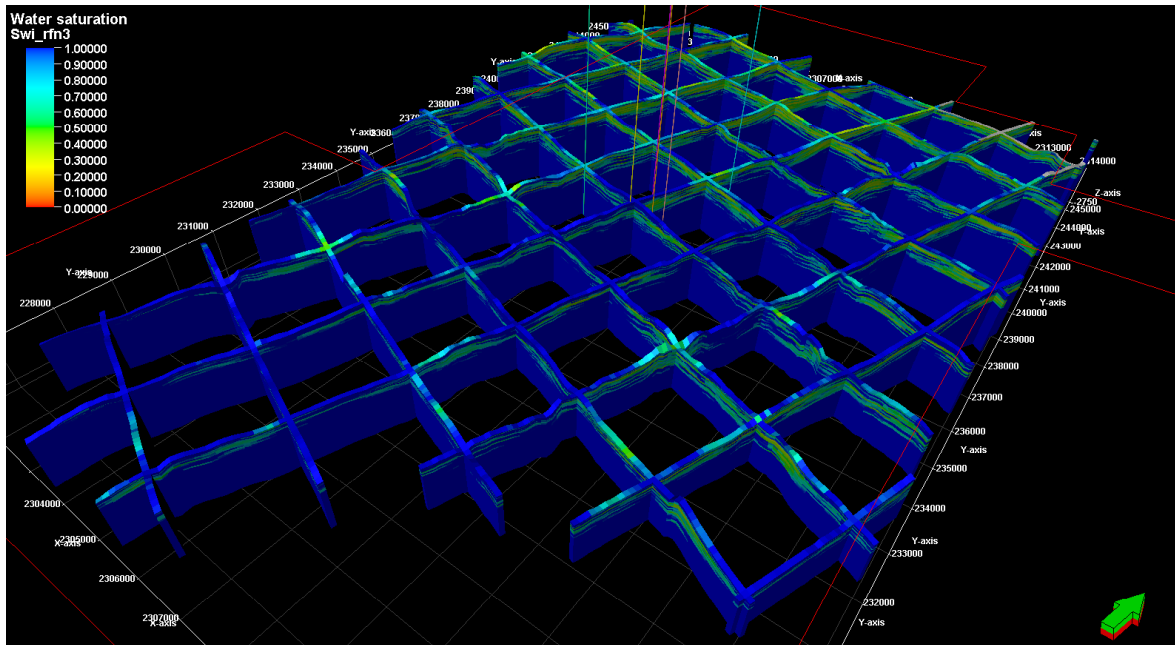


Figure 7. Permeability Model

In Mississippian reservoir, reliable initial water saturation from logs (which could be converted to irreducible water saturation) was not available. But there are NMR data in two of the wells which can provide irreducible water saturation in these wells. The water saturation model (Fig. 8) was derived based on existing porosity and permeability models and assigned Reservoir Quality Indicator (RQI) ranges.



**Figure 8. Updated water saturations model for Wellington Field**

### Capillary pressure and relative permeability

In the absence of special core analysis data, NMR data of Well 1-32 were used to drive capillary pressure curves for different zones of the reservoir and they are on generalized capillary pressure curves and NMR irreducible water saturations. Also, core relative permeability data were missing. Based on estimated end points from well 1-32 and generalized data from other fields, relative permeability curves were generated for all rock types. This method is explained in more detail in Appendix A.

### Reservoir pressure and temperature

Based on temperature log of 1-28 and DST flowing temperature of well 1-32 (DST 2) and well 1-13 in nearby Wildcat field, temperature in the Mississippian reservoir at the Wellington Field was estimated as 121 degree F. To get the initial pressure of the Mississippian reservoir and old DST data before water-flood during early production were studied. Pressures from DSTs in Arbuckle formation for the well KGS #1-32 and #1-28 were extrapolated to get the initial pressure in the Mississippian reservoir. From these calculations it can be concluded that initial pressure in the Mississippian was around 1480 psi with pressure gradient of 0.48 psi/ft. Current reservoir pressure at Wellington Field is measured as 1100 psi.

### Laboratory CO<sub>2</sub> miscibility analysis for Wellington Field conditions

A 40 ft sand packed slim tube equipped with a high-pressure glass capillary and a dome loaded back pressure regulator was used for the multiple contact miscibility study. The porosity of the sand is 35% and the permeability is approximately 1.5 Darcy. The cleaned slim tube was saturated with toluene. The back-pressure was set at the Wellington Field reservoir conditions and the toluene was displaced by a minimum of 2 pore volumes of crude oil.

The CO<sub>2</sub> was injected at constant rate of 125 cc/min using a motorized high pressure pump. The oil produced in the separator at the end of the test was recorded and the oil recovery as function of the original oil in place was calculated for each displacement. Six displacement test were conducted at various back pressures. Minimum Miscibility Pressure (MMP) was found to be within operational range of reservoir conditions.

### **Field operations**

Well KGS 2-32 was perforated from 1,116 m to 1,124 m (Fig. 3) and treated for optimized performance. Several wells within pilot area were re-entered and treated as well. Because Wellington Field is primarily oil producing field and as no significant gas production history, gas separation units and gas flow meters had to be installed at well locations and field battery that collects fluid from pilot area.

The CO<sub>2</sub> injection plan assumed that 100-200 metric tons of CO<sub>2</sub> would be injected daily until a total projected volume of approximately 20,000 metric tonnes was reached by mid-June, 2016. The CO<sub>2</sub> will be transported to the site in trucks in liquid state at a pressure of approximately 17 bar and temperature of -24°C in a liquid state with each truck delivering 20 tons of CO<sub>2</sub>. Surface facilities consisted of: seven portable tanks that could hold up to 70 tonnes of cooled and pressurized CO<sub>2</sub> delivered by trucks; pump system; programmable logic controller (PLC) that can manipulate the control valve in order to not exceed the maximum specified flow rate and to ensure that the bottom hole pressure in the injection well does not exceed the maximum allowable pressure. Total of 1,101 truckloads, 19,803 metric tons, average of 120 tonnes per day were delivered over the course of injection that lasted from January 9 to June 21, 2016. Total expenditures for purchasing CO<sub>2</sub> were \$1,964,000 with overall price for CO<sub>2</sub> of \$90.16 per US ton.

Reservoir pressure recordings were obtained through well testing and fluid level measurements of inactive wells. These pressures were correlated with reservoir simulations to capture field performance dynamics and to guide re-pressurisation of the field (Fig. 9). Also, post water injection sensitivity studies were performed to choose an optimal water injection scenario for pos-CO<sub>2</sub> operations panning. In order to achieve estimated Minimum Miscibility Pressure (MMP) of 120 bar based on reservoir simulations it was planned: (1) to keep current continuous injection volumes for pilot area; (2) inject additional water through KGS 2-32 well at phased rate of 17 and 40 tonnes/day for a duration of approximately one month before the start of CO<sub>2</sub> injection; (3) continue with water injection at 82 tonnes/day at KGS 2-32 after CO<sub>2</sub> injection commences.

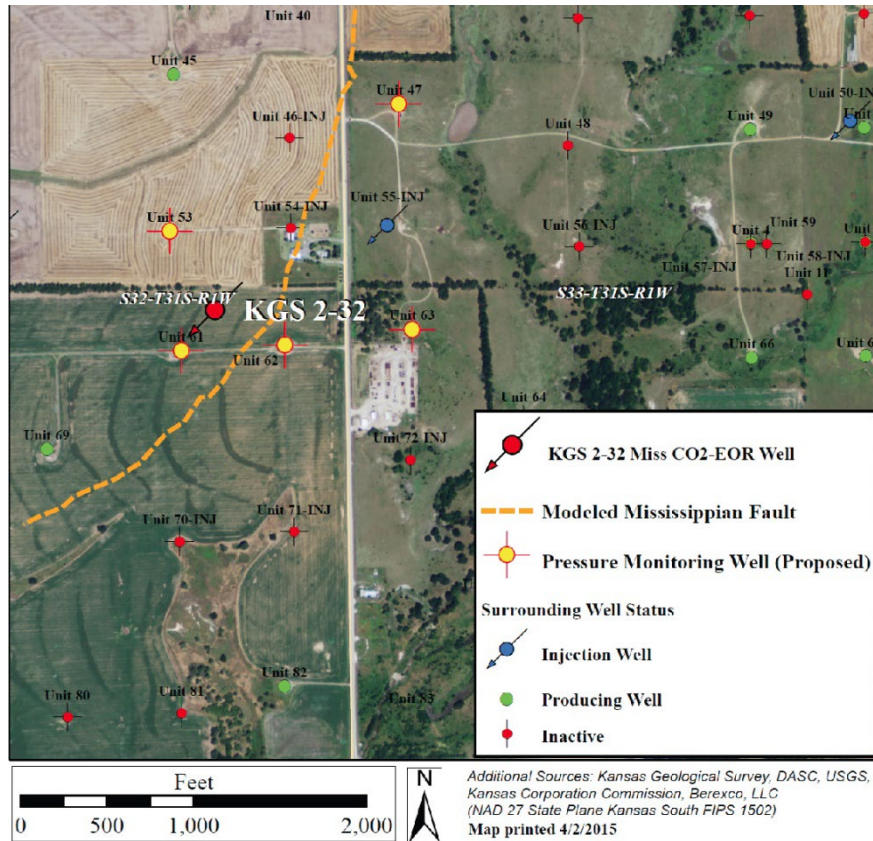


**Figure 9. Pilot area aerial map with marked injection wells, sampled wells, and wells used for SRT Monitoring survey**

Geochemical water analysis of organic and inorganic components was performed in order to understand if this method could be used as an early CO<sub>2</sub> detection system, as a plume location and containment method, and in order to understand a degree of impact of CO<sub>2</sub> on mineral composition, detect changes in water and rock geochemistry as a result of injection. Along with geochemical survey, pressure and production data was recorded at wells and tank batteries.

Based on reservoir simulations, wells surrounding CO<sub>2</sub> injector were grouped in three areas: two inner circles with the radiuses of 182 m and 460 m. Wells within this radius were sampled weekly during the course of CO<sub>2</sub> injection, since January 9, 2016. Wells within third radius of 1 km around KGS 2-32 were sampled after initial break-through at the wells of the first inner circle; however, sampling interval for these wells was chosen according to flood performance and was not strictly set from the beginning of the injection. In total, analysis of 17 wells surrounding injector well was performed. Additional geochemical sampling was performed by contracting Baker and Hughes Oilfield Services that conducted monthly since the start of injection.

Total dissolved solids and pH measurements were analyzed in the field and alkalinity analysis was performed in the lab shortly after sample arrival. These results were used as an early detection for CO<sub>2</sub> arrival at well locations (Fig. 10). On average, wells started to produce CO<sub>2</sub> approximately 2-3 weeks after initial increase in alkalinity. However, some wells did observe

alkalinity increase without free gas production. Collected data contains: cation, anion, and organic components.

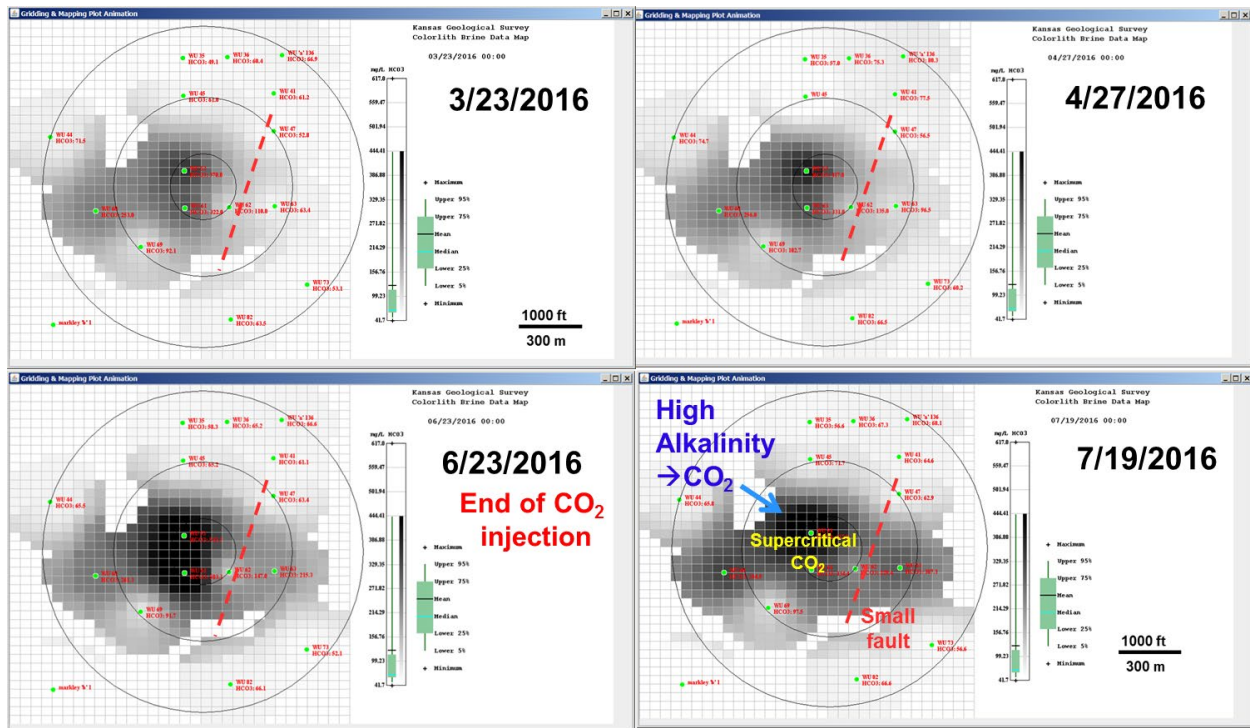


Figure 10. Alkalinity progression

## Reservoir simulations

The main goal for this task of numerical simulations was to determine the outline of the CO<sub>2</sub> front for optimal monitoring of the EOR performance, efficiency, and CO<sub>2</sub> movement in through existing structural elements.

The reservoir simulations were conducted using the Computer Modeling Group (CMG) GEM simulator. GEM is a full Equation of State compositional reservoir simulator with advanced features for modeling the flow of three-phase, multi-component fluids. The code can account for the thermodynamic interactions between three phases: liquid, gas, and solid (for salt precipitates). Mutual solubilities and physical properties can be dynamic variables depending on the phase composition/system state and are subject to well established constitutive relationships which are a function of the system state (pressures, saturation, concentrations, temperatures, etc).

The Petrel based geomodel mesh discussed above consists of 130 x 114 horizontal grid and 32 vertical layers for a total of 451,887 cells. The model domain encompasses a 1.56 miles<sup>2</sup> area and the formations from the base to the top of Mississippian formation. This grid with populated reservoir parameters (permeability, porosity, and water saturation) was imported to CMG Builder where other reservoir properties discussed above were applied. Boundary conditions were determined as Carter-Tracy aquifer with allowed leakage. Historical matching of the field performance was performed with CMOST software from CMG.

Based on preliminary models, the CO<sub>2</sub> front movement is going to be affected by several factors: 1) Existing water flood creates pressure gradients which will stir CO<sub>2</sub> front; 2) Existing faults and associated damage zone are likely to contain and redistribute CO<sub>2</sub> in the reservoir, influencing and directing CO<sub>2</sub> movement (Fig. 11); 3) The most efficient EOR is predicted to be in the vicinity of mapped fault; however, this hypothesis, needs further verification with field implementation; and 4) it is planned to monitor CO<sub>2</sub> front movement with additional seismic equipment (passive and active components) and chemical tracers for improved control and verification of the model. Based on reservoir simulations, optimization patterns for post CO<sub>2</sub> water injection were selected for optimal reservoir performance (Fig. 12).

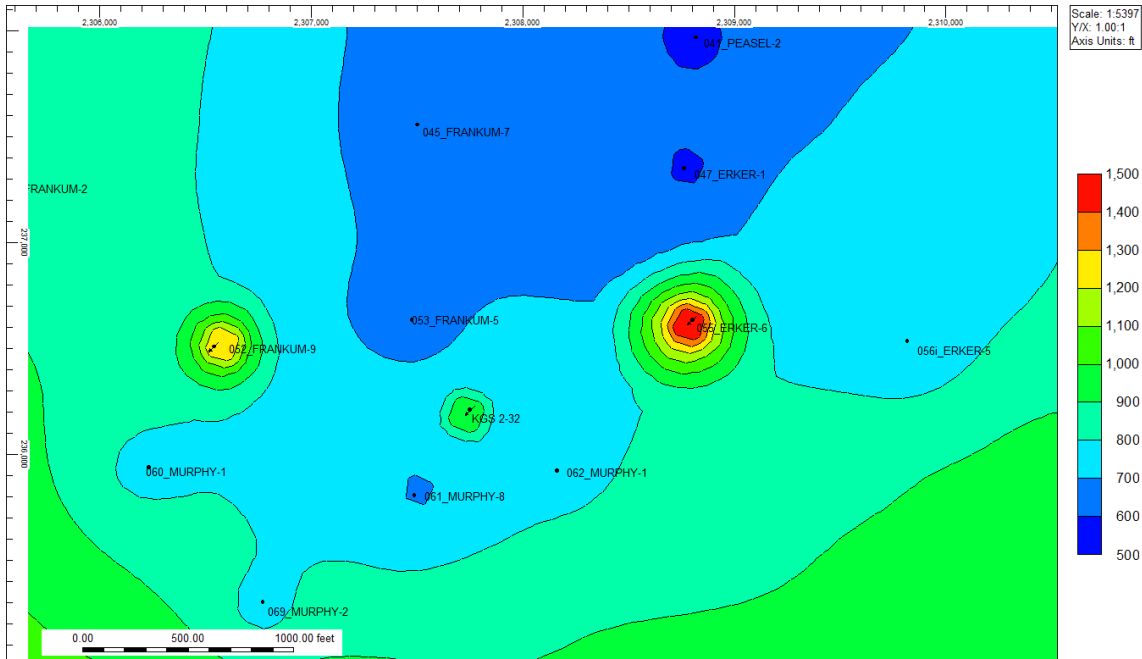


**Figure 11. Modeled and history matched reservoir pressure distribution map (delta psi)**

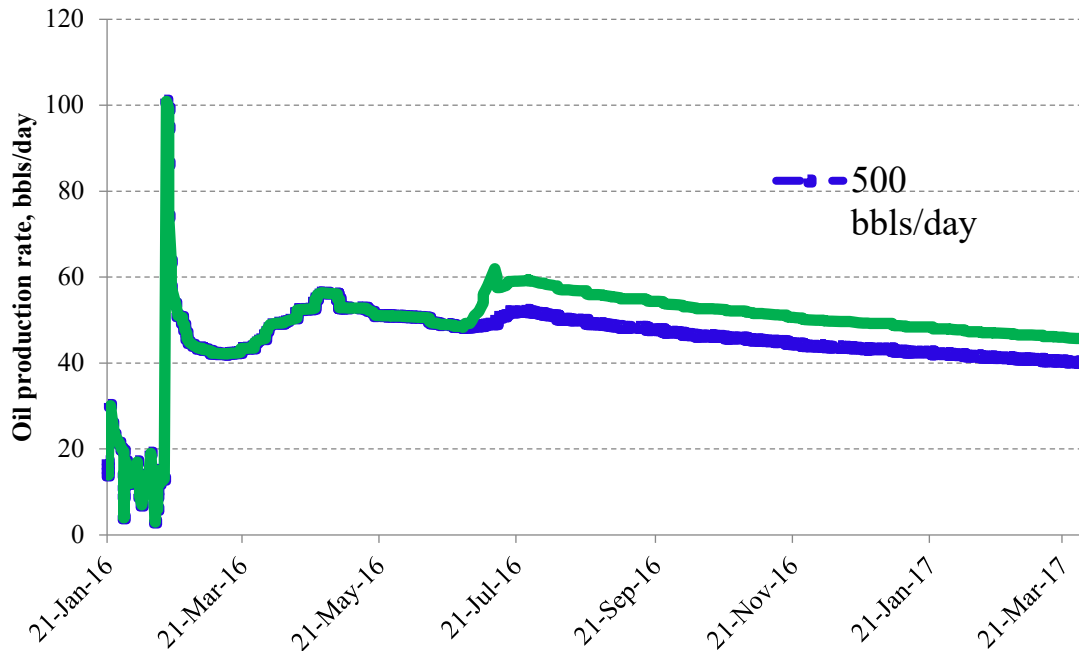


**Figure 12. Modelled oil production forecast that explores sensitivity to water injection volumes at KGS 2-32**

## Results

It is safe to say that, main objectives of this study were met. The CO<sub>2</sub> EOR flood at Wellington Field was carried out safely and efficiently. Oil production has increased with current steady performance: no decline signatures were detected yet. Current incremental average oil production rate is 34 bbls/day and a total of incremental 6,300 bbls of oil were produced by the end of September, 2017 (Fig. 13).

CO<sub>2</sub> injection was performed in a highly controlled and monitored environment (Fig. 14), which is in line with developed rapid-response detection & mitigation procedures and could be applied towards operation & risk management plan for EPA Class VI Well Permit. Simple but robust monitoring technologies proved to be very efficient in detection locating of CO<sub>2</sub>. High CO<sub>2</sub> reservoir retentions with low yields within actively producing field could help to estimate real-world risks of CO<sub>2</sub> geological storage. Only 18% of injected CO<sub>2</sub> was produced back (Fig. 13).

Overall Wellington Field is proving to be a viable field laboratory with high degree of control and understanding of reservoir dynamic performance (Fig. 15).

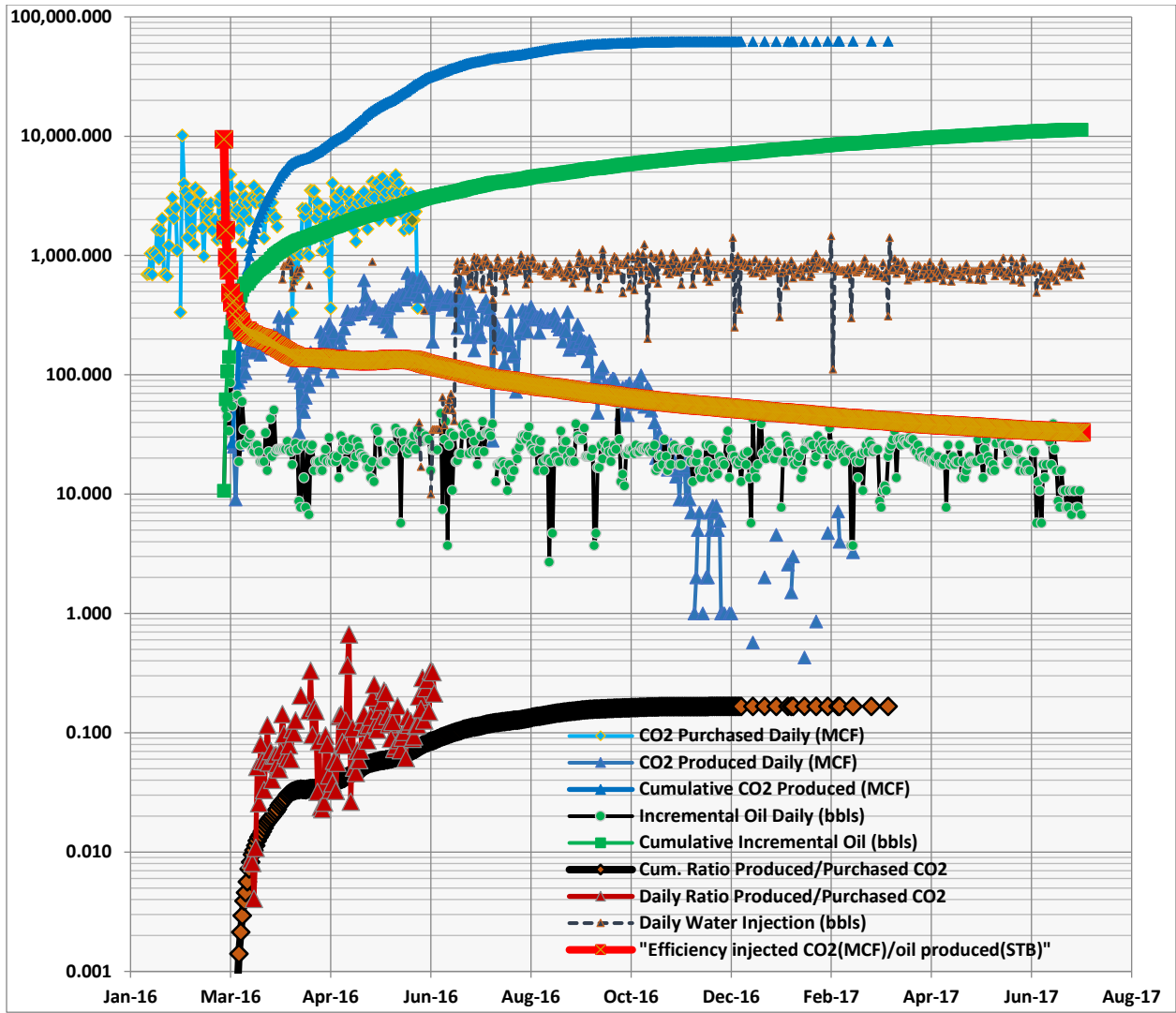


Figure 13. CO<sub>2</sub> injected and CO<sub>2</sub> and oil recovered in pilot scale injection in the Mississippian oil reservoir in Wellington Field.

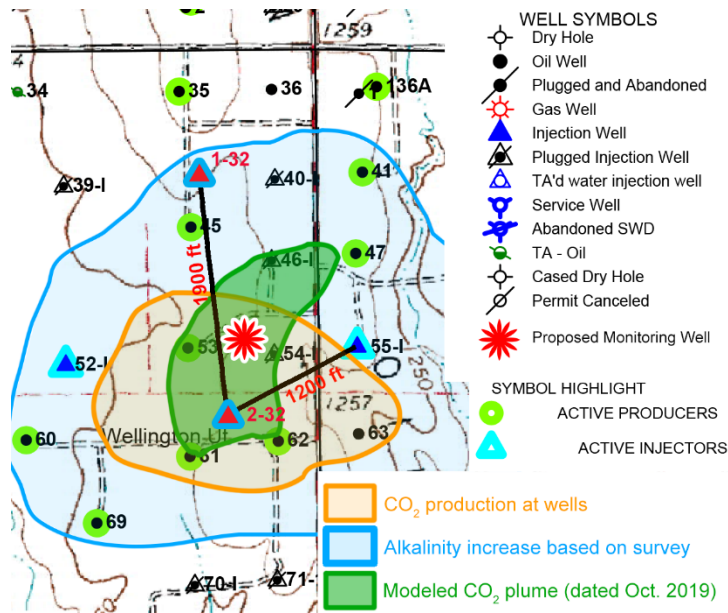


Figure 14. Wellington field map showing well locations and the extent of the CO<sub>2</sub> plume (orange outline) versus observed alkalinity increase versus predicted by simulations CO<sub>2</sub> plume (green outline)

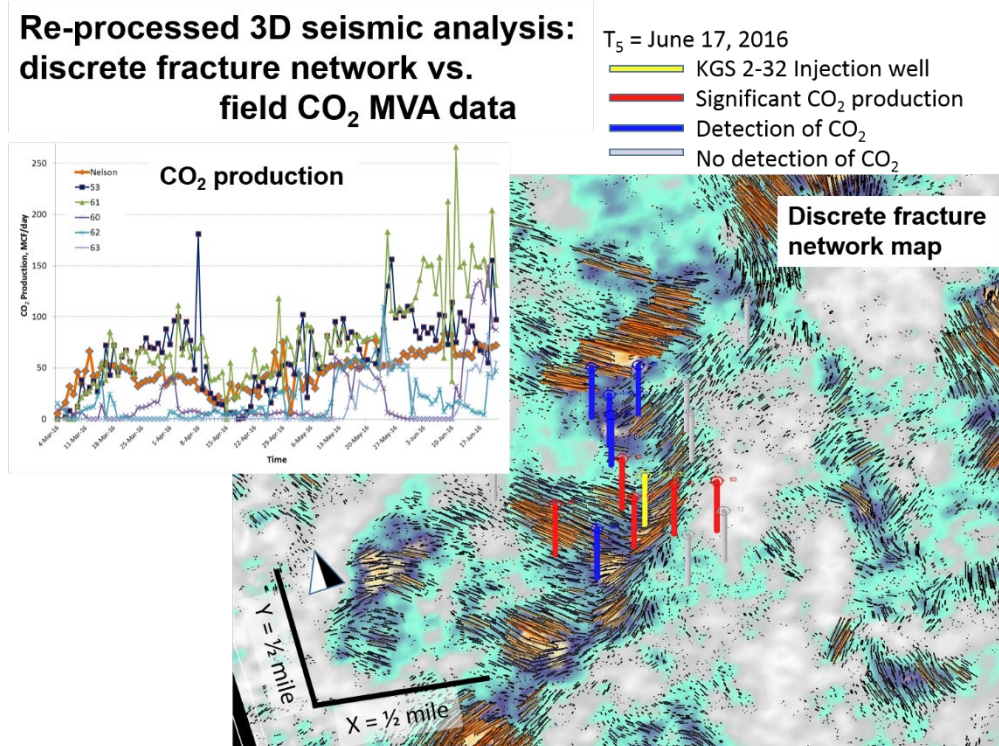


Figure 15. Re-processed 3-D seismic showing fracture network, surveyed well locations, and the extent of the CO<sub>2</sub> plume.

## Decline curve analysis

Harmony software calculated the cumulative oil production for each curve in the table below from the start of the forecast to April 2027. The difference between the two cumulative oil productions is the cumulative additional oil by CO<sub>2</sub> flood (the area between the two curves in Figure 16). The area between the curves equals to ~32 Mstb, which is the cumulative additional oil production by only CO<sub>2</sub> flood. Cumulative oil production by CO<sub>2</sub>+waterflood from initial CO<sub>2</sub> response to April 2027 is ~69 Mstb (Table 1). However, additional observations may change the slope.

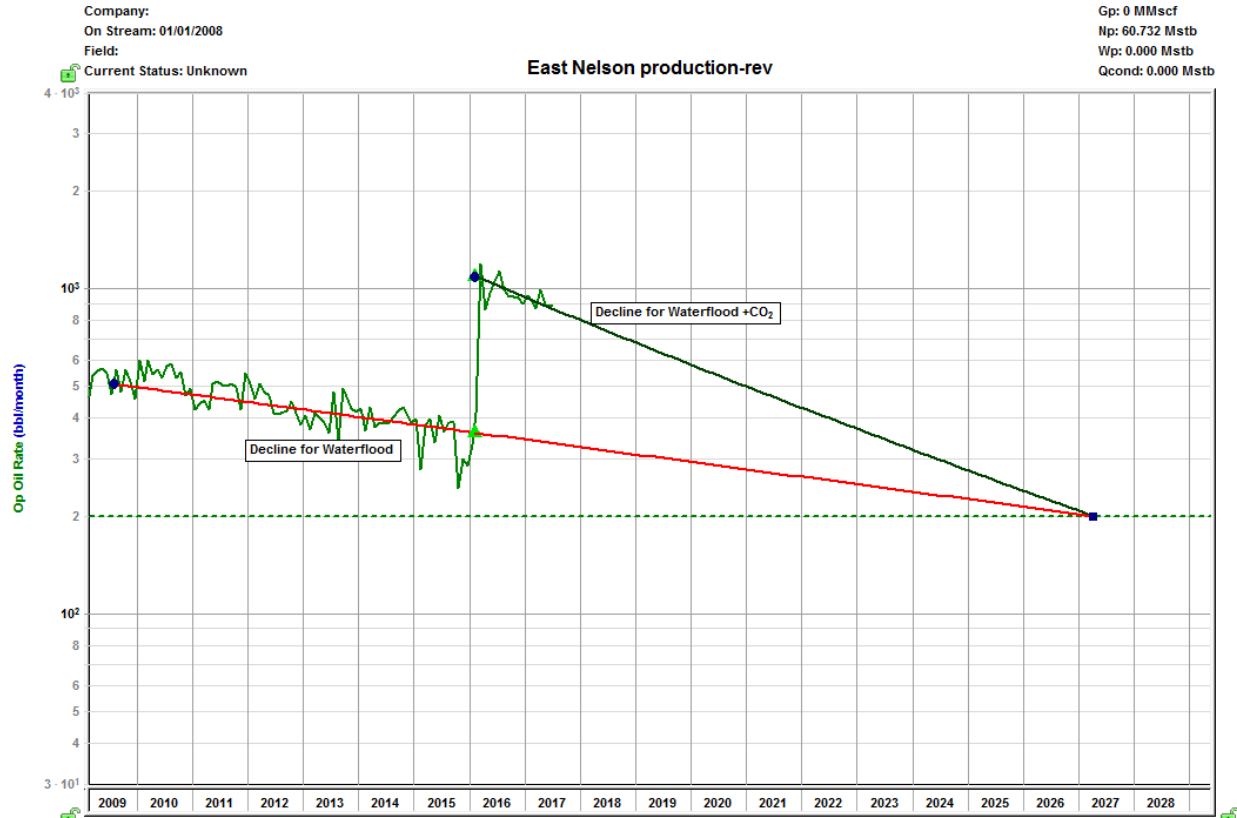


Figure 16. Decline curve analysis for Wellington Field.

Table 1. Cumulative oil production predictions

		Oil Decline							
		From Start of Decline	From Start of Forecast						
Display Name	Analysis Name	Start Date	Initial Oil Rate	Forecast Start Date	Initial Cumulative Oil Production	End Date	Delta Time	Delta Cumulative Oil Production	
		MM/DD/YYYY	stb/d	MM/DD/YYYY	Mstb	MM/DD/YYYY	month	Mstb	
1	East Nelson production-rev	C02 +Waterflood	02/01/2016	35.9	02/01/2016	44.894	04/06/2027	134.134	68.982
2	East Nelson production-rev	Waterflood only	08/01/2009	11.8	02/01/2016	44.894	04/06/2027	134.134	36.542

## Site Characterization and Modeling for Arbuckle Saline Aquifer CO<sub>2</sub> Injection

The Arbuckle Group is a 600-1,000 ft thick and more than 3,500 ft deep carbonate saline aquifer and historically has been a good candidate for various waste disposal operations, such as oil field brine and chemical plant waste disposal. The Arbuckle is currently being considered for commercial scale CO<sub>2</sub> geological storage it is centrally located to multiple major point sources of CO<sub>2</sub> emissions and a large existing pipeline system with established right-of-ways that may be useful for implementing commercial-scale distribution from CO<sub>2</sub> source to sink.

Class I and Class II wells for waste water and hazardous waste disposal have many decades of operation in Kansas (Fig. 17) with hundreds of millions of barrels of oilfield backflow water and hazardous waste disposed over the years in various geologic formations across the state. Only in recent years, with developments of Mississippian Lime Play (MLP) and its high water cuts ranging up to 95%, concerns have been raised due to increase in seismic activity associated with the injection of many 10's of millions of barrels of back-flow brine Arbuckle Group interval. In the area of high volume brine disposal, the Arbuckle overlies a portion of the late Proterozoic Midcontinent Rift System consisting of a km's thick succession of low porosity arkosic sediment, volcanics, and igneous intrusives that are cut by a complex fault network. Some of these older faults were reactivated during the Paleozoic offering the potential permit waste water to enter the basement.

Prior to MLP developments, Arbuckle was extensively used as a disposal target; however, injection volumes rarely exceeded 2,000 bbls (325 tonnes) of brine per day, according to The State Corporation Commission of the State of Kansas (KCC) reported injection volumes. In the early days of MLP development the allowed daily brine injection rates were set to 20,000 bbls per day. With rapid developments of MLP some companies started to operate permitted disposal wells at full capacity that have not been observed before. Some wells even had twin wells that were drilled within few tens of meters from each other and were permitted to inject at the same rate. However, Kansas Corporate Commission (KCC) issues two consecutive orders that downscaled the allowed injection rates within specified areas. Currently, since August 2016, injection rates will be reduced from 16,000 to 8,000 bbls/day within in areas of concern spanning 1,500 sections of Harper, Sumner, Kingman, and Sedgwick counties.

To compare these developments with potential CO<sub>2</sub> geological storage scenario: previously allowed rate of injection of 3,250 tonnes of brine day is roughly equivalent to 1,700 tonnes of CO<sub>2</sub> per day and injected mass of brine of 17.2M tonnes for 2014 in Harper County, KS is roughly equivalent to 9M tonnes of CO<sub>2</sub> per year. This means that some brine disposal wells operated at a rate of comparable to commercial scale CO<sub>2</sub> storage project, and the brine disposed in Harper County is equivalent to the simultaneous operation of nine commercial scale CO<sub>2</sub> geological storage projects. It should be noted that brine disposal volumes in adjoining counties across the Kansas-Oklahoma border were even larger and we believe this combined volume of brine has contributed to the regional induced seismicity.

There is an evidence from independent pressure monitoring gages, UIC Class I well monitoring records, and other sources of regional fluid level and pore pressure increases in Arbuckle reservoir in Kansas and Oklahoma. Competing interests of various industrial groups that include oil and gas, chemical complex, and potentially CO<sub>2</sub> geological storage could collide in the future if regulatory framework is not outlined and expanded.



consists mainly of white, buff, light-gray, cream, and brown crystalline dolomite (Zeller, 1968). Chert is possible in the upper portion of the Arbuckle Group. The top of the Arbuckle in the central portion of Sumner County is at a depth of approximately 4,000 ft below land surface. The Arbuckle Group is regionally extensive throughout Kansas with the exception of some structurally high areas on the Central Kansas uplift and the Nemaha anticline where the Arbuckle has been removed by erosion (Carr, 1986). The elevation to the top of the underlying Precambrian basement in Sumner County varies from 0 ft mean sea level (MSL) in the northeast to -6,000 ft MSL in the southwest (Fig. 19). The Arbuckle generally thickens as a whole from north to south and is thickest (up to 1,100 feet) in south-central Kansas. The east-west and north-south cross sections in Figure 20 highlight the lateral continuity of this group at the Wellington site and in Kansas of the Ozark Plateaus aquifer system and the adjoining Pennsylvanian and Precambrian systems (from Carr et al., 2005).

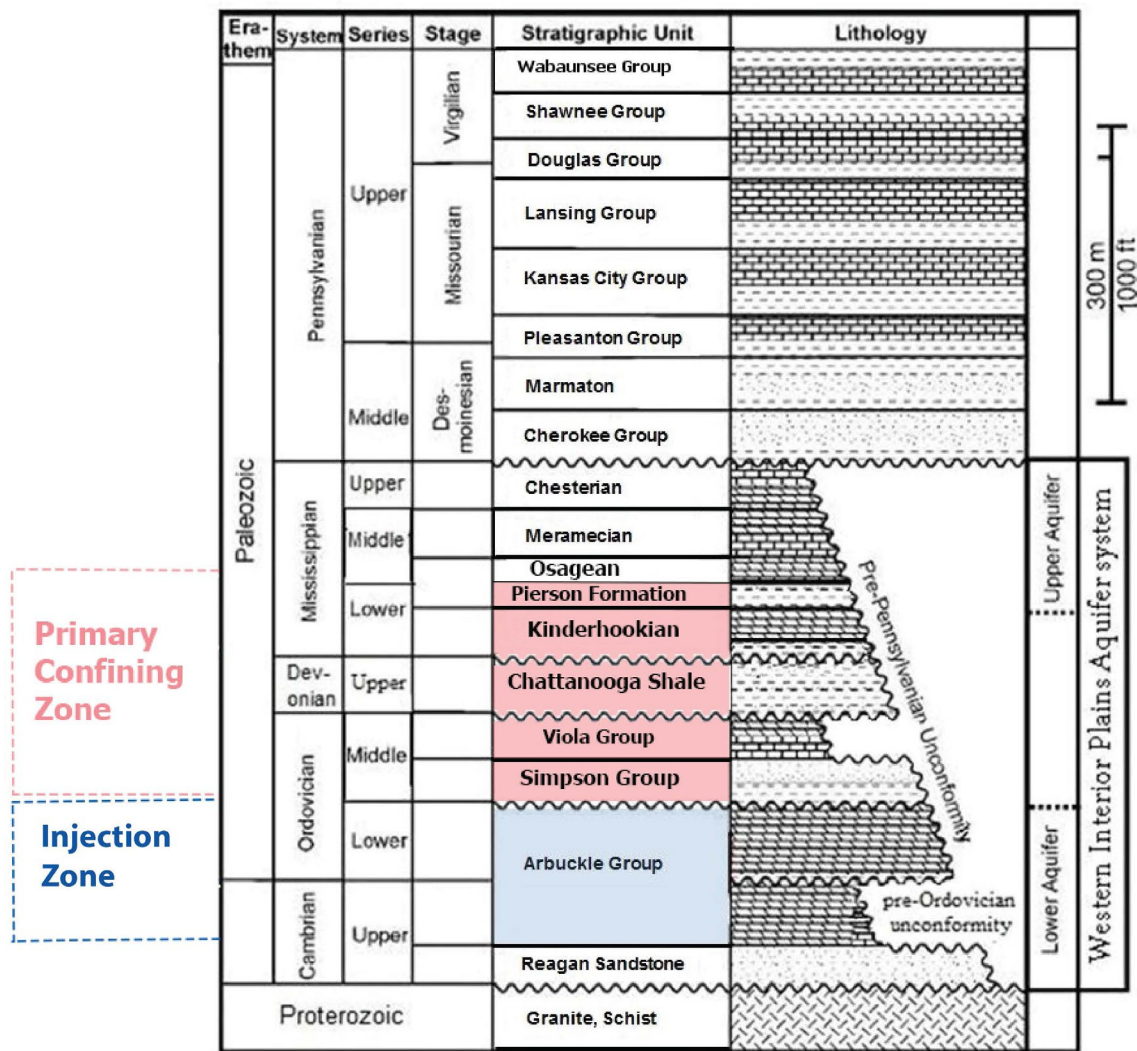


Figure 19. Generalized stratigraphy of Kansas showing the relative position of the lower and upper aquifers

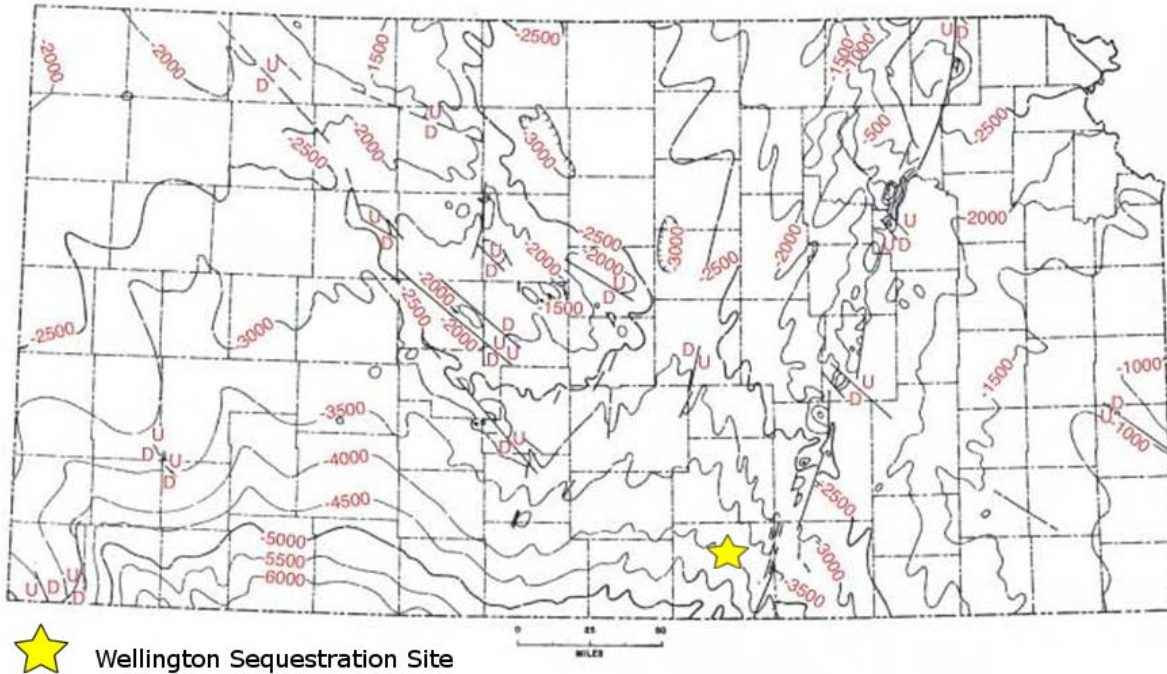
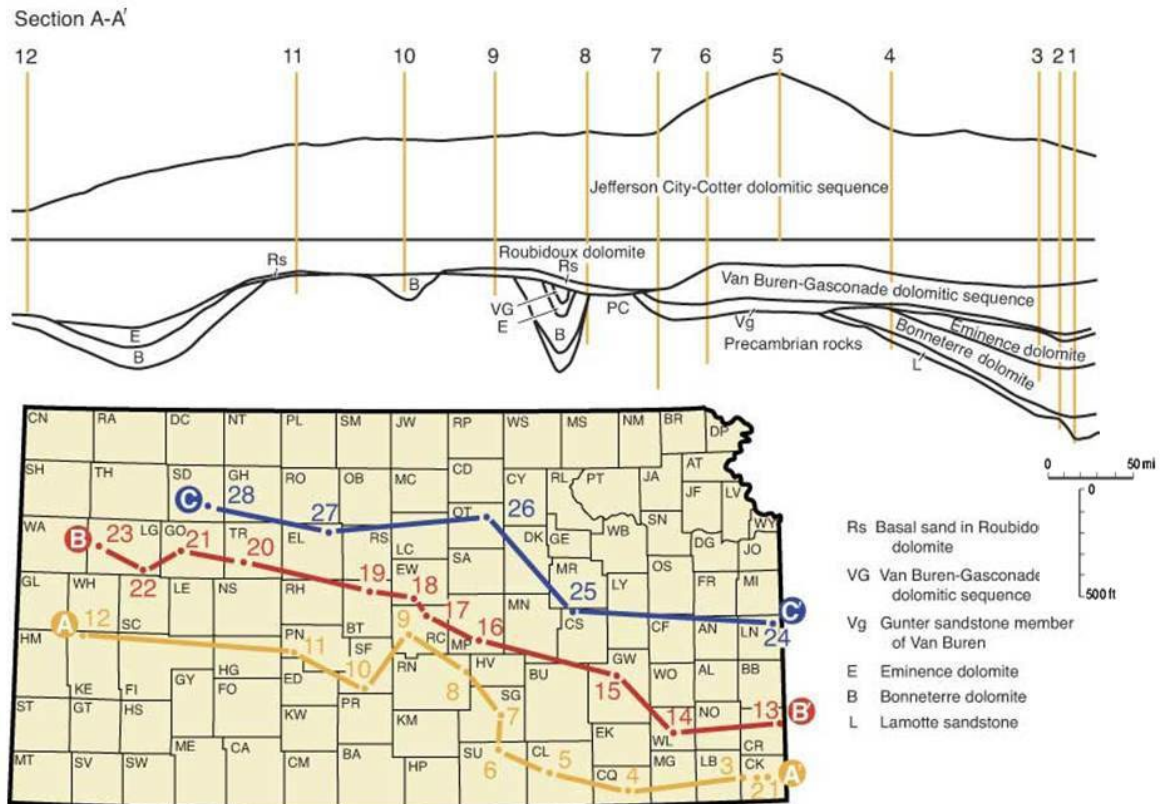
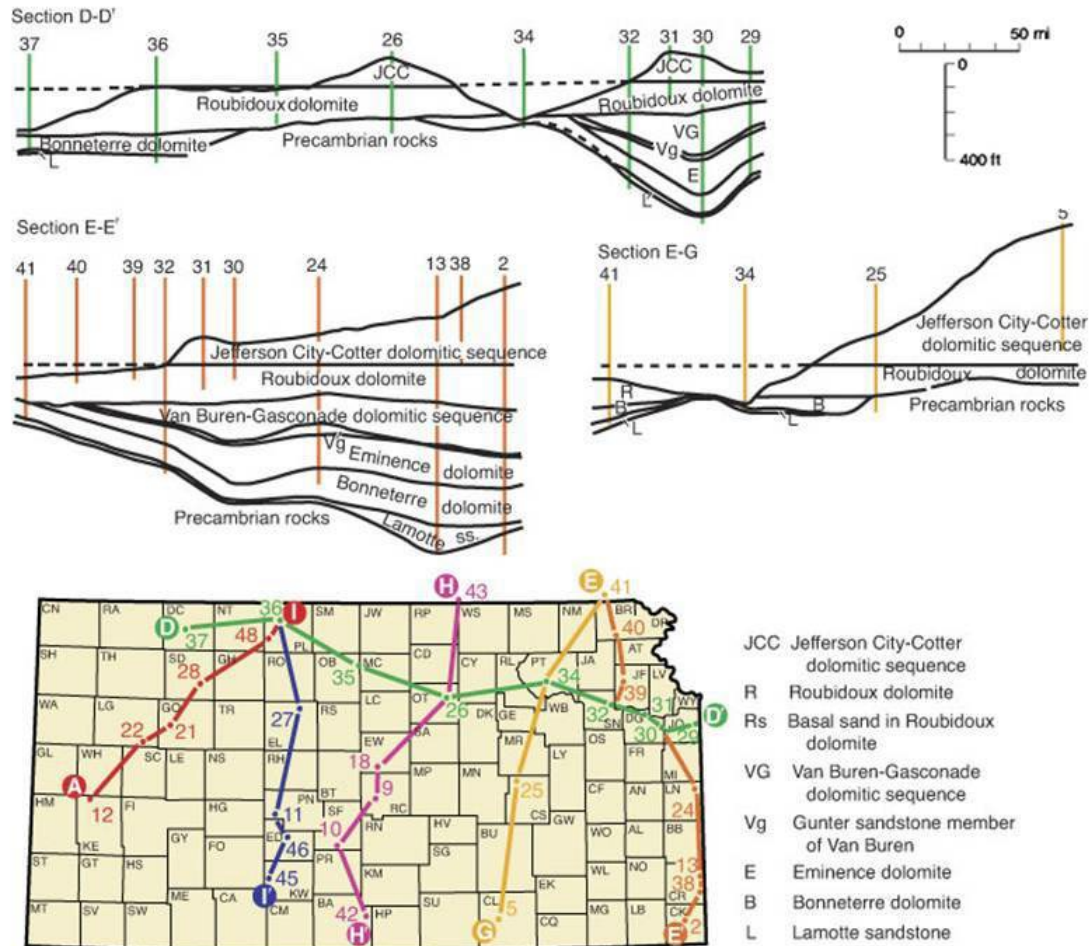


Figure 19. Elevation (ft MSL) to top of Precambrian basement complex in Kansas (from Franseen, 2004)





**Figure 20. Diagrammatic east-west cross section of Cambrian-Ordovician (Arbuckle Group) strata across Kansas (top) and diagrammatic north-south cross section of Cambrian-Ordovician (Arbuckle Group) strata across Kansas (bottom) (from Franseen et al., 2004).**

## Hydrogeology

The Arbuckle aquifer systems in Kansas, Missouri, and Oklahoma make up one of the largest regional-scale saline aquifer systems in North America and are present in both the Western Interior Plains aquifer system (WIPAS) and the Ozark Plateaus aquifer system (OPAS). The WIPAS underlies almost all of Kansas. Table 3.1 lists the stratigraphic units along with the associated geohydrologic units that make up the WIPAS and the geologic units overlying it. The WIPAS is similar to the OPAS, which lies to the east in parts of Missouri and southeastern Kansas. Unlike the OPAS, the WIPAS is naturally saline and yields no freshwater (TDS <1,000 ppm) (Faber, 2010). Sumner County lies in the WIPAS, and Arbuckle brine concentrations within the county are significantly in excess of 10,000 mg/l salinity. The salinity decreases significantly in the eastern part of the state, where the WIPAS merges with the OPAS. Another key feature of the Arbuckle salinity distribution in Kansas is the general increase in Arbuckle TDS from north to south (Fig. 21).

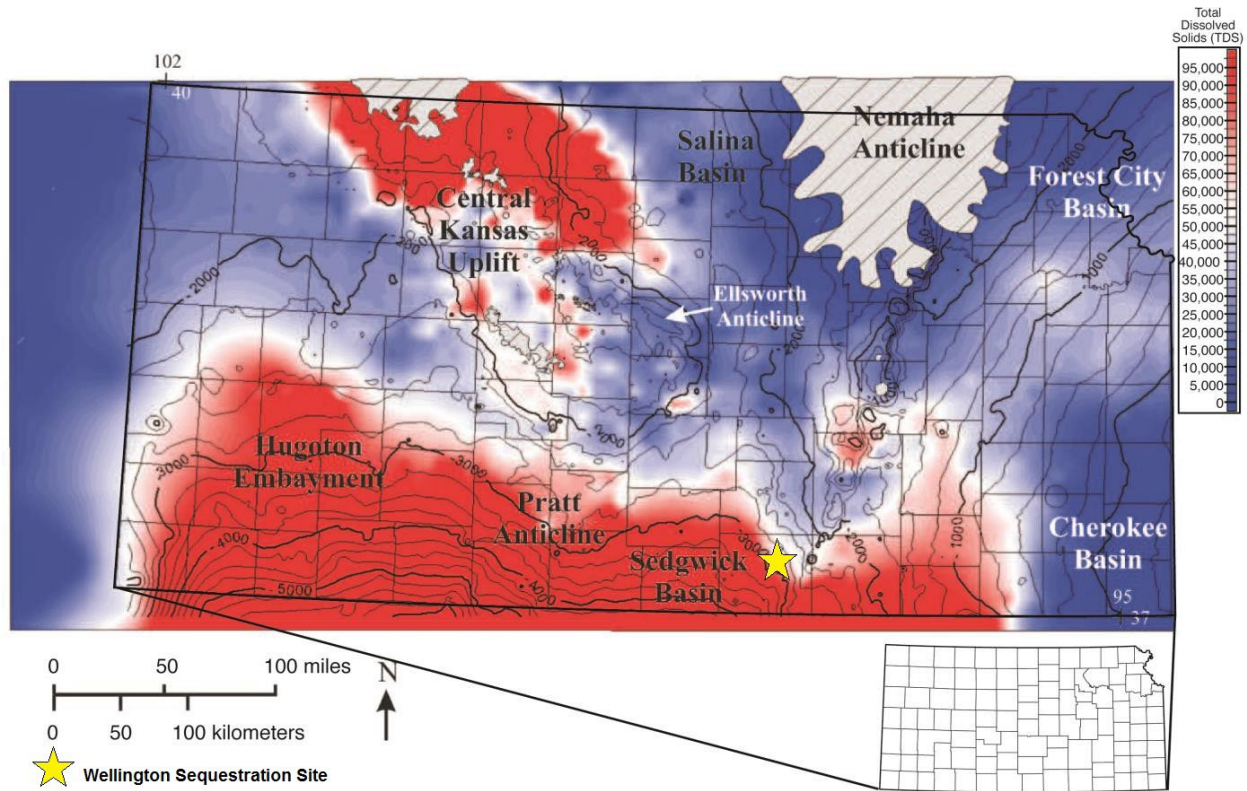


**Figure 21. Total dissolved solids (ppm) in Arbuckle brines. Overlay is the structure (ft, msl) on top of Arbuckle (from Carr et al., 2005).**

Brine salinity distribution in the Arbuckle is also associated with structural features. Dense brines along the Kansas-Oklahoma border are concentrated in Arbuckle structural lows, particularly in southwestern Oklahoma. Arbuckle brine salinity slowly decreases northward and along the eastern side of the Nemaha anticline. An area of relatively dense brine surrounds the Cambridge Arch (northern part of the Central Kansas uplift) and extends southward along the east side of the Central Kansas uplift. On the Central Kansas uplift, small areas of increased TDS concentrations are associated with areas where the Arbuckle has been removed by erosion, or the high tops may be partly due to brine injection from oil field operations (Jorgensen et al., 1993). Relatively low-salinity WIPAS brines (TDS 5,000–20,000 ppm) are located along the Colorado-Kansas border and in north-central Kansas where the Arbuckle has been removed by erosion. At the Wellington test well sites (KGS 1-28 and KGS 1-32), Arbuckle brines from drill-stem tests (DST) and swab tests had TDS values ranging from approximately 48,000 mg/L in the Upper Arbuckle (4,182 ft) to 180,000 mg/L in the lower Arbuckle (5,005 ft).

The ambient pore pressure, temperature, and salinity vary nearly linearly with depth in the Arbuckle Group. By linear extrapolation, the relationship between depth and these three parameters can be expressed by the following equations:

$$\text{Temperature } (^\circ\text{F}) = (0.011 * \text{Depth} + 73.25) \quad \text{Pressure (psi)} = (0.487 * \text{Depth} - 324.8)$$

$$\text{Chloride (mg/l)} = (100.9 * \text{Depth} - 394.786)$$

Where, depth is in feet below kelly bushing (KB)

Using the above relationships, the temperature, pressure, and salinity at the top and bottom of the Arbuckle Group at the injection well site (KGS 1-28) are presented in table 2.

Table 2. Temperature, pressure, and salinity at the top and bottom of the Arbuckle Group at the injection well site (KGS 1-28).

	Top of Arbuckle (4,168 ft)	Bottom of Arbuckle (5,160 ft)
Temperature (°F)	115	130
Pressure (psi)	1,705	2,188
Chloride (mg/l)	25,765	125,858

## Data Acquisition

An extensive suite of geophysical logs were obtained from two 5,000+ feet wells drilled to understand the geology/hydrogeology, and derive petrophysical properties. The purpose of each log and how the data was used to characterize the formation is presented below.

### Array Compensated True Resistivity (ACTR)

CTR involves obtaining multiple measurements of resistivity which reflects conditions at different distances beyond the borehole wall so that the effects of drilling-mud invasion can be factored out for a reading of the true resistivity of the formation. The log data is used for evaluation of (1) formation water salinity variations and (2) the subdivision of pore volume between electrically connected and unconnected porosity, which has important implications regarding permeability, particularly in the injection zone.

### Temperature

Temperature logs from surface to injection zone are used to specify temperature dependent formation properties (formation brine resistivity, solubility, and phase behavior of CO<sub>2</sub>) in the numerical model.

### Compensated Spectral Natural Gamma Ray

The Compensated Spectral Natural Gamma Ray (CSNGR) log provides insight into the mineral composition of the formations. Measurement of natural gamma-radiation of formations, partitioned between the three most common components of naturally occurring radiation in sandstones and shales (potassium, thorium, and uranium) is used for (1) correlation between wells, so that laterally continuous zones can be identified; (2) shale evaluation, which is particularly important in the evaluation of sealing intervals and baffles; and (3) the recognition of “hot” uranium zones, generally resulting from diagenesis and sometimes indicative of fractures.

### Microlog

The Microlog records normal and lateral microresistivity at a much higher vertical resolution than standard resistivity logs, but has less depth of investigation than standard resistivity logs. The data is used to (1) characterize resistivity of thin zones and (2) provide an indication of mudcake buildup as a good diagnostic of permeable zones.

## **Spectral Density Dual Spaced Neutron Log**

This porosity logging suite can be integrated with magnetic resonance imaging (MRI) and neutron-density crossplot (PHND) porosity logs for high grade interpretation of porosity. The photoelectric index (Pe) accompanies modern density logging tools and records the absorption of low-energy gamma rays by the formation in units of barns per electron. Logged value is a direct function of the aggregate atomic number (Z) of the elements in the formation, and so is a sensitive indicator of mineralogy. Pe is combined with neutron porosity, and bulk density information to conduct a Rhomaa-Umma analysis.

## **Extended Range Micro Imager Correlation (ERMIC) Plot**

The high resolution electrical image of borehole wall provided by the (ERMIC) plot is used for recognition and orientation analysis of (1) fractures, both natural and drilling-induced; (2) vuggy porosity, and (3) shaley zones. A consistency is typically noted between the observations from ERMIC, core, and MRI. This correlation can be used to extend the delineation of major pore types in the intervals that are not cored.

## **Magnetic Resonance Image (MRI)**

The MRI log measures the relaxation time of hydrogen within the pores exposed to a magnetic field whose spectrum reflects the distribution of pore sizes. The MRI data can be used to obtain a distribution of the pore size, and estimate permeability and porosity values by calibrating to core measurements. The MRI log is also used to determine the sealing potential of caprock by deriving CO<sub>2</sub> entry pressure estimates in the confining zone.

## **Radial Cement Bond Log (RCBL)**

RCBL tool captures downhole data that ensures reliable cement bond evaluation. The tool is equipped with one omni-directional transmitter, and two omni-directional receivers, as well as eight radial receivers for comprehensive borehole coverage. An inspection of the log will assist ensuring that there is a competent cement bond in the well, and the absence of any vertical channels through which pressurized fluids could migrate upward into USDW's.

## **Helical Computerized Tomography (CT) Scan**

CT scans are used to evaluate the texture of the rocks and to inspect for the presence of very minute fractures in the confining zone.

## **Sonic Log**

The acoustic measurement of porosity records the first arrival of ultrasonic compressional waves and is primarily sensitive to interparticle porosity that occurs between grains or crystals within carbonates and is often referred to as “primary” or “matrix porosity”. In contrast, the MRI, neutron, and density measurements respond to pore spaces at all scales and so provide a measure of total porosity. The difference between the acoustic porosity and the total porosity is termed the “secondary porosity” which can be interpreted to be vuggy porosity, where vugs can range in size anywhere from a dissolved grain to large cavities. The overlay of the MRI porosity with the acoustic (sonic) porosity will typically suggest “vuggy facies” in the carbonate injection zone and

tighter (less complex) “matrix facies” in the baffle zones (if present) within the carbonate injection zone.

### **Geochemical Logs**

Geochemical logs are used to characterize elemental composition and mineralogy and assist in evaluating reaction rates in the presence of free phase CO<sub>2</sub>. The geochemical data can also be used in conjunction with Schlumberger’s Techlog software to estimate hydrogeologic properties such as porosity. (Check with Mina on this).

### **Core Samples**

Core samples were obtained at KGS 1-32 within a 1600 feet interval spanning from the bottom of the Arbuckle into the Cherokee Shale above the Mississippian System. The samples were used for thin-section spectroscopy, geochemical analyses, lab based derivation of permeability of porosity estimates, and fracture investigations.

### **Drill Stem Test (DST) and Other Well Tests**

The purpose of conducting DST’s is to obtain the ambient pressures, obtain geochemical samples, and derive estimates of formation permeability. These tests assist in obtaining permeability estimates in the injection zone and can be used to supplement the permeability estimates derived from DST’s. The analysis is discussed in Appendix B.

### **Geochemical Data**

Formation waters were collected during Drill Stem Tests and swab sampling. The samples were analyzed to establish baseline geochemical conditions and salinity distribution throughout the Arbuckle injection zone. Various geochemical studies were conducted in order to validate the geologic characterization derived from core and log studies.

The ion composition analyses indicate that the Arbuckle Group is indeed highly stratified with high permeability zones in the top and bottom of this system. The data also indicates that there is sharp hydraulic separation between the Arbuckle Group and the Mississippian system, suggesting the presence of a competent caprock. The biomass concentrations and microbial counts also indicate the presence of a highly stratified Arbuckle reservoir.

Oxygen and hydrogen isotope analyses were conducted in order to obtain an understanding of the hydrodynamics of the Arbuckle system. The data suggests that the brines from the lower Arbuckle cluster tightly together and have values distinct from the upper Arbuckle. The upper Arbuckle brines have distinctly different  $\delta D$  and  $\delta^{18}O$  values than in lower Arbuckle. This is in conformity with observations and conclusions from core, well logs, ion composition, and biochemistry data discussed above.

### **Reservoir Characterization**

#### **Porosity estimations**

The Arbuckle is a triple-porosity system of interparticle, fracture, and vuggy pores. Typically, fracture porosity in carbonates is small in volume (1 to 2%) and so difficult to discriminate, as

contrasted with vuggy porosity, whose evaluation shows distinctive differences between core and logs. In zones with minimal vuggy porosity, there is good agreement between core and logged porosity. In sections with significant vuggy porosity, MRI based effective porosity (need to mention how this was derived) is usually greater than core porosity. A good example is shown in the section between 4900 and 5150 feet depth that contains the injection zone interval (see Figure 22). This figure demonstrates that the most reliable estimator of effective porosity that includes both interparticle and vuggy porosity is the MRI log.

In vuggy zones, core porosity measurements are biased towards low values. Further evidence of the ability of the MRI log to discriminate vugs is provided by Figure 23, where the degree of vugginess observed from core examination of the entire Arbuckle is matched with “megaporosity” from the MRI log as the summed porosities with T2 relaxation times of greater than one second. In conclusion, effective porosity from the MRI log was used as the porosity deliverable to other evaluation modules.

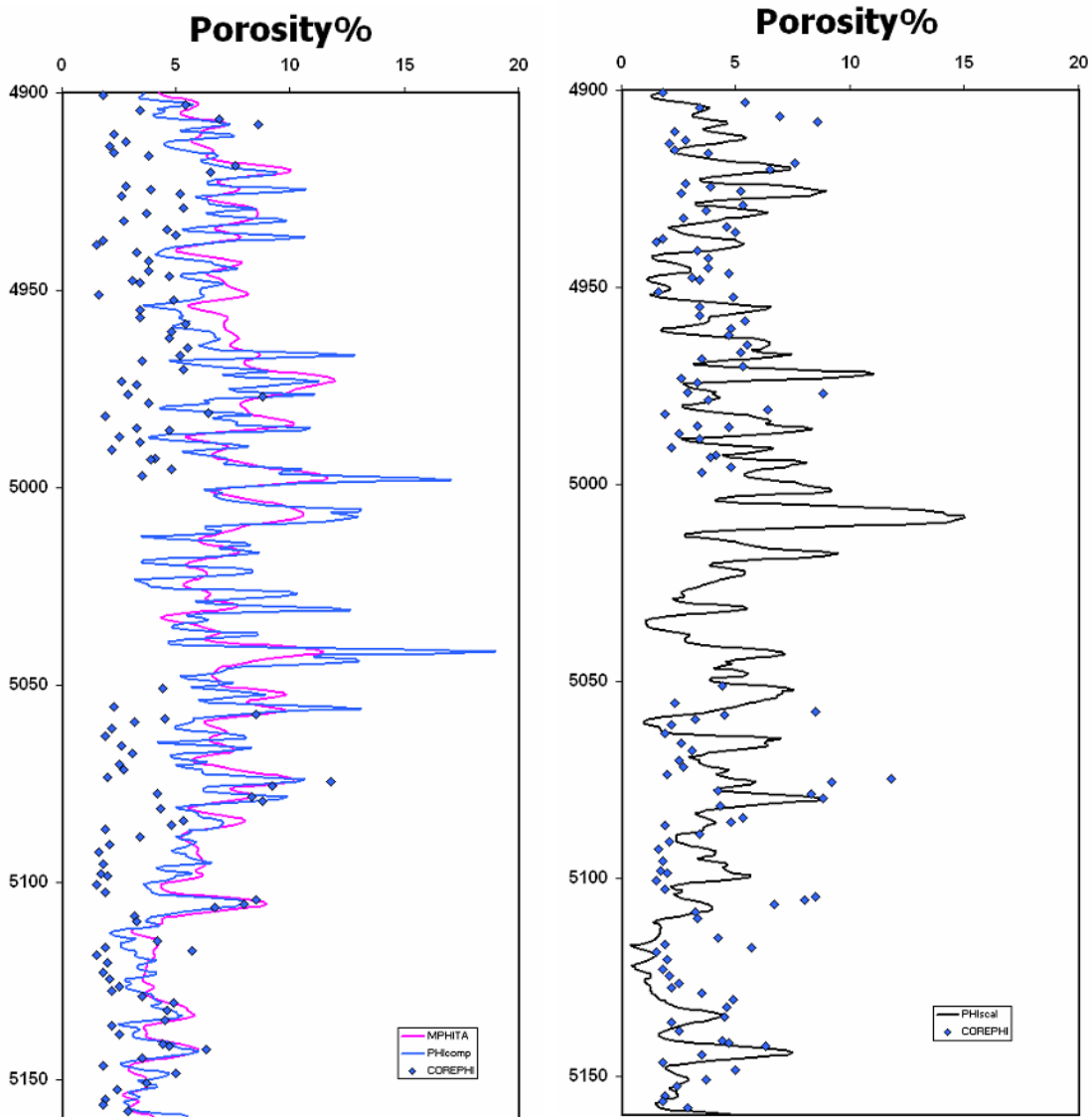


Figure 22. KGS Wellington #1-32 injection zone interval: overlay of MRI effective porosity and neutron-density porosity curves with core porosity measurements (left) and overlay of sonic (acoustic) porosity curve with core measurements (right).

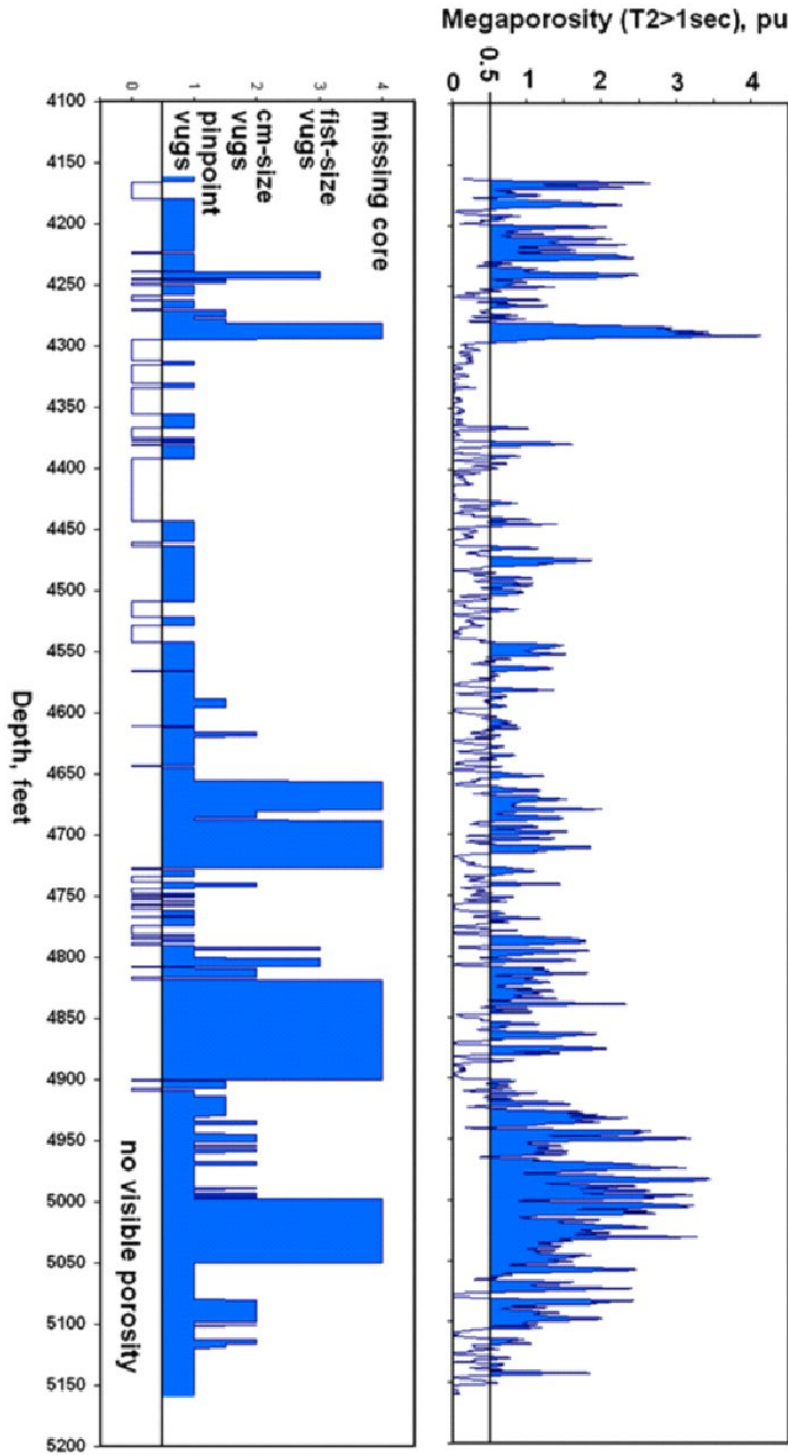


Figure 23. Visual observation of vugs from core in the Arbuckle of KGS Wellington #1-32 (left) compared with summed porosities of the MRI log with T2 relaxation times greater than one second

(right).

The total porosity corresponds to the porosity measured by the MRI. This is subdivided between "fast porosity" which approximately matches the core porosity (labelled as PHIip, for interparticle or matrix porosity) and "slow porosity", considered to represent vugs (the sum of both PHIVugc and PHIVugnc). In a separate calculation, the MRI porosity was subdivided between connected and non-connected porosity in the electrical sense, based on the resistivity log. By incorporating the resistivity result, the vuggy porosity seen by the MRI is partitioned between non-connected vugs (PHIVugnc) and connected vugs (PHIVugc). It is tempting to make a hydraulic interpretation of this electrical result in thinking of the connected vugs as perhaps solution-enlarged fractures and the non-connected vugs as isolated vugs that do not contribute to flow. More detailed explanation of methods and discussion of results of log analysis and porosity estimations are presented in Appendix C.

### **Permeability estimations**

It was decided to calculate permeability by relating core based Flow Zone Indicator (FZI) to the function  $1/(Swir*Phi)$  using the technique suggested by Fazelalavi and others (2013, attached). Swir refers to the irreducible water saturation and Phi refers to the formation porosity.

Pore structure in Arbuckle is very complex and there are a lot of variations in pore size distribution (unimodal, bimodal and trimodal) versus depth in very short intervals. Due to this complexity and non-homogeneity in pore size distribution, the Arbuckle permeability was calculated based on pore size classification (Micro, Meso and Mega pores). FZI in each pore size class was correlated to  $1/(Swir*Phi)$  of the same class.

Permeability was calculated based on correlations between FZI from core and  $1/(Swir*phi)$  from log. FZI from core data was calculated using (K90) permeability and  $1/(swir*phi)$  was calculated using effective porosity and irreducible water saturation from the NMR log. FZI and  $1/(swir*phi)$  were sorted from low to high values. All FZI values less than 2 and  $1/(swir*phi)$  values less than 48 were assigned for micro pore sizes which correspond to permeability values less 0.5 milliDarcy (mD). Similarly, FZI from 2 to 11 and  $1/(swir*phi)$  from 48 to 106 were considered for meso pore sizes which correspond to permeability from about 0.5 to 25 mD. Finally, FZI from 11-150 and  $1/(swir*phi)$  from 106 to 851 were considered for mega pore sizes which correspond to permeability greater than 25 mD.

The calculated permeability is plotted versus depth in Figure 25 where they are compared with core permeability. The Figure 24 is an example of derived permeability for Arbuckle reservoir and a full account of permeability estimations for the entire Arbuckle interval is presented in Appendix D. Calculated Micro pore permeability is shown by brown dots in this plot while Meso and Mega pore permeability values are shown by green and blue dots respectively. Series 1 in the figure represents the continuous distribution of permeability derived by the method. A fairly good match between the calculated and core permeabilities can be inferred from the figure.

### Permeability vs. Depth

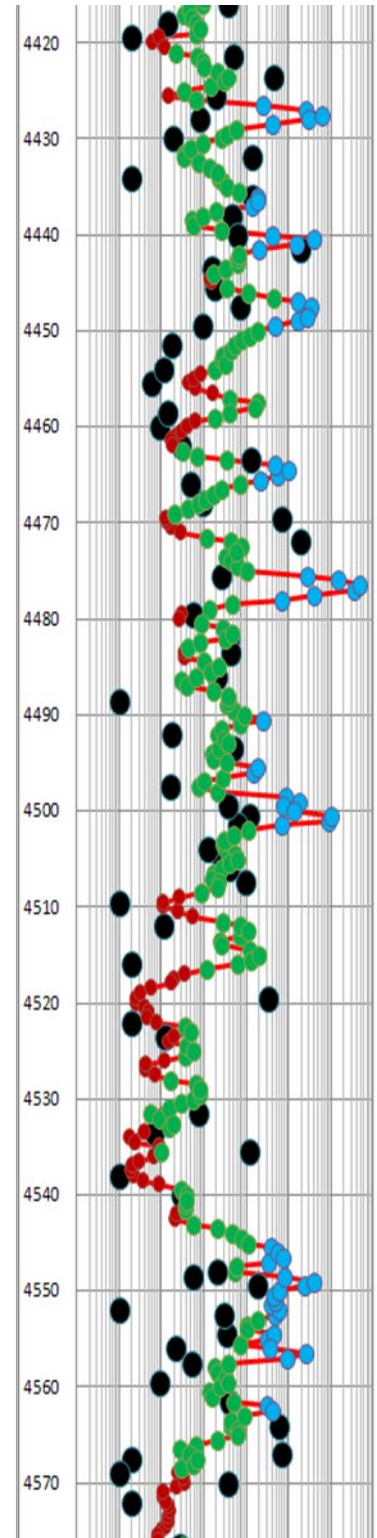
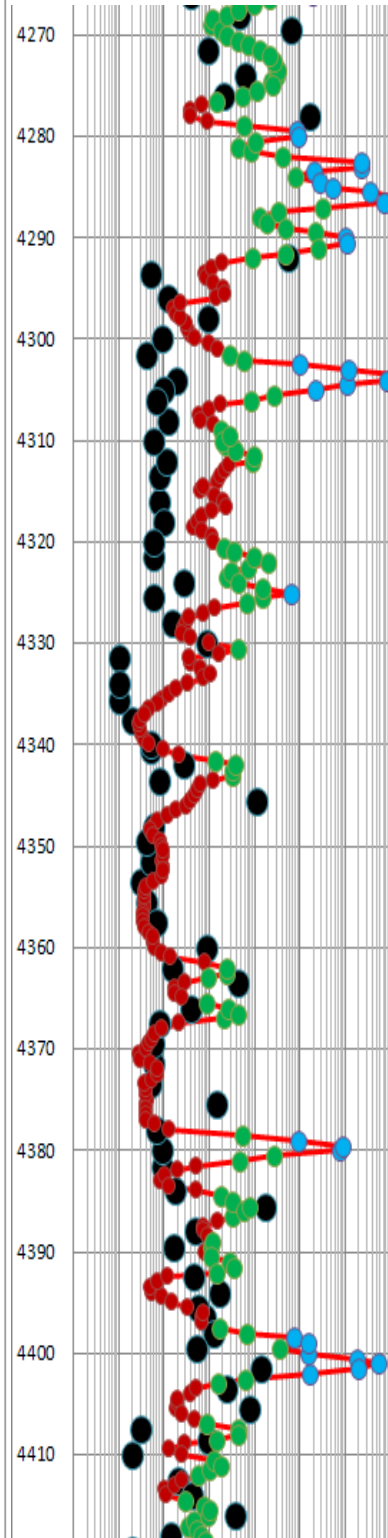
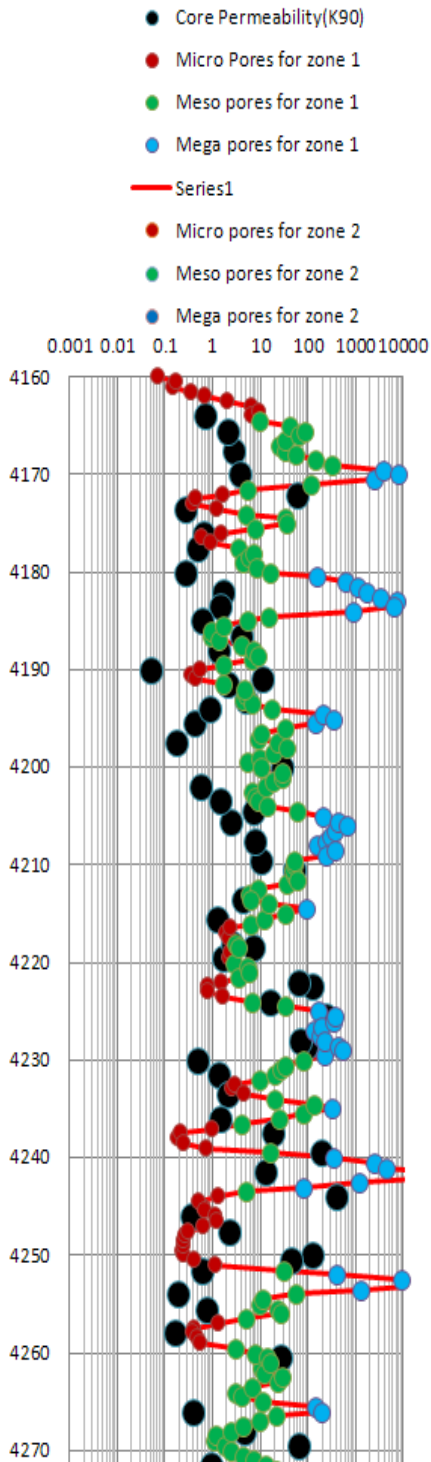


Figure 24. Comparison of core and estimated permeabilities

## Characterization of Confining Zone

The Chattanooga Shale is expected to provide much more confinement than the Simpson Group underneath it. The maximum entry pressure in the Chattanooga Shale at KGS 1-28 is 11,840 psi in the mercury-air system and 956 psi in the CO<sub>2</sub>-brine system. As discussed in the modeling section, the maximum induced CO<sub>2</sub> pressure at the top of the Arbuckle/base of the Simpson Shale is approximately 13 psi. Therefore, the primary confining zone is expected to confine the injected CO<sub>2</sub> in the Arbuckle aquifer.

## Estimating Structural Leakage Potential

South-central Kansas, although historically stable, has experienced an increase in seismic activity since 2013. The correlation with brine disposal operations has renewed interest in the role of fluids in fault reactivation, specifically in the crystalline basement, where the majority of events have occurred. This study focuses on determining the suitability of CO<sub>2</sub> and brine injection into a Cambro-Ordovician reservoir (Arbuckle Group) for long-term storage and a shallower Mississippian reservoir for enhanced oil recovery (EOR) in Wellington Field, Sumner County, Kansas. Our approach for determining the potential for injection-induced seismicity has been to (1) map subsurface faults and estimate in-situ stresses, (2) perform slip and dilation tendency analysis to identify optimally oriented faults relative to the estimated stress field, and (3) determine the pressure changes required to induce slip, both at reservoir depth and basement depth. Through the use of 3D seismic reflection data, 12-near vertical faults were identified with fault planes striking between 325° to 049° and the majority oriented NNE, consistent with nodal planes from moment tensor solutions from recent earthquakes in Kansas and Oklahoma. Fault lengths range from 210 to 4,450+ m and vertical separations range from 12-33 m. The majority of faults cut through both reservoirs, with a number that clearly cut the top basement reflector. Drilling-induced tensile fractures (N=40) identified from image logs and inversion of moment tensor solutions (N=70) are consistent with the maximum horizontal stress (SHmax) oriented ~EW. Stress magnitudes were estimated using step rate tests (Shmin = 18.4 MPa), density logs (Sv = 36.6 MPa), and calculations from wells with drilling induced tensile fractures (SHmax = 31.3-45.9 MPa) at the gauge depth of 1,484m (Fig. 25). Slip and dilation tendency analysis indicates that faults striking <020° are stable under reservoir conditions, whereas faults striking 020°-049° may have a moderate to high risk for reactivation with increasing pore fluid pressure. These faults would require a pore fluid pressure increase of at least 1.1 MPa to 7.6 MPa at 1,117 m (Mississippian) and 1.31 MPa to 9.8 MPa at 1,484 m (Arbuckle) to reach failure. Given the proposed injection volume, it is unlikely that faults will be reactivated at reservoir depths. However, at basement depths, high rate injection operations could reach pressures beyond the critical threshold for slip, as demonstrated by the large number of injection induced earthquakes west of the study area.

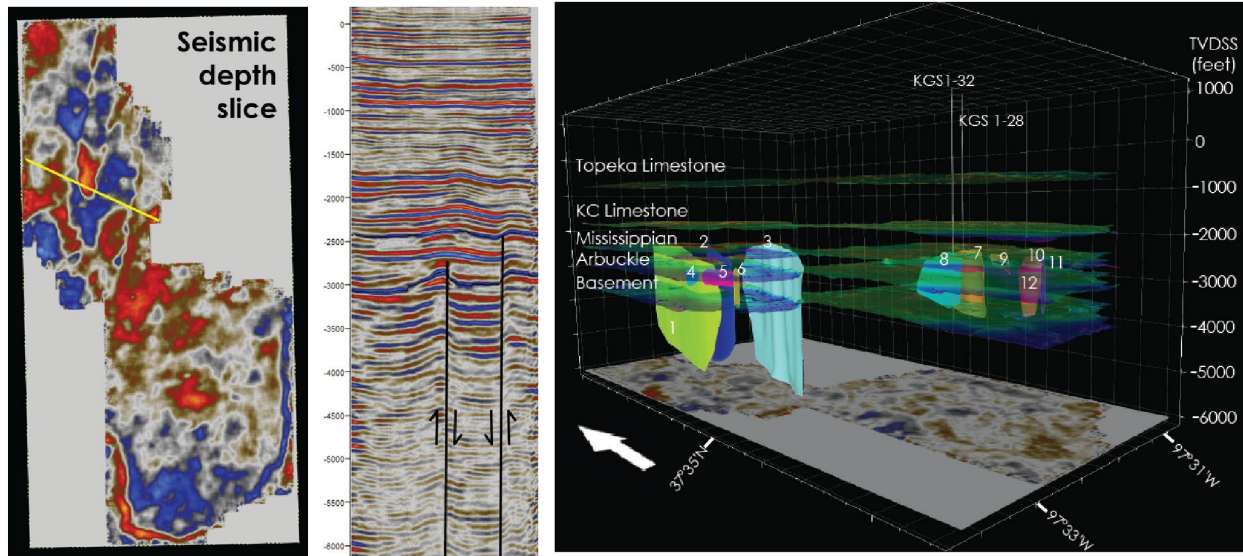


**Figure 25. Map view of fault locations and seismic profile cross-section (left) and 3D view of mapped fault (right)**

### **Geochemistry Based Evidence of Competent Upper Confining Zone**

Geochemical logs and thin sections were analyzed for mineralogy and soil characterization to enable reaction kinetics modeling and determining potential for plugging pore space due to mineral precipitation

#### **Ion Composition**

Due to their conservative nature, bromine and chlorine are especially useful in differentiating salinity sources and establishing the basis of brine mixture in the subsurface (Whittemore, 1995). Bromine, chlorine, and sulfate concentrations of brine from nine depths in the Arbuckle and three depths in the Mississippian formations were evaluated. The Br-/Cl- and SO42-/Cl- weight ratios versus chloride concentration for the Arbuckle saline aquifer and Mississippian reservoir at Wellington are presented in Figure 26 from which it is clear that the geochemical composition of the Mississippian waters is markedly different than that of the Arbuckle. The salinity within the Mississippian varies between approximately 120,000 mg/l and 135,000 mg/l versus approximately 30,500 mg/l in the underlying upper Arbuckle. Similarly, the SO42-/Cl- ratio of approximately 0.002 in the Mississippian formation is significantly different than the range of this ratio of 0.002-0.0055 in the upper Arbuckle. Collectively, the chloride and SO42-/Cl- data suggest a hydraulic separation between the Mississippian and the Arbuckle systems, which supports the conceptualization of a tight upper confining zone.

#### **Isotopic Characterization**

Oxygen and hydrogen isotope distributions present another opportunity to assess hydraulic connectivity between the Arbuckle Group and the Mississippian System. Figure 27 shows the  $\delta D$  vs  $\delta^{18}O$ , reported as the difference between the  $^{18}O/^{16}O$  and  $2H/1H$  abundance ratios of the samples vs. the Vienna Standard Mean Ocean Water (VSMOW) in per mil notation ( $\text{‰}$ ) for the Arbuckle and Mississippian samples. Best fit regression lines for each formation, compared with the global

meteoric water line (GMWL) and modern seawater is also presented which suggests different water isotopic composition in the Arbuckle and Mississippian systems.

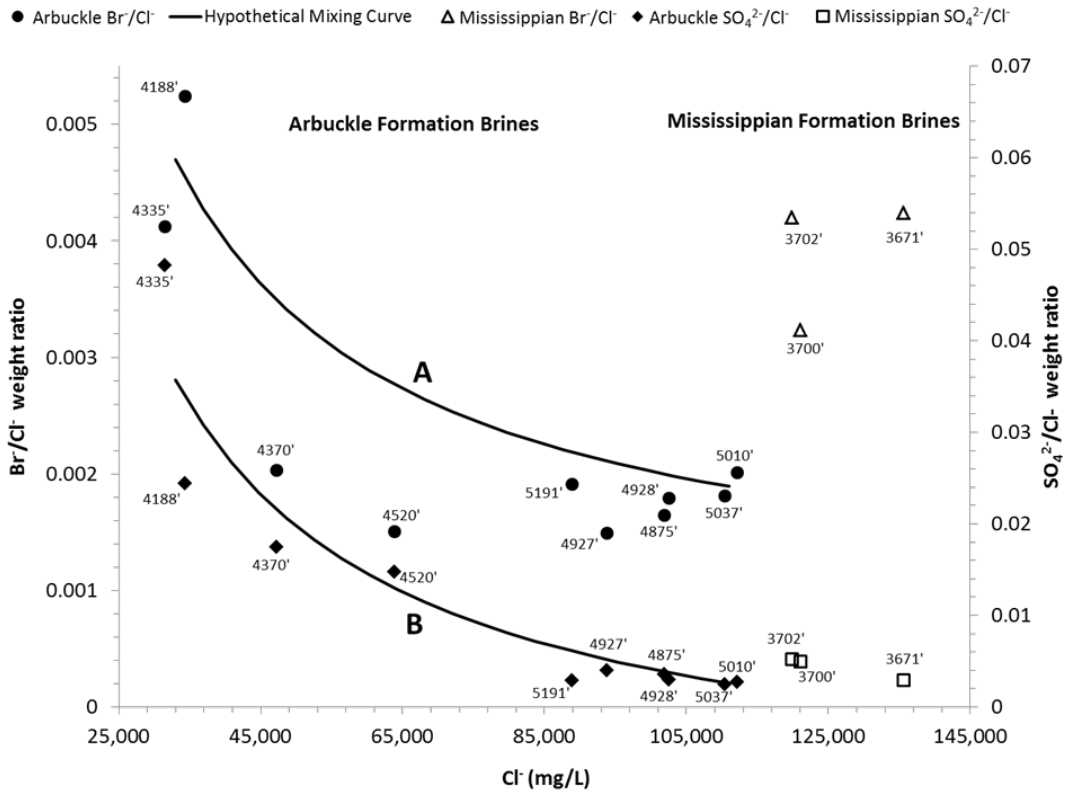
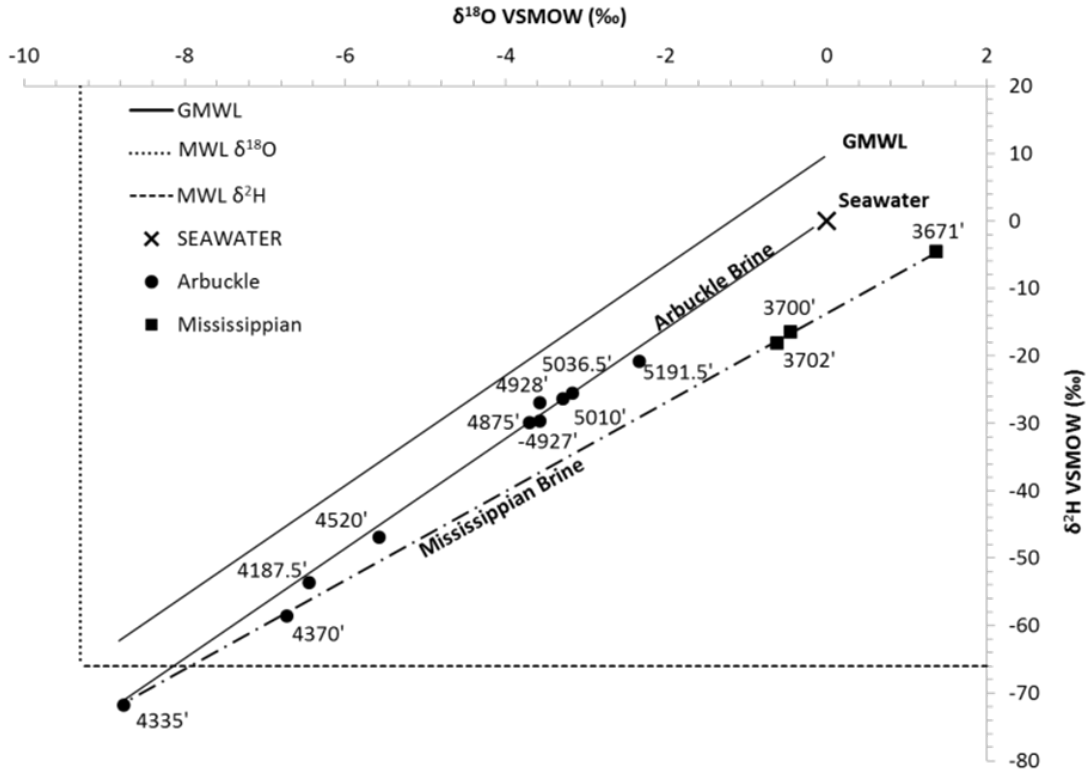
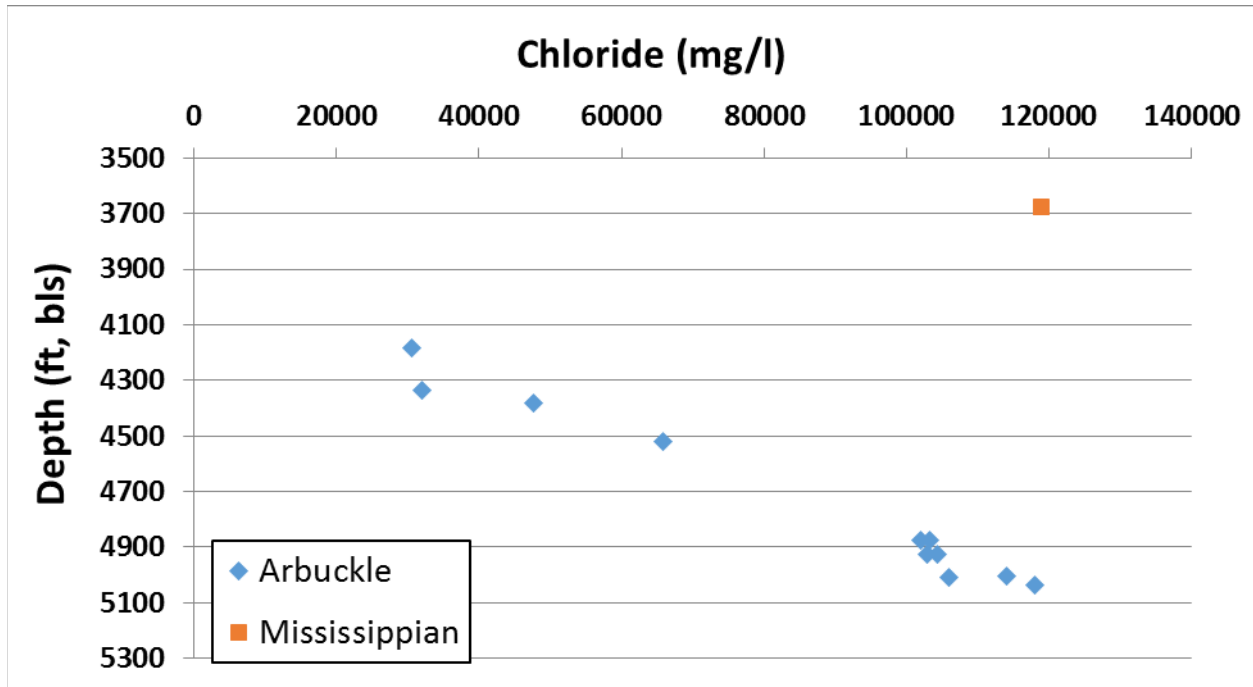


Figure 26. Br/Cl⁻ and SO₄²⁻/Cl⁻ weight ratios versus chloride concentration for the Arbuckle saline aquifer and Mississippian oil producing brines at Wellington, Kansas. Also shown are the hypothetical mixing curves for Br-/Cl- (A) and SO₄²⁻/Cl- (B) (Scheffer, 2012)



**Figure 27  $\delta\text{D}$  vs  $\delta^{18}\text{O}$  (‰, VSMOW) for the Arbuckle and Mississippian reservoirs (Scheffer, 2012)**

The chloride distribution in Arbuckle and Mississippian systems at KGS 1-28 and KGS 1-32, obtained from data collected during Drill Stem Testing (DST) and swabbing, is presented in Figure 28. The chloride gradient in the Arbuckle approximates a linear trend with chloride concentration increasing from approximately 30,500 mg/l in the Upper Arbuckle to as much as 118,000 mg/l in the injection zone. Chloride concentration in the Mississippian formation at 119,000 mg/l is substantially higher than in the upper Arbuckle. The large difference in chloride concentrations between the Mississippian and upper Arbuckle supports the conceptualization that the confining zone separating the Arbuckle aquifer from the Mississippian reservoir is tight, and that there are no conductive faults in the vicinity of the Wellington site that hydraulic link the two systems.



**Figure 28. Chloride distribution within the Arbuckle aquifer and Mississippian reservoir at KGS 1-28 and KGS 1-32.**

Ca/Sr molar ratios plotted against Ca/Mg molar ratios of Arbuckle data (Fig. 29) with trends for dolomitization and calcite recrystallization as described in McIntosh (2004). This plot clearly shows two groupings within the Arbuckle samples. The upper Arbuckle shows a calcite recrystallization signature while the lower Arbuckle shows the influence of dolomitization on brine chemistry. This presents evidence that the upper and lower Arbuckle have different hydrochemical regimes (Barker et al., 2012).

The Br-/Cl- ratio provides further evidence of the separation of the upper and lower high permeability zones in the Arbuckle. As can be inferred from Figure 29, the Br-/Cl- values of the lower Arbuckle varies over a narrow range in the neighborhood of 0.002, while the variation is much larger (between 0.002 and 0.0055) in the upper Arbuckle. A hypothetical Br-/Cl- mixing curve (Curve A, Figure X) was calculated using averaged end-member values from the two deepest samples in the Arbuckle (5010 ft and 5036 ft) and the two shallowest samples in the Arbuckle (4182 ft and 4335 ft) to examine mixing of reservoir fluids for purposes of evaluating connectivity throughout the reservoir. In the lower Arbuckle samples, Br-/Cl- concentrations remained relatively consistent, but increased sharply in the upper Arbuckle. This suggests possible different brine origins for the lower and upper regions of the Arbuckle. Regardless of the origin, the data suggests that the brines in the upper and lower Arbuckle are distinctly different and there does not appear to be any mixing between the two zones; supporting the hypothesis of the presence of low permeability baffle zone between the upper Arbuckle and the lower injection interval which was also inferred from the permeability data.

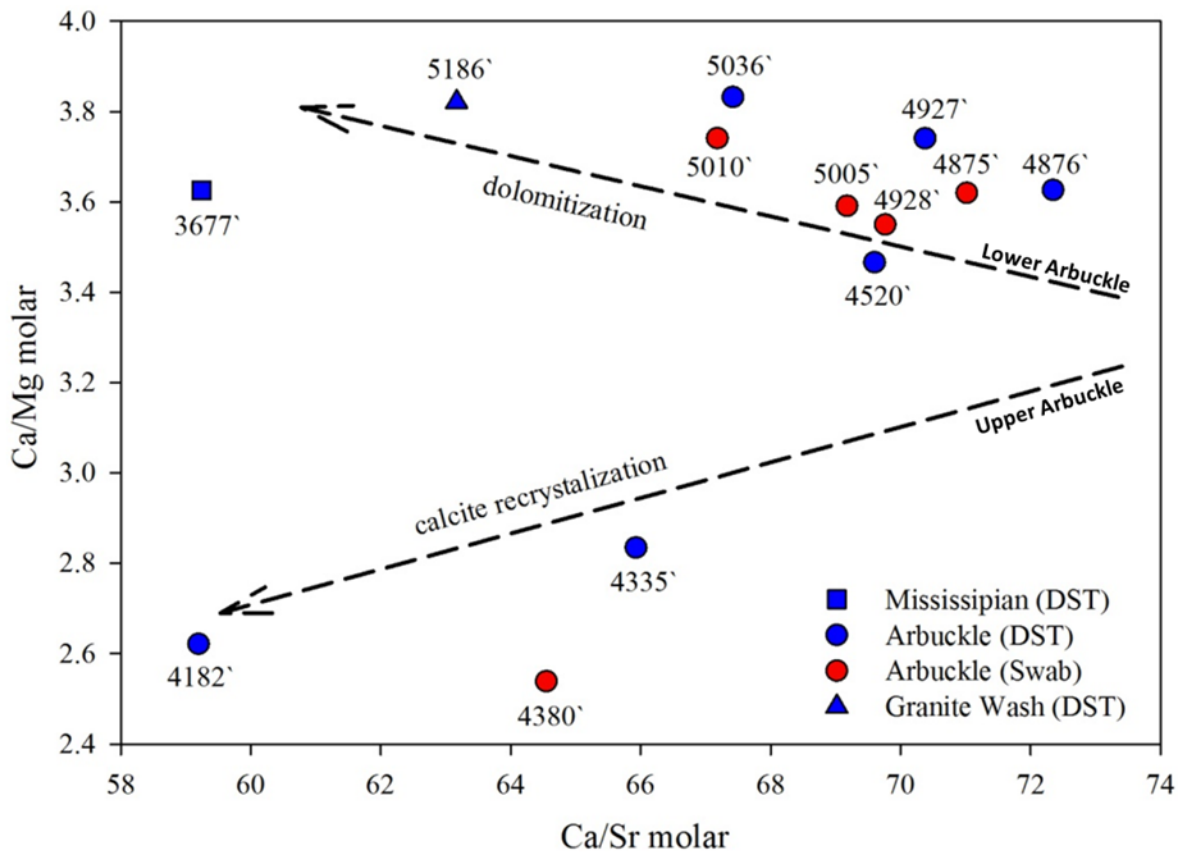
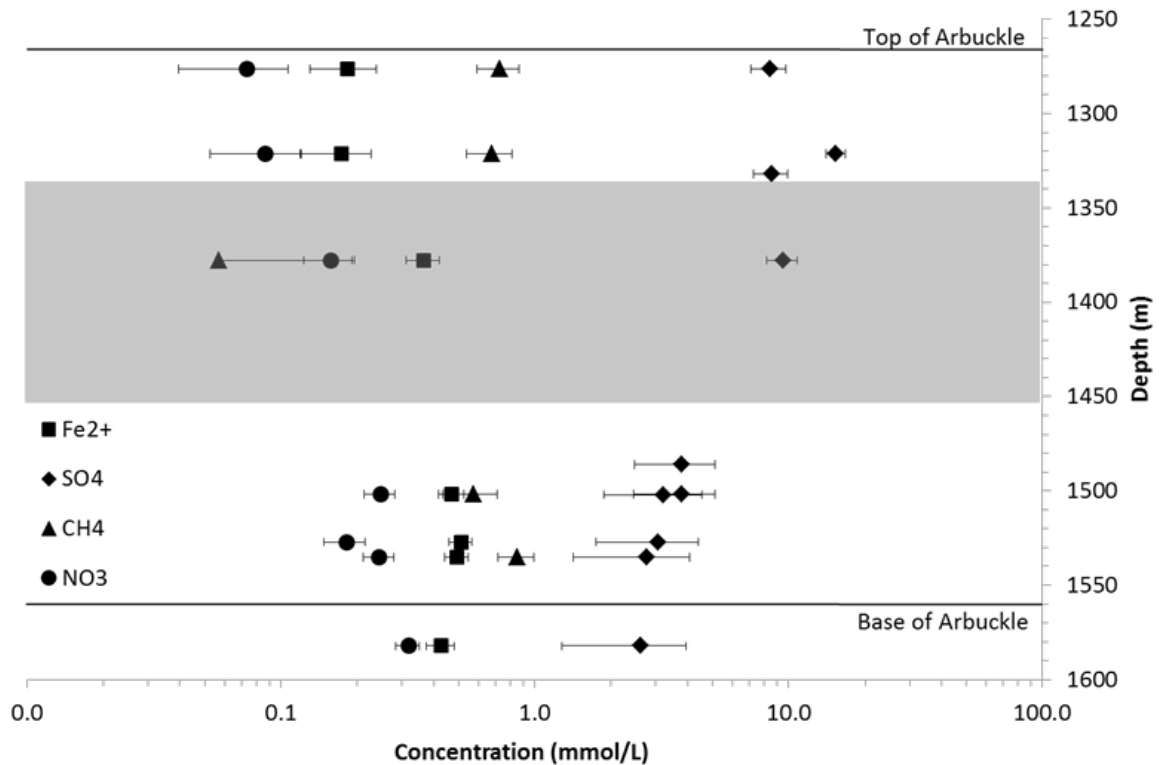


Figure 29. Ca/Sr vs Ca/Mg molar ratios showing trends of dolomitization and calcite recrystallization (from Barker et al., 2012).

### Biogeochemistry

The concentration of the redox reactive ions ferrous iron, sulfate, nitrate, and methane ( $\text{Fe}^{2+}$ ,  $\text{SO}_4^{2-}$ ,  $\text{NO}_3^-$ ,  $\text{CH}_4$ ) can be used as evidence of biological activity in the subsurface (Scheffer, 2012). In oxygen restricted sediments that are rich in organic carbon such as the Arbuckle, stratification would follow the redox ladder with aerobes at shallower depths where oxygen is available, followed by nitrate, iron, and sulfate reducers (in this order), and methanogens at the deepest level based on availability of terminal electron acceptors. Because there is a paucity of oxygen in the Arbuckle, typical stratification of microbial metabolisms would involve dissimilar iron reducing bacteria (DIRB) above sulfate reducing bacteria (SRB) above methanogens. This biogenic stratification would be manifested by a zone with increased reduced iron over decreasing sulfate (or increasing sulfide) over increasing methane. However, as shown in Figure 30 there appears to be two separate trends observed in the Arbuckle aquifer; one trend 4.40, for samples above the suspected baffle (1277 m; 4190 ft to 1321 m; 4334 ft) in the upper Arbuckle, and one trend below the suspected baffle (1378 m; 4521 ft to 1582 m; 5190 ft) in the lower Arbuckle. This suggests a reset of the biogeochemistry due to lack of hydraulic communication between the Upper and Lower Arbuckle.



**Figure 30. Concentrations of redox reactive ions; ferrous iron, sulfate, methane, and nitrate (Fe<sup>2+</sup>, SO<sub>4</sub><sup>2-</sup>, CH<sub>4</sub>, NO<sub>3</sub><sup>-</sup>) in the Arbuckle reservoir (Scheffer, 2012).**

### Microbial Diversity

Biomass concentrations of  $2.1 \times 10^6$ ,  $1.9 \times 10^7$  and  $2.6 \times 10^{-3}$  cells/ ml were determined using the quantitative polymerase chain reaction (qPCR) procedures at depths of 1277m (4190ft), 1321m (4334ft), and 1378m (4520ft) respectively. The lowest biomass coincides with the low permeability baffle zone in the mid Arbuckle (1378 m; 4520 ft). Decreased flow through the baffle zone could decrease nutrient recharge and lead to nutrient depletion (Scheffer, 2012). The highest biomass and most unique sequences occurred in the upper Arbuckle at 1321 m (4334 ft) as shown in Figure 31.

The free-living microbial community was also examined in the Arbuckle aquifer. Results show 43% diversity at a depth of 1277 m (4190 ft), 62% diversity at 1321 m (4334 ft), and 39% diversity at 1378 m (4520 ft), which follows the same trend as biomass shown in Figure 31. Notably, the microbial communities from 1277 m (4190 ft) and 1321 m (4334 ft) are very similar to one another and vary distinctly from the community detected at 1378 m (4520 ft). Nine genera of bacteria were detected at 1277 m (4190 ft) and 1321 m (4334 ft). Seven genera of bacteria were detected at 1378 m (4520 ft). Alkalibacter, Bacillus and Erysipelthrix were found at the two shallower depths but not at 1378 m (4520 ft). Dethiobacter was detected only at the deeper depth of 1378 m (4520 ft).

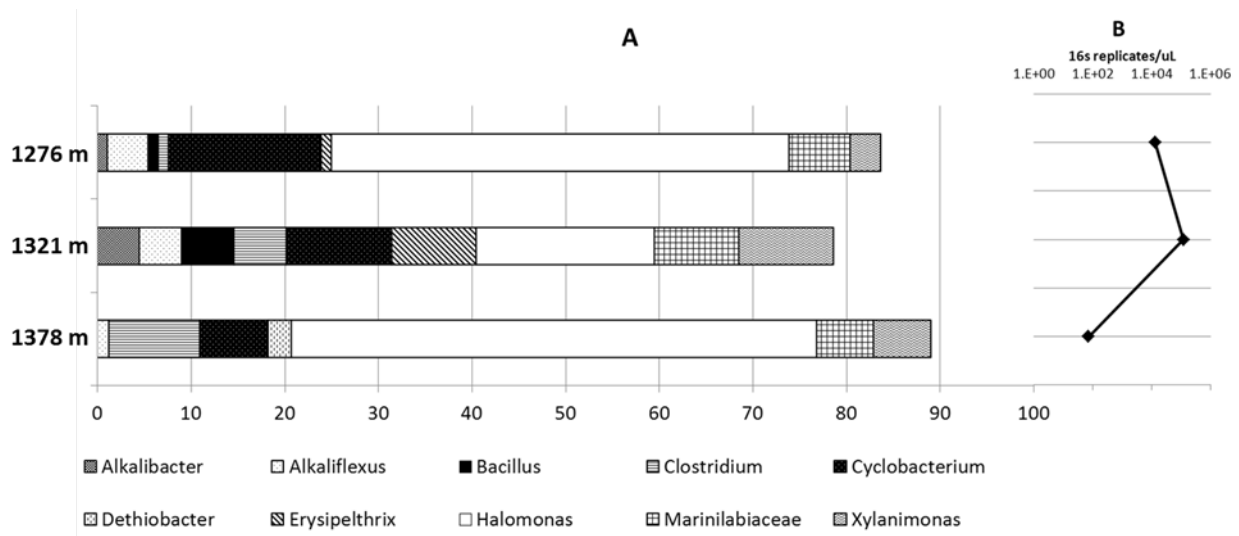


**Figure 31. Arbuckle aquifer microbial profile showing the distribution of bacteria in the Arbuckle (A), and the DNA concentration (B) (from Scheffer, 2012).**

### Conceptual Model and Geologic Models

The simulation model spans the entire thickness of the Arbuckle aquifer. The CO<sub>2</sub> is to be injected in the lower portion of the Arbuckle in the interval 4,910–5,050 feet, which has relatively high permeability based on the core data collected at the site. Preliminary simulations indicated that the bulk of the CO<sub>2</sub> will remain confined in the lower portions of the Arbuckle because of the low permeability intervals in the baffle zones and also shown in analysis of geologic logs at wells KGS 1-28 and KGS 1-32. Therefore, no-flow boundary conditions were specified along the top of the Arbuckle. The specification of a no-flow boundary at the top is also in agreement with hydrogeologic analyses presented, which indicate that the upper confining zone—comprising the Simpson Group, the Chattanooga Shale, and the Pierson formation—has very low permeability, which should impede any vertical movement of groundwater from the Arbuckle Group. Evidence for sealing integrity of the confining zone and absence of transmissive faults include the following:

- 1) under-pressured Mississippian group of formations relative to pressure gradient in the Arbuckle,
- 2) elevated chlorides in Mississippian group of formations relative to brine recovered at the top of the Arbuckle,
- 3) geochemical evidence for stratification of Arbuckle aquifer system and presence of a competent upper confining zone.

Additionally, entry pressure analyses indicate that an increase in pore pressure of more than 956 psi within the confining zone at the injection well site is required for the CO<sub>2</sub>-brine to penetrate through the confining zone. As discussed in the model simulation results section below, the maximum increase in pore pressure at the top of the Arbuckle is less than 1.5 psi under the worst-case scenario. This small pressure rise at the top of the Arbuckle is due to CO<sub>2</sub> injection below the lower vertical-permeability baffle zones present in the middle of the Arbuckle Group, which confines the CO<sub>2</sub> in the injection interval in the lower portions of the Arbuckle Group. The confining zone is also documented to be locally free of transmissive fractures based on fracture

analysis conducted at KGS 1-28 (injection well). There are no known transmissive faults in the area. It should be noted that an Operation Plan For Safe and Efficient Injection has been submitted to the EPA, which has a provision for immediate cessation of injection should an anomalous pressure drop be detected owing to development or opening of fractures.

Based on the above evidence, it is technically appropriate to restrict the simulation region within the Arbuckle Group for purposes of numerical efficiency, without compromising predictions of the effects of injection on the plume or pressure fronts. Because of the presence of the Precambrian granitic basement under the Arbuckle Group, which is expected to provide hydraulic confinement, the bottom of the model domain was also specified as a no-flow boundary. Active, real-time pressure and temperature monitoring of the injection zone at the injection and monitoring wells will likely be able to detect any significant movement of CO<sub>2</sub> out of the injection zone along fractures. Also, the 18-seismometer array provided by Incorporated Research Institutions for Seismology (IRIS) will detect small seismicity and their hypocenters within several hundred feet resolution to provide additional means to monitor the unlikely movement of CO<sub>2</sub> above or below the Arbuckle injection zone.

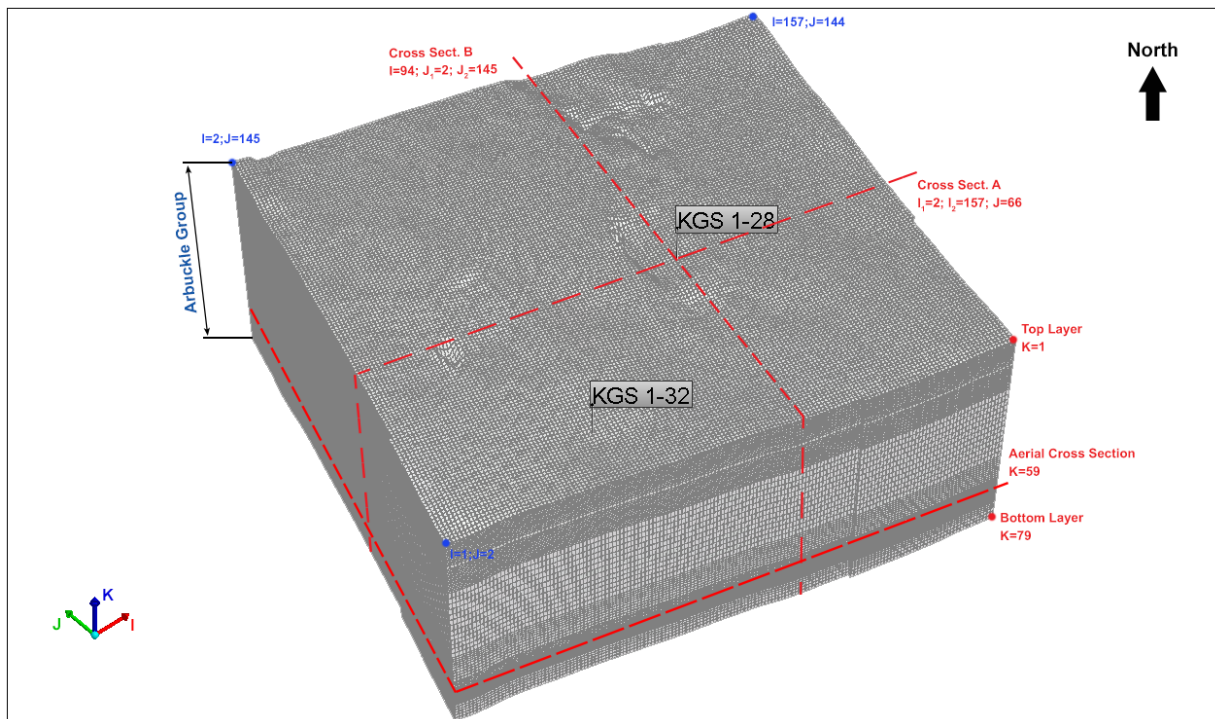


**Figure 32a. Model mesh in 3-D showing location of Arbuckle injection (KGS 1-28) and monitoring (KGS 1-32) wells along with the east-west and north-south cross sections.**

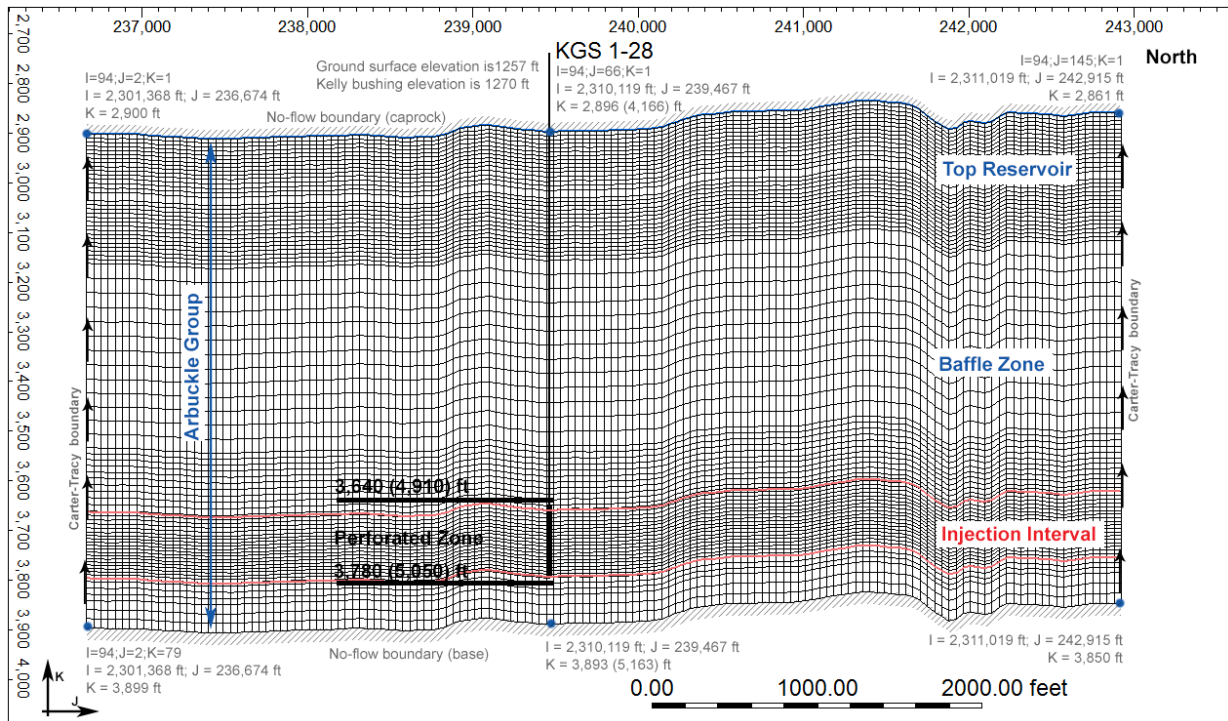
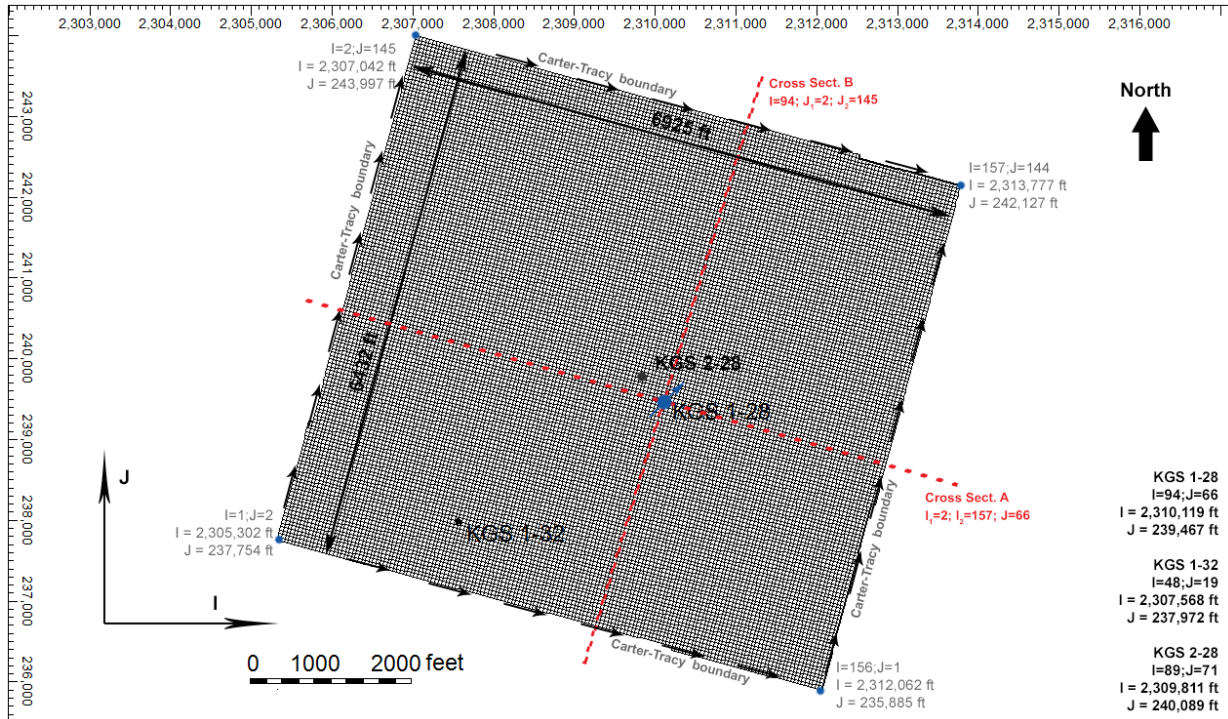


Figure 32b. North-south cross section of model grid along column 94 showing boundary conditions.

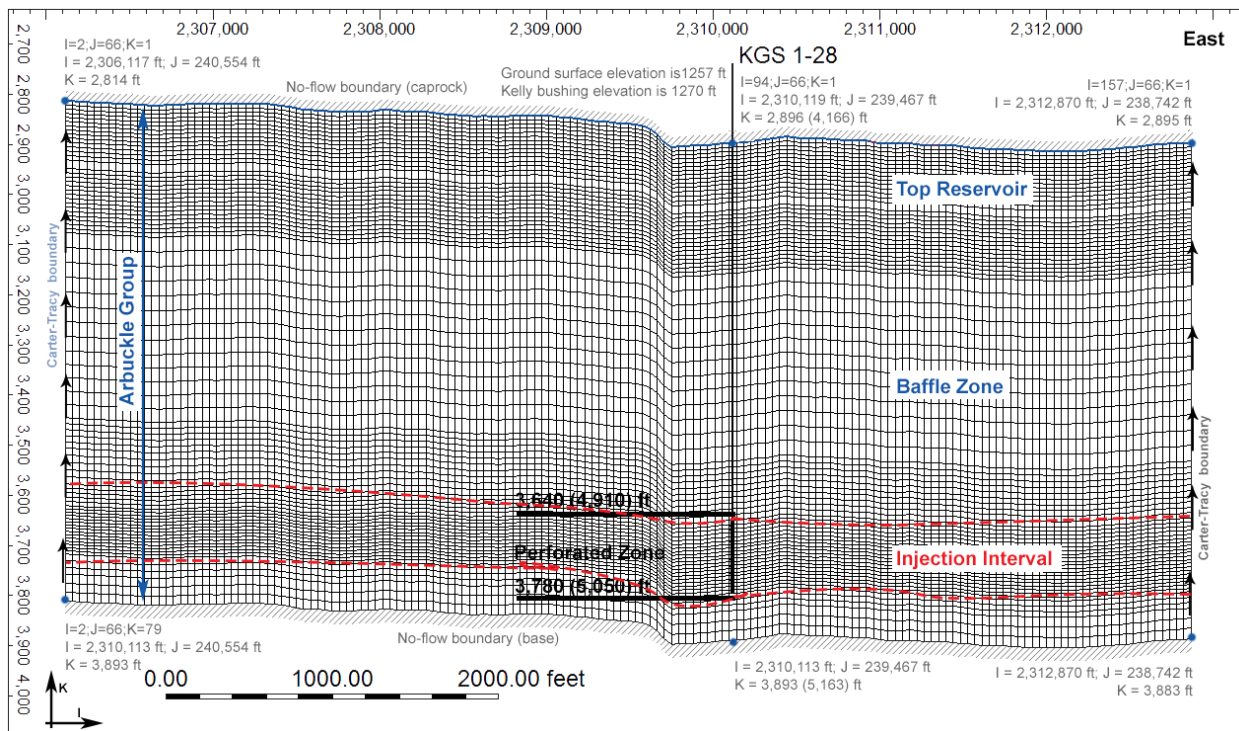


Figure 32c. East-west cross section of model grid along row 66 showing boundary conditions.

## Modeled Processes

Physical processes modeled in the reservoir simulations included isothermal multi-phase flow and transport of brine and CO<sub>2</sub>. Isothermal conditions were modeled because the total variation in subsurface temperature in the Arbuckle Group from the top to the base is only slightly more than 10°F (which should not significantly affect the various storage modes away from the injection well) and because it is assumed that the temperature of the injected CO<sub>2</sub> will equilibrate to formation temperatures close to the well. Also, non-isothermal sensitivity simulations were conducted for the EPA in which it was demonstrated that including temperature as a variable impacts the plume extent and the pressure distribution only minimally. Uniform salinity concentration was assumed as the effects of water salinity on the simulated AoR were found to be negligible (less than 0.5%).

Subsurface storage of CO<sub>2</sub> occurs via the following four main mechanisms:

- structural trapping,
- aqueous dissolution,
- hydraulic trapping, and
- mineralization.

The first three mechanisms were simulated in the Wellington model. Mineralization was not simulated as geochemical modeling indicated that due to the short-term and small-scale nature of the pilot project, mineral precipitation is not expected to cause any problems with clogging of pore

space that may reduce permeability and negatively impact injectivity. Therefore, any mineral storage that may occur will only result in faster stabilization of the CO<sub>2</sub> plume and make projections presented in this model somewhat more conservative with respect to the extent of plume migration and CO<sub>2</sub> concentrations.

### Model Operational Constraints

The bottomhole injection pressure in the Arbuckle should not exceed 90% of the estimated fracture gradient of 0.75 psi/ft (measured from land surface). Therefore, the maximum induced pressure at the top and bottom of the Arbuckle Group should be less than 2,813 and 3,483 psi, respectively, as specified in table 3. At the top of the perforations (4,910 ft), pressure will not exceed 2,563 psi.

Table 3. Maximum allowable pressure at the top and bottom of the Arbuckle Group based on 90% fracture gradient of 0.675 psi/ft.

Depth (feet, bls)	Maximum Pore Pressure (psi)
4,166 (Top of Arbuckle)	2,813
4,910 (Top of Perforation)	3,314
5,050 (Bottom of Perforation)	3,408
5,163 (Bottom of Arbuckle)	3,483

### Geostatistical Reservoir Characterization of Arbuckle Group

Statistical reservoir geomodeling software packages have been used in the oil and gas industry for decades. The motivation for developing reservoir models was to provide a tool for better reconciliation and use of available hard and soft data (fig. 33). Benefits of such numerical models include 1) transfer of data between disciplines, 2) a tool to focus attention on critical unknowns, and 3) a 3-D visualization tool to present spatial variations to optimize reservoir development. Other reasons for creating high-resolution geologic models include the following:

- volumetric estimates;
- multiple realizations that allow unbiased evaluation of uncertainties before finalizing a drilling program;
- lateral and top seal analyses;
- integration (i.e., by gridding) of 3-D seismic surveys and their derived attributes assessments of 3-D connectivity;
- flow-simulation-based production forecasting using different well designs;
- optimizing long-term development strategies to maximize return on investment.

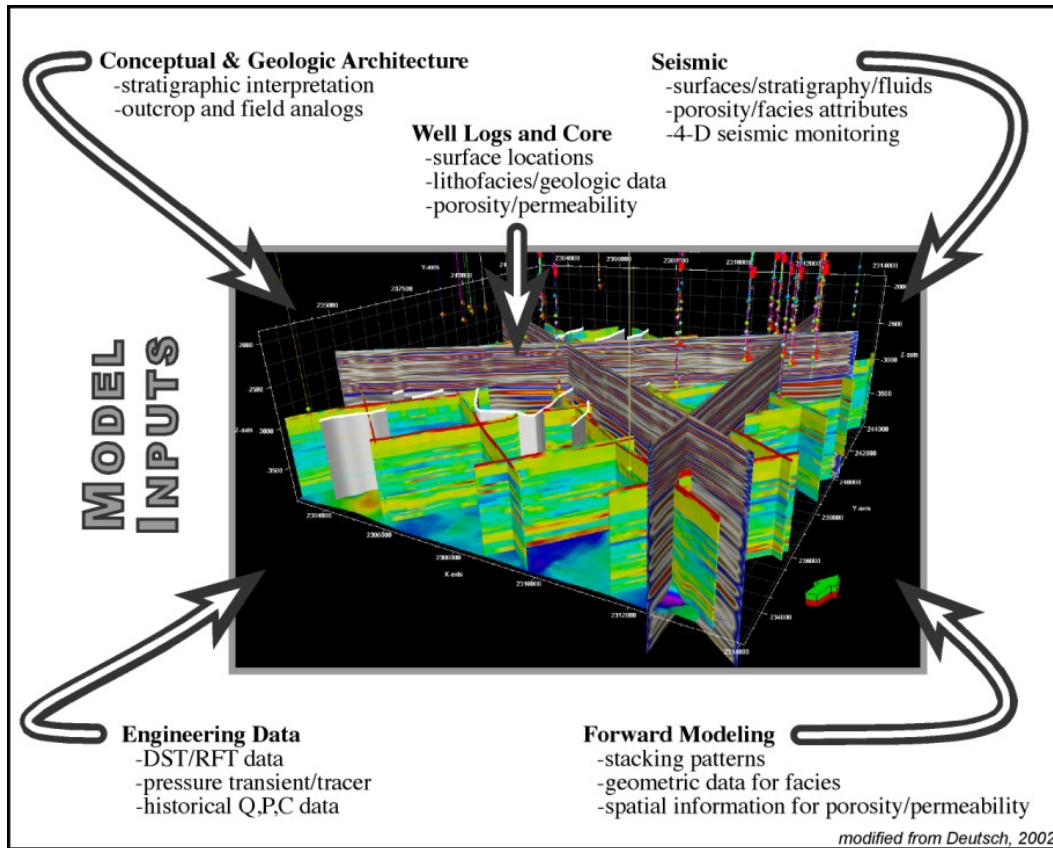


**Figure 33. A static, geocellular reservoir model showing the categories of data that can be incorporated (modified from Deutsch, 2002).**

Although geocellular modeling software has largely flourished in the energy industry, its utility can be important for reservoir characterization in CO<sub>2</sub> research and geologic storage projects, such as the Wellington Field. The objective in the Wellington project is to integrate various data sets of different scales into a cohesive model of key petrophysical properties, especially porosity and permeability. The general steps for applying this technology are to model the large-scale features followed by modeling progressively smaller, more uncertain, features. The first step applied at the Wellington Field was to establish a conceptual depositional model and its characteristic stratigraphic layering. The stratigraphic architecture provided a first-order constraint on the spatial continuity of facies, porosity, permeability, saturations, and other attributes within each layer. Next, facies (i.e., rock fabrics) were modeled for each stratigraphic layer using cell-based or object-based techniques. Porosity was modeled by facies and conditioned to “soft” trend data, such as seismic inversion attribute volumes. Likewise, permeability was modeled by facies and collocated, co-kriged to the porosity model.

### Geological Model

Lower Arbuckle core from Wellington reveals sub-meter-scale, shallowing-upward peritidal cycles. The two common motifs are cycles passing from basal dolo-mudstones/wackestones into algal dololaminites or matrix-poor monomict breccias. Bioclasts are conspicuously absent. Breccias are clast-supported, monomictic, and angular, and their matrix dominantly consists of cement. They are

best classified as crackle to mosaic breccias (Loucks, 1999) because there is little evidence of transportation. Lithofacies and stacking patterns (i.e., sub-meter scale, peritidal cycles) are consistent with an intertidal to supratidal setting. Breccia morphologies, scale (<0.1 m), mineralogy (e.g., dolomite, anhydrite, length-slow chalcedony), depositional setting, greenhouse climate, and paleo-latitude (~15° S) support mechanical breakdown processes associated with evaporite dissolution. The Arbuckle-Simpson contact (~800 ft above the proposed injection interval) records the super-sequence scale, Sauk-Tippecanoe unconformity, which records subaerial-related karst landforms across the Early Phanerozoic supercontinent Laurentia.

### Facies Modeling

The primary depositional lithofacies were documented during core description at KGS 1-32. A key issue was reconciling large variations between permeability measurements derived from wireline logs (i.e., nuclear resonance tool), whole core, and step-rate tests. Poor core recovery from the injection zone resulted from persistent jamming, which is commonly experienced in fractured or vuggy rocks. Image logs acquired over this interval record some intervals with large pores (cm scale) that are likely solution-enlarged vugs (touching-vugs of Lucia, 1999; fig. 35). Touching-vug fabrics commonly form a reservoir-scale, interconnected pore system characterized by Darcy-scale permeability. It is hypothesized that a touching-vug pore system preferentially developed within fracture-dominated crackle and mosaic breccias—formed in response to evaporite removal—which functioned as a strataform conduit for undersaturated meteoric fluids (fig. 36). As such, this high-permeability, interwell-scale, touching-vug pore system is largely strataform and, therefore, predictable.

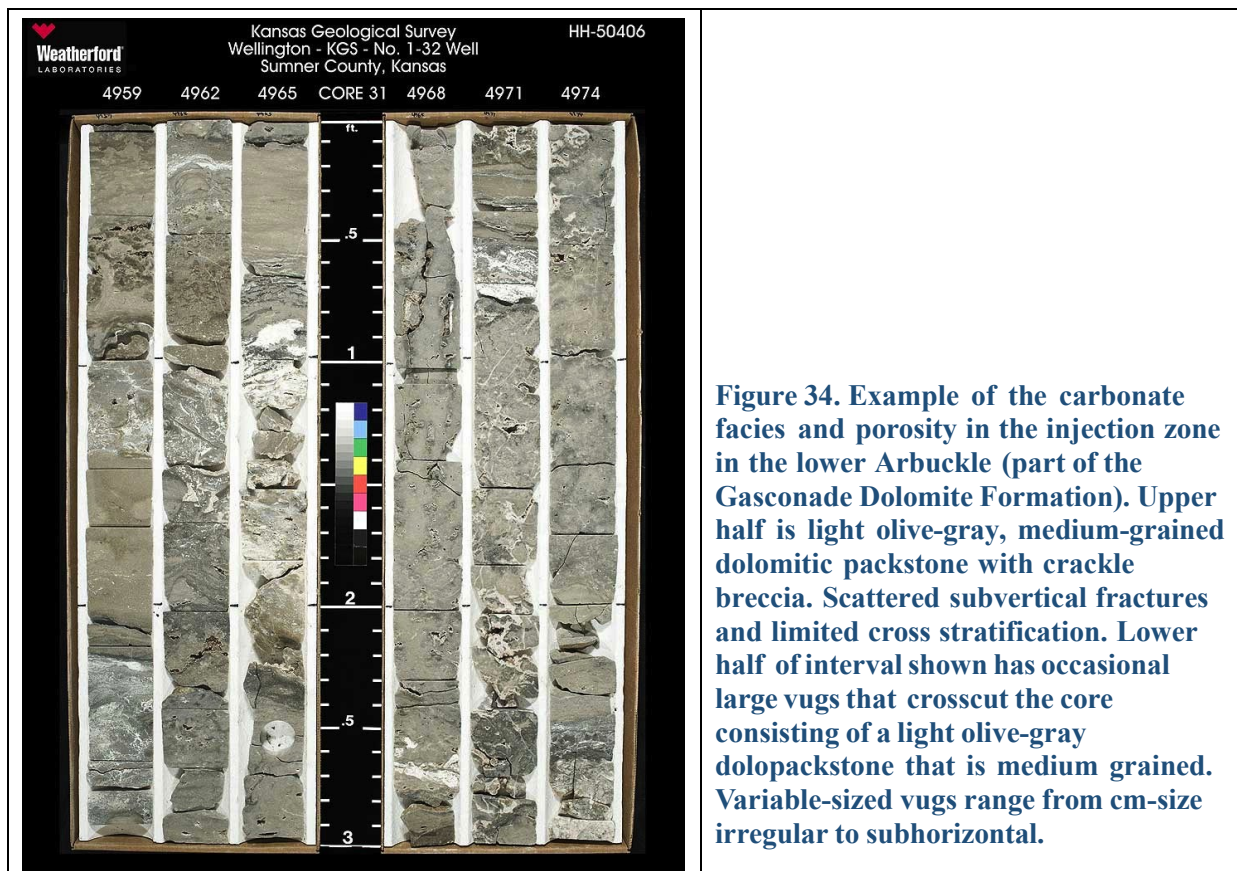


**Figure 34. Example of the carbonate facies and porosity in the injection zone in the lower Arbuckle (part of the Gasconade Dolomite Formation). Upper half is light olive-gray, medium-grained dolomitic packstone with crackle breccia. Scattered subvertical fractures and limited cross stratification. Lower half of interval shown has occasional large vugs that crosscut the core consisting of a light olive-gray dolopackstone that is medium grained. Variable-sized vugs range from cm-size irregular to subhorizontal.**

## Petrophysical Properties Modeling

The approach taken for modeling a particular reservoir can vary greatly based on available information and often involves a complicated orchestration of well logs, core analysis, seismic surveys, literature, depositional analogs, and statistics. Because well log data were available in only two wells (KGS 1-28 and KGS 1-32) that penetrate the Arbuckle reservoir at the Wellington site, the geologic model also relied on seismic data, step-rate test, and drill-stem test information. Schlumberger's Petrel™ geologic modeling software package was used to produce the current geologic model of the Arbuckle saline aquifer for the pilot project area. This geomodel extends 1.3 mi by 1.2 mi laterally and is approximately 1,000 ft in thickness, spanning the entire Arbuckle Group as well as a portion of the sealing units (Simpson/Chattanooga shale).

### 4.3 Porosity Modeling

In contrast to well data, seismic data are extensive over the reservoir and are, therefore, of great value for constraining facies and porosity trends within the geomodel. Petrel's volume attribute processing (i.e., genetic inversion) was used to derive a porosity attribute from the prestack depth migration (PSDM) volume to generate the porosity model (fig. 37). The seismic volume was created by re-sampling (using the original exact amplitude values) the PSDM 50 ft above the Arbuckle and 500 ft below the Arbuckle (i.e., approximate basement). The cropped PSDM volume and conditioned porosity logs were used as learning inputs during neural network processing.

A correlation threshold of 0.85 was selected and 10,000 iterations were run to provide the best correlation. The resulting porosity attribute was then re-sampled, or upscaled (by averaging), into the corresponding 3-D property grid cell.

The porosity model was constructed using sequential Gaussian simulation (SGS). The porosity logs were upscaled using arithmetic averaging. The raw upscaled porosity histogram was used during SGS. The final porosity model was then smoothed. The following parameters were used as inputs:

- I. Variogram
  - a. Type: spherical
  - b. Nugget: 0.001
  - c. Anisotropy range and orientation
    - i. Lateral range (isotropic): 5,000 ft
    - ii. Vertical range: 10 ft
- II. Distribution: actual histogram range (0.06–0.11) from upscaled logs
- III. Co-Kriging
  - a. Secondary 3-D variable: inverted porosity attribute grid
  - b. Correlation coefficient: 0.75

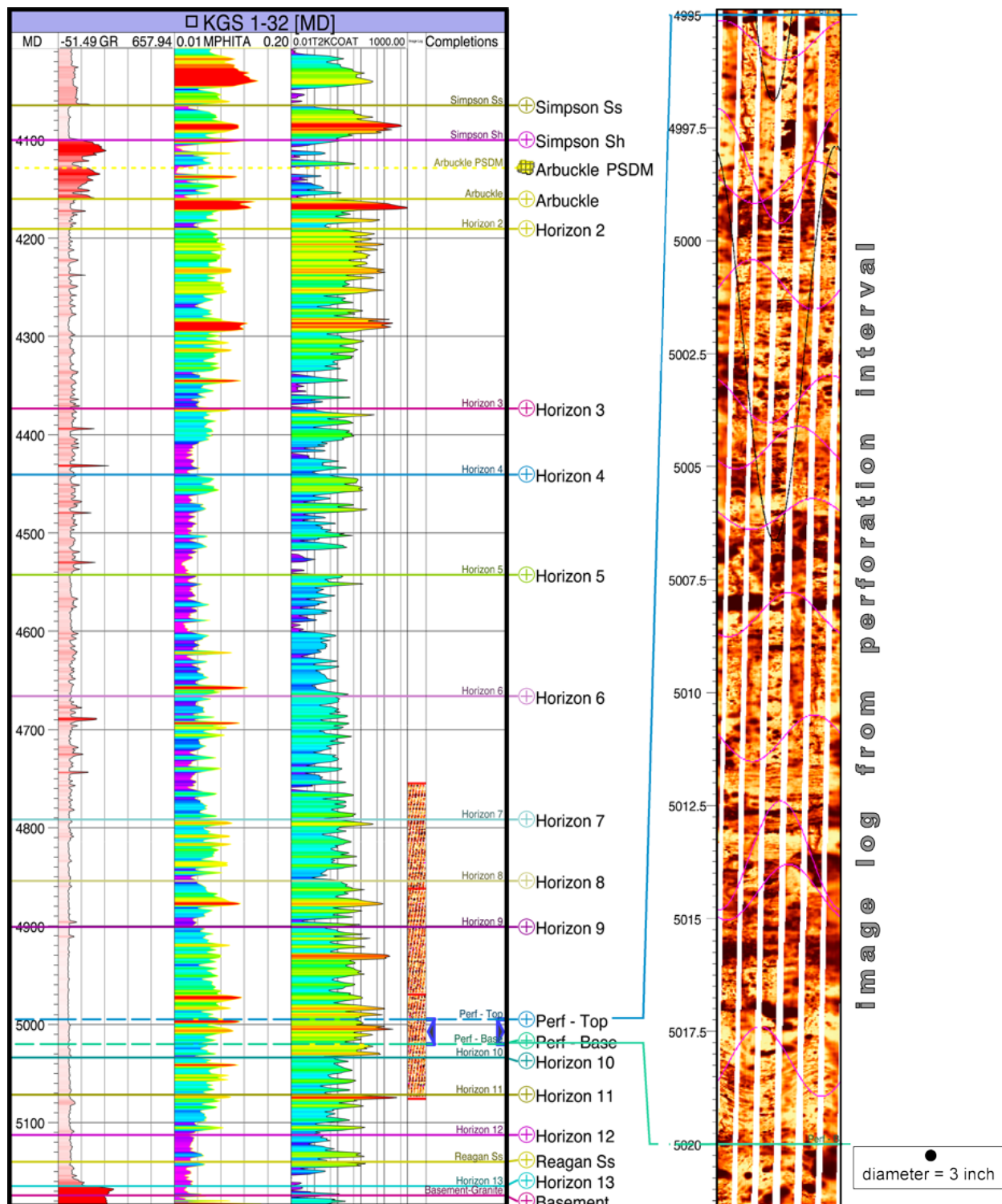


Figure 35. Geophysical logs within the Arbuckle Group at KGS 1-32. (Notes: MPHITA represents Haliburton porosity. Horizon markers represent porosity package. Image log on right presented to provide example of vugs; 3-in diameter symbol represents size of vug).

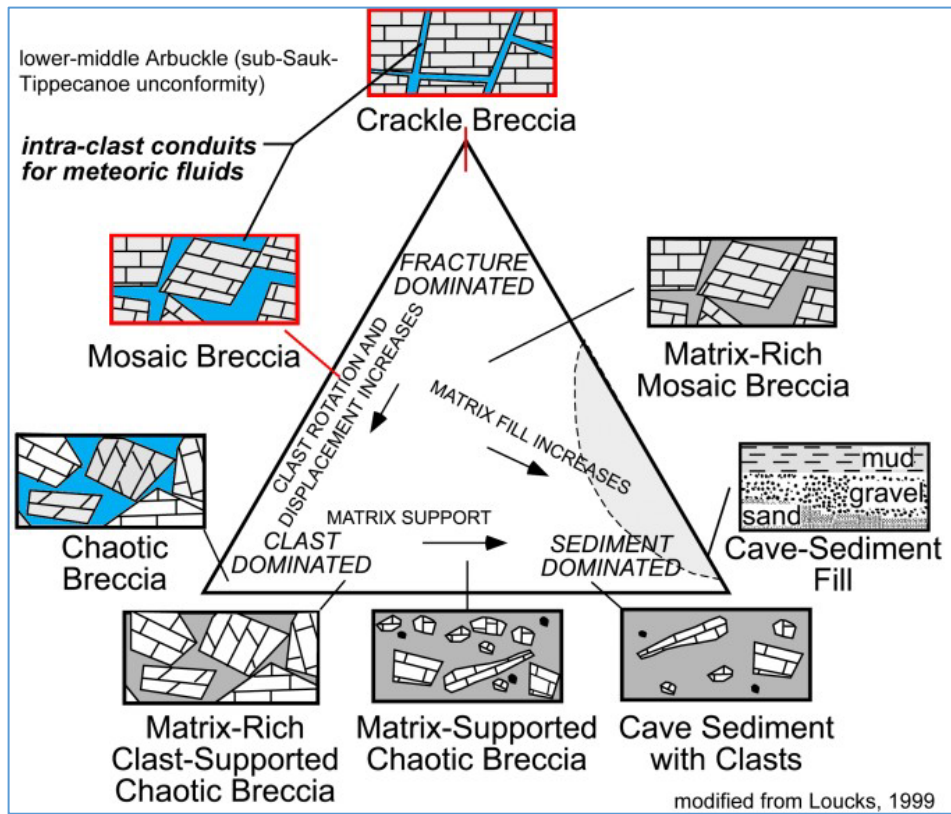


Figure 36. Classification of breccias and clastic deposits in cave systems exhibiting relationship between chaotic breccias, crackle breccias, and cave-sediment fill (source: Loucks, 1999).

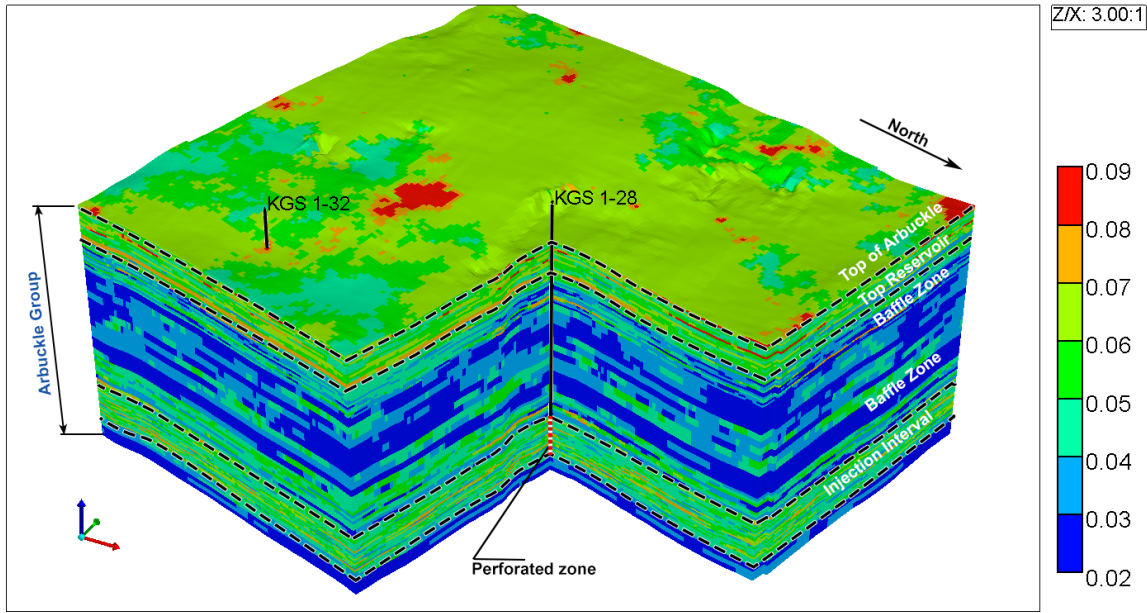


Figure 37. Upscaled porosity distribution in the Arbuckle Group based on the Petrel geomodel.

### Permeability Modeling

The upscaled permeability logs shown in fig. 35 were created using the following controls: geometric averaging method; logs treated as points; and method set to simple. The permeability model was constructed using SGS. Isotropic semi-variogram ranges were set to 3,000 ft horizontally and 10 ft vertically. The permeability was collocated and co-Kriged to the porosity model using the calculated correlation coefficient (~0.70). The resulting SGS-based horizontal and vertical permeability distributions are presented in fig. 38a–f, which shows the relatively high permeability zone selected for completion within the injection interval. Table 4 presents the minimum, maximum, and average permeabilities within the Arbuckle Group in the geomodel.

Table 4. Hydrogeologic property statistics in hydrogeologic characterization and simulation models.

Property	Reservoir Characterization Geomodel			Reservoir Simulation Numerical Model		
	min	max	avg	min	max	avg
Porosity (%)	3.2	12.9	6.8	3.2	12.9	6.7
Horizontal Permeability (mD)	0.05	23,765	134.2	0.05	23,765	130.7
Vertical Permeability (mD)	.005	1,567	387	0.005	1,567	385

### Arbuckle Reservoir Flow and Transport Model

Extensive computer simulations were conducted to estimate the potential impacts of CO<sub>2</sub> injection in the Arbuckle injection zone. The key objectives were to determine the resulting rise in pore pressure and the extent of CO<sub>2</sub> plume migration. The underlying motivation was to

determine whether the injected CO<sub>2</sub> could affect the USDW or potentially escape into the atmosphere through existing wells or hypothetical faults/fractures that might be affected by the injected fluid.

As in all reservoirs, there are data gaps that prevent an absolute or unique characterization of the geology and petrophysical properties. This results in conceptual, parametric, and boundary condition uncertainties. To address these uncertainties, comprehensive simulations were conducted to perform a sensitivity analysis using alternative parameter sets. A key objective was to derive model parameter sets that would result in the most negative impacts (the worst-case scenario; i.e., maximum formation pressures and largest extent of plume migration). However, simulations involving alternative parameter and boundary conditions that resulted in more favorable outcomes were also conducted to bracket the range of possible induced system states and outcomes.

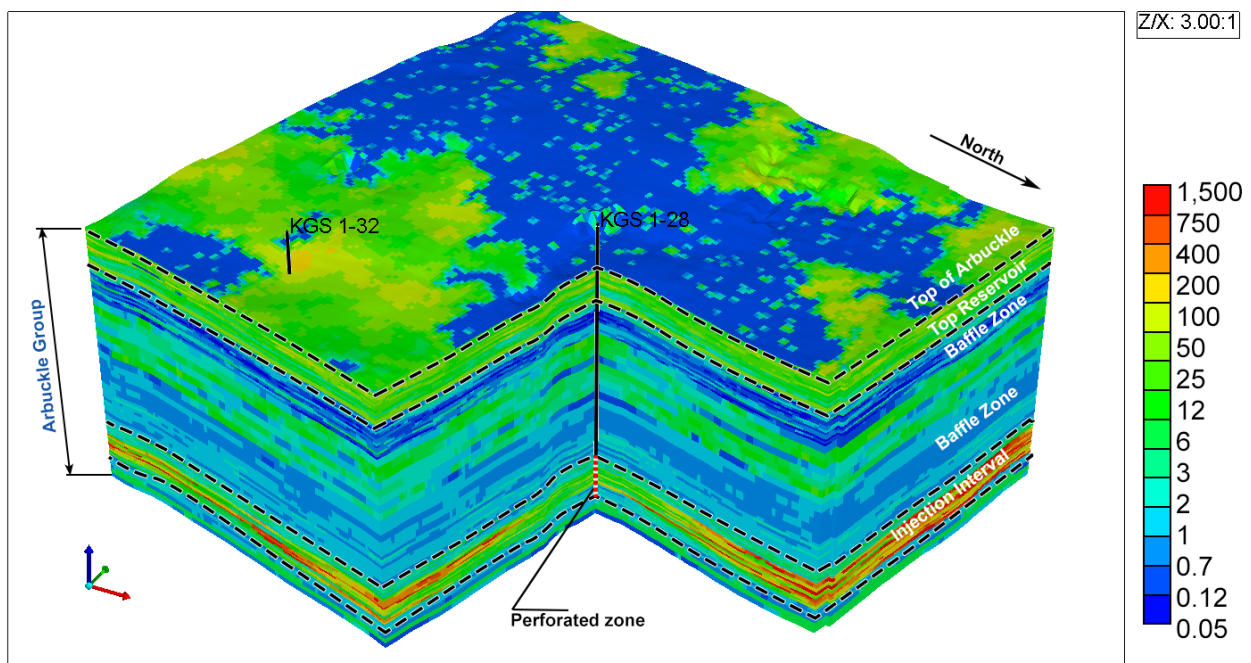
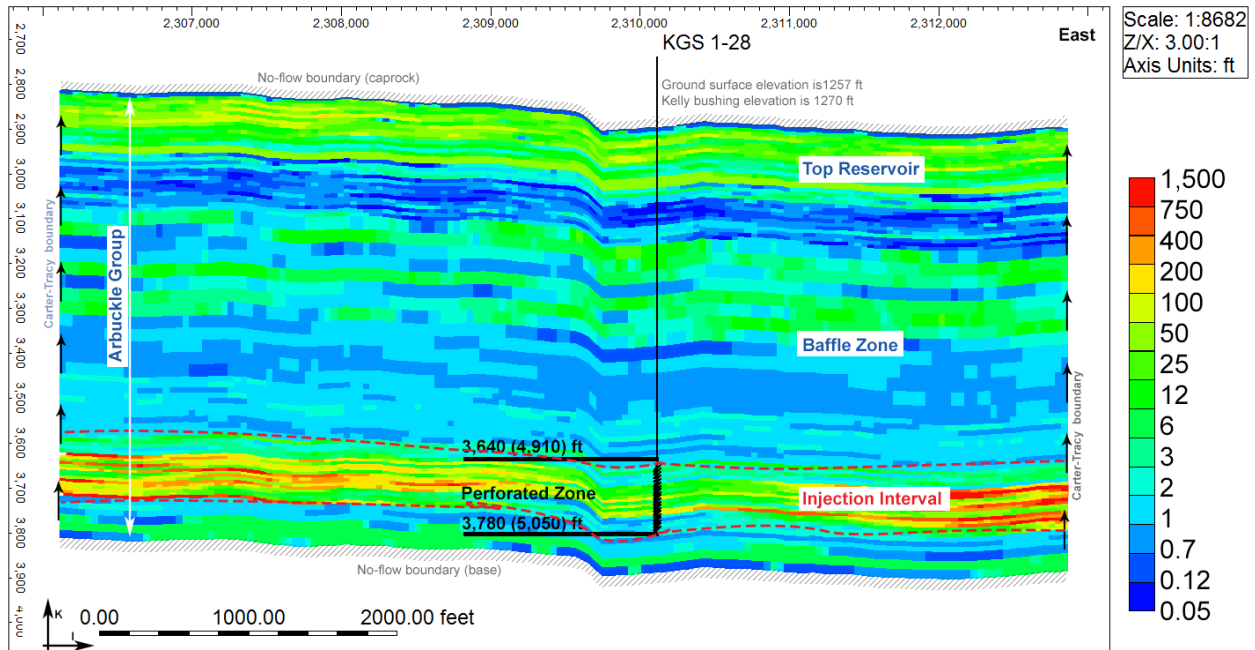
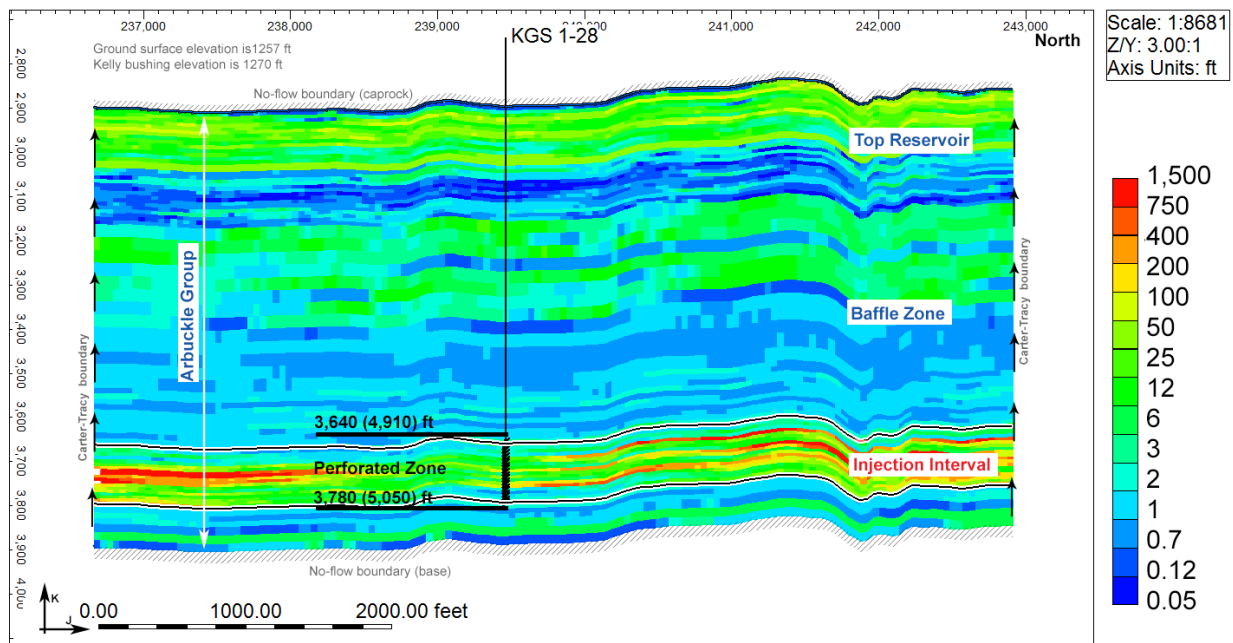


Figure 38a. Upscaled horizontal permeability (mD) distributions in the Arbuckle Group derived from Petrel geo-model.



**Figure 38b. Horizontal permeability (mD) distribution within an east-west cross section through the injection well (KGS 1-28), vertical cross-section A. Location of cross section shown in fig. 32a.**



**Figure 38c. Horizontal permeability (mD) distribution within a north-south cross section through the injection well (KGS 1-28), vertical cross-section B. Location of cross section shown in fig. 32a.**

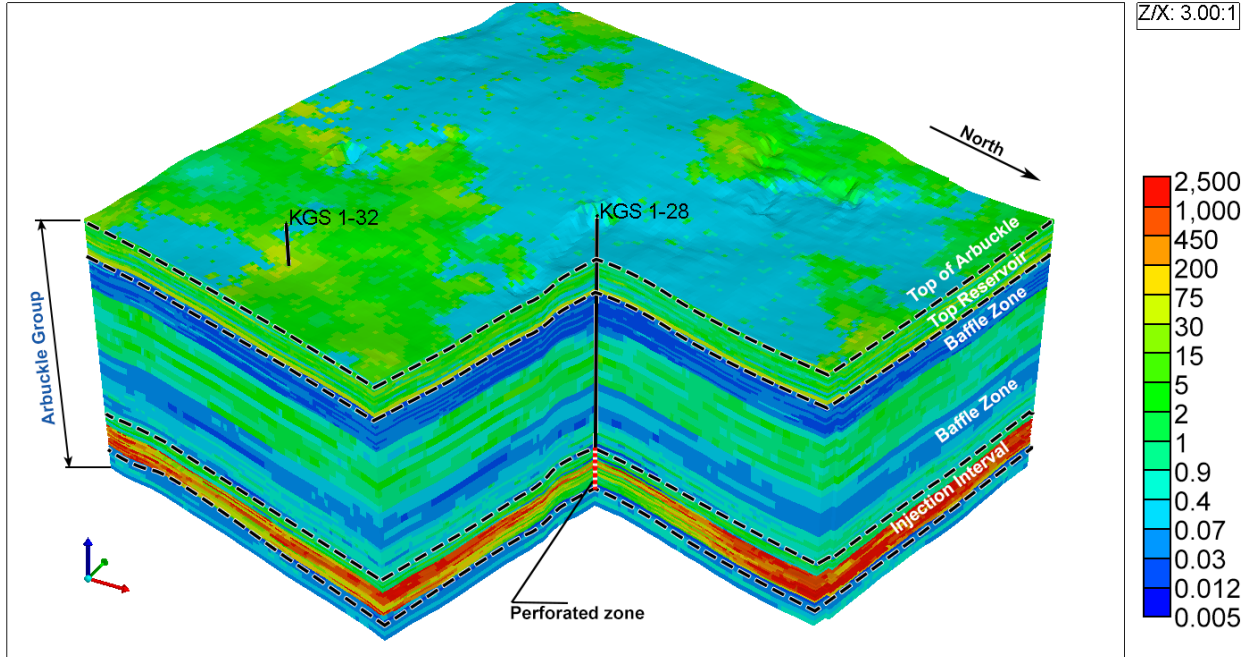


Figure 38d. Upscaled vertical permeability (mD) distributions in the Arbuckle Group derived from Petrel geomodel.

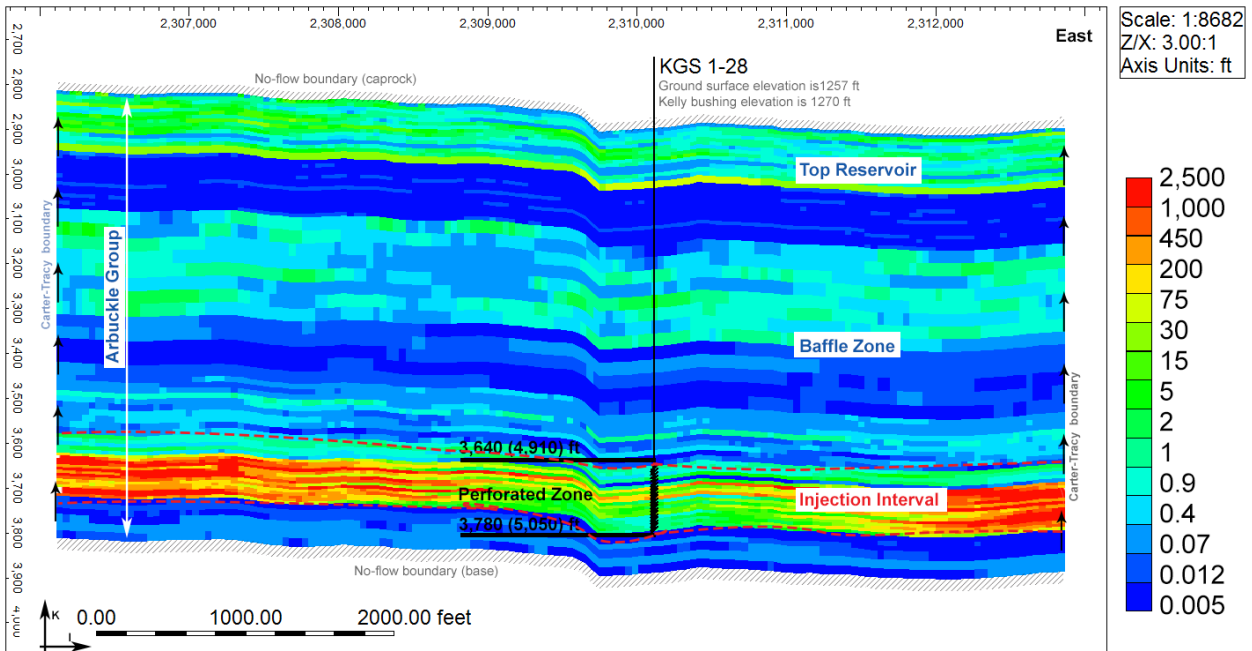
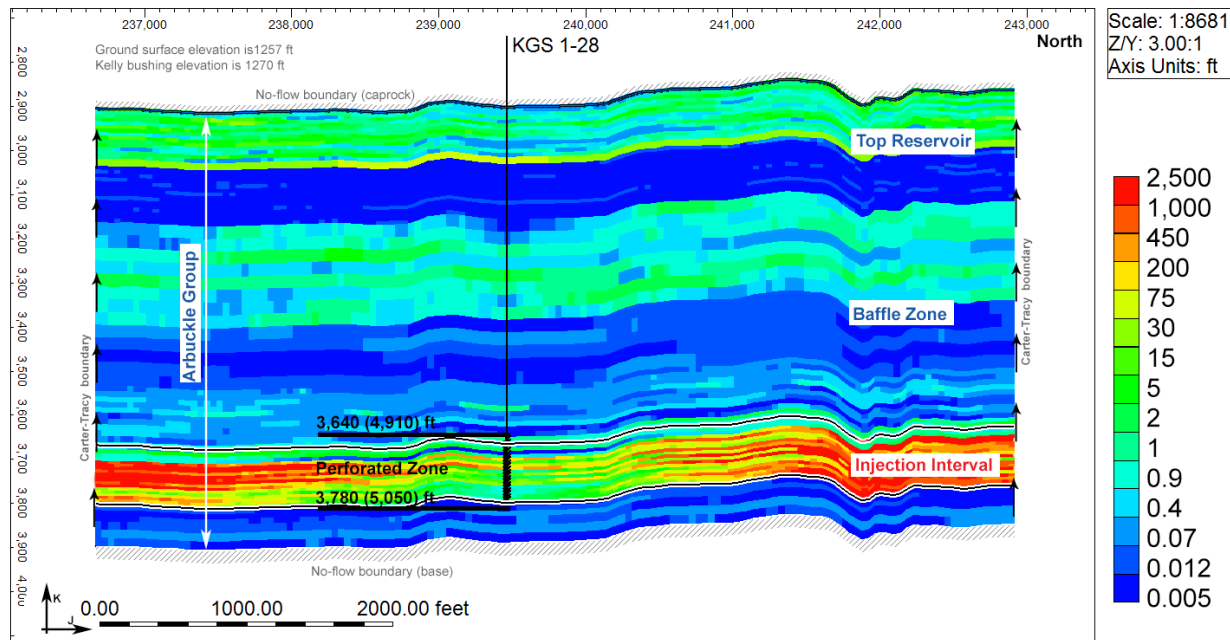


Figure 38e. Vertical permeability (mD) distribution within an east-west cross section through the injection well (KGS 1-28), vertical cross-section A. Location of cross section shown in fig. 32a.



**Figure 38f. Vertical permeability (mD) distribution within a north-south cross section through the injection well (KGS 1-28), vertical cross-section B. Location of cross section shown in fig. 32a.**

### Simulation Software Description

The reservoir simulations were conducted using the Computer Modeling Group (CMG) GEM simulator. GEM is a full equation of state compositional reservoir simulator with advanced features for modeling the flow of three-phase, multi-component fluids and has been used to conduct numerous CO<sub>2</sub> studies (Chang et al., 2009; Bui et al., 2010). It is considered by DOE to be an industry standard for oil/gas and CO<sub>2</sub> geologic storage applications. GEM is an essential engineering tool for modeling complex reservoirs with complicated phase behavior interactions that have the potential to impact CO<sub>2</sub> injection and transport. The code can account for the thermodynamic interactions between three phases: liquid, gas, and solid (for salt precipitates). Mutual solubilities and physical properties can be dynamic variables depending on the phase composition/system state and are subject to well-established constitutive relationships that are a function of the system state (pressures, saturation, concentrations, temperatures, etc.). In particular, the following assumptions govern the phase interactions:

- Gas solubility obeys Henry's Law (Li and Nghiem, 1986)
- The fluid phase is calculated using Schmit-Wenzel or Peng-Robinson (SW-PR) equations of state (Sørense and Whitson, 1992)
- Changes in aqueous phase density with CO<sub>2</sub> solubility, mineral precipitations, etc., are accounted for with the standard or Rowe and Chou correlations.
- Aqueous phase viscosity is calculated based on Kestin, Khalifa, and Correia (1981).

### Model Mesh and Boundary Conditions

The Petrel-based geomodel mesh discussed above consists of a 706 x 654 horizontal

grid and 79 vertical layers for a total of 36,476,196 cells. The model domain spans from the base of the Arbuckle Group to the top of the Pierson Group. To reduce reservoir simulation time, this model was upscaled to a 157 x 145 horizontal mesh with 79 layers for a total of 1,798,435 cells to represent the same rock volume as the Petrel model for use in the CMG simulator. The thickness of the layers varies from 5 to 20 ft based on the geomodel, with an average of 13 feet.

Based on preliminary simulations, it was determined that due to the small scale of injection and the presence of a competent confining zone, the plume would be contained within the Arbuckle system for all alternative realizations of reservoir parameters. Therefore, the reservoir model domain was restricted to the Arbuckle aquifer with no-flow boundaries specified along the top (Simpson Group) and bottom (Precambrian basement) of the Arbuckle group. The specification of no-flow boundaries along the top and bottom of the Arbuckle Group is justified because of the low permeabilities in the overlying and underlying confining zones. The permeability in the Pierson formation was estimated to be as low as 1.6 nanoDarcy (nD;  $1.0^{-9}$  Darcy).

The simulation model, centered approximately on the injection well (KGS 1-28), extends approximately 1.2 mi in the east-west and 1.3 mi in the north-south orientations. Vertically, the model extends approximately 1,000 ft from the top of the Precambrian basement to the bottom of the Simpson Group. As discussed above, the model domain was discretized laterally by 157 x 145 cells in the east-west and north-south directions and vertically in 79 layers. The lateral boundary conditions were set as an infinite-acting Carter-Tracy aquifer (Dake, 1978; Carter and Tracy, 1960) with leakage. This is appropriate since the Arbuckle is an open hydrologic system extending over most of Kansas. Sensitivity simulations indicated that the increases in pore pressures and the plume extent were not meaningfully different by using a closed boundary instead of a Carter-Tracy boundary.

## **Hydrogeologic Properties**

Geologic and hydrologic data pertaining to the Arbuckle Group are detailed in Sections 3 and 4 of the permit application. Site-specific hydrogeologic properties were used to construct a geomodel at the Wellington site. The porosity and permeability of the geomodel were upscaled to the coarser grid using a weighted averaging approach so that the total pore space volume in the Petrel geomodel was maintained in the upscaled reservoir simulation model. As shown in figs. 39a–b and 40, the qualitative representation (i.e., the shape) of the permeability and porosity distribution remained similar in both the geo and reservoir models. The upscaled reservoir grid was imported from Petrel into CMG Builder, where the model was prepared for dynamic simulations assuming an equivalent porous medium model with flow limited to only the rock matrix. The minimum, maximum, and average porosity and permeabilities in the reservoir model are documented in table 4 alongside the statistics for the geomodel.

## **Rock Type Assignment**

Nine rock types and corresponding tables with capillary pressure hysteresis were developed based on reservoir quality index (RQI) ranges, where RQI is calculated for each grid cell using the formula:

$$RQI = 0.0314 \sqrt{Perm/Porosity}$$

Using RQI ranges, rock types are assigned using CMG Builder’s Formula Manager. The resulting maps of rock type distribution in the model are shown in fig. 41a–c. The division of the nine rock-types (RT) was based on dividing the irreducible water saturation into nine ranges to find their equivalent RQI as shown in table 5. Relative permeability and capillary pressure curves were calculated for each of the nine RQI values.

Table 5.RQI and Relative Permeability Types assignments (RT)

RT	RQI		Ave RQI
	RQI from	RQI To	
1	40	10	25
2	10	2.5	6.25
3	2.5	1	1.75
4	1	0.5	0.75
5	0.5	0.4	0.45
6	0.4	0.3	0.35
7	0.3	0.2	0.25
8	0.2	0.1	0.15
9	0.1	0.01	0.055

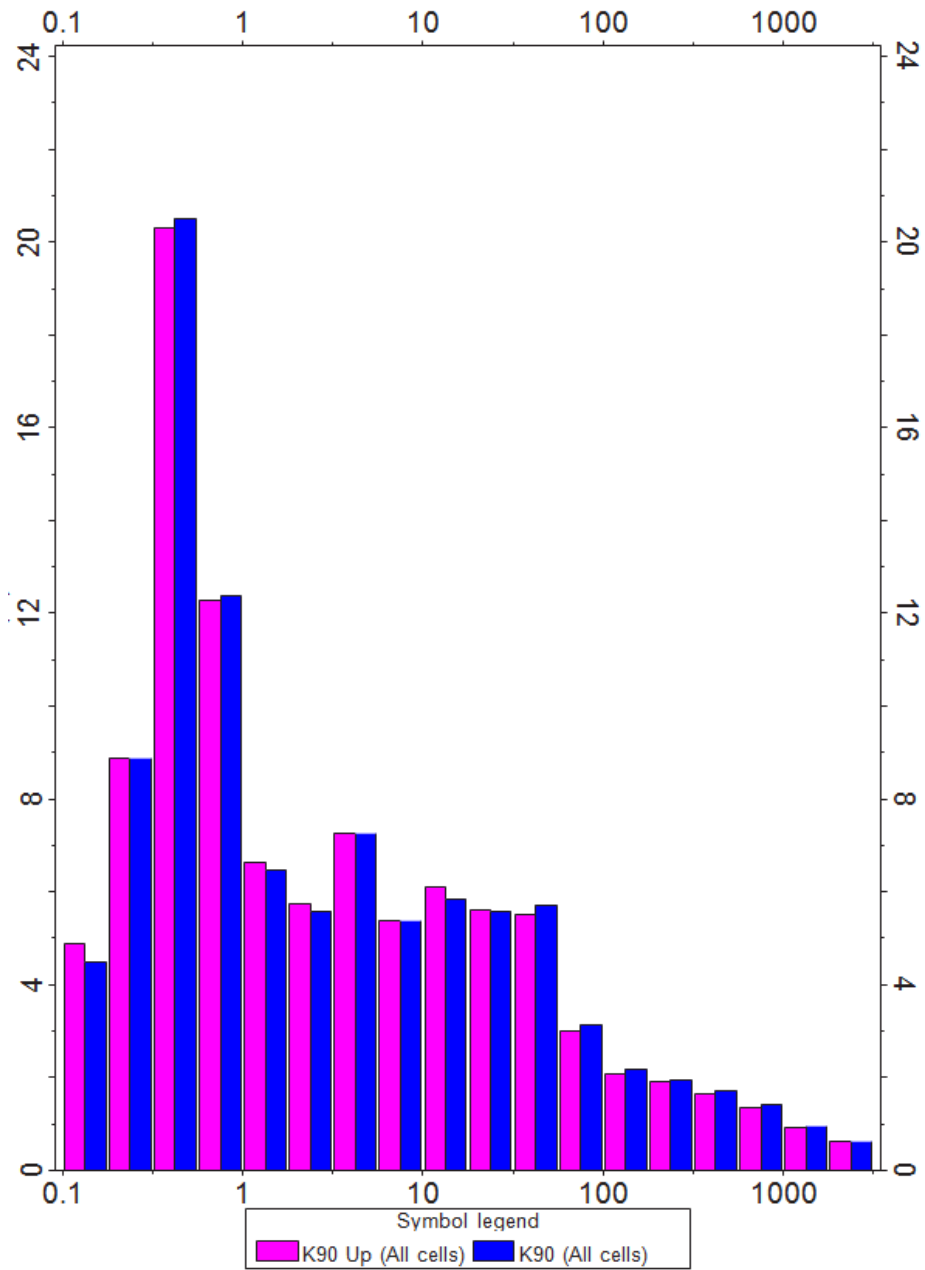


**Figure 39a. Horizontal permeability distribution histogram comparison for original (blue) and upscaled (pink) model properties. (Note: x-axis represents permeability in milliDarcy, mD.)**

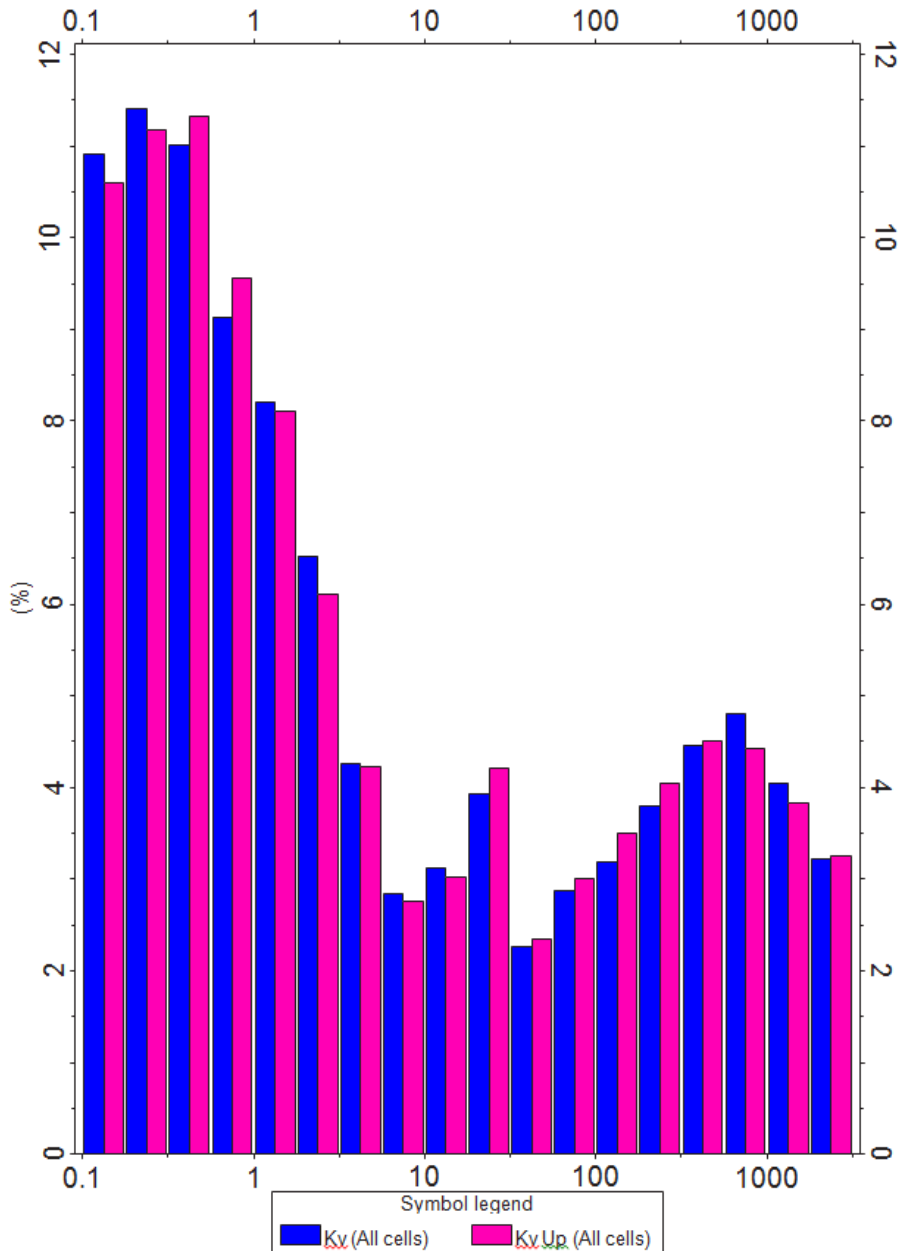
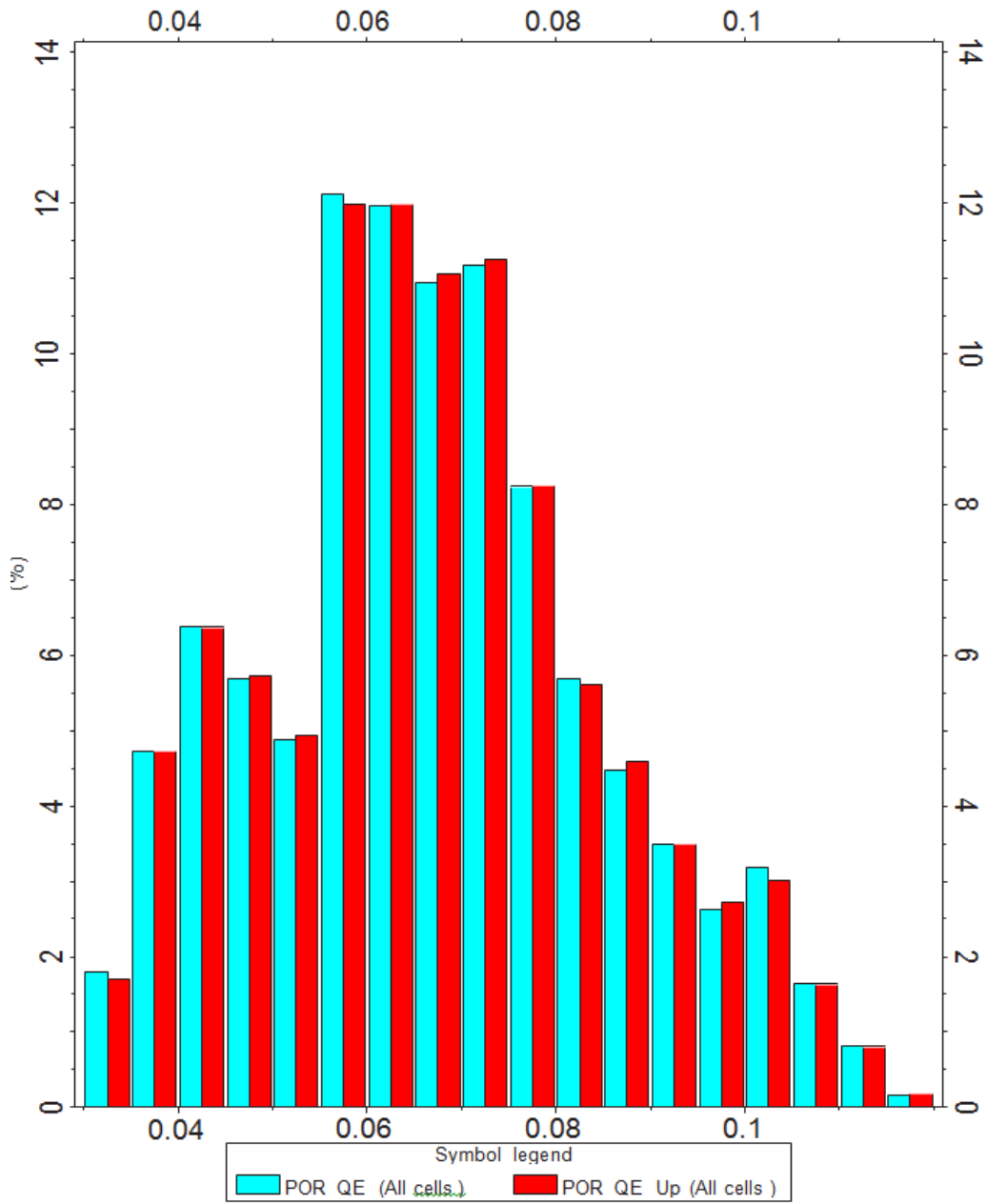


Figure 39b. Vertical permeability distribution histogram comparison for original (blue) and upscaled (pink) model properties. (Note: x-axis represents permeability in milliDarcy, mD.)



**Figure 40. Porosity distribution histogram comparison for original and upscaled model properties. (Note: x-axis represents porosity.)**

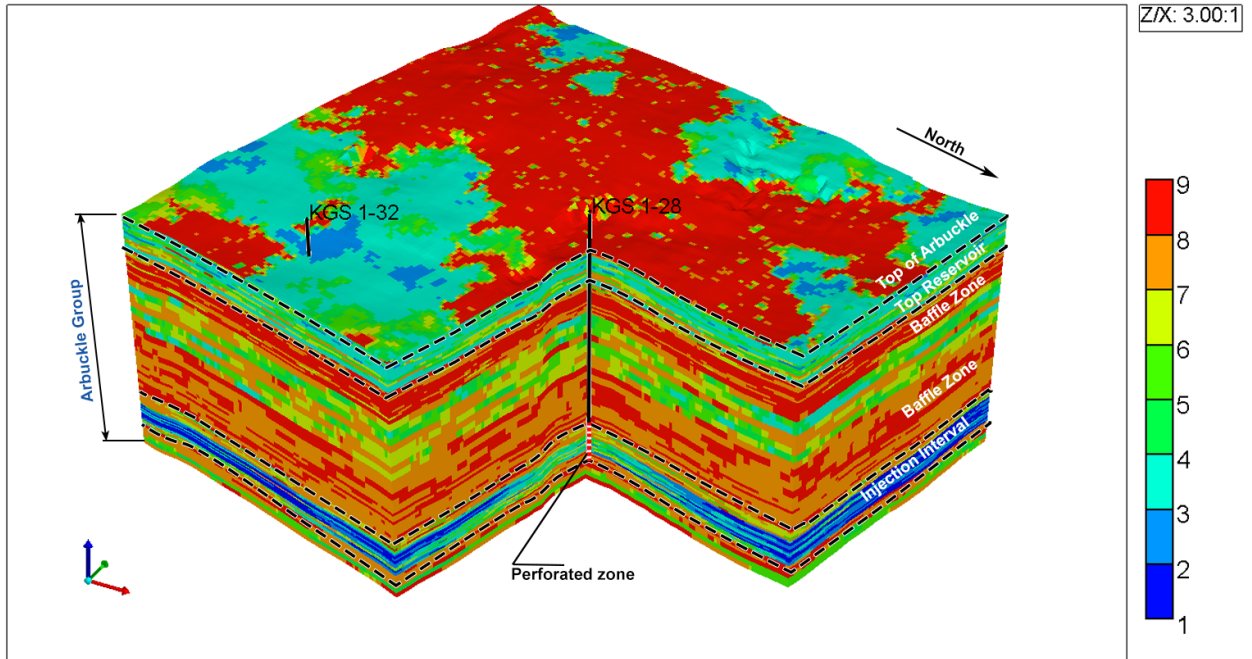


Figure 41a. Rock type distribution model.

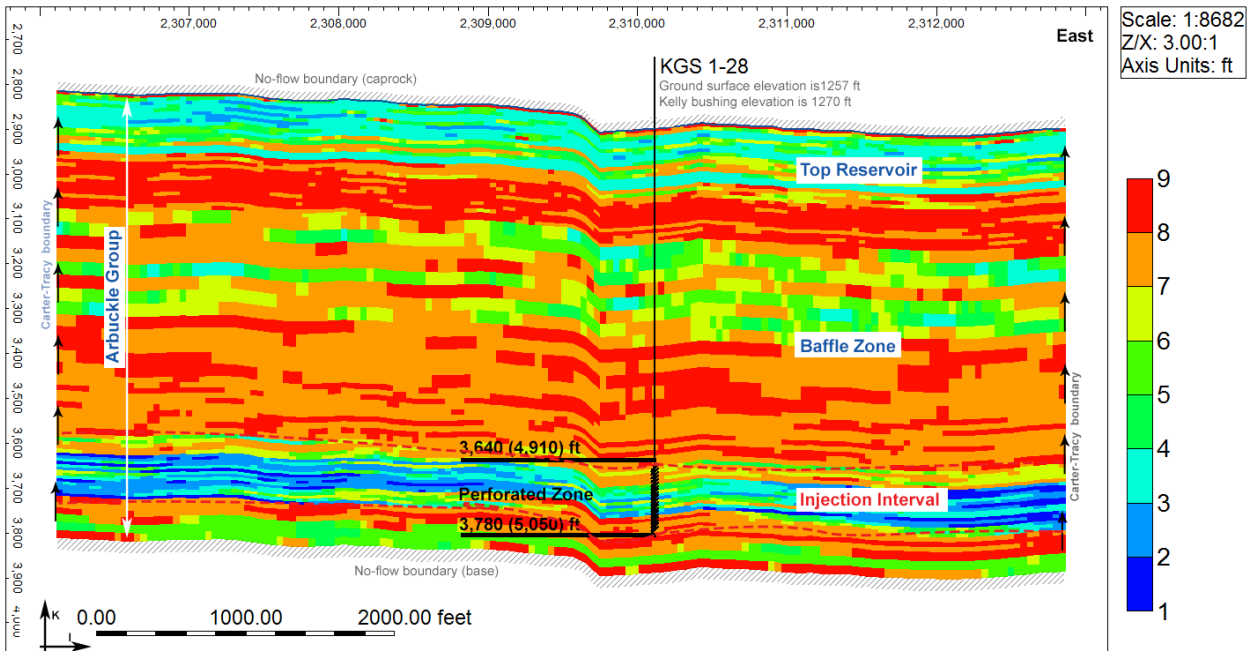
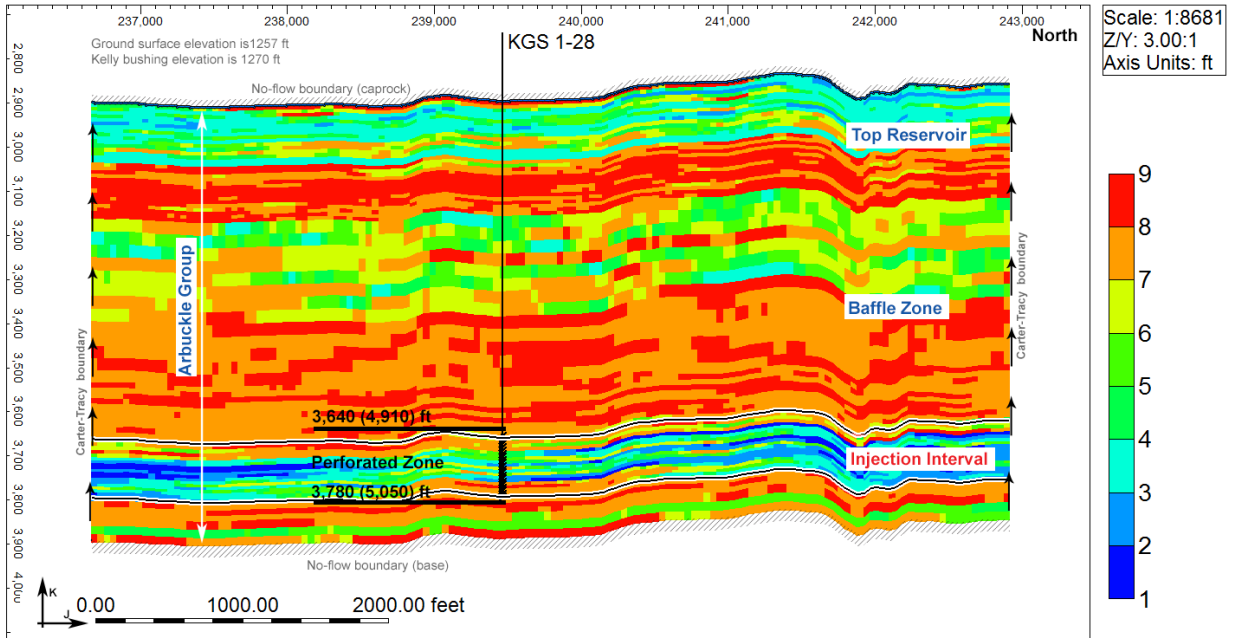


Figure 41b. Rock type distribution model, distribution within an east-west cross section through the injection well (KGS 1-28), vertical cross-section A.



**Figure 41c. Rock type distribution within a north-south cross section through the injection well (KGS 1-28), vertical cross-section B.**

## 5.6 Relative Permeability

Nine sets of relative permeability curves for both drainage and imbibition were calculated for the nine rock types. These sets of relative permeability curves were calculated based on a recently patented formula (SMH reference No: 1002061-0002) that relates the end points to RQI, thereby resulting in a realistic relative permeability data set. The validation of the method is presented below under Validation of the Capillary Pressure and Relative Permeability Methods. Literature experimental studies, including Krevor and Benson (2012, 2015), indicate that the maximum experimental  $\text{CO}_2$  saturation ( $\text{SCO}_{2\text{max}}$ ) and maximum  $\text{CO}_2$  relative permeability ( $\text{KrCO}_{2\text{max}}$ ) in higher permeability samples typically do not reach their actual values and are lower than expected. The authors note that the cause of low experimental end points are the unattainable high capillary pressure in the high permeability core samples. Calculations based on the new patented method addresses and resolves this issue. The highest maximum  $\text{CO}_2$  relative permeability ( $\text{KrCO}_{2\text{max}}$ ) for drainage curves from literature (Bennion and Bachu, 2007) is 0.54, which is lower than expected; however, the highest maximum  $\text{CO}_2$  relative permeability using the new method is 0.71, which is a more realistic value. As noted above, measured relative permeabilities from literature do not represent the end points of relative permeability curves and they need to be adjusted. Using this new method,  $\text{SCO}_{2\text{max}}$  and  $\text{KrCO}_{2\text{max}}$  are scaled up to reasonable values.

Highest and lowest Corey  $\text{CO}_2$  exponent values from Bennion and Bachu (2010) were selected and they were assigned to the nine RQI values in a descending order from high to low. The full range of RQI assignments and relative permeability tables can be found in Appendix E. An example of capillary pressure and relative permeability for both drainage and imbibition is presented in table 6. Corey Water exponents for different permeabilities from literature did not show much variability. Therefore, average values were used for both drainage and imbibition curves. Figure 42a presents relative permeability curves for an RQI value of 0.35 for illustrative

purposes. Figure 42b presents the same set of curves for the full range of RQI values. Residual CO<sub>2</sub> saturation (SCO<sub>2r</sub>) for calculating imbibition curves was needed. SCO<sub>2r</sub> was calculated based on a correlation between residual CO<sub>2</sub> saturation (SCO<sub>2r</sub>) and initial CO<sub>2</sub> saturation (SCO<sub>2i</sub>) (Burnside and Naylor, 2014).

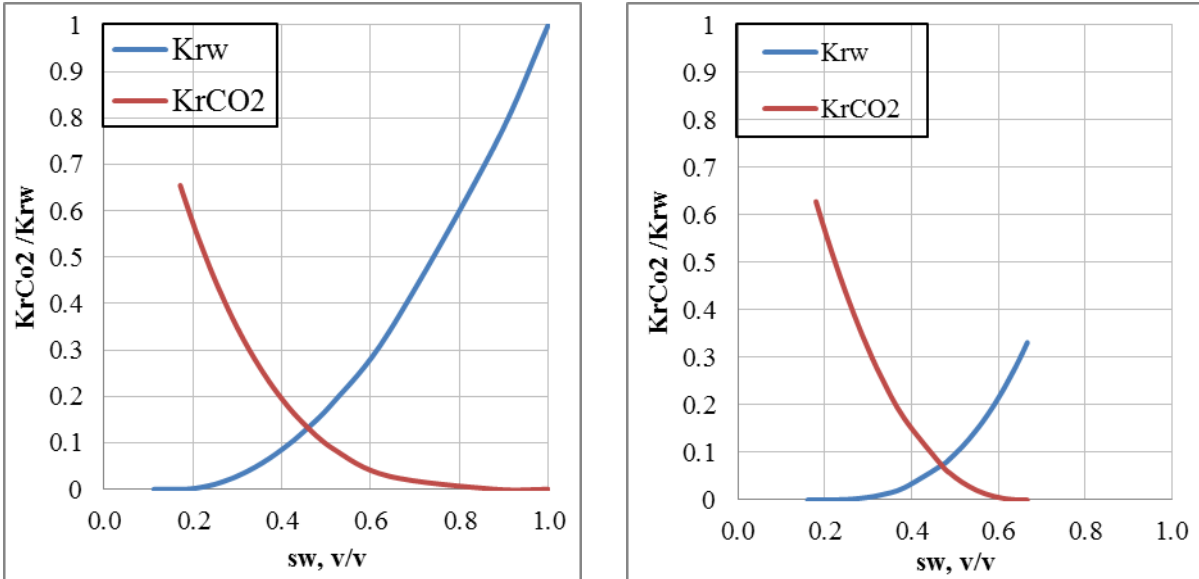
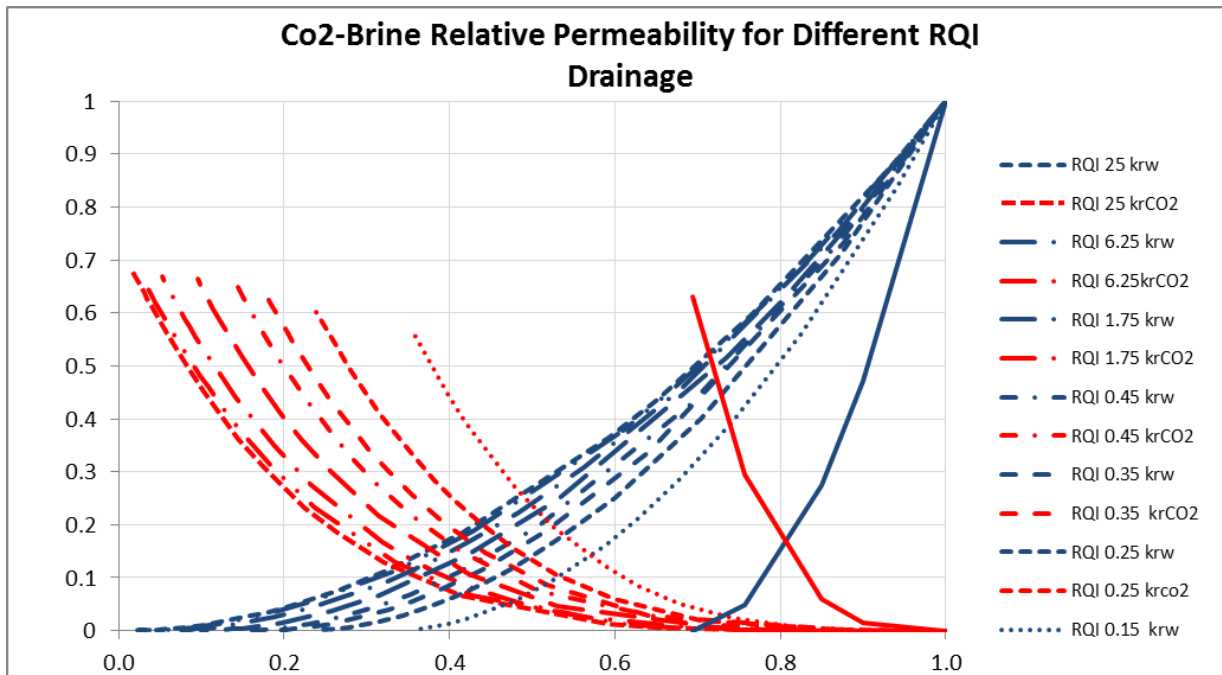


Figure 42a. Calculated relative permeability for drainage (left) and imbibition (right) for RQI=0.35.



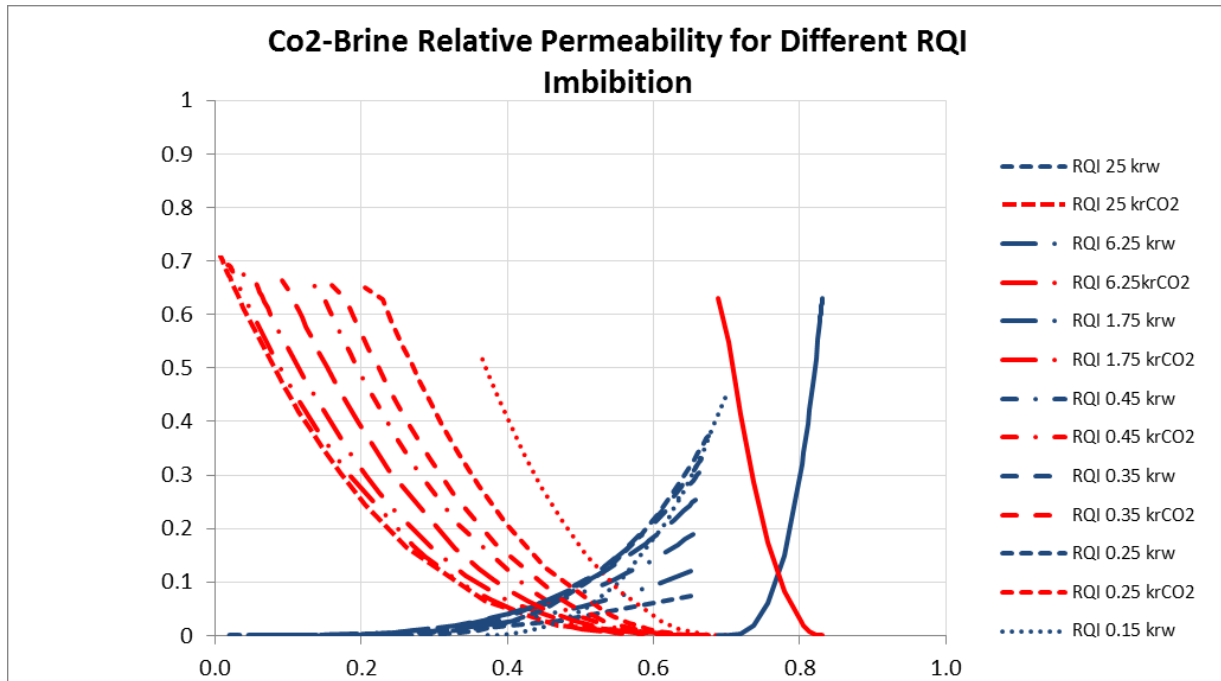


Figure 42b. Calculated relative permeability for drainage (top) and imbibition (bottom) for full set of RQI.

Table 6. Example of capillary pressure and relative permeability drainage and imbibition tables for rock type 6 (RQI=0.35).

**Drainage Curves**

RQI range from 0.3-0.4-AveRQI=0.35				
Pc	Sw	sCO <sub>2</sub>	Krw	krCO <sub>2</sub>
1	1.000	0.000	1.000	0.000
2	0.877	0.123	0.735	0.001
3	0.641	0.359	0.338	0.029
4	0.518	0.482	0.190	0.086
5	0.443	0.557	0.119	0.148
6	0.392	0.608	0.080	0.205
7	0.354	0.646	0.056	0.257
8	0.326	0.674	0.041	0.302
9	0.304	0.696	0.030	0.341
10	0.286	0.714	0.023	0.375
12	0.258	0.742	0.013	0.432
14	0.238	0.762	0.008	0.478
18	0.211	0.789	0.003	0.545

**Imbibition Curves**

RQI range from 0.3-0.4-AveRQI=0.35				
Pc	Sw	sCO <sub>2</sub>	Krw	krCO <sub>2</sub>
0	0.666	0.334	0.331	0.000
0.00	0.665	0.335	0.328	0.000
0.01	0.663	0.337	0.325	0.000
0.02	0.660	0.340	0.319	0.000
0.03	0.657	0.343	0.313	0.000
0.04	0.654	0.346	0.308	0.000
0.05	0.652	0.348	0.302	0.000
0.06	0.649	0.351	0.297	0.000
0.07	0.646	0.354	0.292	0.000
0.08	0.643	0.357	0.287	0.000
0.09	0.640	0.360	0.282	0.001
0.1	0.638	0.362	0.277	0.001
0.2	0.612	0.388	0.234	0.003

20	0.201	0.799	0.002	0.571
25	0.183	0.817	0.000	0.620
30	0.171	0.829	0.000	0.655
40	0.156	0.844	0.000	0.655
50	0.146	0.854	0.000	0.655
60	0.140	0.860	0.000	0.655
70	0.135	0.865	0.000	0.655
80	0.131	0.869	0.000	0.655
90	0.129	0.871	0.000	0.655
100	0.126	0.874	0.000	0.655
150	0.119	0.881	0.000	0.655
200	0.116	0.884	0.000	0.655
300	0.112	0.888	0.000	0.655

0.3	0.589	0.411	0.200	0.008
0.4	0.569	0.431	0.171	0.013
0.5	0.550	0.450	0.148	0.020
0.6	0.532	0.468	0.128	0.029
0.7	0.516	0.484	0.112	0.038
0.8	0.501	0.499	0.098	0.047
0.9	0.487	0.513	0.086	0.057
1	0.474	0.526	0.076	0.067
2	0.383	0.617	0.026	0.172
3	0.329	0.671	0.011	0.261
4	0.293	0.707	0.005	0.333
5	0.267	0.733	0.002	0.390
6	0.248	0.752	0.001	0.437
7	0.233	0.767	0.001	0.476
8	0.221	0.779	0.000	0.508
9	0.211	0.789	0.000	0.536
10	0.203	0.797	0.000	0.559
12	0.189	0.811	0.000	0.598
14	0.180	0.820	0.000	0.629
20	0.160	0.840	0.000	0.655
30	0.144	0.856	0.000	0.655
40	0.135	0.865	0.000	0.655
50	0.129	0.871	0.000	0.655
60	0.126	0.874	0.000	0.655
70	0.123	0.877	0.000	0.655
80	0.121	0.879	0.000	0.655
90	0.119	0.881	0.000	0.655
100	0.117	0.883	0.000	0.655
150	0.113	0.887	0.000	0.655
200	0.111	0.889	0.000	0.655
300	0.109	0.891	0.000	0.655

## Capillary Pressure Curves

Nine capillary pressure curves were calculated for drainage and imbibition for nine RQI values based on a recently patented formula (SMH reference No: 1002061-0002). The formula constitutes a function for the shape of  $P_c$  curves and functions for the end points that are entry pressure ( $P_{\text{entry}}$ ) and irreducible water saturation ( $S_{\text{wir}}$ ). The end points are correlated to RQI.  $P_{\text{entry}}$  was calculated from entry radius (R15) and Winland (R35). There is a relationship between R35 and R15 and a relationship between  $P_{\text{entry}}$  and R15; therefore,  $P_{\text{entry}}$  can be calculated from R15 derived from R35.  $S_{\text{wir}}$  was calculated from the NMR log at a  $P_c$  equal to 20 bars (290 psi). To calculate imbibition curves, a residual  $\text{CO}_2$  saturation ( $\text{CO}_{2r}$ ) value was needed.  $\text{CO}_{2r}$  was calculated from a relationship between initial  $\text{CO}_2$  saturation and  $\text{CO}_{2r}$  as discussed above. The capillary pressure curves for drainage and imbibition for RQI of 0.35 are presented in fig. 43. The capillary pressure data for the full set of RQI values are presented in Appendix E.

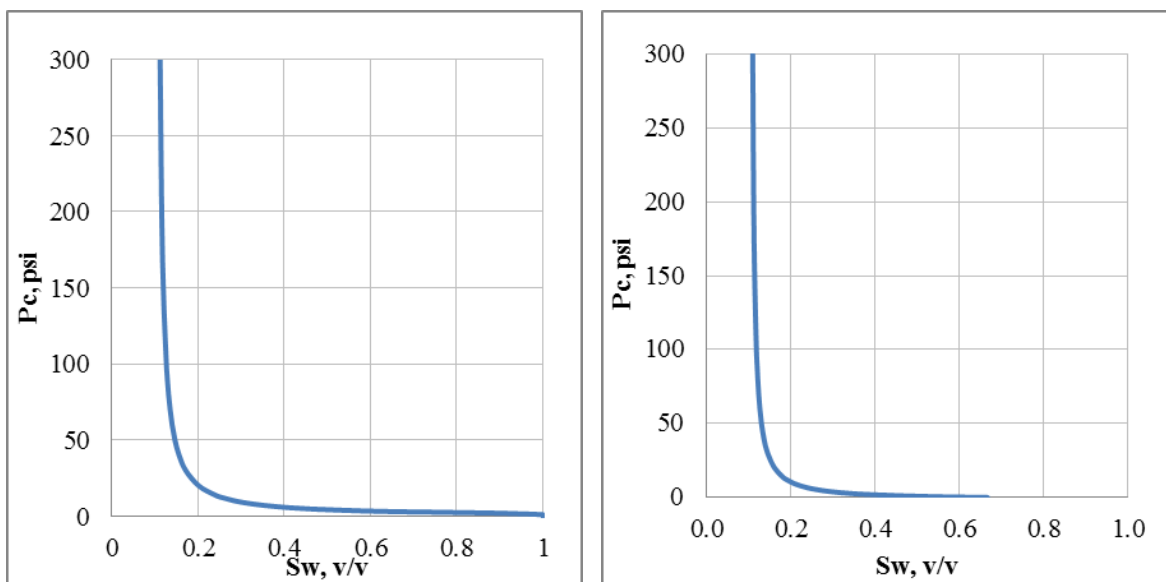


Figure 43. Capillary pressure curves for drainage (left) and imbibition (right) for an RQI value of 0.35.

## Validation of the Capillary Pressure and Relative Permeability Methods

The capillary pressure and relative permeability curves were estimated in the laboratory for the Mississippian Reservoir as part of the Wellington Mississippian Enhanced Oil Recovery (EOR) project located approximately a mile southwest of the Wellington  $\text{CO}_2$  storage site. The laboratory-derived curves were used to validate the relative permeability and capillary pressure approach for the Arbuckle discussed above and this was deemed reasonable since the same approach that was used in the Mississippian was also used for the Arbuckle.

Two core plug samples with similar RQI values were sent to Core Laboratories for capillary pressure and relative permeability measurements. The relative permeability and capillary pressure curves were calculated twice for the Mississippian reservoir—before and after the core results were obtained from the laboratory. The initial estimation of  $P_c$  curves was based on the end points that were calculated from the NMR log. As shown in fig. 44a, there is a slight difference between the calculated  $P_c$  and measured  $P_c$  before calibration. However, there is an excellent match between the calculated  $P_c$  and the measured  $P_c$  after calibration using the core

measured end points. Similarly, as shown in fig. 44b, there is a slight difference between the initial calculated relative permeability and measured relative permeability, but the match is excellent after calibration.

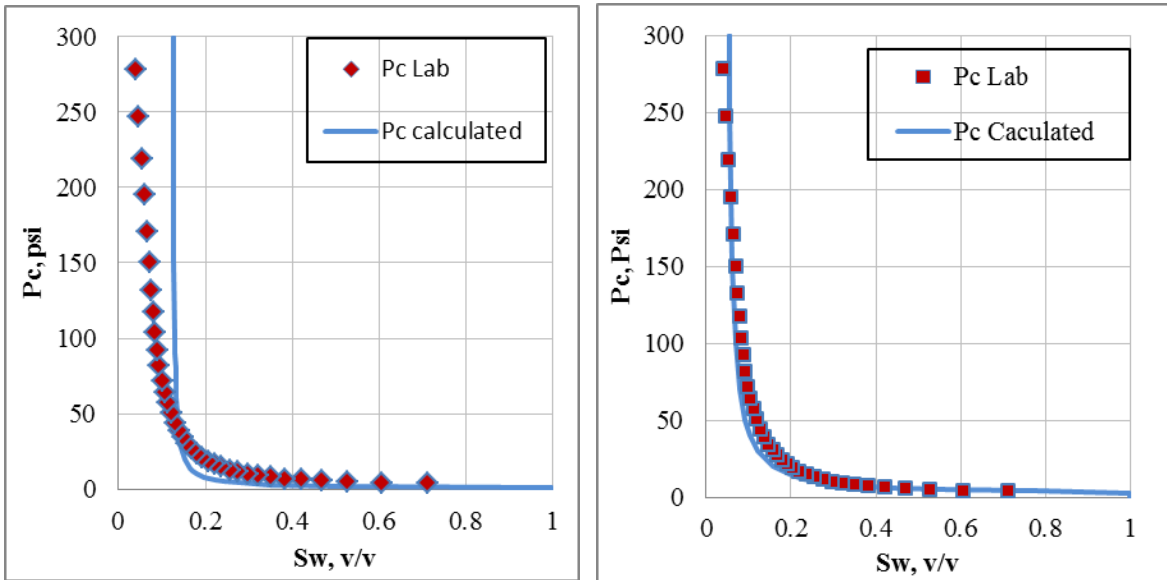


Figure 44a. Capillary pressure curves for an RQI value of 0.2 before calibration (left) and after calibration (right).

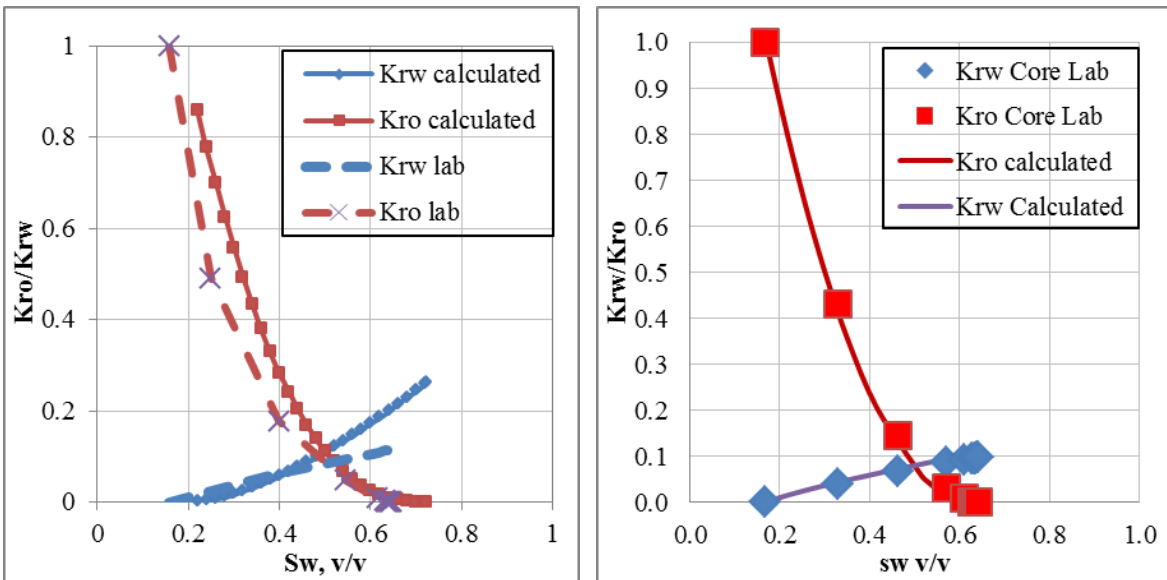


Figure 44b. Relative permeability curves for an RQI value of 0.16 before calibration (left) and after calibration (right).

### Initial Conditions and Injection Rates

Table 7 lists the initial conditions specified in the reservoir model. The simulations were conducted assuming isothermal conditions, but a thermal gradient of 0.008 °C/ft was considered

for specifying petrophysical properties that vary with layer depth and temperature such as CO<sub>2</sub> relative permeability, CO<sub>2</sub> dissolution in formation water, etc. The original static pressure in the injection zone (at a reference depth of 4,960 ft) was set to 2,093 psi and the Arbuckle pressure gradient of 0.48 psi/ft was assumed for specifying petrophysical properties. A 140 ft thick perforation zone in well KGS 1-28 was specified between 4,910 and 5,050 ft. A constant brine density of 68.64 lbs/ft<sup>3</sup> (specific gravity of 1.1) was assumed. A total of 40,000 metric tons (MT) of CO<sub>2</sub> was injected in the Arbuckle formation over a period of nine months at an average injection rate of 150 tons/day

Table 7. Model input specification and CO<sub>2</sub> injection rates.

Temperature	60 °C (140 °F)
Temperature Gradient	0.008 °C/ft
Pressure	2,093 psi (14.43 MPa) @ 4,960 ft RKB
Perforation Zone	4,910-5,050 ft
Perforation Length	140 ft (model layers 54 to 73)
Injection Period	9 months
Injection Rate	150 tons/day
Total CO <sub>2</sub> injected	40,000 MT

## 5.10 Permeability and Porosity Alternative Models

The base-case reservoir model has been carefully constructed using a sophisticated geomodel as discussed in Section 5.3, which honors site-specific hydrogeologic information obtained from laboratory tests and log-based analyses. However, to account and test for sensitivity of hydrogeologic uncertainties, a set of alternate parametric models were developed by varying the porosity and horizontal hydraulic permeability. Specifically, the porosity and permeability were increased and decreased by 25% following general industry practice (FutureGen Industrial Alliance, 2013). This resulted in nine alternative models, listed in table 7. Simulation results based on all nine models were evaluated to derive the worst-case impacts on pressure and migration of the plume front for purposes of establishing the AoR and ensuring that operational constraints are not exceeded

Table 7. Nine alternative permeability-porosity combination models (showing multiplier of base-case permeability and porosity distribution assigned to all model cells).

Alternative Models	Base Porosity x 0.75	Base Porosity	Base Porosity x 1.25
Base Permeability x 0.75	K-0.75/Phi-0.75	K-0.75/Phi-1.0	K-0.75/Phi-1.25
Base Permeability	K-1.0/Phi-0.75	K-1.0/Phi-1.0	K-1.0/Phi-1.25
Base Permeability x 1.25	K-1.25/Phi-0.75	K-1.25/Phi-1.0	K-1.25/Phi-1.25

## 6. Reservoir Simulation Results

For the simulations, 40,000 MT of CO<sub>2</sub> were injected into the KGS 1-28 well at a constant rate of approximately 150 tons per day for a period of nine months. Although Berexco is seeking a permit for injecting 40,000 tons, it is likely that only 26,000 tons will be injected due to budgetary constraints. At the request of the EPA, an alternate set of simulations were conducted with a total injection volume of only 26,000 tons. All simulation results presented below for 40,000 tons are repeated for an injection volume of 26,000 tons in Appendix F. Note that only the simulation result figures are provided in Appendix A; the context for each figure is the same as provided in the following description for an injection volume of 40,000 tons. For example, fig. A.14a (in Appendix A), which shows the extent of the free-phase CO<sub>2</sub> plume at six months from commencement of injection for an injection volume of 26,000 tons is equivalent to fig. 14a below, which shows the plume extent at six months from the start of injection for an injection volume of 40,000 tons.

A total of nine models representing three sets of alternate permeability-porosity combinations as specified in table 7 were simulated with the objective of bracketing the range of expected pressures and extent of CO<sub>2</sub> plume migration.

The extent of lateral plume migration depends on the particular combination of permeability-porosity in each of the nine alternative models. These two parameters are independently specified in CMG as they are assumed to be decoupled. A high-permeability value results in farther travel of the plume due to gravity override, buoyancy, and updip migration. Similarly, a low effective porosity for the same value of permeability results in farther travel for the plume as compared to high porosity as the less-connected pore volume results in faster pore velocity. The high-permeability/low-porosity combination (k-1.25/phi-0.75) resulted in the largest horizontal plume dimension. In contrast, the highest induced pressures were obtained for the alternative model with the lowest permeability and the lowest porosity (k-0.75/phi-0.75).

## CO<sub>2</sub> Plume Migration

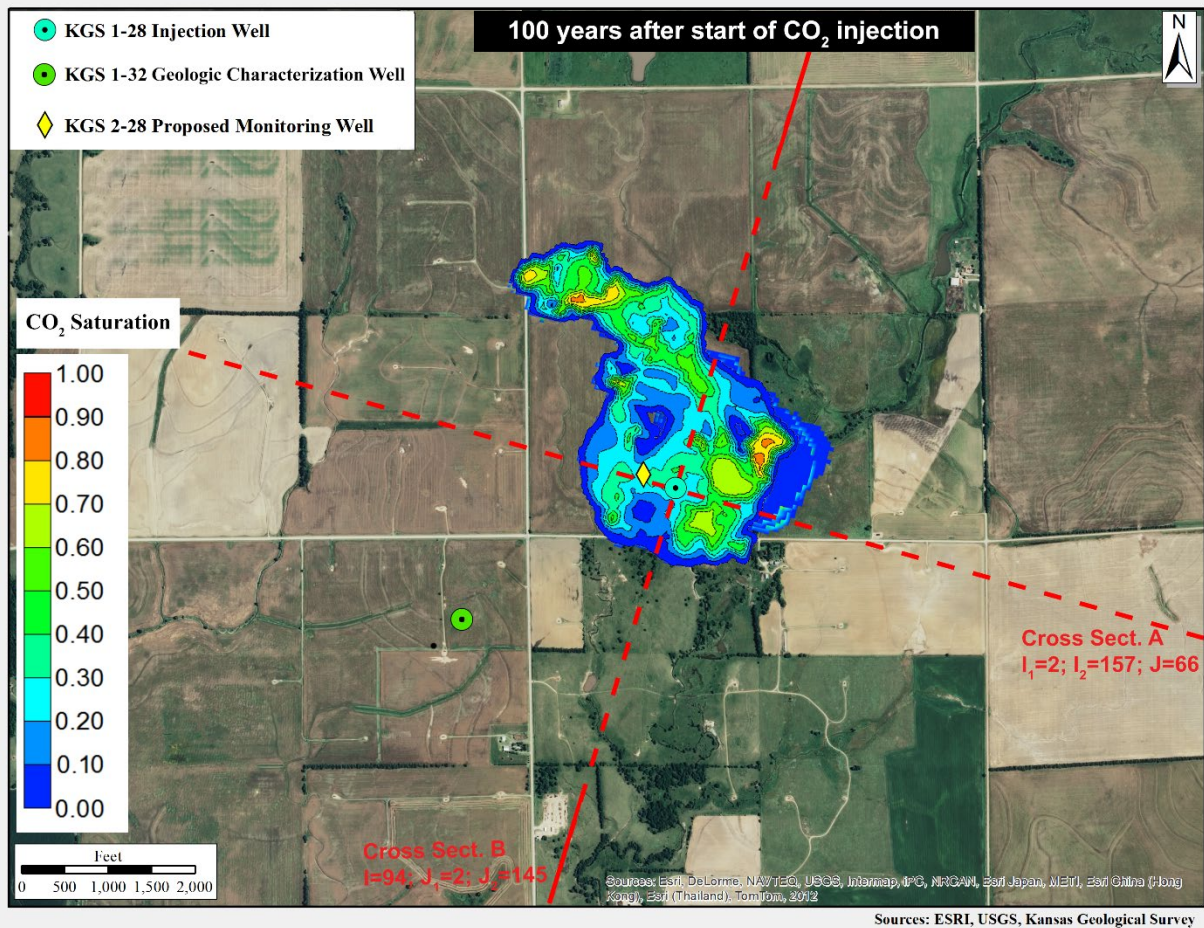
Figure 45 shows the maximum lateral migration of the CO<sub>2</sub> plume in the injection interval (elevation 5,010 ft) for the largest areal migration case (k-1.25/phi-0.75). The plume grows rapidly during the injection phase and is largely stabilized by the end of the second year. The plume at the end of 100 years (fig. 45) has spread only minimally since cessation of injection and has a maximum lateral spread of approximately 2,150 ft from the injection well. It does not intercept any well other than the proposed Arbuckle monitoring well KGS 2-28, which will be constructed in compliance with Class VI injection well guidelines.

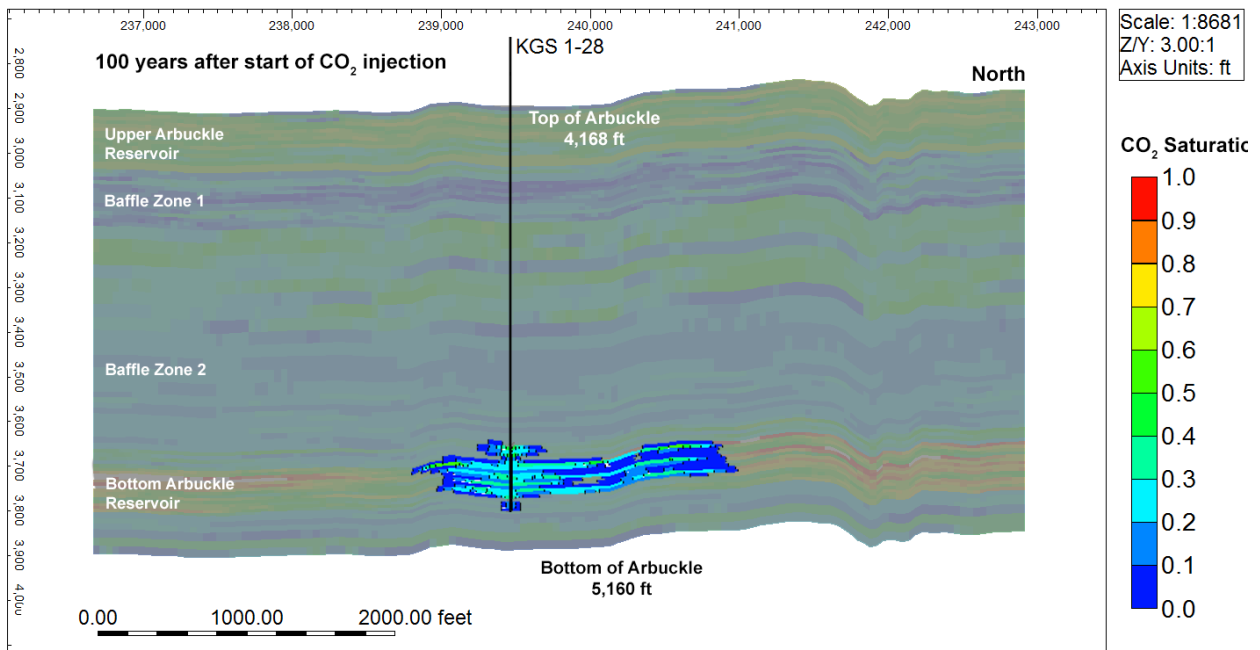
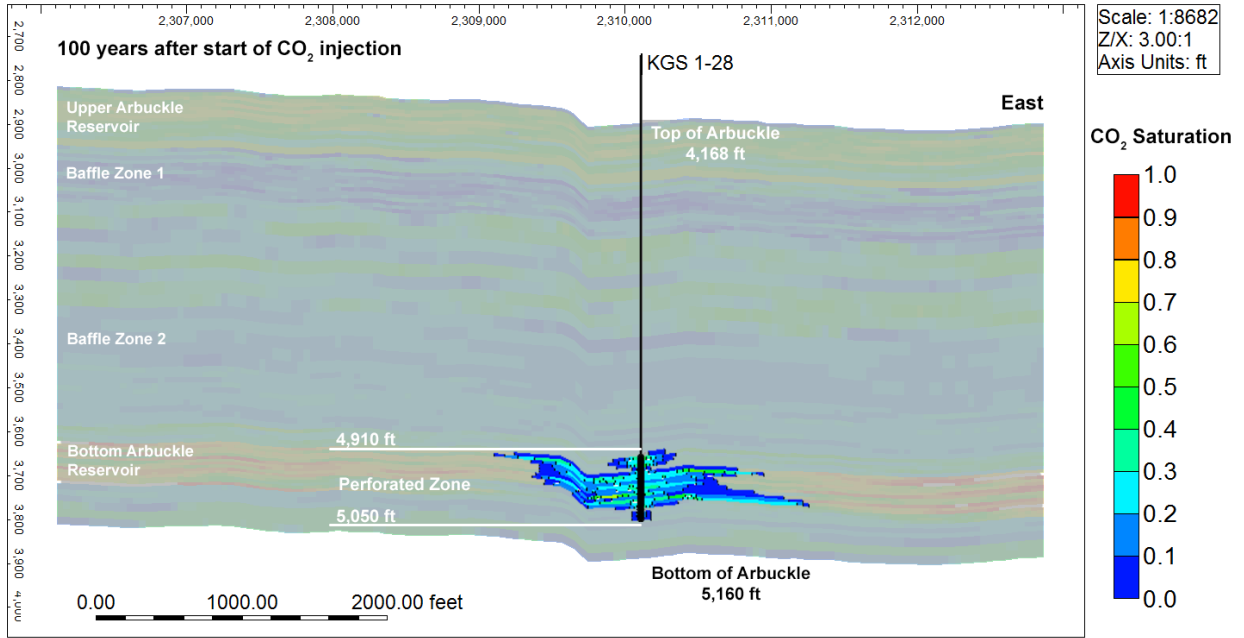
The evolution of the maximum lateral extent of the free phase plume is shown in fig. 46 for the maximum plume spread case (k-1.25/phi-0.75). The plume grows rapidly during the injection period and up to the second year from commencement of injection. Thereafter, the plume has stabilized to a maximum lateral extent of approximately 2,150 ft. The plume only intercepts the proposed Arbuckle monitoring well KGS 2-28, which will be built to be in compliance with Class VI design and construction requirements. There are no additional natural or artificial penetrations that will allow CO<sub>2</sub> to escape upward from the Arbuckle injection zone.

Figure 47 shows the extent of vertical plume migration for the fast vertical migration case (k-1.25/phi-0.75), the base case (k-1.00/phi-1.00), and the high pressure case (k-0.75/phi-0.75). The free-phase plume remains confined in the injection interval (lower Arbuckle) because of the presence of the low-permeability baffle zones above the injection interval. For all three cases, the plume remains confined in the injection interval in the lower Arbuckle.

To account for uncertainties of CO<sub>2</sub> movement in the vertical direction, an alternate vertical permeability model was also developed in which the vertical permeability parameter was increased by 50% along with a porosity of 75% (k=1.50/phi=0.75). Figure 47 presents the extent of vertical migration of the free phase plume for this case in addition to the three cases already described. The figure shows that the CO<sub>2</sub> migrates approximately 30 ft higher for the altered vertical permeability case, but it does not penetrate the low permeability baffle zone in the middle of the Arbuckle and stays contained within the lower Arbuckle injection zone.

The simulation results discussed above are expected to represent conservative estimates of plume migration because the present CMG simulations neglect mineral sequestration trapping. Additionally, the modeling results presented in this document do not simulate convection cells, which as demonstrated recently by Pau et al. (2010) can greatly accelerate the dissolution rate. Because of time and computational constraints, these mechanisms were ignored, and therefore the storage rates and quantities are likely to be underestimated, thus ensuring that the projections presented in this application provide a “worst-case” scenario.





**Figure 45. Free-phase CO<sub>2</sub> plume in aerial and cross-sectional view for the largest migration alternative model ( $k=1.25/\phi=0.75$ ) at 100 years from start of injection.**

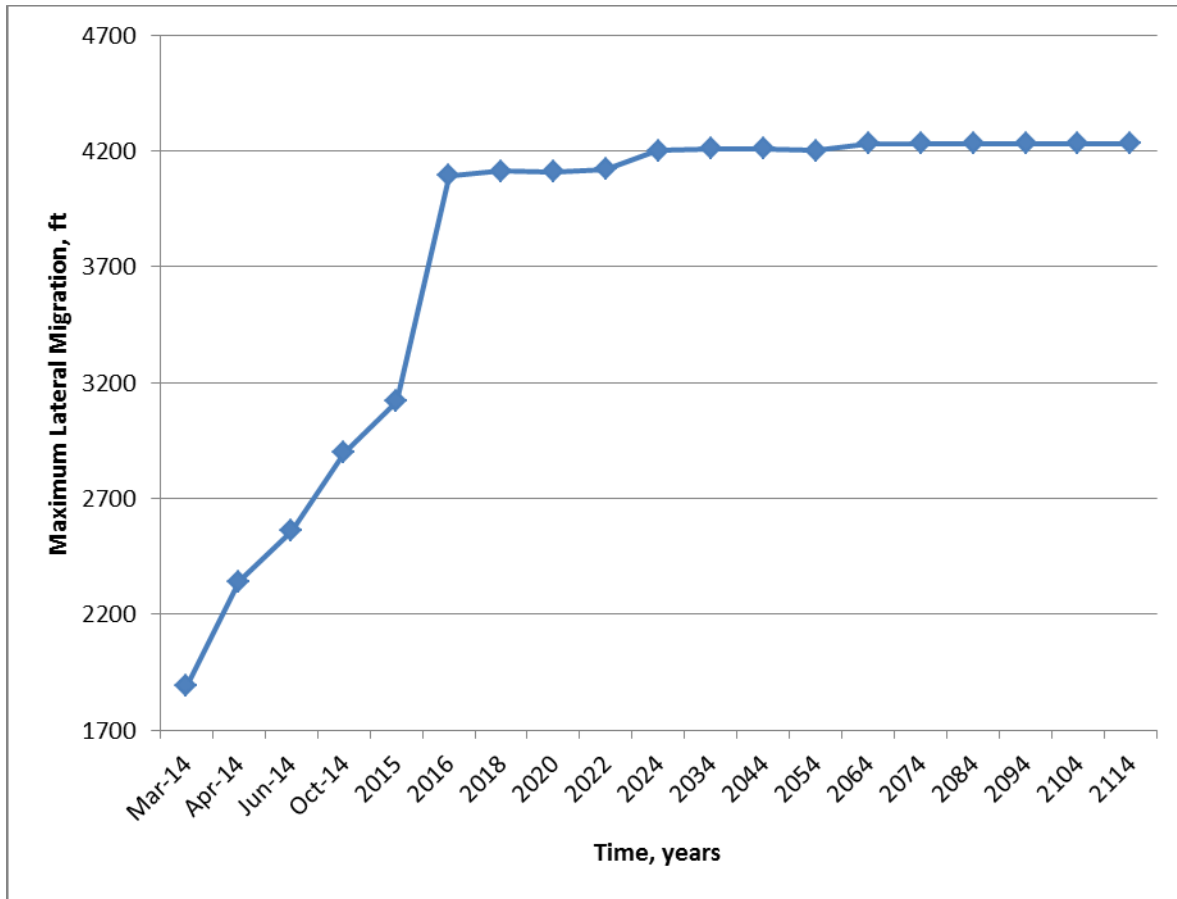


**Figure 46. Maximum lateral extent of CO2 plume migration (as defined by the 0.5% CO2 saturation isoline) for the largest plume migration case k-1.25/phi-0.75.**

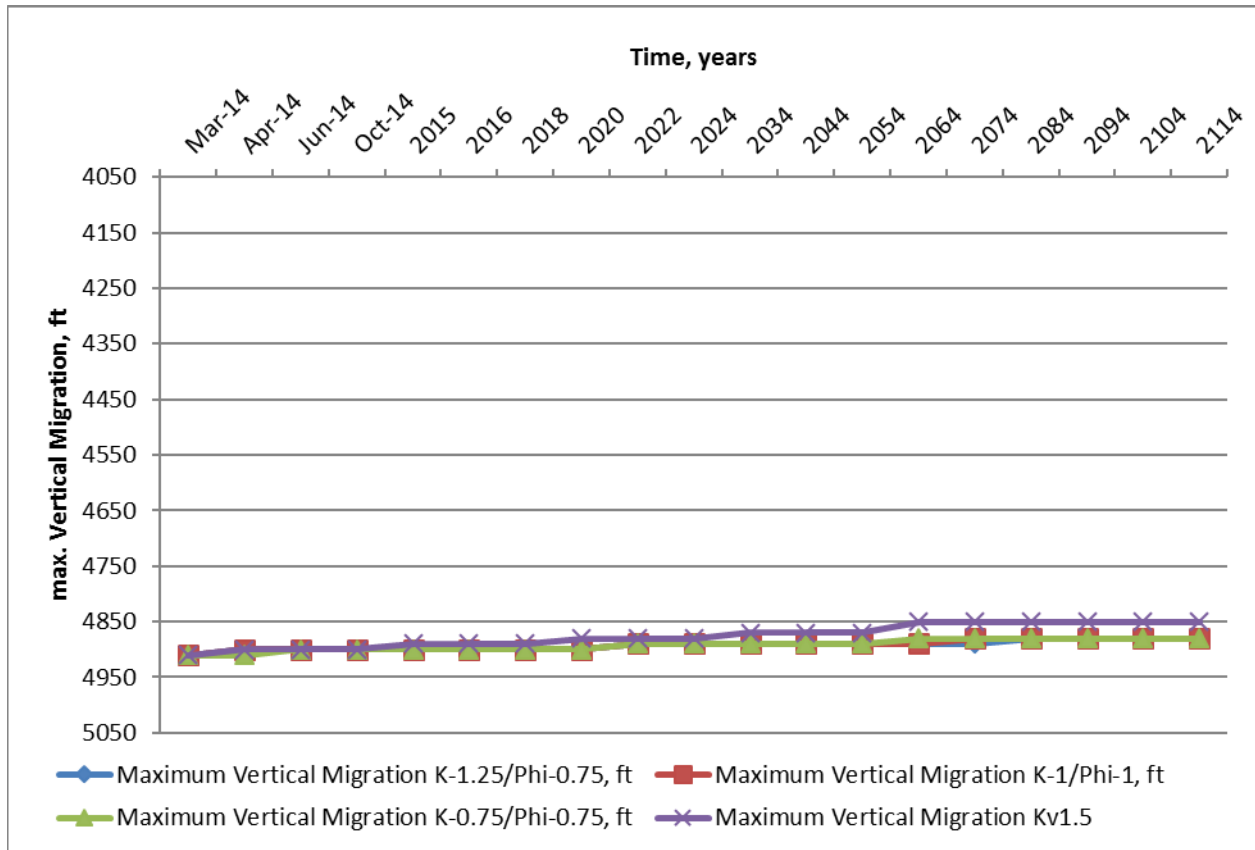


**Figure 47. Maximum vertical extent of free-phase CO2 migration for the two alternative cases that result in the maximum plume spread (k-1.25/phi-0.75) and the maximum induced pressure (k-0.75/phi-0.75) along with base case (k-1.0/phi-1.0) and vertical permeability sensitivity case (k-1.25/phi-0.75).**

### Simulated Pressure Distribution

Figure 48 presents the bottomhole pressure (at a reference depth of 5,050 ft) for the highest pressures alternative model (k-0.75/phi-0.75). The pressure increases to 2,485 psi upon commencement of injection and then gradually drops during the injection period as the capillary effects are overcome. The pressure decreases to pre-injection levels upon cessation of injection. The rise in pressure to 2,485 psi upon commencement of injection represents an increase of 392 psi over pre-injection levels and results in a pressure gradient of 0.515 psi/ft, which is less than the maximum allowable pressure gradient of 0.675 psi/ft corresponding to 90% of the fracture gradient (0.75 psi/ft).

Figure 19 presents the change in pore pressure at the base of the confining zone (Simpson Group) for the k-0.75/phi-0.75 alternate model that resulted in the highest pressures. The maximum pressure increase at the end of the injection period of approximately 1.15 psi is fairly small and well below the entry pressure of 956 psi for the confining zone.

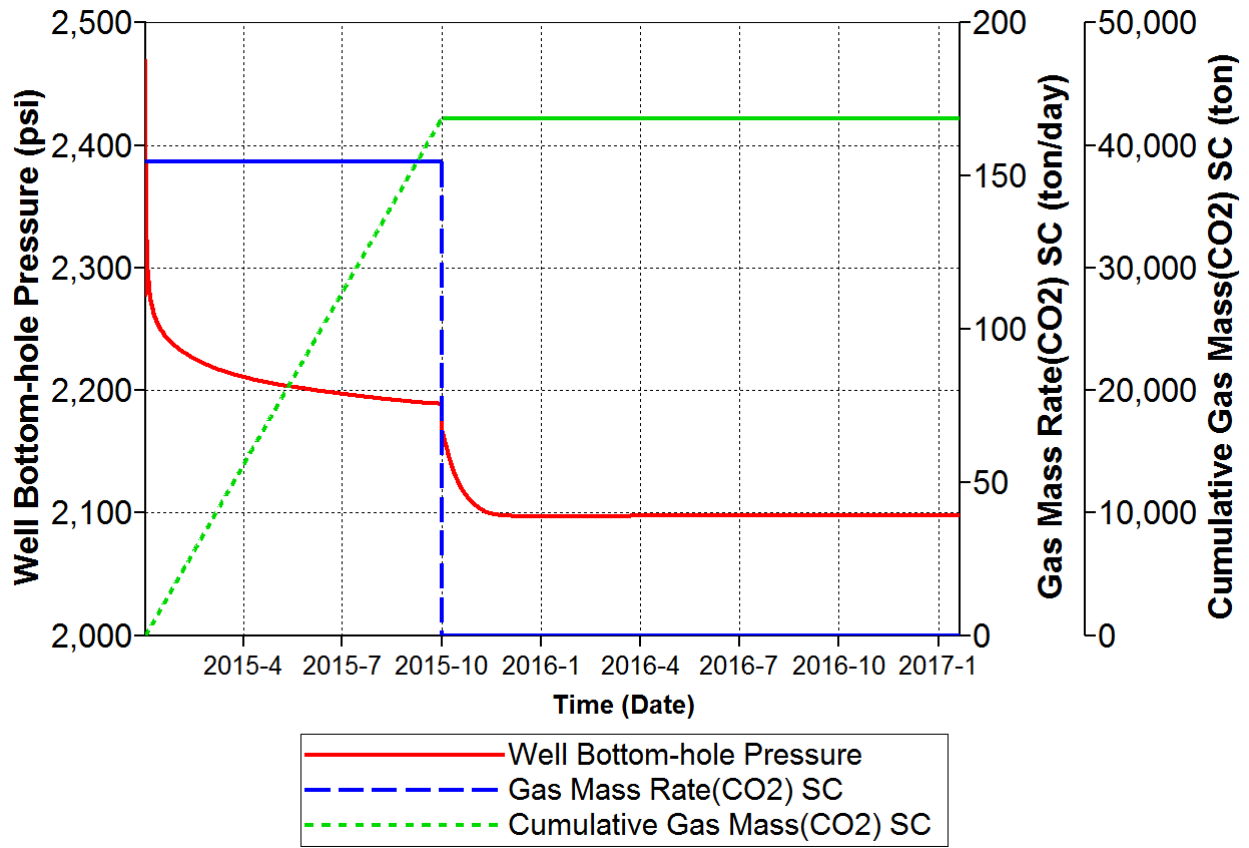


Figure 48. Maximum well bottomhole pressure at a depth of 5,050 ft for the minimum porosity and minimum permeability case ( $k=0.75/\phi=0.75$ ).

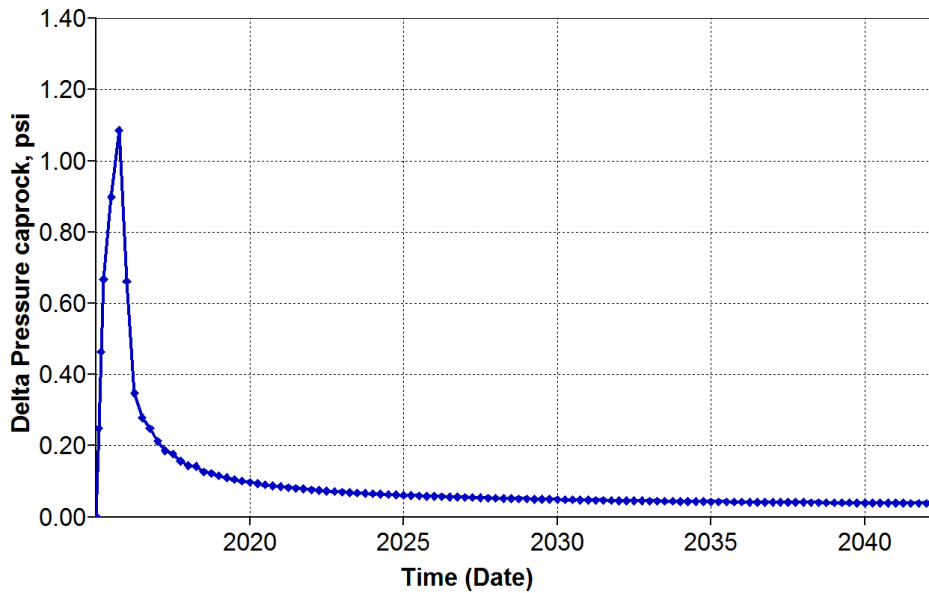
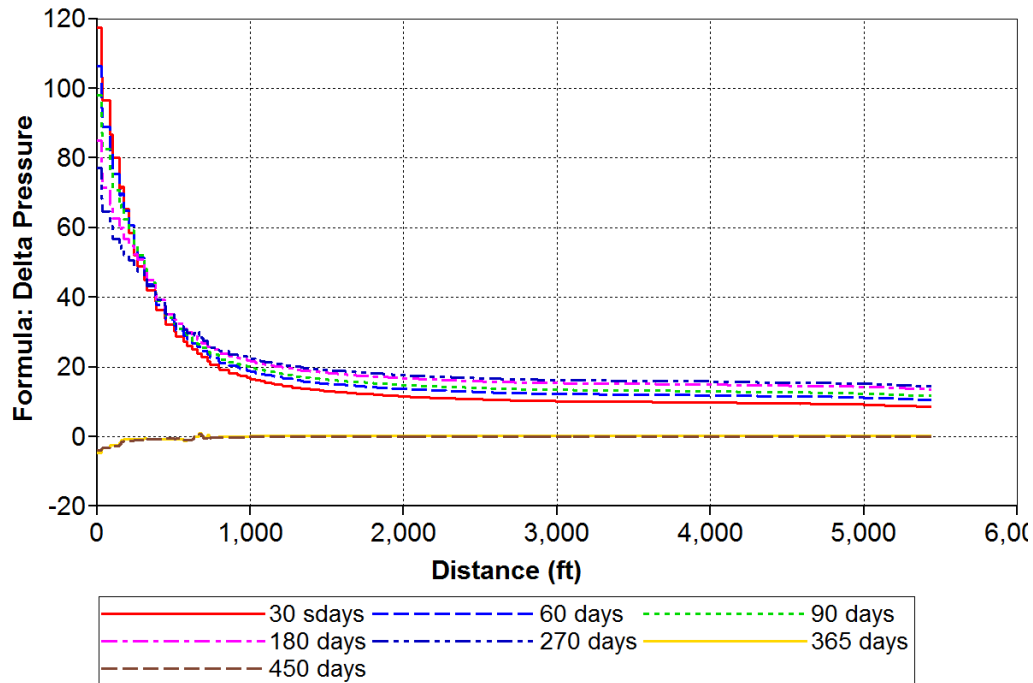


Figure 49. Change in pore pressure at the base of the confining zone (i.e., base of Simpson Group) at the injection well site for the maximum induced pressure ( $k=0.75/\phi=0.75$ ).

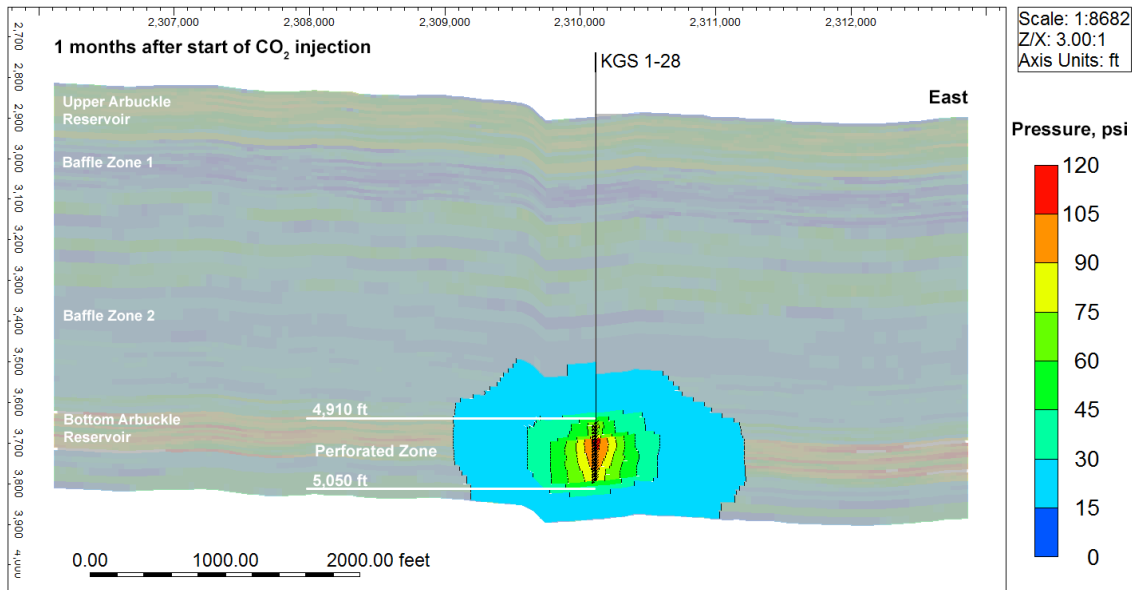
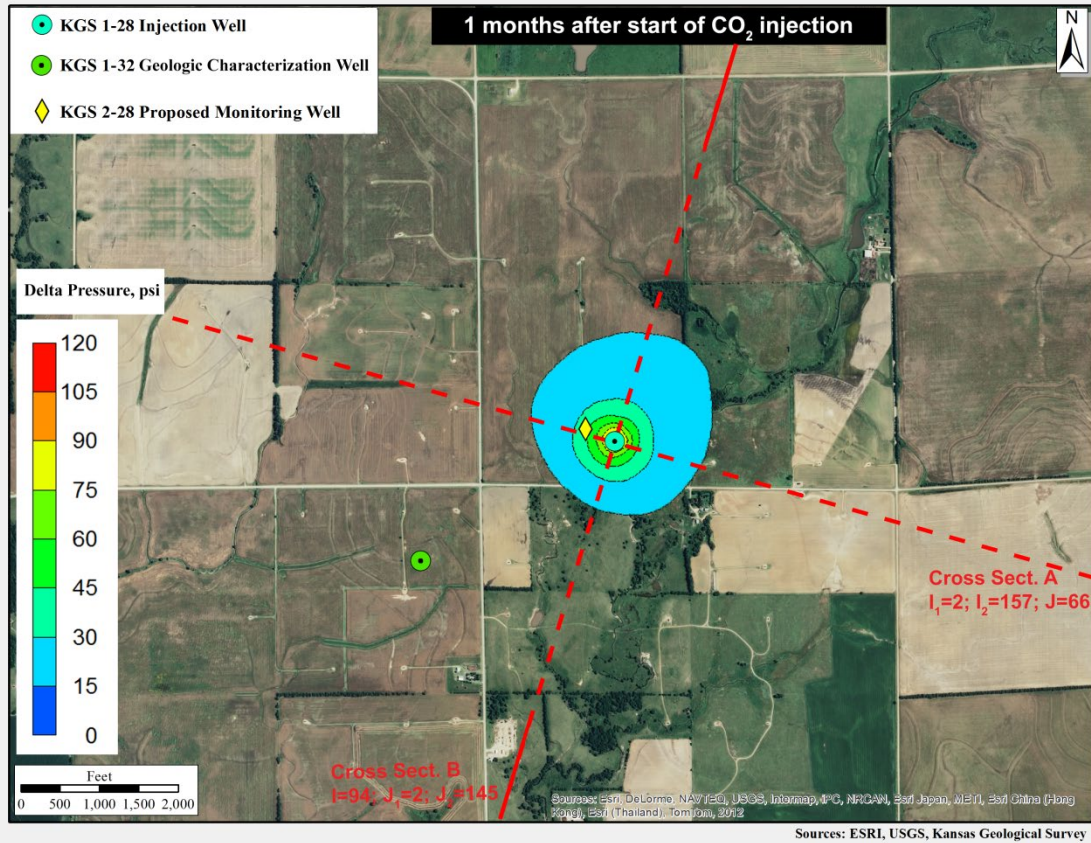


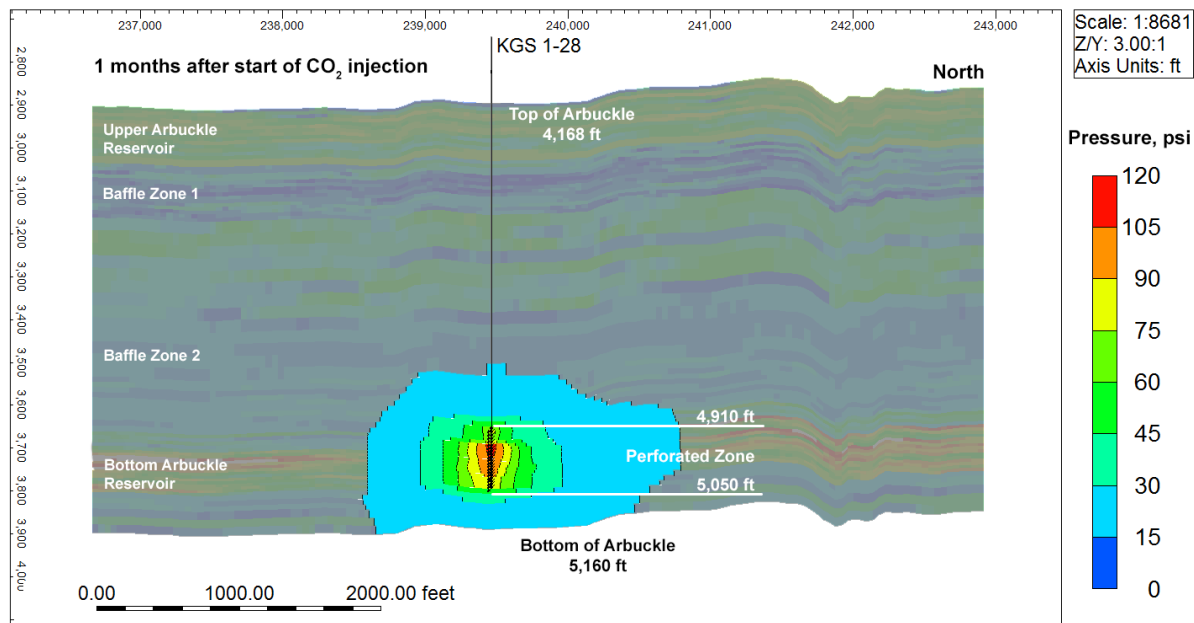
**Figure 50. Pore pressure as a function of lateral distance from the injection well (KGS 1-28) at seven time intervals for the highest induced pressure case ( $k=0.75/\phi=0.75$ ).**

Figure 51 presents the lateral distribution of pressure in the Arbuckle injection interval (at an elevation of 4,960 ft) for the  $k=0.75/\phi=0.75$  case, which resulted in the maximum induced pore pressures. The pressures increase from commencement of injection to nine months and then drop significantly by the end of the first year (three months after operations stop). The pressures also drop very rapidly at short distances from the injection well at the end of the nine-month injection period, as shown in fig. 50. The pressures at the end of the nine-month injection period drop from about 120 psi a short distance from the injection well to less than 15 psi at the geologic characterization well, KGS 1-32, which is approximately 3,500 ft southwest of the injection well. The maximum induced pressure at the model boundary is only 7–12 psi.

Figure 51 also shows the vertical pressure distribution for the maximum induced pressure case ( $k=0.75/\phi=0.75$ ). The confining effect of the mid-Arbuckle baffle zones is evident in the plots as the large pressure increases are mostly restricted to the injection interval. The pressures decline rapidly at a short distance from the injection well. The pressures throughout the model subside to nearly pre-injection levels soon after injection stops.

For more detailed explanation of modeling results, consult with KGS Open File Report 2016-29.





**Figure 51. Simulated maximum increase in pressure in aerial and cross-sectional view at one month from start of injection for the low permeability–low porosity ( $k=0.75/\phi=0.75$ ) alternative case, which resulted in the largest simulated pressures.**

## **Seismic reservoir characterization of the Mississippian and Arbuckle at Wellington Field for monitoring the injection of CO<sub>2</sub>**

The Mississippian reservoir and Arbuckle saline aquifer in Kansas are good candidates for CO<sub>2</sub> injection operations. The Mississippian is an oil producing reservoir that can benefit by CO<sub>2</sub> injection for enhanced oil recovery (EOR). The Arbuckle is an extensive, thick saline aquifer with significant potential for CO<sub>2</sub> storage. Both carbonate units are heterogeneous, fractured, highly challenging to characterize reservoirs. Seismic methods have been used at other settings for reservoir characterization and CO<sub>2</sub> monitoring. This investigation examined the utility of active source surface seismic for characterization of Mississippian and Arbuckle reservoir properties in southern Kansas, and for monitoring CO<sub>2</sub>. In addition to the highly heterogeneous nature of carbonate reservoirs, the Mississippian thickness is below seismic resolution and the Arbuckle consists of numerous flow units, also below seismic resolution, which limit the effectiveness of conventional seismic analysis methods. This investigation used three-dimensional (3D) seismic imaging along with advanced analysis methods in order to map below-resolution reservoir

thickness, porosity distribution, and fracture density and orientation. Time-lapse two-dimensional (2D) seismic was assessed for its ability to monitor CO<sub>2</sub> injected in the Mississippian reservoir. Analysis of post-stack 3D seismic data at the Mississippian reservoir showed the response of a gradational velocity transition (ramp velocity function) where thicker reservoir units corresponded with lower reflection amplitudes, lower frequency and a 90° phase change. Reflection amplitude was correlated to Mississippian reservoir thickness. Pre-stack gather analysis showed that porosity zones of the Mississippian and Arbuckle reservoirs exhibit characteristic AVO response. Simultaneous AVO inversion estimated P- and S-Impedances, which along with formation porosity logs and post-stack seismic data attributes were incorporated in multi-attribute linear-regression analysis and predicted reservoir porosity with an overall correlation of 0.90 to well data. The 3D survey gather azimuthal anisotropy analysis (AVAZ) provided information on the fault and fracture network and showed good agreement to the regional stress field and well data. Mississippian reservoir porosity and fracture predictions agreed well with the observed mobility of injected CO<sub>2</sub> in KGS well 2-32. Fluid substitution modeling predicted acoustic impedance reduction in the Mississippian carbonate reservoir introduced by the presence of CO<sub>2</sub>. Ongoing seismic data analysis at the writing of this report is evaluating the utility of time-lapse seismic for imaging injected CO<sub>2</sub> in the Mississippian reservoir. This work demonstrates that advanced seismic interpretation methods can be used successfully for characterization of the Mississippian reservoir and Arbuckle saline aquifer.

## INTRODUCTION

Seismic imaging methods are evaluated for their effectiveness in characterizing the Mississippian reservoir and Arbuckle saline aquifer at Wellington field in south-central Kansas. Both units are highly heterogeneous, fractured carbonates. Three-dimensional (3D) seismic imaging along with time-lapse two-dimensional (2D) seismic are used to predict reservoir properties and monitor CO<sub>2</sub> injected in the Mississippian. Figure S-1 displays the location of Wellington seismic data. Background information on the geologic setting as well as seismic data used in this investigation is provided in the MS Thesis by Sirazhiev (2012) (Appendix S-B) and the MS Thesis by Fadolkarem (2015) (Appendix S-C).

Seismic data analysis methods employed for characterization of the Mississippian and Arbuckle at Wellington Field are summarized as follows:



### *Key Findings*

A gradational porosity decrease at the top of the Mississippian reservoir corresponds to a gradational P-wave velocity increase.

A gradational or “ramp” velocity function results in the integral of the seismic wavelet with lower amplitude, lower frequency content and a 90 degree phase shift corresponding to thicker reservoir zones.

The characteristic seismic amplitude response of the top of the Mississippian is used to predict reservoir thickness when true thickness is  $1/16\lambda$ - $5/16\lambda$  (5–25 m) ( $\lambda$  = wavelength).

Post-stack model-based acoustic impedance inversion provides reliable porosity predictions for reservoir thickness range of  $1/8\lambda$ - $7/16\lambda$  (10-35 m).

### *Background*

Mississippian chert reservoirs are important hydrocarbon resources in North America. These reservoirs are highly heterogeneous, typically below seismic resolution and, therefore, present a challenging task for predicting reservoir properties from seismic data (e.g. Mazzullo et al., 2009; Montgomery et al., 1998; Rogers and Longman, 2001; Watney et al., 2001).

In this study we conducted post-stack seismic attribute analysis of the Mississippian chert reservoir at the Wellington Field, south-central Kansas using well-log and 3D PSTM seismic data. The microporous cherty dolomite reservoir exhibits a characteristic vertical gradational porosity reduction and associated increase in acoustic velocity, known as a ramp-transition velocity function. The primary objective of this study was to investigate possible relationships of the reservoir thickness and porosity with post-stack seismic attributes, including inverted acoustic impedance.

### *Methods*

We examined the seismic response of a ramp-transition velocity function in order to predict the thickness of the Mississippian chert reservoir. The Mississippian top is characterized by a vertical gradational porosity decrease and a corresponding ramp velocity increase that results in a gradational impedance increase (Figure S-2). We employed seismic wedge modeling using both synthetic and original sonic logs to aid the interpretation and investigate the resolution limits of the seismic data. A characteristic amplitude decrease and wavelength increase (frequency

decrease) is observed at the top of the Mississippian as reservoir thickness increases (Figure S-3). Seismic amplitude is shown to predict reliably reservoir thickness in the range of 5-25 m.

Post-stack model-based inversion of the seismic data was used to derive the acoustic impedance model of the subsurface. The resolution of the model-based inversion was evaluated for the case of the gradational impedance increase within the Mississippian reservoir interval using synthetic wedge models (Figure S-3). Multilinear regression analysis is used to transform the inverted acoustic impedance to porosity distribution within the Mississippian reservoir. The reliability of the predicted porosity model is tested by cross-validation during the multilinear regression analysis.

### *Results*

The analysis of well log and seismic data revealed that the reservoir exhibits different characteristics across fault #1 which divides the Wellington Field diagonally from the southwestern corner to the northeastern corner.

The reservoir in the southeastern part of the field is characterized by a vertical gradational porosity decrease (from 25-30% to 4-6%), variable thickness (6-20 m), lower seismic amplitude and frequency content and a locally developed double reflector. In addition, a high correlation between seismic amplitude and reservoir thickness conformable with the theoretical amplitude response of a ramp-transition velocity function is observed. The amplitude envelope was used to predict the reservoir thickness in this part of the field (Figure S-4).

The Mississippian reservoir in the north-western part of the field has more heterogeneous porosity distribution within the reservoir interval, thins in the north-north-west direction, while no clear relationship was found between reservoir thickness and instantaneous seismic attributes.

The model-based inversion result and predicted porosity model supported the well-log and seismic attribute interpretation (Figure S-5). The reliability of the predicted porosity model is tested by cross-validation. Resolution limits were determined as  $1/16\lambda$  for the amplitude envelope attribute and  $1/8\lambda$  for the model-based inversion within the Mississippian reservoir characterized by a vertical gradational porosity reduction.

Results of this research could benefit the characterization of similar chert as well as clastic and carbonate reservoirs characterized by downward porosity reduction. In addition to predicting the reservoir porosity and thickness, the seismic response of a ramp-transitional velocity function

related to downward porosity reduction might be useful in understanding depositional and diagenetic histories of such reservoirs.

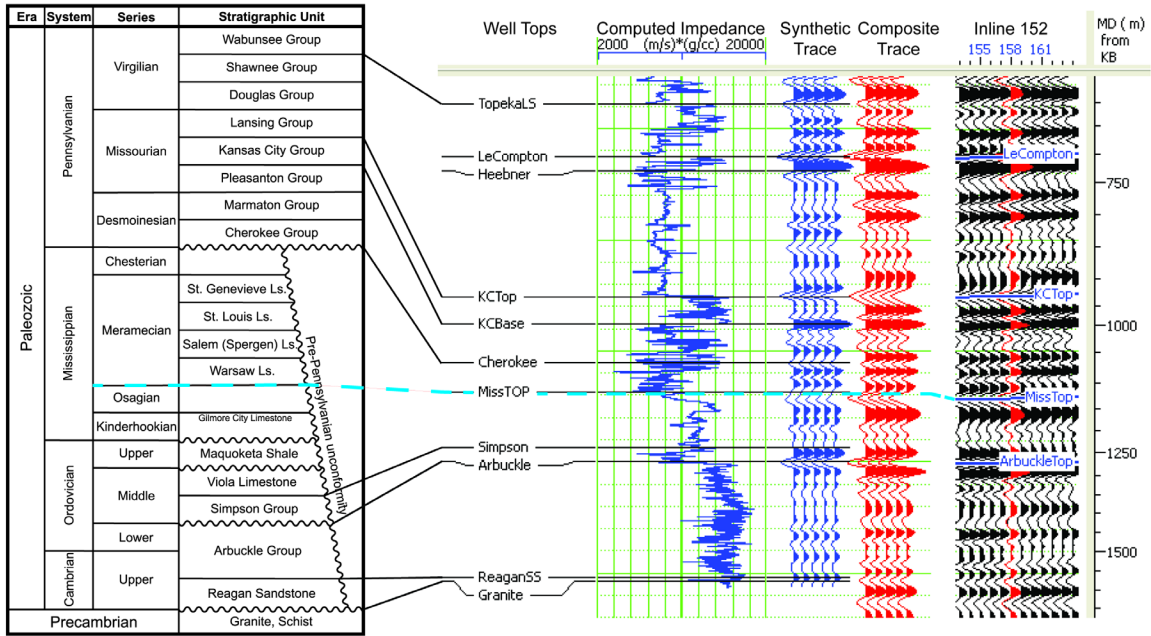


Figure S-2: From left to right: generalized stratigraphic section of central Kansas (Modified from Nissen et al. (2009), originally from Cansler (2000)); well tops, computed impedance log, synthetic (blue) and seismic (red) traces at well #15-191-22591; part of inline #152. The Mississippian reservoir top is identified by the blue dashed line.

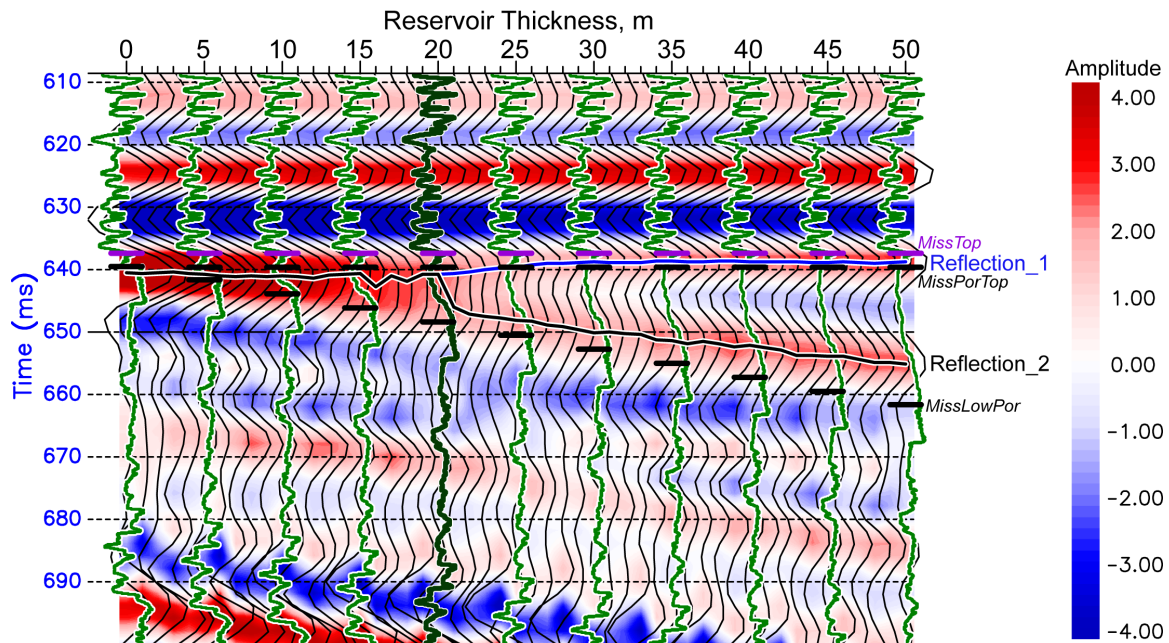


Figure S-3: Synthetic seismic section of the reservoir wedge model constructed at well #15-191-22591. Original sonic log is shown in dark green (corresponds to reservoir thickness of 20 m). Synthetic sonic logs calculated by stretching and squeezing the original log within the Mississippian reservoir are shown in light green for every 5th trace.

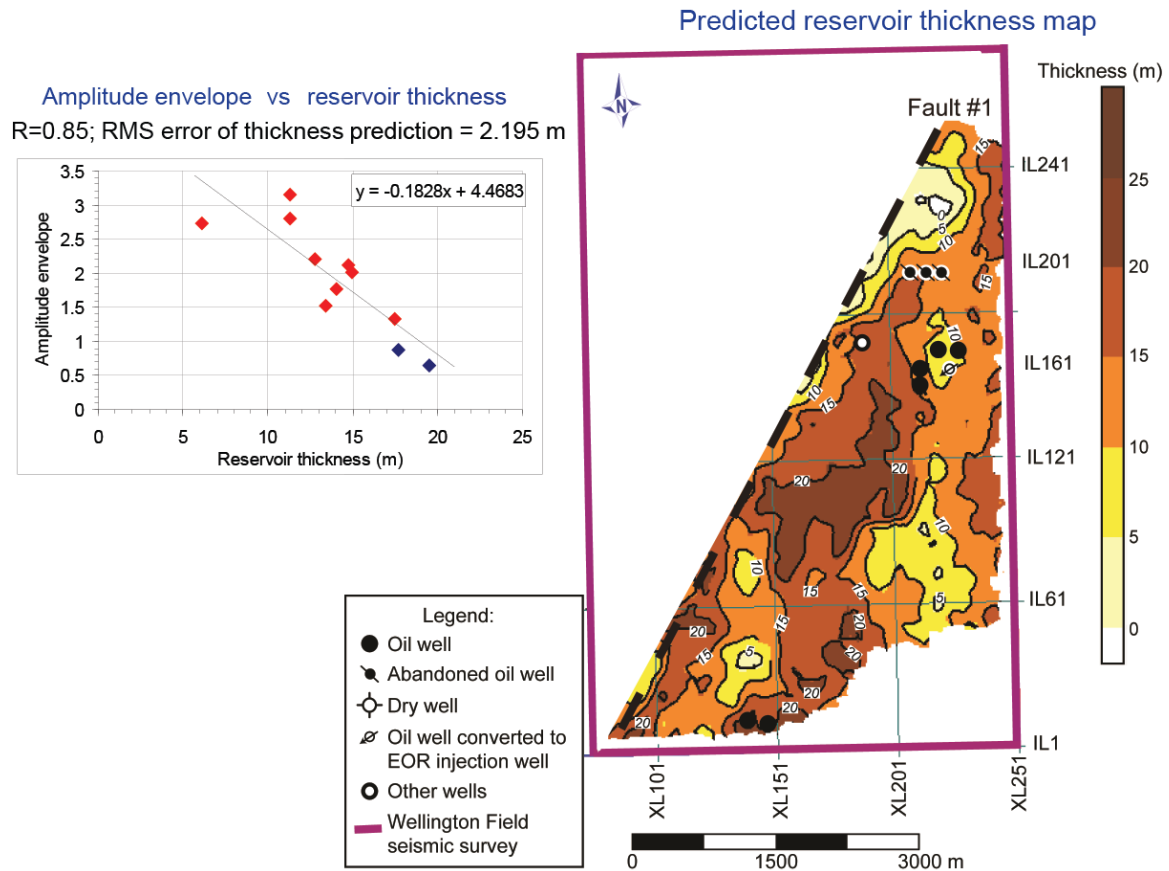


Figure S-4: (left) Crossplot of amplitude envelope of the Mississippian Top horizon averaged around well locations within 9 closest traces versus the Mississippian reservoir thickness. (right) Map of the thickness of the Mississippian reservoir at the Wellington Field predicted from the amplitude envelope.

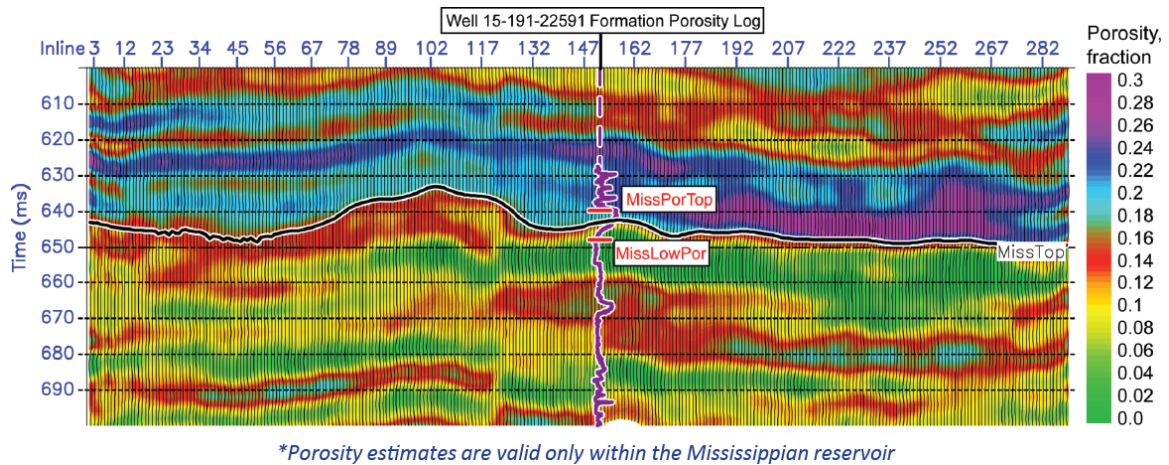


Figure S-5: Result of the formation porosity prediction from the inverted impedance volume across the inline #152 with overlain original formation porosity log at well #15-191-22591.

## **II. Pre-stack seismic AVO analysis and impedance inversion for determination of Mississippian reservoir thickness and porosity distribution, and Arbuckle flow unit delineation**

For detailed description refer to the MS Thesis by Fadolkarem (2015) (Appendix S-C).

### *Key Findings*

High porosity zones in the Mississippian and the Arbuckle Group exhibit characteristic AVO (amplitude variation with offset) response.

AVO classification can be employed to identify the porous zones at Wellington Field 3D volume using the intercept-gradient cross plotting technique.

Simultaneous AVO impedance inversion results in improved estimation of Mississippian reservoir and the Arbuckle Group properties than model-based inversion of post-stack data.

The resolution limit of simultaneous AVO inversion within the Mississippian chert reservoir was determined using wedge modeling as 10 m, which corresponds to 1/8 of a wavelength.

Flow units in the Arbuckle are mapped using AVO analysis and Simultaneous AVO impedance inversion.

Multi-Attribute Linear Regression Analysis porosity predictions benefit by incorporating P- ( $Z_P$ ) and S-impedance ( $Z_S$ ) data obtained from simultaneous AVO Inversion of pre-stack seismic gathers.

Best porosity prediction at the Mississippian reservoir is achieved when the multi-attribute transform is constrained within the Mississippian reservoir.

Optimum porosity prediction at the Arbuckle is achieved when the multi-attribute transform is derived between the Cherokee Group top (above Arbuckle) and the Reagan Sandstone top (Arbuckle base) using the eleven wells that have formation porosity logs including the wells that did not penetrate the Arbuckle Group.

The Mississippian reservoir thins to the northwest. The deeper Arbuckle Group has five main low impedance and high porosity zones that are deeper in the eastern and southeastern parts of the Wellington field.

### *Background*

In this study we conduct pre-stack seismic analysis of the Mississippian reservoir and the Arbuckle Group at the Wellington Field, south-central Kansas, using 3D pre-stack migrated seismic gathers. We examine pre-stack seismic attributes on both real and synthetic seismic data in order to identify the porous reservoir zones, and to find out if using pre-stack seismic data for porosity prediction can improve the reservoir characterization. Specifically we examine the utility of AVO analysis and impedance inversion for characterization of the Mississippian and Arbuckle reservoirs. We also evaluate the use of multi-attribute regression for porosity prediction in the two reservoirs. This work helps advance the understanding of the capabilities and limitations of pre-stack seismic methods for predicting reliably Mississippian reservoir thickness and porosity and for mapping flow units in the Arbuckle.

The Mississippian reservoir is a microporous cherty dolomite reservoir that exhibits downward gradational porosity decrease resulting in a corresponding increase in velocity. It is typically thin (15 m) and below seismic resolution. The deeper Cambrian-Ordovician Arbuckle Group is a thick succession of interbedded dolomudstones, pack-grainstones, vuggy brecciated zones, and thin dolomudstone and shale beds (Watney et al., 2013). The Arbuckle aquifers are highly heterogeneous and compartmentalized with individual reservoir units below seismic resolution. Therefore, it is challenging to identify reservoirs or predict their properties from the seismic data (Franseen et al., 2003; Watney et al., 2001).

### *Methods*

In this study we investigate the AVO response of the Mississippian reservoir and the porous zones of Arbuckle Group. We examine if the AVO classification can be used for identifying the porous zones at Wellington Field in both the Mississippian and the Arbuckle. Also, we perform simultaneous AVO inversion of the pre-stack migrated gathers for prediction of P-wave impedance ( $Z_p$ ), S-wave impedance ( $Z_s$ ) and density ( $\rho$ ), and compare results to previous post-stack model-based inversion. The resolving power of the resulting inversion volumes is evaluated by correlating the inversion results with real well log real data.

We also test the utility of multi-attribute transforms for reservoir porosity prediction. We incorporate inverted P-impedance ( $Z_p$ ) and S-impedance ( $Z_s$ ) obtained from pre-stack simultaneous AVO inversion, formation porosity well logs and post-stack seismic data in a multi-attribute linear-regression analysis in order to derive multi-attribute transforms that are used to

predict porosity values in the seismic survey volume of the Wellington Field. The reliability of porosity prediction is tested by blind wells that are excluded from the analysis. Also, the porosity prediction is evaluated by correlating predicted porosity traces with formation porosity well logs.

## *Results*

### *i) Mississippian and Arbuckle Reservoir AVO Classification*

Porosity zones of the dolomitic reservoirs in both the Mississippian and the Arbuckle Group are shown to exhibit Class IV AVO response (Figure S-6a) which is characterized by negative intercept (A) and positive gradient (B) leading to A-B crossplots located in the fourth quadrant (Figure S-6b). This AVO classification was employed to identify and delineate the porous zones in the Wellington Field 3D seismic.

AVO analysis was conducted using A-B cross plotting over the time window between the top of the Arbuckle horizon and the Basement horizon. Fourth quadrant Class IV cross plot points highlighted by the red polygon shown in figure S-6b correspond to regions marked by red color in the seismic section shown in figure S-6c. Those red highlighted zones (identified by arrows) are high porosity zones as confirmed by the porosity log at well #15-121-22591. The high porosity zones in the Arbuckle Group have been correlated to distinct flow units. Therefore, AVO analysis is shown to be capable of delineating porous intervals that form flow units across the Arbuckle group. AVO analysis employed at the Mississippian shows that Class IV AVO response corresponds to the porous reservoir section, as confirmed by well data (Figure S-7).

### *ii) Pre-stack Seismic Inversion (Simultaneous AVO Inversion)*

Simultaneous AVO inversion uses pre-stack gathers to invert simultaneously for P- and S-Impedance, and density (Hampson et al., 2005). The inverted P-impedance ( $Z_P$ ) by simultaneous AVO Inversion showed better correlation with the real P-impedance from well logs, and lower RMS inversion error compared to post-stack model based inversion conducted previously (Sirazhiev, 2012). Figure S-8 shows a comparison of seismic inversion results with measured properties at well #15-121-22591.

At the Arbuckle Group five main low-impedance, high-porosity zones are observed. The low impedance zones in the inverted P-impedance volume show good contrast with the surrounding higher impedance zones, which allows mapping their extent across the Wellington

Field (Figure S-9). Distinct flow units identified in the Arbuckle correlate spatially with the low P-impedance zones, therefore impedance can be used to map deleneate flow uints at the Arbuckle (Figure S-9).

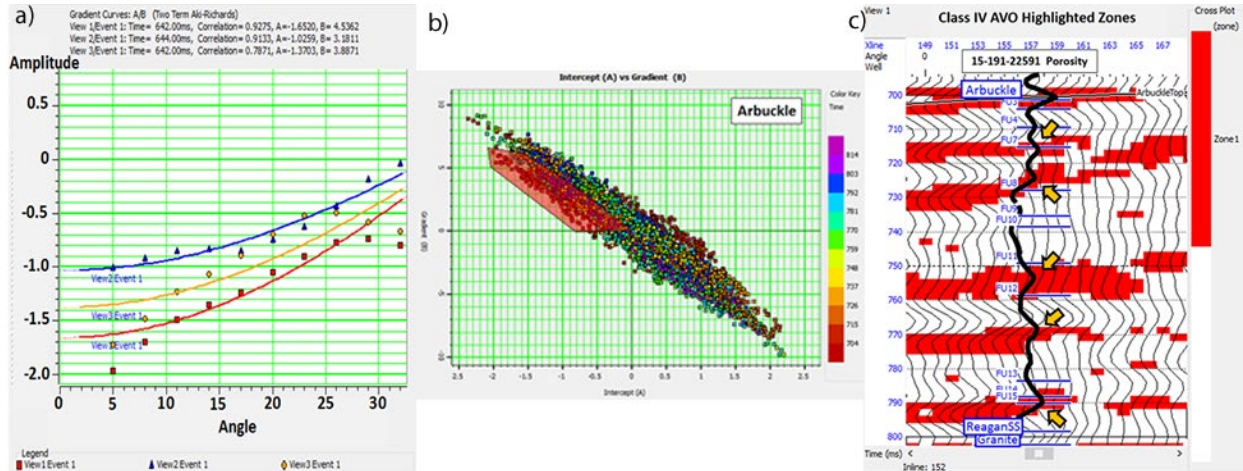


Figure S-6: Arbuckle AVO analysis. a) Amplitude extracted from seismic angle gathers at wells #15-121-22591, #15-121-22590 and #15-121-20789 with trend lines indicating Class IV AVO response. b) A-B crossplots with the red polygon highlighting Class IV AVO response. c) Class IV AVO highlighted zones on Inline #152 that correspond to the A-B cross plots highlighted by the red polygon in figure 1b.

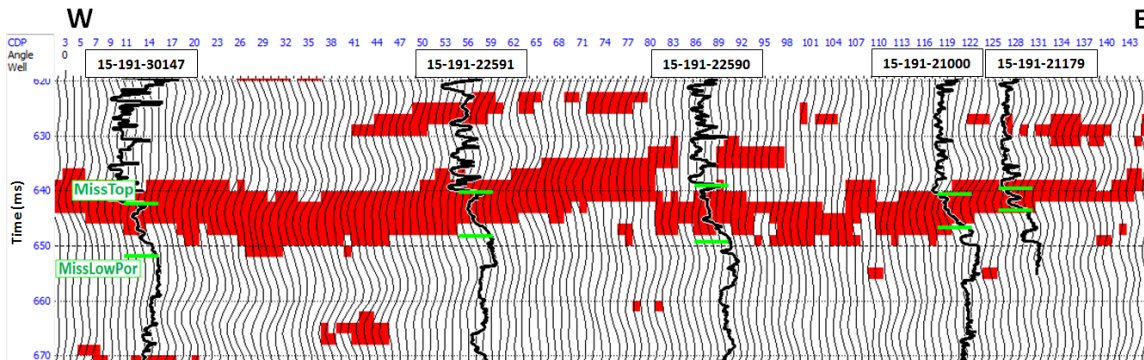


Figure S-7: Mississippian AVO analysis. Class IV AVO highlighted zones (red color) on seismic data displayed along with porosity logs at the Mississippian reservoir. AVO highlighted zones are in good agreement with reservoir porous zones.

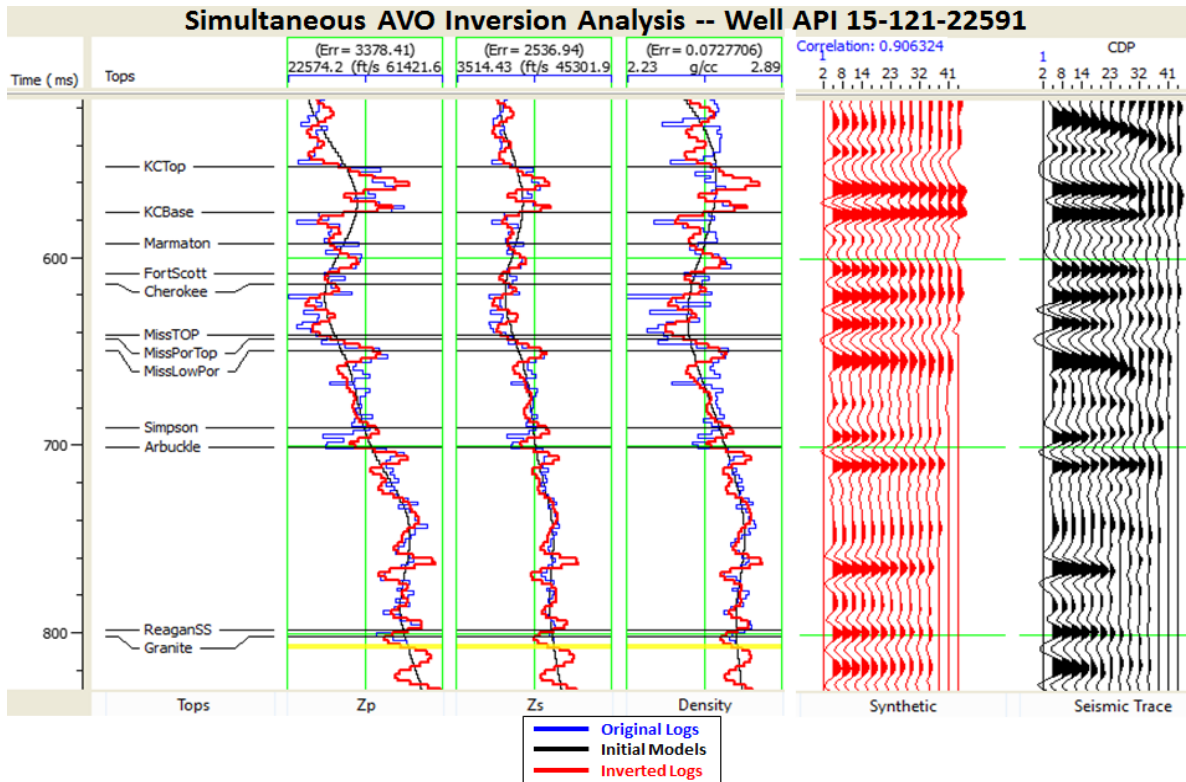


Figure S-8: Analysis of simultaneous AVO inversion at well location #15-191-22591. From left to right: 1) Well tops. 2) Inverted traces (red), original well logs (blue) and initial models (black) of  $Z_p$ ,  $Z_s$  and density. 3) Synthetic seismic gather (red). 4) Real seismic gather (black). The inverted traces (red) show a good match with the original logs (blue). The synthetic seismic gather shows a high correlation of 0.91 with the real seismic gather (black) at the well location.

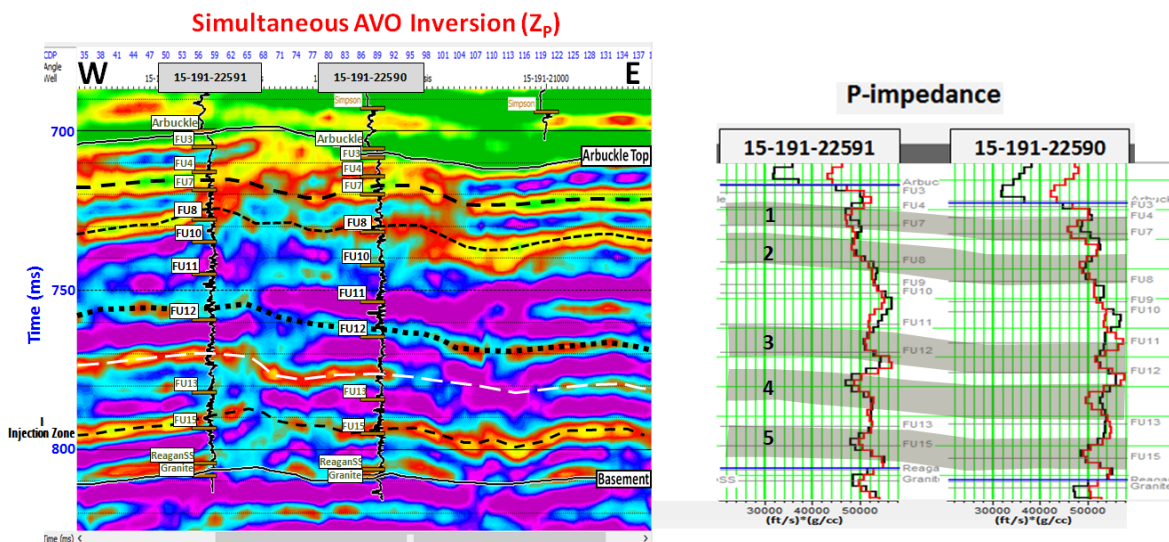


Figure S-9: Arbuckle flow unit identification. (left) Simultaneous AVO inverted  $Z_p$  cross section. Five low impedance zones are picked by the dashed lines. (right) Measured P-impedance logs (Black) from wells #15-121-22590 and #15-121-22591, and the inverted P-impedance traces (Red) at the two well locations. Five distinct low impedance zones shaded in grey correspond to Arbuckle flow units.

iii) *Mississippian Reservoir Porosity Prediction (multi-attribute linear-regression analysis)*

Porosity prediction within the Mississippian reservoir is achieved when the multi-attribute transform is derived only within the Mississippian reservoir. The multi-attribute transform in this case does not provide meaningful porosity values outside the Mississippian reservoir but it shows great contrast between the Mississippian reservoir and the surrounding formation which helps in delineating the Mississippian reservoir around the seismic volume. Figure S-10 shows good agreement between predicted porosity logs (red curves) and original porosity logs (black curves) within the Mississippian reservoir with an overall cross correlation of 0.90. Figure S-11 displays predicted porosity profiles from seismic data along with porosity logs exhibiting good agreement. A map of Mississippian reservoir porosity is shown in Figure S-12.

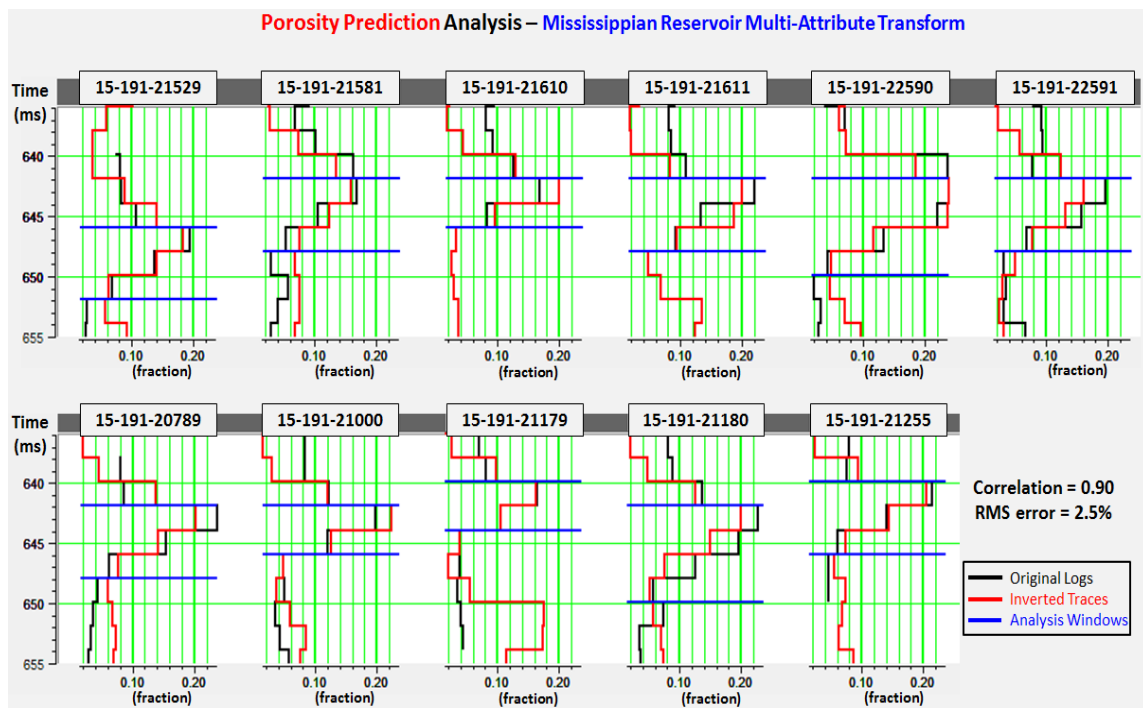


Figure S-10: Analysis of the predicted porosity by the multi-attribute transform within the Mississippian reservoir (blue horizontal lines define the analysis window) at 11 well locations. The predicted porosity traces (red) show a good agreement with the original formation porosity logs (black) with an overall correlation of 0.90 for all wells.

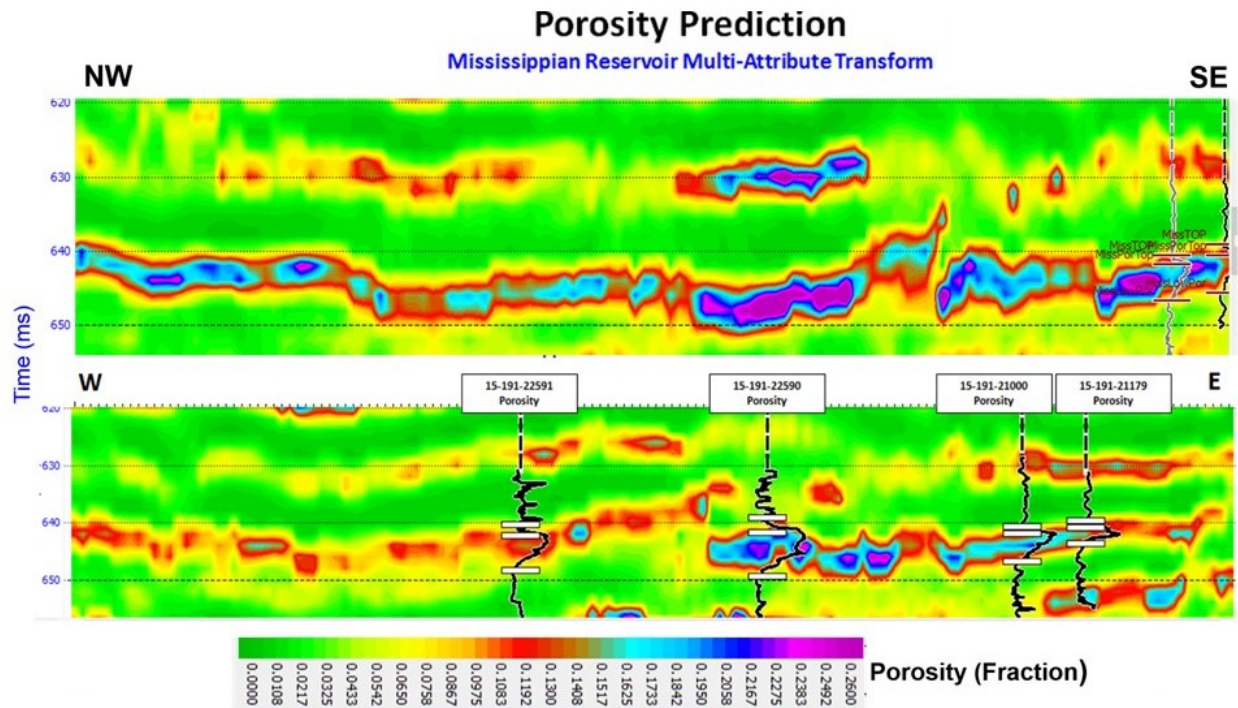


Figure S-11: (upper) NW-SE cross section of predicted porosity at the Mississippian reservoir showing thinning to the NW. (lower) E-W cross section of predicted porosity. Porosity well curves are displayed over the predicted porosity profiles showing good agreement.

iv) *Arbuckle Reservoir Porosity Prediction*

At the Arbuckle Group, a multi-attribute transform derived within the Arbuckle interval only provided good porosity prediction at the two well locations that penetrated the Arbuckle, but it did not provide reasonable porosity values away from the two wells. This may be due to limited well control within the Arbuckle. Unlike the Mississippian reservoir, the optimum porosity prediction quality within the Arbuckle was achieved when the multi-attribute transform was derived between the Cherokee Group top (above Arbuckle) and the Reagan Sandstone top (Arbuckle base) using the eleven wells that have formation porosity logs including the wells that did not penetrate the Arbuckle Group. The Arbuckle Group has five main low impedance and high porosity zones that are deeper in the eastern and southeastern parts of the Wellington field (Figure S-13). The depth change of the five zones is attributed to the post-Mississippian SW-NE trending normal fault. The resultant porosity prediction volume shows good agreement with the results of A-B cross plotting technique for both the Mississippian and the Arbuckle. Class IV AVO zones

highlighted by the A-B cross plotting technique correlate with high porosity values in the porosity prediction volume. (Figure S-13).

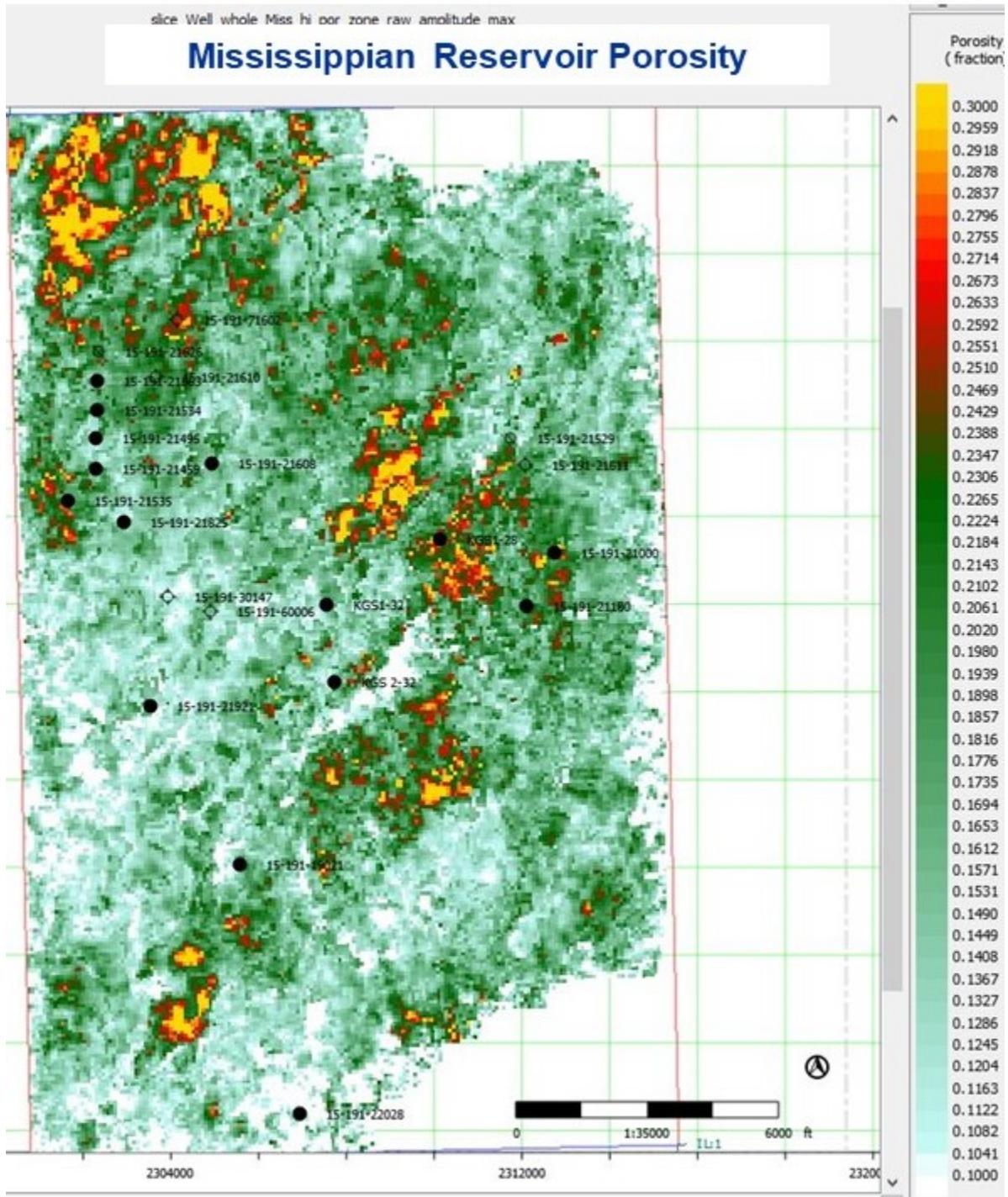


Figure S-12: Map of maximum Mississippian reservoir porosity predicted from the seismic data.

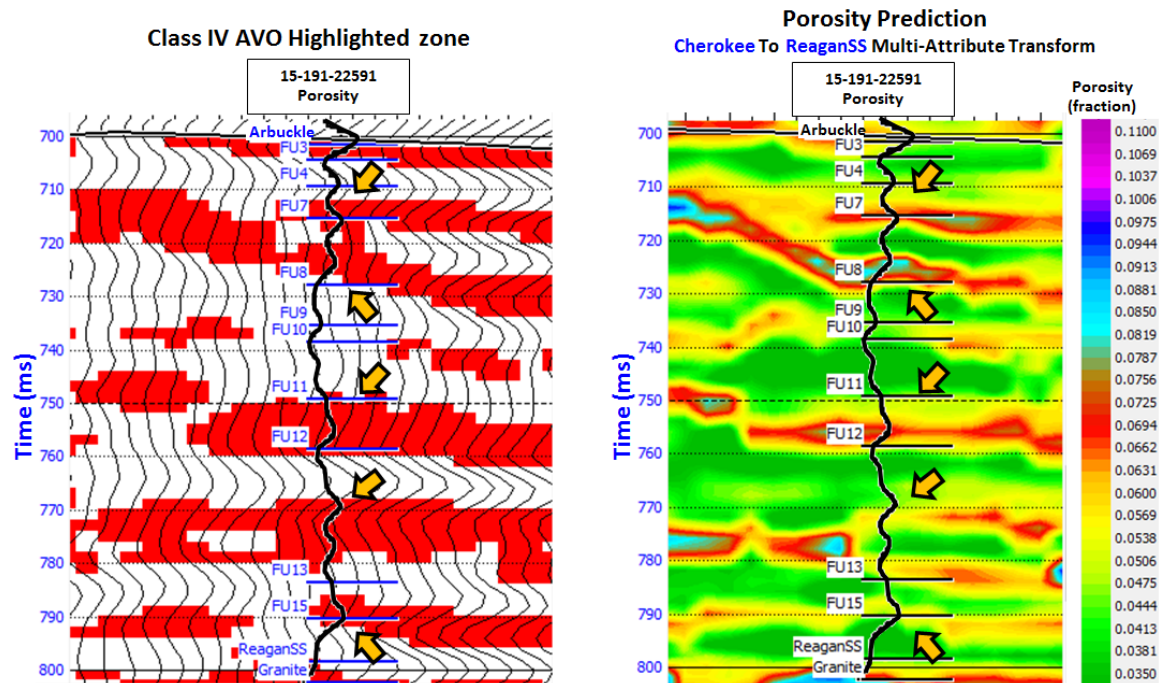


Figure S-13. (Left) Cross section of Class IV AVO highlighted zone by the A-B cross plotting technique along inline #152. (Right) Cross section of predicted porosity by the second multi-attribute transform along inline #152. The same Class IV AVO highlighted zones show high porosity values in the porosity prediction cross section. Black curves are formation porosity logs of well #15-121-22591. Horizontal lines identify mapped flow units in the Arbuckle. A good agreement is observed between flow units and predicted porosity.

### III Pre-stack seismic AVAZ (amplitude variation with azimuth) analysis for determination of Mississippian and Arbuckle fracture density and orientation

#### Key findings

Azimuthal anisotropy is detected in 3D P-P pre-stack gathers.

Seismic anisotropy analysis results support known large scale features (faults) in the field.

Seismic anisotropy results are consistent with well log observations and geomechanical models at Wellington field.

Fracture patterns mapped in the Mississippian are in agreement with observed CO<sub>2</sub> migration paths.

## *Background*

Previous investigations by Sirazhiev (2012) and Fadolkarem (2015) mapped reservoir thickness and porosity distribution at Wellington field. This work examines if the 3D P-wave reflection seismic can quantify azimuthal anisotropy in the Mississippian cherty dolomite and Lower Ordovician Arbuckle Group dolomite. Carbonates exhibit anisotropy due to varied crystalline structure, porosity geometry and fractures. The results obtained can provide insight into the *in situ* stress, relative fracture density and orientation in the two reservoirs as well as preferential fluid migration paths.

## *Methods*

Seismic anisotropy is observed as the variation in seismic velocity and amplitude with orientation of wave propagation. Accounting for seismic anisotropy can quickly become computationally complex and difficult to constrain. If a simplifying model can be applied to the geology however, accounting for the anisotropy is facilitated. Defining a plane of isotropy can decrease the complexity. In horizontal planes of isotropy, observed in shales and thin bed sequences, the simplifying model is referred to as Vertically Transverse Isotropy (VTI) or Radial Anisotropy and is interpreted as AVO. Vertical planes of isotropy due to stress and vertical fractures is considered Horizontally Transverse Isotropy (HTI) or Azimuthal Anisotropy (Ruger, 1998; Thomsen, 2002; Lynn, 2016). This study focuses on azimuthal anisotropy to visualize the stress and fractures.

Accounting for anisotropy in data has several important implications for subsurface imaging. Anisotropy correction in a horizon can provide improved depth constraint. Not accounting for anisotropy can lead to over migration of dipping features as well as under estimation of depth in horizontal features in a Pre-Stack Depth Migrated (PSDM) survey that otherwise appears to be well focused (Hawkins et al, 2001). Anisotropy analysis can also provide understanding into reservoir characteristics and planning. With high quality wide azimuth-wide offset surveys, improved pre-stack coverage can improve on Amplitude Variation with Offset (AVO), as well as allow for stress and reservoir mechanics calculations through Amplitude Variation with Azimuth (AVAZ) (Gray et al, 2012). The orientation of the plane of isotropy is analogous to the direction of maximum horizontal stress ( $\sigma_H$ ) and fracture orientation.

## Results

### i) Fracture mapping

Azimuthal analysis of the 3D P-P wave data collected in Wellington provides a sense of the anisotropy in the top of the Mississippian and Arbuckle. A defining feature observed in both is a fault (black line) that trends northeast through the three green wells in figures S-14 and S-15. The fault is associated with discrete facies changes across the field (Sirazhiev, 2012; Fadolkarem, 2015). The perceived fracture pattern surrounding the fault in the Arbuckle is also within the range of  $\sigma_H$  and fracture orientations as determined from Schwab (2016).

Azimuthal anisotropy of the Mississippian and Arbuckle is shown in figures S-14 and S-15 respectively. Results are consistent with observed rock properties known to cause detectable variations in seismic data; fracture and maximum horizontal stress direction. Large scale features such as faults are indirectly observed by its effect on the surrounding material. Fractures observed in FMI logs are consistent with patterns observed in the Wellington field seismic azimuthal analysis (Figure S-15).

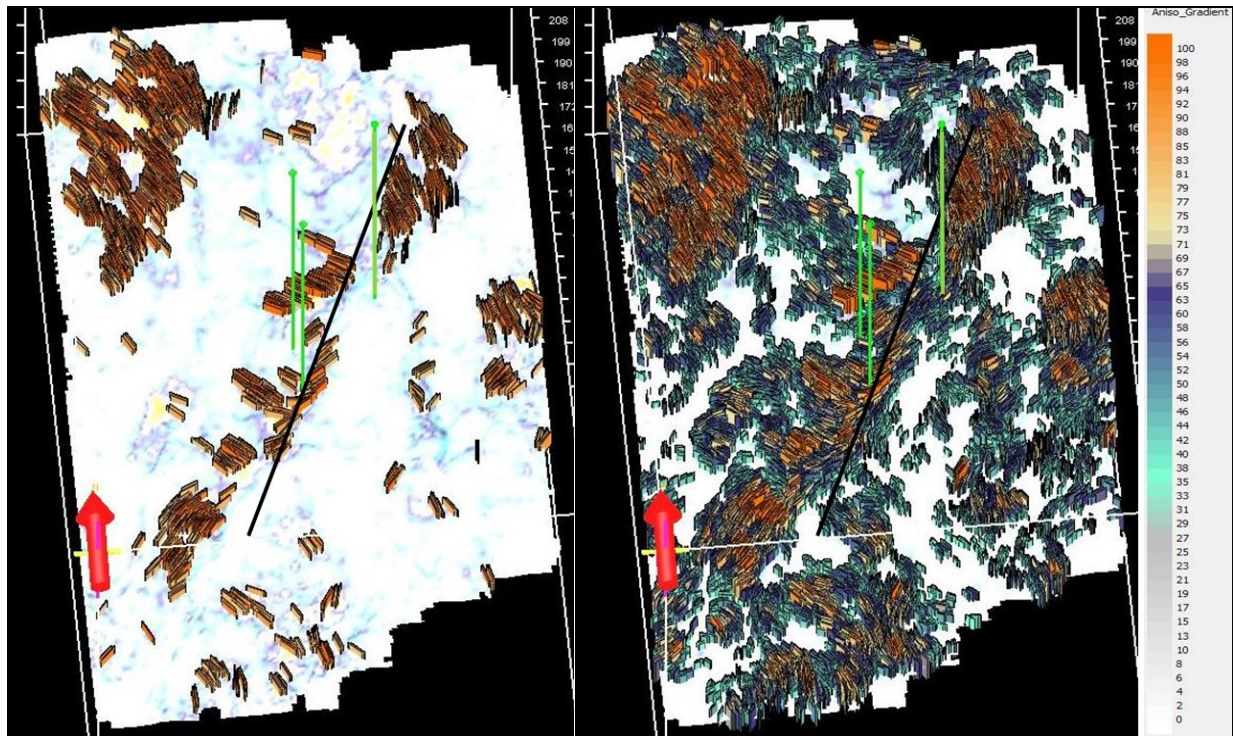


Figure S-14: Mississippian anisotropy. Tilted perspective of the azimuthal planes of isotropy at the high porosity top of the Mississippian Chert. The left panel illustrates a higher degree of anisotropy (66%-100%) to the isotropic plane. The right panel illustrates smaller degrees of anisotropy (33%-100%). The orientation can be interpreted as fractures and stress direction, and the size and color is the degree of anisotropy. The black line is the fault as also mapped by Sirazhiev (2012) and Fadolkarem (2015). Green lines show wells KGS #1-32, #1-28 and 2-32.

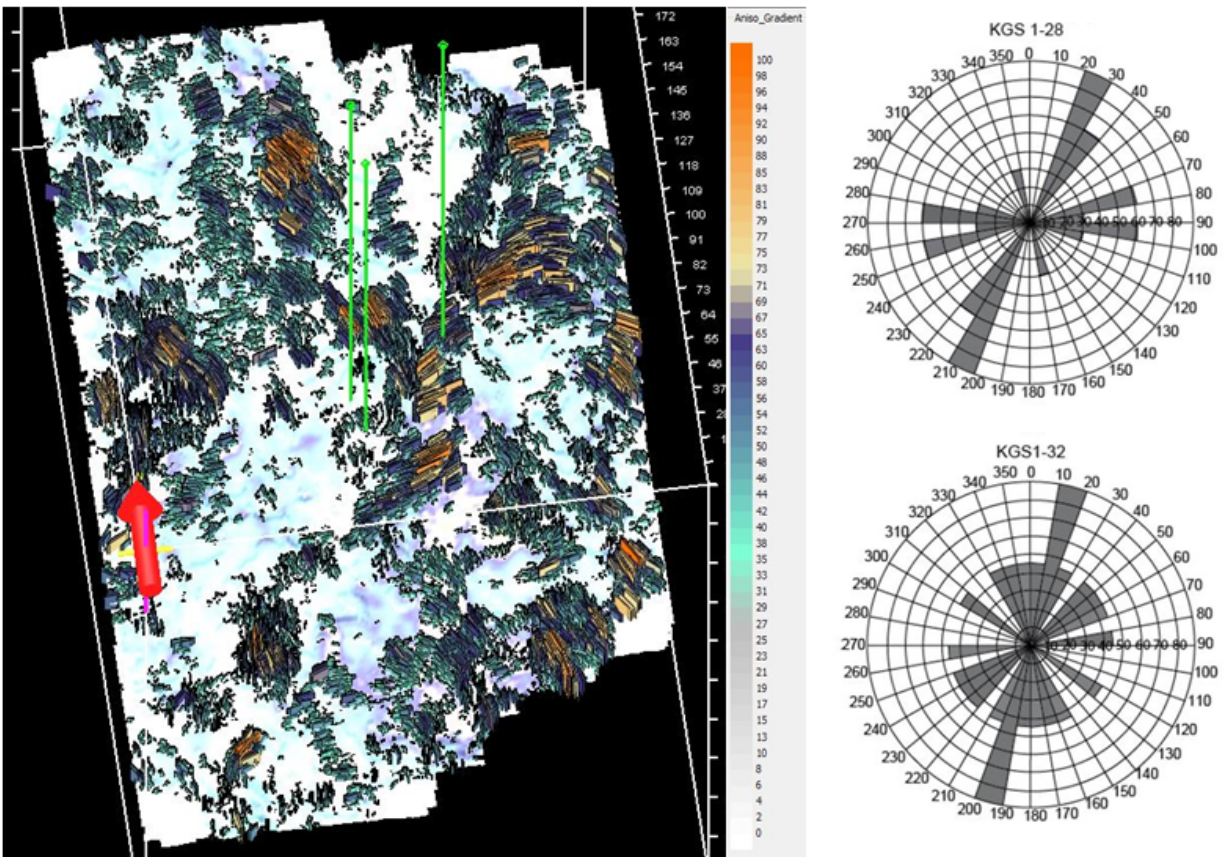


Figure S-15: Arbuckle anisotropy. (left) Tilted perspective of the azimuthal planes of isotropy average throughout the Arbuckle. The panel illustrates a higher degree of anisotropy (25%-100%) to the isotropic plane. The orientation can be interpreted as fractures and stress direction, and the size and color is the degree of anisotropy. The black line is the fault as also mapped by Sirazhiev (2012) and Fadolkarem (2015). Green lines show wells KGS #1-32, #1-28 and 2-32. (right) Natural open fractures observed in FMI Logs in wells KGS 1-28 and 1-32 (from Schwab 2016).

ii) *CO<sub>2</sub> monitoring*

The Mississippian reservoir fracture and porosity predictions from 3D seismic are compared to the monitored mobility of the CO<sub>2</sub> injected in well KGS 2-32 in spring 2016. Early time monitoring of the CO<sub>2</sub> injection is shown to follow preferential paths along fractures delineated by the seismic data (Figure S-16). CO<sub>2</sub> breakthrough is observed along boreholes aligned with the mapped dominant fractures. At the completion of the injection CO<sub>2</sub> appears to be distributed more evenly in the Mississippian reservoir, although the influence of porosity and fracture distribution on CO<sub>2</sub> mobility is still evident in figure S-17.

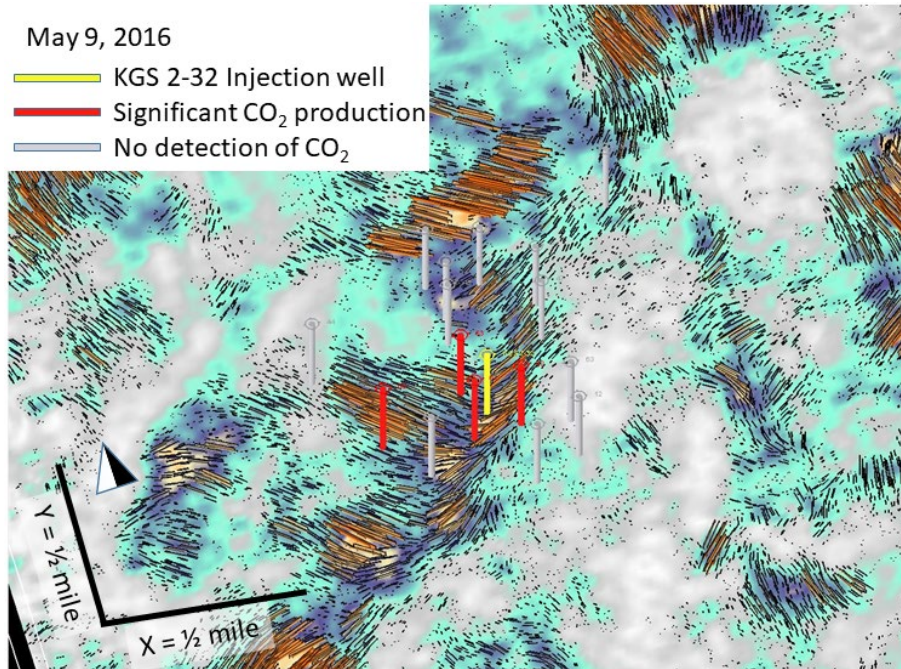


Figure S-16: Mississippian anisotropy map shown along with the injection well KGS 2-32 (yellow), wells with significant CO<sub>2</sub> production (red) and neighboring wells with no detection of CO<sub>2</sub> (grey).

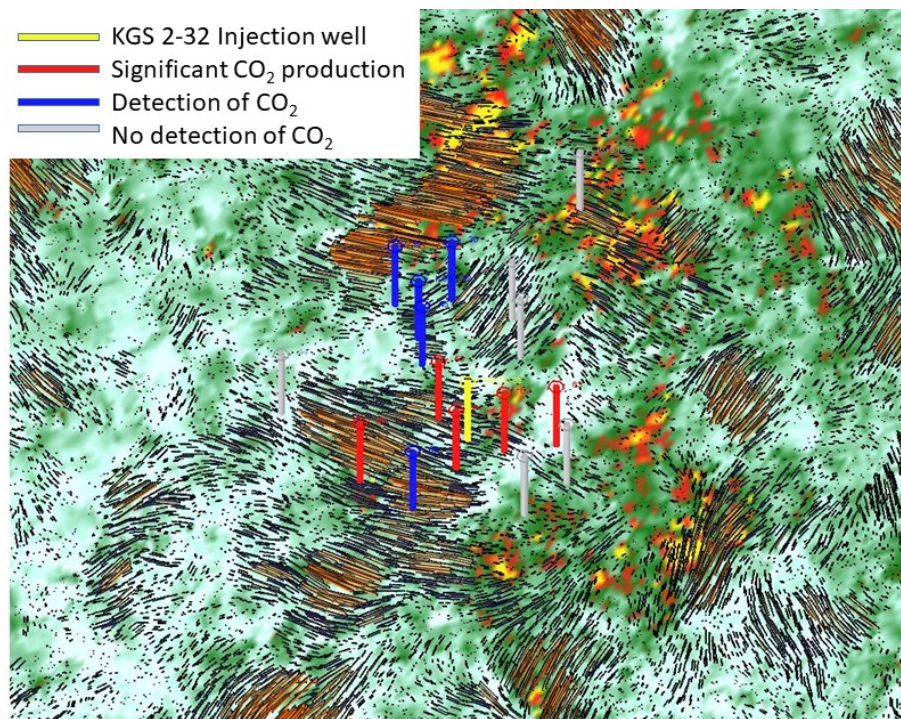


Figure S-17: Mississippian anisotropy map with porosity overlay in color (yellow/red = high porosity; white = low porosity), shown along with the injection well KGS 2-32 (yellow), wells with significant CO<sub>2</sub> production (red), detection of CO<sub>2</sub> (blue), and wells with no detection of CO<sub>2</sub> (grey).

## IV Time-lapse seismic assessment of CO<sub>2</sub> injection in the Mississippian reservoir

### *Key Findings*

- Fluid substitution modeling evaluates the impact of CO<sub>2</sub> injection in the acoustic impedance of the Mississippian reservoir.
- Synthetic seismograms at three well locations are used to interpret pre- and post-CO<sub>2</sub> injection seismic response.
- Time-lapse 2D post-stack seismic data analysis does not show evidence of the injected CO<sub>2</sub>, likely due to low saturation.
- Ongoing analysis is examining the response of pre-stack seismic, AVO analysis and impedance inversion for CO<sub>2</sub> detection in the Mississippian reservoir

### *Background*

The purpose of this study is to assess time-lapse seismic monitoring of CO<sub>2</sub> migration within the Mississippian reservoir and its effectiveness for enhanced oil recovery (EOR). In spring 2016 a CO<sub>2</sub> injection pilot study of the Mississippian cherty dolomite reservoir in Wellington Field was conducted to determine the feasibility of CO<sub>2</sub> for EOR in this area. A 3D P-P seismic survey and two 2D seismic lines (lines 01 and 02) were acquired in 2010, prior to the injection, and a final 2D seismic line (line 03) was acquired post-injection (Figure S-1). Comparison of pre- and post-CO<sub>2</sub> injection seismic along with fluid substitution reservoir modeling and synthetic seismogram generation are used to evaluate seismic monitoring of CO<sub>2</sub> in the Mississippian.

### *Methods*

A classical fluid substitution method for predicting seismic response is the Biot-Gassmann, commonly known as Gassman model. However, heterogeneous pore properties of carbonates can prevent accurate estimation of pore fluid effects (Adam et al 2006, Misaghi et al 2010). Another method for estimating the effect of fluid substitution in carbonates is the patchy saturation model which assumes a homogeneous medium with patchy fluid saturation (Vega et al, 2007). The Gassmann and Patchy models were tested with Hampson Russell Suite (HRS) to evaluate amplitude effects of CO<sub>2</sub> substitution in the Mississippian reservoir. Estimated CO<sub>2</sub> parameters at the reservoir conditions were used to calculate the seismic effects. Well log data for density, porosity, lithologic constituents,  $V_p$  and  $V_s$  were included in the model. Initial conditions were set to 100% water with a systematic 2% increase in CO<sub>2</sub> up to 100% CO<sub>2</sub> saturation. CO<sub>2</sub> saturation

at the injection well can be as high as 80%-90%. Diffusion away from the well and compressibility effects of CO<sub>2</sub> mixed in water exhibit different elastic effects depending on the substitution model used. Synthetic seismic traces at the injection wells were computed for each scenario.

A 2D seismic line (03) acquired immediately after completion of the CO<sub>2</sub> injection in June 2016 is compared with pre injection data. The initial comparison evaluates post-stack data. Pre-stack seismic analyses are ongoing.

### Results

Comparison of the post-stack, post-injection 2-D seismic line and an arbitrary seismic line extracted from the 3-D P-P seismic survey do not reveal any significant amplitude changes in the post-stack seismic data (Figures S-18-S-19). This can be the result of the high matrix incompressibility of carbonate rocks and the relatively small amount of CO<sub>2</sub> injected in this experiment. Further analysis will include AVO and pre-stack analysis of the seismic data which is expected to exhibit greater sensitivity to changes in reservoir fluid content with reflectivity changes up to 10% (Figure S-20).

Synthetic seismograms were created for each 2-D seismic line and their respective wells. Pre-injection seismic lines 01 and 02 were tied with wells KGS #1-32 and KGS #1-28, respectively, while the post-injection 2-D seismic line was tied with the original KGS #2-32, the injection well (Figures S-21, S-22, S-23). The synthetic traces show good agreement with the observed field seismic data.

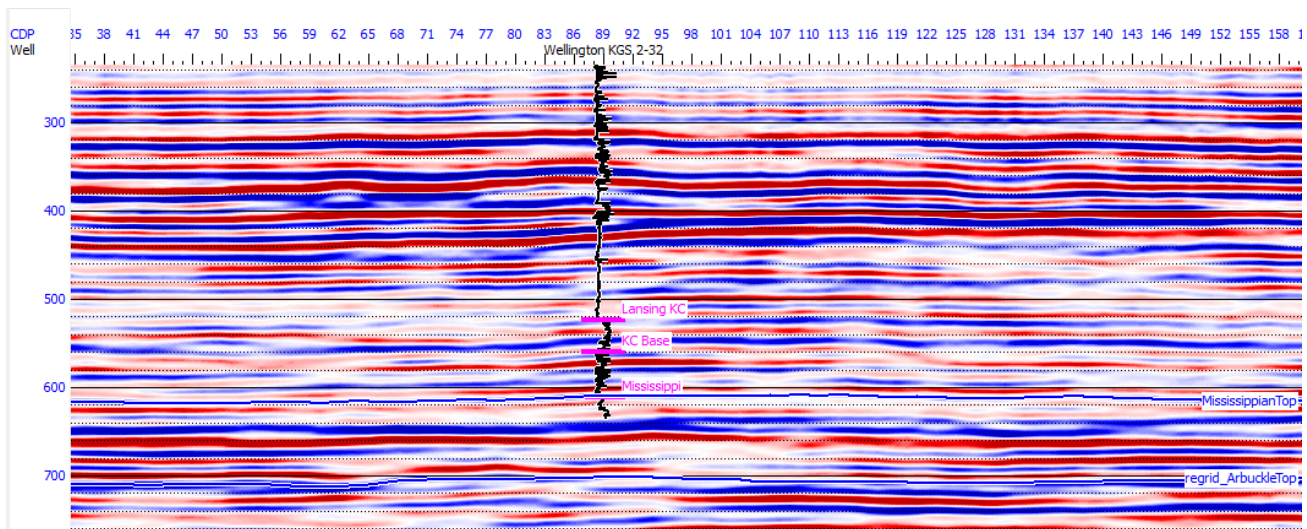


Figure S-18. Arbitrary line extracted from the 3-D P-P seismic survey, displaying the location of the CO<sub>2</sub> injection well KGS 2-32.

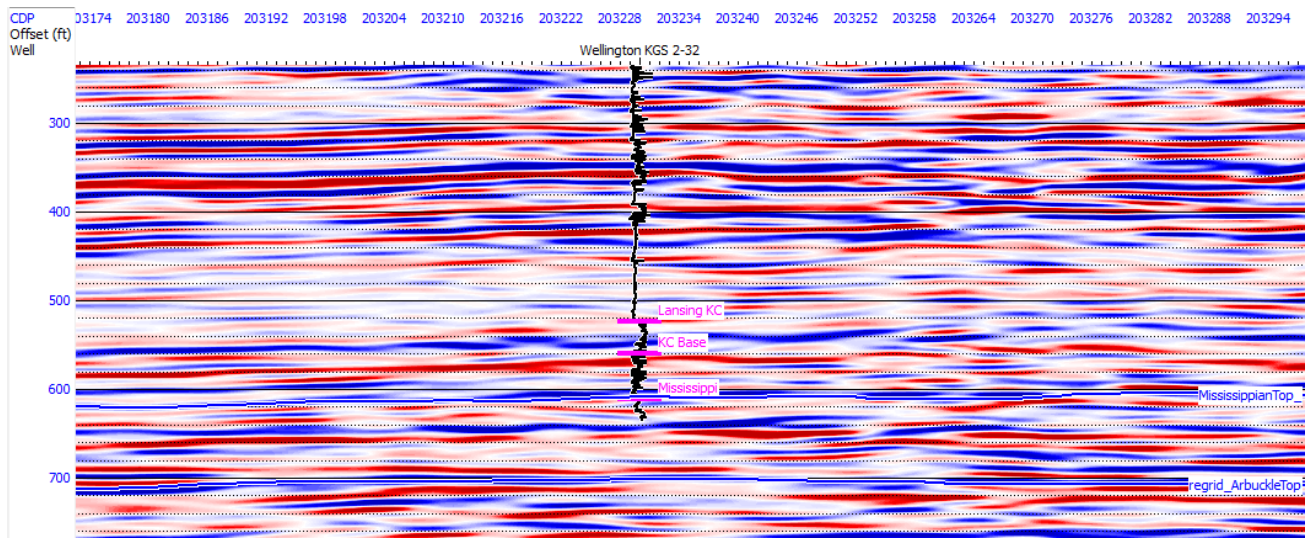


Figure S-19. 2-D seismic line 03 acquired post-injection, displaying the location of well KGS 2-32.

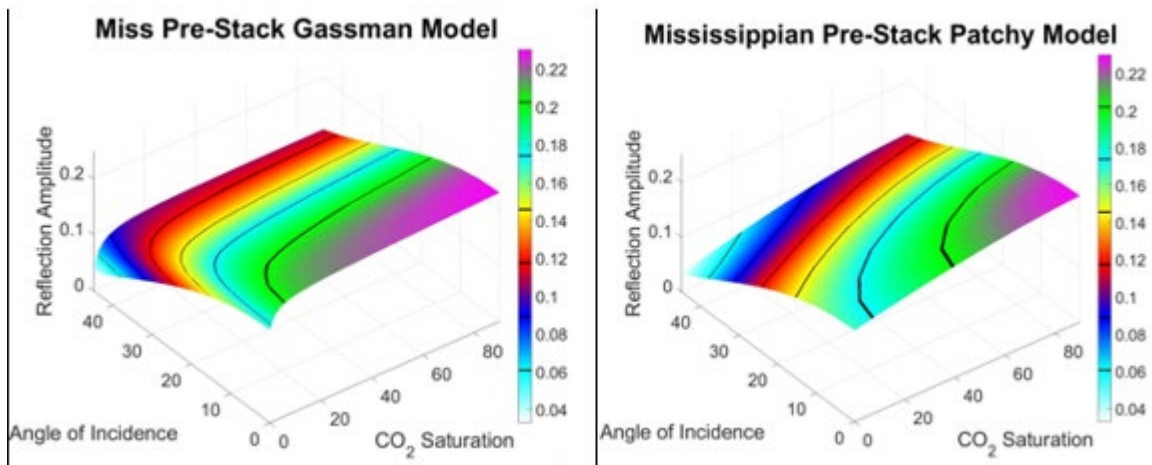


Figure S-20. Gassmann (left) and Patchy (right) models for the Mississippian reservoir exhibit reflectivity changes up to 10% suggesting the potential for measurable amplitude changes in pre-stack seismic data analysis.

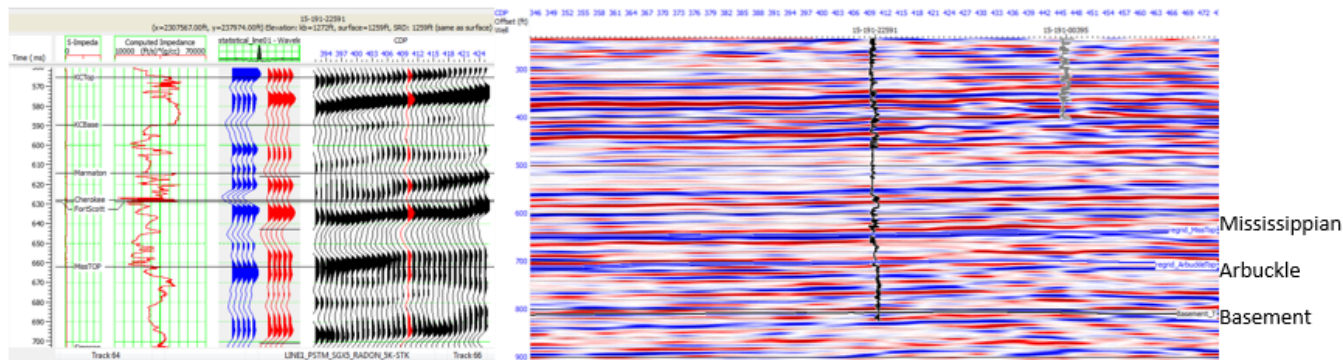


Figure S-21. Synthetic seismogram "tying" well KGS 1-32 and 2-D seismic line 01.

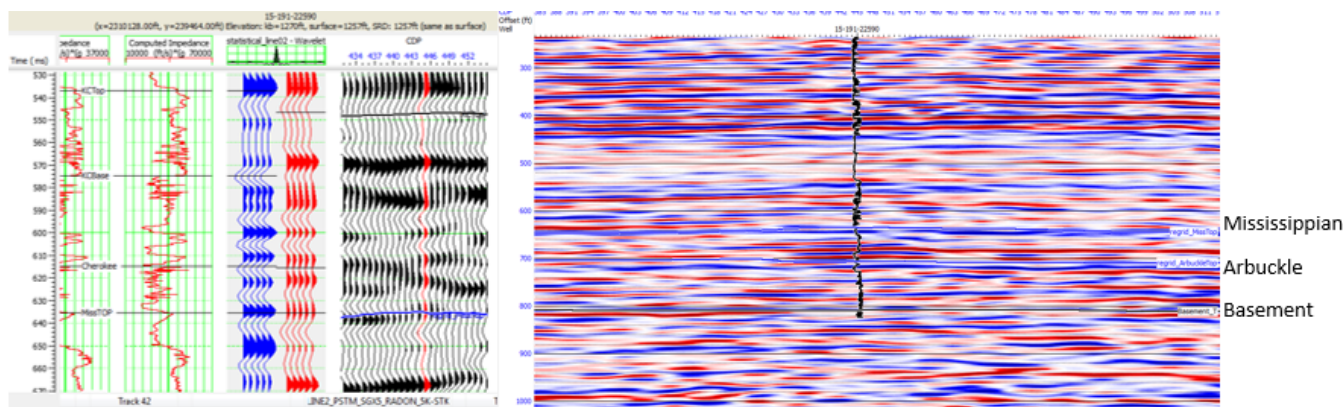


Figure S-22. Synthetic seismogram "tying" well KGS 1-28 to 2-D seismic line 02.

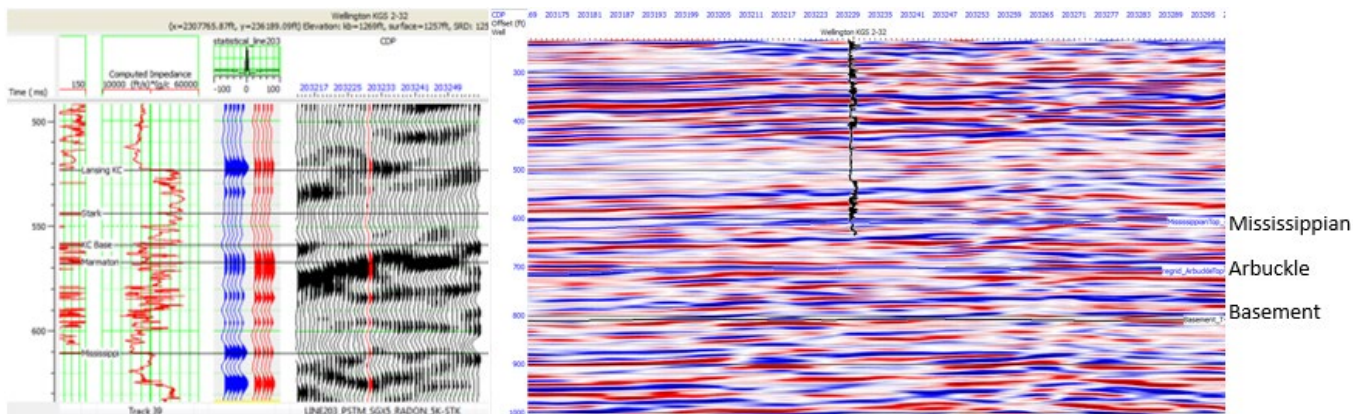


Figure S-23. Synthetic seismogram "tying" well KGS 2-32 and 2-D seismic line 03 (post-injection).



## **Passive seismic monitoring of earthquake activity near the CO<sub>2</sub> injection site at Wellington field, south-central, Kansas**

Seismicity in the United States midcontinent has increased by orders of magnitude over the past decade. Spatiotemporal correlations of seismicity to wastewater injection operations have suggested that injection-related pore fluid pressure increases are inducing the earthquakes. In this investigation, we examine earthquake occurrence in southern Kansas and northern Oklahoma and its relation to the change in pore pressure. The main source of data comes from the Wellington Array in the Wellington oil field, in Sumner County, KS, which has monitored for earthquakes in central Sumner County, KS since early 2015. The seismometer array was established to monitor CO<sub>2</sub> injection operations at Wellington field. Although no seismicity was detected in association with the spring 2016 Mississippian CO<sub>2</sub> injection, the array has recorded over 2,500 earthquakes in the region and is providing valuable understanding to induced seismicity. A catalog of earthquakes was built from this data and was analyzed for spatial and temporal changes, stress information, and anisotropy information. The region of seismic concern has been shown to be expanding through use of the Wellington earthquake catalog, and has revealed a northward progression of earthquake activity reaching the metropolitan area of Wichita. The stress orientation was also calculated from this earthquake catalog through focal mechanism inversion. The calculated stress orientation was confirmed through comparison to other stress measurements from well data and previous earthquake studies in the region. With this knowledge of the stress orientation, the anisotropy in the basement could be understood. This allowed for the anisotropy measurements to be correlated to pore pressure increases. The increase in pore pressure was monitored through time-lapse shear-wave anisotropy analysis. Since the onset of the observation period in 2010, the orientation of the fast shear-wave has rotated 90°, indicating a change associated with critical pore pressure build up. The time delay between fast and slow shear wave arrivals has increased, indicating a corresponding increase in anisotropy induced by pore pressure rise. *In-situ* near-basement fluid pressure measurements corroborate the continuous pore pressure increase revealed by the shear-wave anisotropy analysis over the earthquake monitoring period.

This research is the first to identify a change in pore fluid pressure in the basement using seismological data and it was recently published in the AAAS journal *Science Advances* (Nolte et al., 2017). The shear-wave splitting analysis is a novel application of the technique, which can be

used in other regions to identify an increase in pore pressure. This increasing pore fluid pressure has become more regionally extensive as earthquakes are occurring in southern Kansas, where they previously were absent. These monitoring techniques and analyses provide new insight into mitigating induced seismicity's impact to society.

## INTRODUCTION

Passive seismic monitoring was established in 2015 at Wellington oil field in order to monitor planned CO<sub>2</sub> injections for EOR in the Mississippian reservoir and sequestration in the Arbuckle saline aquifer. Local seismicity is recorded by an array of 18 seismometers at and near Wellington field. While no earthquakes were recorded in association with the spring 2016 CO<sub>2</sub> injection in the Mississippian reservoir, over 2,500 local induced seismicity events data have been recorded (Figure S-24). The seismic network, earthquake catalog and data analyses are described in the MS Thesis by Nolte (2017) (Appendix S-D).

Passive seismic data investigations at Wellington Field are summarized as follows:

- I. Monitoring the northward advance on injection induced seismicity in southern Kansas.
- II. Understanding injection induced seismicity in the midcontinent through shear-wave anisotropy analysis.

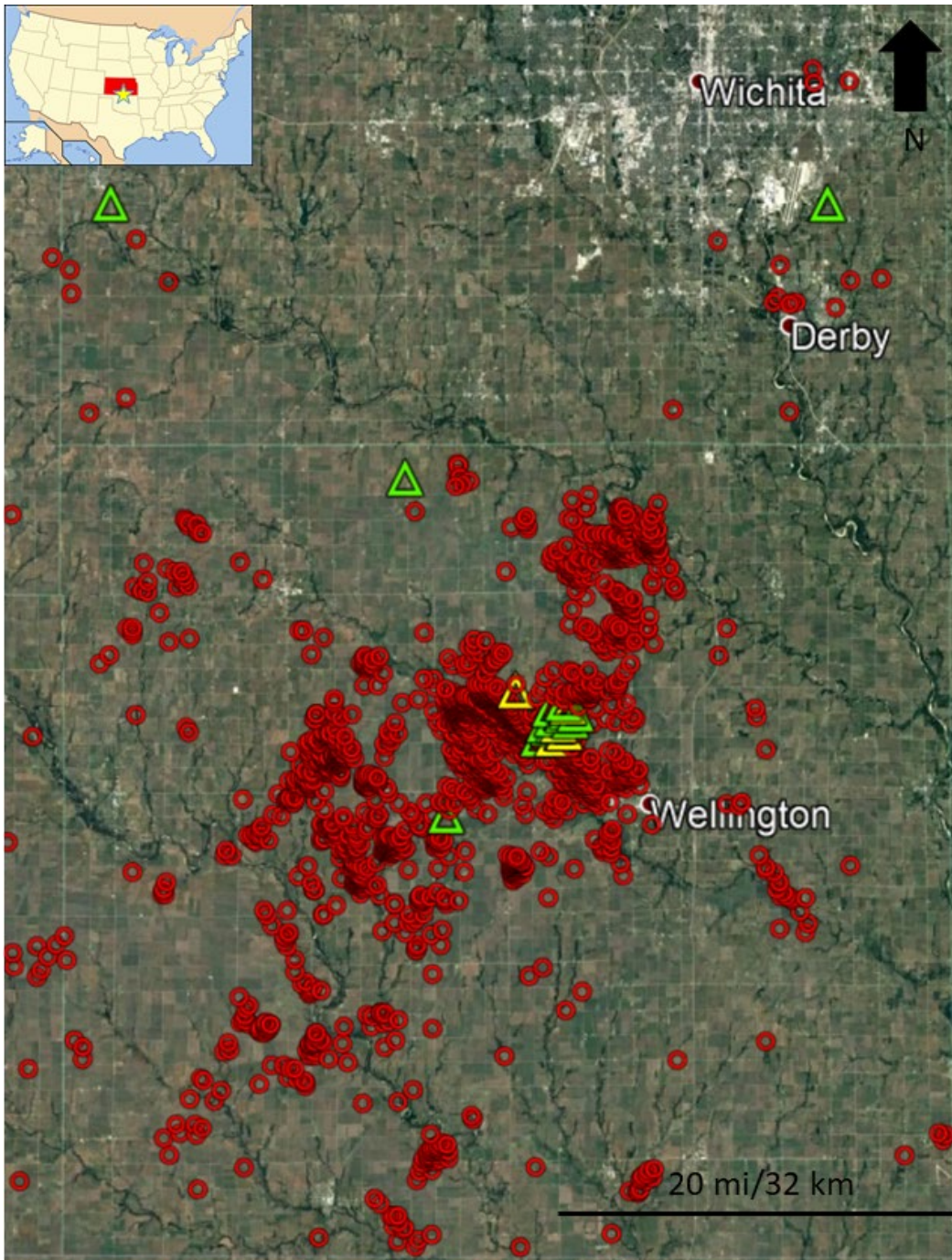


Figure S-24: This map shows 2,522 southern Kansas earthquakes that occurred from May 2015 - July 2017. Earthquake magnitudes range from 0.4 to 3.6 magnitude. A 3.0 magnitude earthquake is usually felt by humans. Red circles indicate earthquakes. Triangles indicate seismometers of the Wellington array.

## **I Monitoring the northward advance on injection induced seismicity in southern Kansas**

For detailed description refer to the MS Thesis by Nolte (2017) (Appendix S-D)

### *Key Findings*

- The number of earthquakes in southern Kansas continues to increase.
- Over the last two years earthquakes have been advancing northward, from northern Oklahoma to southern Kansas.
- The regions affected by induced seismicity are growing.

### *Background*

Kansas and Oklahoma have seen a drastic increase in seismicity in recent years with magnitude 3 and larger events increasing ~30 fold in 2014 compared to the historical average. Recent evidence has indicated an increase in basement pore pressure as the cause of the increased seismic activity. This increased pore pressure has been predicted through modeling to be caused by high volume injection wells disposing of brine water in the Arbuckle formation (Ellsworth, 2013). The high pore fluid pressures are causing ancient fault systems to reactivate and slip. The region of seismic concern has grown over the past 7 years and the growth in affected area is believed to be associated with the movement of a higher pore fluid pressure zone in the basement, which is expanding outwards from high-rate injection wells.

### *Methods*

The Kansas Geological Survey (KGS) has installed a seismometer array in the Wellington oil field with the objective to monitor for potentially induced seismicity from CO<sub>2</sub> injections in the Arbuckle and Mississippian carbonate reservoirs. However, during this period of monitoring, the issue of induced seismicity from fluid injection in the Arbuckle has grown, and data from the array has been used to monitor for regional earthquakes. Data from the Wellington array has been used to clearly demonstrate a northward trend of earthquakes in Kansas

### *Results*

Earthquakes near the Wellington oil field have been recorded and cataloged since April of 2015. A total of nearly 2400 earthquakes occurred in the study area over this time period. The

moment magnitude ( $M_w$ ) scale has been used because it is the standard for very local/induced seismicity (Stork, 2014). The magnitudes have ranged from  $M_w$  0.4 to 3.8 in Kansas. Magnitudes are calculated from the spectral energy of the earthquake (Stork 2014) in the open-source software SeisAn (Havskov, 1999). All earthquake locations from the Wellington array can be seen in figure S-25.

The first earthquakes in Kansas occurred very near the Oklahoma border, in Sumner and Harper counties. Earthquakes are now occurring in many more counties in southern Kansas, including Sedgwick County, home to the largest city in Kansas, Wichita. Earthquakes have occurred within the Wichita metro, but have been relatively small and unfelt ( $M_w < 2.5$ ). The Wellington array is in an optimal location to continue to monitor the movement and potential risk of induced seismicity in Kansas. As larger, felt earthquakes are occurring along the Kansas/Oklahoma border, the array will be able to assess areas of potentially higher seismic concern, in an effort to help mitigate risk.

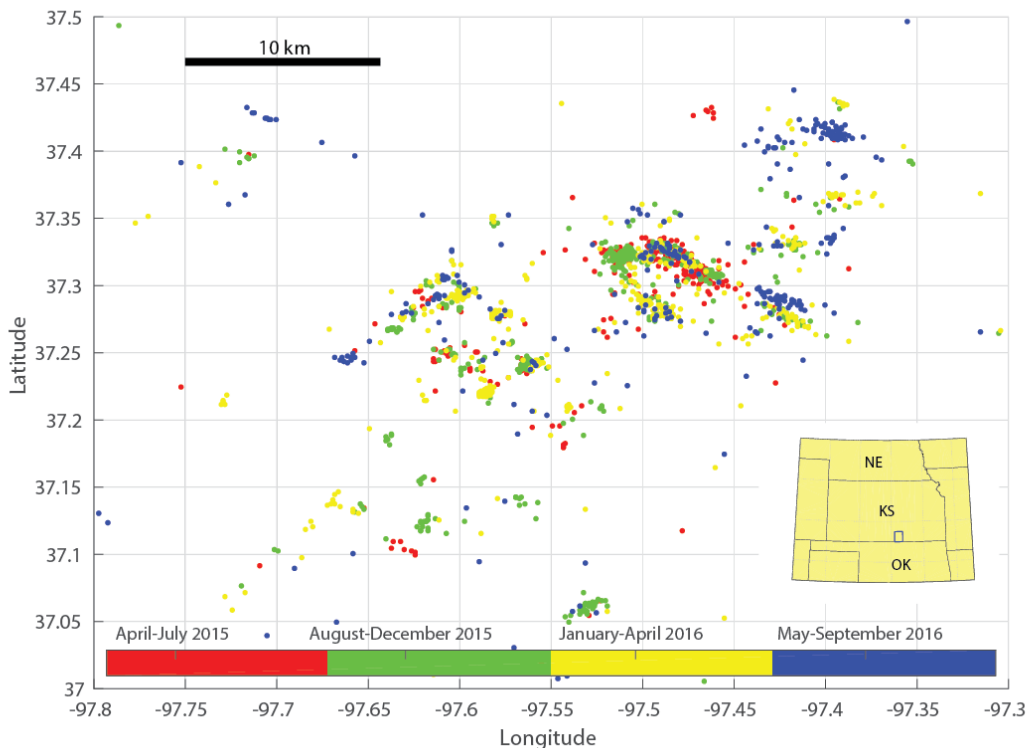


Figure S-25: Map of 1898 events observed between April 2015 and December 2016 in western Sumner County. Earthquakes are colored by time of occurrence. Red colors correspond to oldest earthquakes whereas blue colors are the most recent earthquakes. blue colors are more common to the northeast of the map, indicating northward progression.

The advancement of induced seismicity in Kansas demonstrates that large-volume injection induced pore-pressure increases can have impacts on regional seismicity. Shallow basement pore pressure increase appears to impact seismicity several 10's of kilometers away from individual injection wells. Far reaching pore pressure changes can be of concern to populated regions from Texas to Ohio that are currently facing injection induced seismicity. Additional monitoring of induced seismicity is needed in order to understand the underlying processes and effectively mitigate the risk associated with induced earthquakes

## **II Understanding injection induced seismicity in the midcontinent through shear-wave anisotropy analysis**

For detailed description refer to the MS Thesis by Nolte (2017) (Appendix S-D)

Journal publication: "Shear-Wave Anisotropy Reveals Pore Fluid Pressure-Induced Seismicity in the US Midcontinent" by Nolte et al. (2017), Science Advances (Appendix S-E)

### *Key Findings*

- Previous models suggest increasing pore pressure from high-volume wastewater injection is inducing seismicity in Oklahoma and Kansas.
- Shear- wave anisotropy analysis presented in this investigation is the first direct evidence provided by seismological observations to detect the increase in pore fluid pressure.
- Pressure monitoring in well KGS 1-28 confirms the pressure increase in the study area.

### *Background*

Seismicity in the midcontinent of the United States has seen a dramatic increase from the historical average of 21 magnitude ( $M \geq 3$ ) earthquakes per year to 188  $M > 3$  earthquakes in 2011 (Ellsworth, 2013). High levels of seismicity persist to date, with 688  $M > 3$  earthquakes in 2014 (Rubinstein and Mahani, 2015). Spatiotemporal analysis of earthquakes and wastewater injection in the Arbuckle point to pore fluid pressure increases as the cause of increased seismicity across the central US (Ellsworth, 2013; Keranen et al., 2014), but direct evidence from seismological data has not been documented (Keranen et al., 2014). Time-lapse earthquake shear-wave (S-wave) split

analysis, presented in this investigation, demonstrates that pore fluid pressure in the shallow basement has increased over time to a critical pressure, and is the cause of the increased seismicity.

### *Methods*

This study examines if the recent seismicity in northern Oklahoma and southern Kansas exhibits changes in shear wave anisotropy (i.e. fast S-wave  $\Phi$  flips and increased dt scatter), which would constitute direct evidence of critical pore pressure build-up along the raypaths traveled. The time-lapse earthquake data analyzed spans the period from 2010 to 2016. A total of 120 earthquakes of magnitude ( $M_w$ ) 2 or greater were used for this study. Most events were in the range of  $M_w$  2 –  $M_w$  3, the largest event was an  $M_w$  4.3, and all earthquakes occurred in the shallow basement (1-11 km depth). Earlier events in 2010-2012 came from northern Oklahoma, given the scarcity of earthquakes in southern Kansas at that time. Since 2013, there has been increased seismicity in south-central Kansas. *In-situ* downhole pressure measurements in the Arbuckle Group saline aquifer, approximately 30 m above basement, were obtained from the KGS 1-28 well in the Wellington oil field.

### *Results*

There is a 90° flip in the  $\Phi$  of events that occurred in 2015-2016 (Figure S-26, A3) compared to events from an earlier time window (2010-2015) (Figure S-26, A1, A2). The early solution of  $\Phi$  is in the direction of the maximum horizontal stress in the region (~75°) as calculated from earthquake focal mechanisms and from well-bore sonic log data analysis (Alt, 2016). In the histogram corresponding to the 2015-2016 earthquakes (Figure S-26, A3), the fast shear wave orientation  $\Phi$  is offset by approximately 90° from the maximum horizontal stress, causing it to align with the minimum horizontal stress. This rotation in  $\Phi$  and the narrow timeframe of its occurrence provide evidence of a change that may be anthropogenic. Such changes in  $\Phi$  have previously been identified as an effect of pore fluid pressure increases, where the ray path travels through rock that is critically stressed by pore fluid for a longer distance than rock that is not critically stressed by pore fluid (Zinke and Zoback, 2000; Crampin et al., 2004). These studies have also identified large deviation in dt shown to be associated with pore fluid pressure changes.

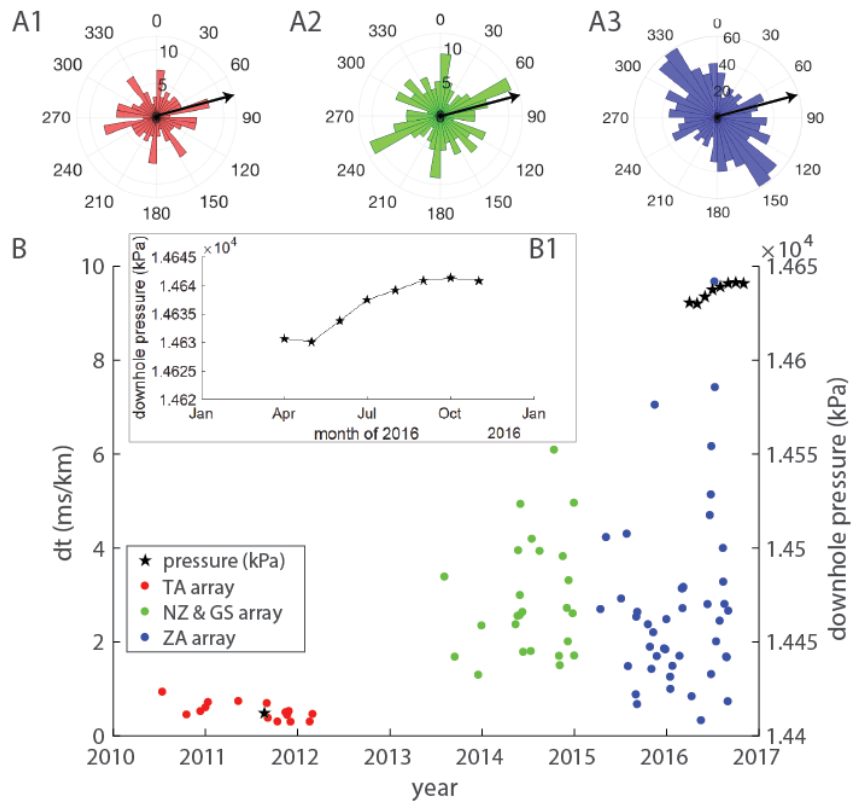


Figure S-26: (A1) Polar histogram of  $\Phi$  from TA events 201-2012 (red). The most common  $\Phi$  value is near the maximum horizontal stress of  $\sim 75^\circ$  along with flipped values at  $\sim 330^\circ$ . Zero degree values are most often null solutions. (A2) Polar histogram of  $\Phi$  from NZ & GS events 2013-2015 (green) showing common solutions in line with maximum horizontal stress as well as solutions  $90^\circ$  off of maximum horizontal stress. (A3) Polar histogram of  $\Phi$  from ZA events 2015-2016 (blue) showing the most common solution to be  $90^\circ$  off of the maximum horizontal stress, a direct indicator of critical pore fluid pressure. Arrows indicate the orientation of maximum horizontal stress at  $75^\circ$ . (B) Average  $dt/km$  of earthquakes from 2011 through 2016, showing a steady increase over time, as well as an increase in variance of data. Black stars showing average pressure per month from down hole pressure monitoring in KGS 1-28, in Wellington Oil field. The initial pressure measurement was obtained when the well was drilled in August 2011. Inset B1 is an expanded view of monthly pressure observations from April to November 2016.

The analysis shows increasing values, range, and scatter in  $dt$  estimates (Figure S-26B). The increase in  $dt$  suggests increasing anisotropy of the rock, often associated with the fracture density and aperture width (Crampin, 1999). It is likely that the basement has become critically stressed by increasing pore fluid pressure. The pore fluid pressure increase reduces the effective stress on the rock, which previously kept fractures that were not parallel to the maximum horizontal stress closed (Crampin et al., 2004). Increasing pore fluid pressure can cause fractures to shear or dilate, increasing the anisotropy and the magnitude of  $dt$ .

The observed flip in  $\Phi$  as well as the increase in average  $dt$  and the increase in  $dt$  scatter are interpreted as direct evidence of an increase in pore fluid pressure over time. These changes correlate with downhole pressure data acquired at the KGS 1-28 well in the lower Arbuckle saline aquifer, near the basement. Bottomhole pressure has increased more than 200 kPa since 2011, when the well was drilled (Figure S-26B). The borehole remained idle until April of 2016, when a pressure sensor was installed for continuous monitoring of the lower Arbuckle. The high resolution pressure measurements since April show that downhole pressures are increasing at a rate of 3-4 kPa per month (Figure S-26B1).

The shear-wave splitting analysis presented here, correlated with downhole pressure monitoring data, is the first direct evidence of increasing pore pressure in the region detected by seismic observations. These results show that analyzing the change in anisotropy of the basement is an effective means of identifying critical changes in pore fluid pressure that are the likely cause of fault reactivation and earthquakes in the region (Ellsworth, 2013; Walsh and Zoback, 2016). This methodology could be applied to other regions of potentially induced seismicity to verify that increasing pore fluid pressure related to deep well injection is the underlying cause of seismicity increases.

## Pressure Monitoring in the Arbuckle Formation in the Wellington KGS 1-28

The continuous pressure monitoring in the lower Arbuckle was set up because a large rate and high volume brine disposal in the area is believed to be responsible for the induced seismicity. The assumption in the case of the testing in the Arbuckle is that the observed pressure is being transmitted at depth in the basement where faults are critically stressed, requiring a small force to move. To date the vast majority of earthquakes have occurred in the shallow basement. Trilobite Testing of Hays Kansas installed the pressure gauge in the Wellington KGS 1-28 at about 5020 feet depth from surface. The instrument is programmed to sample every second with an accuracy of 0.1 psi. About a week of pressure data is sent to KGS as a Comma Separated Values (CSV) file. A Java computer program was developed to analyze the pressure data from the Wellington KGS 1-28 to understand the pressure changes, to remove solar & lunar Tidal pressures along with barometric pressure changes. The idea is that it is possible remove, account for, or explain natural every day influences and investigate only the geological influences and identify fluid movement due to brine injection, micro quake swarms, etc. Figure 52 is an illustration of the raw pressure measurement in psig units over a 4 day period, 30 July to 2 August 2016.

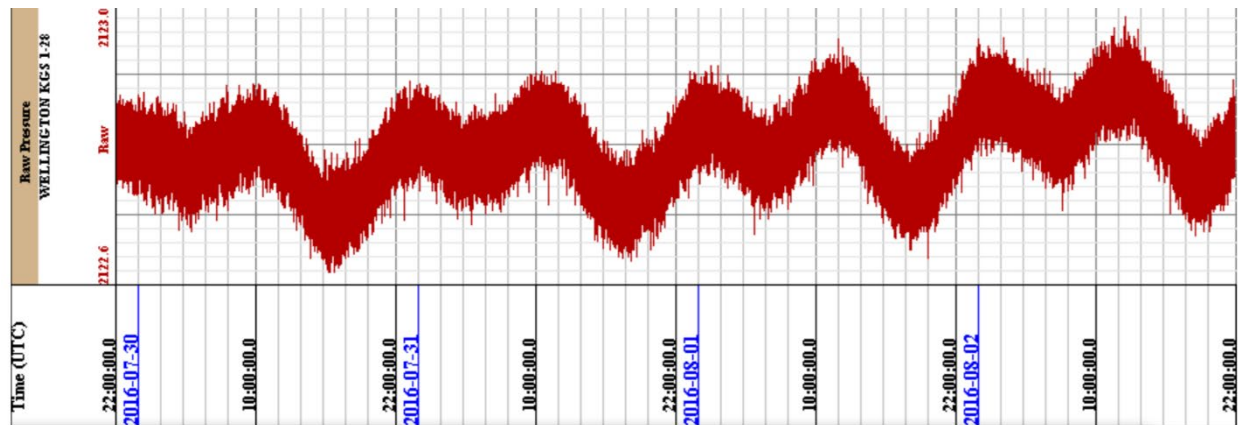
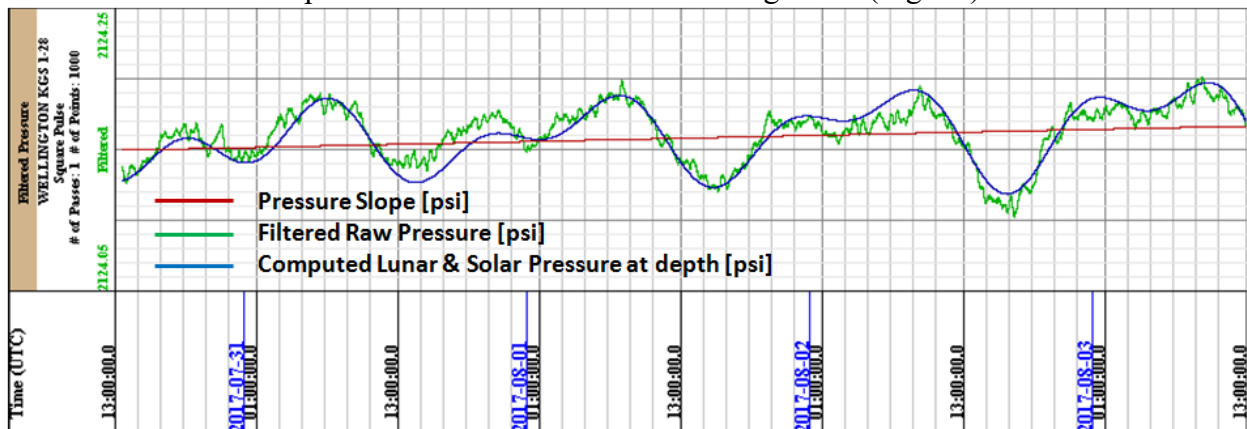


Figure 52. Raw Pressure Data Measurements in the Wellington KGS 1-28 between 30 July to 2 August 2016.

The computer program filtered the noise from the raw pressure data, compute the lunar & solar tidal pressures along with the barometric pressures influence, and then subtract that from the raw pressure data. In an ideal situation if these are the only pressures influencing the pressure measurements then the pressure data should result in a straight line (Fig. 53).



**Figure 53. Filtered Raw Pressure vs. Computed Lunar & Solar Pressure at depth.**

The computed lunar & solar pressure at depth (blue colored curve) coincides agreeable well with the measured filtered raw pressure (green colored curve). The deviations will be attributed to the barometric pressure influence, which will be explained next. If both the lunar & solar pressure and the barometric pressure were removed from the filtered raw pressure data the resultant pressure curve would line up on the pressure slope (red colored curve) accounting for all the known outside influences.

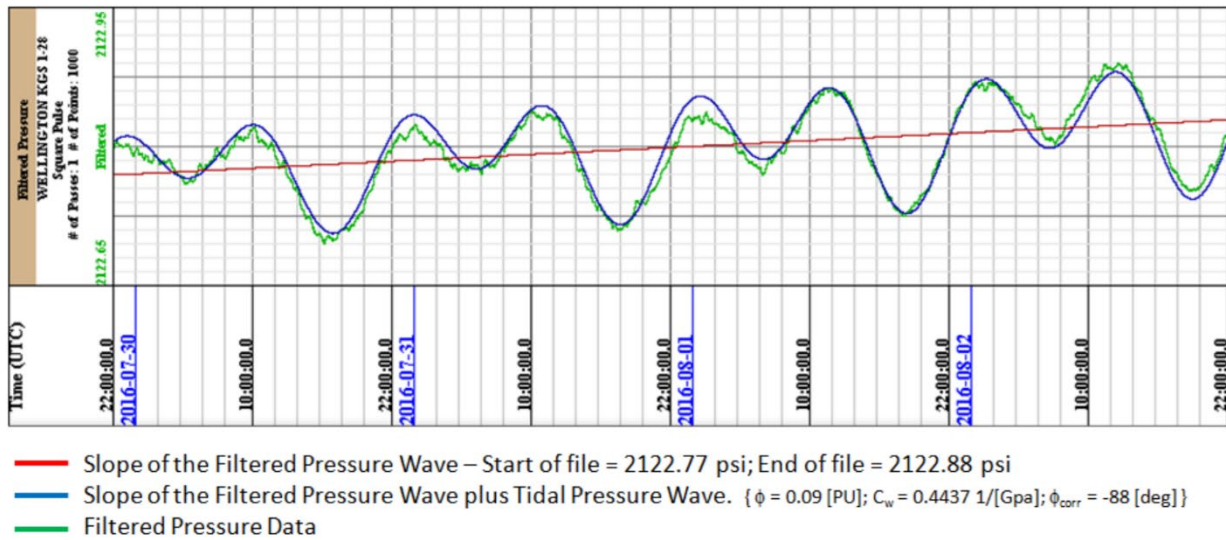


**Figure 54. Filtered pressure data with the computed lunar & solar pressure wave**

We do not have the exact height of the water column above the pressure sensor, so the only way to incorporate the barometric pressure influence at the pressure sensor is to estimate what the measured pressure data should be at the sensor. The atmospheric pressure at Wellington KGS 1-28 is about 14.11 psi from the calculation of ideal altitude versus pressure curve. Ideally if the lunar & solar pressure curve is subtracted from the measured data then the measured data should be a straight line. It is basically a straight line in the image below (Figure 55) but there are deviations.

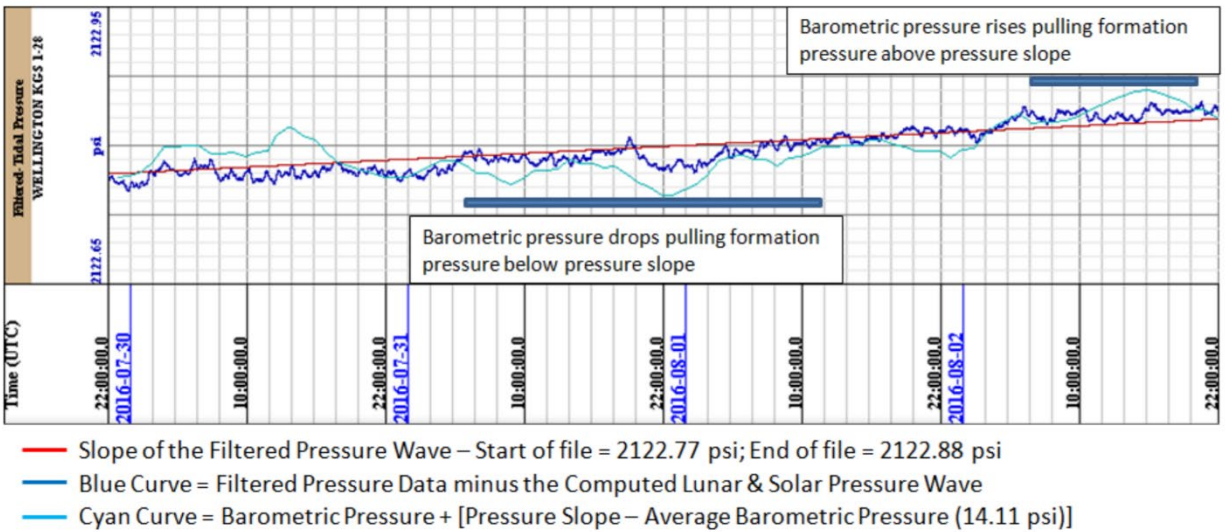


**Figure 55. Lunar & Solar Pressure Wave removed from measured pressure data.**

A pressure curve is constructed by adding the barometric pressure measured at Strother Field Airport with the difference of the Pressure Slope and 14.11 psi the average ideal barometric pressure at this elevation and overlaying that on the measured data. It can be seen that there is some comparison with the measured data. Ideally if the barometric pressure is measured at Wellington KGS 1-28 then the computed barometric pressure should line up exactly with the linear pressure curve and any deviations from that would be other geological effects, i.e. fluid movement, etc.

## Conclusions

As a result of CO<sub>2</sub> injection observed incremental average oil production increase is ~68% with only ~18% of injected CO<sub>2</sub> produced back. Simple but robust monitoring technologies along with sophisticated active and passive seismic monitoring methods proved to be very efficient in detection and locating of CO<sub>2</sub>. High CO<sub>2</sub> reservoir retentions with low yields within actively producing field could help to estimate real-world risks of CO<sub>2</sub> geological storage. Wellington filed CO<sub>2</sub> EOR was executed in a controlled environment with high efficiency.

The Kansas Geological Survey (KGS) collected, compiled, and analyzed available data, including well logs, core data, step rate tests, drill stem tests, 2D and 3D seismic data, water level measurements, and others types of data. Several exploratory wells were also drilled and core was collected and modern suites of logs were analyzed. Reservoir properties were populated into several site specific geological models. The geological models illustrate the highly heterogeneous nature of the Arbuckle Group.

The Arbuckle Group carbonate saline aquifer is Oklahoma and Kansas has been utilized extensively for waste disposal purposes since 1935. UIC Class I and Class II wells target Arbuckle Group as the primary disposal zone in the region. However, recent developments of Mississippian Lime Play and other industrial activities are exerting unprecedented pressure on Arbuckle saline aquifer use as an industrial waste disposal reservoir. There is an evidence gathered during the course of this project, independent pressure monitoring gages, UIC Class I well monitoring

records, and other sources of regional fluid level and pore pressure increases in Arbuckle reservoir in Kansas and Oklahoma. Competing interests of various industrial groups that include oil and gas, chemical complex, and potentially CO<sub>2</sub> geological storage could collide in the future if regulatory framework is not outlined and expanded.

*Key accomplishments for this project include:*

- Approximately 20,000 metric tons of CO<sub>2</sub> was injected in the upper part of the Mississippian reservoir. Total of 1,101 truckloads, 19,803 metric tons, average of 120 tonnes per day were delivered over the course of injection that lasted from January 9 to June 21, 2016.
- Well logs, core data, step rate tests, drill stem tests, 2D and 3D seismic data, water level measurements, and others types of data were collected, compiled, and analyzed. Several exploratory wells were also drilled and core was collected and modern suites of logs were analyzed. Reservoir properties were populated into several site specific geological models.
- Earthquakes near the Wellington oil field have been recorded and cataloged since April of 2015. A total of nearly 2400 earthquakes occurred in the study area over this time period.
- The shear-wave splitting analysis presented here, correlated with downhole pressure monitoring data, is the first direct evidence of increasing pore pressure in the region detected by seismic observations.
- Azimuthal analysis of the 3D P-P wave data collected in Wellington provides a sense of the anisotropy in the top of the Mississippian and Arbuckle and reveals a fracture map for the field. Results are consistent with observed rock properties known to cause detectable variations in seismic data; fracture and maximum horizontal stress direction. Large scale features such as faults are indirectly observed by its effect on the surrounding material. Fractures observed in FMI logs are consistent with patterns observed in the Wellington field seismic azimuthal analysis. The Mississippian reservoir fracture and porosity predictions from 3D seismic are compared to the monitored mobility of the CO<sub>2</sub> injected in well KGS 2-32 in spring 2016.
- The analysis of well log and seismic data revealed that the reservoir exhibits different characteristics across fault which divides the Wellington Field diagonally from the southwestern corner to the northeastern corner.
- Mississippian and Arbuckle reservoir AVO classification and pre-stack Seismic Inversion (Simultaneous AVO Inversion) were completed.

*Lesson learned during this project include:*

- This case study provides an inside that CO<sub>2</sub> EOR and geological storage could be successfully applied for Kansas carbonate reservoirs if CO<sub>2</sub> sources and associated infrastructure are ready and available.
- The geological models illustrate the highly heterogeneous nature of the Arbuckle and Mississippian Groups. Vertical and horizontal variability results in several distinct hydro-stratigraphic units. It is essential to account for this heterogeneity when constricting models, forecasting outcomes of operations, and estimating risks.
- Permitting pilot scale non-commercial project for geological storage is a major challenge. The detailed outline of lessons learned during permit application process is outlined in a separate attached document.
- More detailed resource capacity studies are essential for shared use of a pore space for both CO<sub>2</sub> geological storage and other waste management.

*Data gaps identified during this project include:*

- Information on the interface between sedimentary formations (Arbuckle Group, Reagan, etc.) and granite basement is virtually nonexistent. It is essential to conduct more drilling, coring, and hydrological testing in the Mid-Continent region.
- A far-field/regional injection test in Arbuckle Group would permit determination of hydrogeologic properties of faults and other heterogeneities to better address pressure propagation and its role in induced seismicity.
- Continues pore pressure and seismic monitoring in near granite basement intervals is also essential for understanding induced seismicity and other problems associated with shared use of pore space in the Mid-Continent.

## **References**

Bennion, B., and Bachu, S., 2007, Relative permeability characteristics for supercritical CO<sub>2</sub> displacing water in a variety of potential sequestration zones: Society of Petroleum Engineers, SPE-95547-MS.

Bennion, B., and Bachu, S., 2010, Drainage and imbibition CO<sub>2</sub>/brine relative permeability curves at reservoir conditions for high-permeability carbonate rocks: Society of Petroleum Engineers, SPE 134028-MS.

Benson, S., 2005, Overview of geologic storage of CO<sub>2</sub>, in carbon dioxide capture for storage in deep geologic formations, Volume 2—Results from the CO<sub>2</sub> capture project: Elsevier Publishing, UK.

Burnside, N. M., and Naylor, M., 2014, Review and implications of relative permeability of CO<sub>2</sub>/brine systems and residual trapping of CO<sub>2</sub>: Int. J. Greenh. Gas Control, 23, p. 1–11

Bui, L. H., Tsau, J. S., and Willhite, G. P., 2010, Laboratory investigations of CO<sub>2</sub> near-miscible application in Arbuckle Reservoir: SPE Improved Oil Recovery Symposium, Tulsa, Oklahoma, 24–28 April 2010, SPE Publication 129710.

Carter, R. D., and Tracy, G. W., 1960, An improved method for calculating water influx: Petroleum Transactions, AIME, v. 219, p. 415–417.

Chang, K. W., Minkoff, S. E., and Bryant, S. L., 2009, Simplified model for CO<sub>2</sub> leakage and its attenuation due to geological structures: Energy Procedia, v. 1, p. 3,453–3460.

Dake, L. P., 1978, Fundamentals of Reservoir Engineering, Chapter 9, Elsevier Scientific Publishing Co., 1978.

FutureGen Industrial Alliance, 2013, Underground injection control permit applications for FutureGen 2.0 Morgan County Class VI UIC Wells 1, 2, 3, and 4, Jacksonville, Illinois.

Kestin, J., Khalifa, H. E., and Correia, R. J., 1981, Tables of the dynamic and kinematic viscosity of aqueous NaCl solutions in the temperature range 20–150 °C and the pressure range 0.1–35 MPa: Journal of Physical and Chemical Reference Data, NIST, v. 10, p. 71–88.

- Krevor, P., and Benson, S. M., 2012, Capillary pressure and heterogeneity for the CO<sub>2</sub>/water system in sandstone rocks at reservoir conditions: *Advances in Water Resources*, v. 38, p. 48–59, ISSN: 0309-1708
- Krevor, P., and Benson, S. M., 2015, Accurate determination of characteristic relative permeability curves: *Advances in Water Resources*, v. 83, p. 376–388
- Li, Y. K., and Nghiem, L. X., 1986, Phase equilibrium of oil, gas and water/brine mixtures from a cubic equation of state and Henry's Law: *Canadian Journal of Chemical Engineering*, June, p. 486–496.
- Loucks, R. G., 1999, Paleocave carbonate reservoirs: Origins, burial-depth modifications, spatial complexity, and reservoir implications: *The American Association of Petroleum Geologists, Bulletin*, v. 83, no. 11.
- Lucia, F. J., 1999, *Carbonate reservoir characterization*: New York, Springer-Verlag, 226 p.
- Pau, G. S. H., Bell, J. B., Pruess, K., Almgren, A. S., Lijewski, M. J., and Zhang, K., 2010, High resolution simulation and characterization of density-driven flow in CO<sub>2</sub> storage in saline aquifers: *Advances in Water Resources*, v. 33, no. 4, p. 443–455.
- Søreide, I., and Whitson, C. H., 1992, Peng-Robinson predictions for hydrocarbons, CO<sub>2</sub>, N<sub>2</sub>, and H<sub>2</sub>S with pure water and NaCl brine: *Fluid Phase Equilibria*, v. 77, p. 217–240.
- Holubnyak, Y., Watney, L., Rush, J., Bidgoli, T., Williams, E., and Gerlach, P., 2016, Calculation of CO<sub>2</sub> storage capacity for Arbuckle Group in southern Kansas: Implications for a seismically active region: 13th International Conference on Greenhouse Gas Control Technologies, Lausanne, Switzerland
- The State Corporation Commission of the State of Kansas (KCC), KGS #2-32 Class II Well Design Approval, July, 2014
- Holubnyak Y., Watney W., Rush J., Fazelalavi M., Reservoir evaluation and modeling of pilot scale CO<sub>2</sub> EOR project in Mississippian Lime at Wellington Field in Southern Kansas, *Energy Procedia* 63, 7732-7739
- FazelAlavi, M., FazelAlavi, M., and FazelAlavi, M., Wellington Field, Mississippian Formation Preliminary Reservoir Description (Permeability, Capillary Pressure, and Relative Permeability), Kansas Geological Survey Open File Report, 2015-26
- Reservoir Modeling of CO<sub>2</sub> Injection in Arbuckle Saline Aquifer at Wellington Field, Sumner County, Kansas, Kansas Geological Survey Open File Report 2016-29
- S. Crampin, 1999, Calculable fluid-rock interactions. *Geological Society, London*. **156**. 501-514.
- S. Crampin, S. Peacock, Y. Gao, S. Chastin, 2004, The Scatter of time-delays in shear-wave splitting above small earthquakes. *Geophysics Journal International*. **156**. 39-44.
- W.L. Ellsworth, 2013, Injection-Induced Earthquakes. *Science*. **341**. 1225942.

- J. Havskov, L. Ottemoller, 1999, SeisAn Earthquake analysis software, *Seismological Research Letters*, **70**.
- K.M. Keranen, M. Weingarten, G.A. Abers, B.A. Bekins, S. Ge, 2014, Sharp increase in central Oklahoma seismicity since 2008 induced by massive wastewater injection. *Science*. **345**. 448-451
- J.L. Rubinstein, A.B. Mahani, 2015, Myths and Facts on Wastewater Injection, Hydraulic Fracturing, Enhanced Oil Recovery, and Induced Seismicity. *Seismological Research Letters*. **86**. 1060-1067.
- F.R. Walsh, M.D. Zoback, 2015, Oklahoma's recent earthquakes and saltwater disposal. *Science Advances*. **1**. e1500195
- W.L. Yeck, M. Weingarten, H.M. Benz, D.E. McNamara, E.A. Bergman, R.B. Herrman, J.L. Rubinstein, P.S. Earle, 2016, Far-field pressurization likely caused one of the largest injection induced earthquakes by reactivating a large preexisting basement fault structure. *Geophysical Research Letters*. **43**.
- J.C. Zinke, M.D. Zoback, 2000, Structure-related and stress-induced shear-wave velocity anisotropy: observations from microearthquakes near the Calaveras fault in central California. *Bulletin of the Seismological Society of America*. **90**. 1305-1312
- Adam, L., M. Batzle, I. Brevik, 2006, Gassmann's fluid substitution and shear modulus variability in carbonates at laboratory seismic and ultrasonic frequencies: *Geophysics*, v 71, no. 6, F173-F183.
- Fadolalkarem, Y., 2015, Pre-Stack Seismic Attribute Analysis of the Mississippian Chert and the Arbuckle Group at the Wellington Field, south-central Kansas. University of Kansas master's thesis.
- Franseen, E.K., Byrnes, A.P., Cansler, J. R., Steinhauff, D.M., Carr, T.R., and Dubois, M.K., 2003, Geologic Controls on Variable Character of Arbuckle Reservoirs in Kansas: An Emerging Picture: Kansas Geological Survey Open-file Report 2003-59, 30 p.
- Gray, D., Anderson, P., Logel, J., Delbecq, F., Schmidt, D., Schmid, R., 2012, Estimation of stress and geomechanical properties using 3D seismic data: *First Break*, v. 30, p. 59-68.
- Hampson, D., Russell, B., and Bankhead, B., 2005, Simultaneous inversion of pre-stack seismic data: Ann. Mtg. Abstracts, Society of Exploration Geophysicists.

- Hawkins, K., Leggott, R., Williams, G., Kat, H., 2001, Addressing Anisotropy in 3-D prestack depth migration: A case study from the Southern North Sea: The Leading Edge, May, p528-535.
- Mazzullo, S. J., B. W. Wilhite, and I. W. Woolsey, 2009, Petroleum reservoirs within a spiculite-dominated depositional sequence: Cowley Formation (Mississippian: Lower Carboniferous), south-central Kansas: AAPG Bulletin, v. 93, no.12, p.1649-1689.
- Misaghi, A., S. Landro, and A. Javaherian, 2010, A comparison of rock physics models for fluid substitution in carbonate rocks: Exploration Geophysics, v. 41, p. 146-154.
- Montgomery, S. L., 1998, Thirtyone formation, Permian Basin, Texas: structural and lithologic heterogeneity in a lower Devonian chert reservoir: AAPG Bulletin, v. 82, no. 1, p. 1-24.
- Lynn, H., 2016, Applied Azimuthal Anisotropy: Geophysical Society of Houston Webinar series.
- Nissen, S. E., T. R. Carr, K. J. Marfurt, and E. C. Sullivan, 2009, Using 3-D seismic volumetric curvature attributes to identify fracture trends in a depleted Mississippian carbonate reservoir: implications for assessing candidates for CO<sub>2</sub> sequestration, *in* M. Grobe, J. C. Pashin, and R. L. Dodge, eds., Carbon dioxide sequestration in geological media—State of the science: AAPG Studies in Geology 59, p. 297–319.
- Rogers, J. P., and M. W. Longman, 2001, An introduction to chert reservoirs of North America, 2001, AAPG Bulletin, v. 85, no.1, p. 1-5.
- Ruger, A., 1998, Variation of P-wave reflectivity with offset and azimuth in anisotropic media: Geophysics, v. 63, no. 3, p 935-947.
- Schwab, A., 2016, Characterizing the potential for fault reactivation related to fluid injection through subsurface structural mapping and stress field analysis, Wellington Field, Sumner County, KS: M.S. thesis, University of Kansas.
- Sirazhiev, A., 2012, Seismic Attribute Analysis of the Mississippian Chert at the Wellington Field, south-central Kansas. University of Kansas master's thesis.
- Thomsen, L., 2002, Understanding seismic anisotropy in exploration and exploitation: SEG/EAGE Distinguished instructor short course and text
- Vega, S., K. Berteussen, Y. F. Sun, and A. A. Sultan, 2007, Is Gassmann the best model for fluid substitution in heterogeneous carbonates: 77th Annual International Meeting, SEG, Expanded Abstract, p.1575-1578

- Watney, W. L., W. J. Guy, and A. P. Byrnes, 2001, Characterization of the Mississippian chert in south-central Kansas: AAPG Bulletin, v. 85, no.1, p. 85-113.
- Bradley, J. S. (1975). Abnormal formation pressure. AAPG Bulletin, 59(6), 957-973.
- Crabtree, B., Christensen, J., (2012). CO<sub>2</sub>-EOR Potential in the MGA Region, Great Plains Institute for Sustainable Development Report
- Goebel, E. D. (1968). Mississippian rocks of western Kansas. AAPG Bulletin, 52(9), 1732-1778.
- Graham, B. L., Haga, L. N., Nolte, K. A., Tsoflias, G. P., and W. L. Watney (2017), Fracture Mapping and Feasibility of Monitoring CO<sub>2</sub> in situ From Seismic Data at the Mississippian Carbonate Reservoir, Wellington Oil Field, South-Central Kansas, in DOE NETL Mastering the Subsurface Through Technology Innovation, Partnerships and Collaboration: Carbon Storage and Oil and Natural Gas Technologies Review Meeting, Pittsburgh, PA, August 1-3, 2017.
- Holubnyak, Y., Watney, W., Birdie, T., Rush, J., Fazelalavi, M., Wreath, D., (2017). Pilot Scale CO<sub>2</sub> EOR in Mississippian Carbonate Reservoir at Wellington Field in South-Central Kansas, Energy Procedia, EGYPRO30710.
- KGS oil and gas wells database, Kansas Geological Survey, <http://www.kgs.ku.edu/Magellan/Qualified/>, (accessed 12/1/2017).
- Lugn, A. L. (1935). The Pleistocene Geology of Nebraska: Nebraska Geol. Survey, Bull. 10, pp. 1-223.
- Lee, W., and Merriam, D. F. (1954). Preliminary Study of the Structure of Western Kansas. State Geological Survey of Kansas, University of Kansas.
- Nelson, P. H., and Gianoutsos, N. J. (2011). Evolution of overpressured and underpressured oil and gas reservoirs, Anadarko Basin of Oklahoma, Texas, and Kansas (No. 2011-1245). US Geological Survey.
- Newell, K. D., Watney, W. L., Cheng, W. L., and Brownrigg, R. L. (1987). Stratigraphic and spatial distribution of oil and gas production in Kansas.
- Scheffer, A. (2012). Geochemical and Microbiological Characterization of the Arbuckle Saline Aquifer, a Potential CO<sub>2</sub> Storage Reservoir; Implications for Hydraulic Separation and Caprock Integrity (Doctoral dissertation, University of Kansas).

- Schwab, D.R., Bidgoli, T.S., Taylor, M. H., (2017) Characterizing the potential for injection-induced fault reactivation through subsurface structural mapping and stress field analysis, Wellington Field, Sumner County, *Journal of Geophysical Research: Solid Earth*
- Sorenson, R. P. (2005). A dynamic model for the Permian Panhandle and Hugoton fields, western Anadarko basin. *AAPG bulletin*, 89(7), 921-938.
- Watney, W. L., Guy, W. J., and Byrnes, A. P. (2002). Characterization of the Mississippian Osage chert in south-central Kansas: Kansas Geological Survey, Open-file Report 2002-50.
- Zeller, D. E. (1968). Stratigraphic succession in Kansas. *Kansas Geological Survey Bulletin*, 189. <http://www.kgs.ku.edu/Publications/Bulletins/189/> (accessed 12/12/2017)

### Seismic References

- Adam, L., M. Batzle, I. Brevik, 2006, Gassmann's fluid substitution and shear modulus variability in carbonates at laboratory seismic and ultrasonic frequencies: *Geophysics*, v 71, no. 6, F173-F183.
- Crampin, S., 1999, Calculable fluid-rock interactions. *Geological Society, London*. **156**. 501-514.
- Crampin, S., S. Peacock, Y. Gao, S. Chastin, 2004, The Scatter of time-delays in shear-wave splitting above small earthquakes. *Geophysics Journal International*. **156**. 39-44.
- Ellsworth, W.L., 2013, Injection-Induced Earthquakes. *Science*. **341**. 1225942.
- Fadolalkarem, Y., 2015, Pre-Stack Seismic Attribute Analysis of the Mississippian Chert and the Arbuckle Group at the Wellington Field, south-central Kansas. University of Kansas master's thesis.
- Franseen, E.K., Byrnes, A.P., Cansler, J. R., Steinhaff, D.M., Carr, T.R., and Dubois, M.K., 2003, Geologic Controls on Variable Character of Arbuckle Reservoirs in Kansas: An Emerging Picture: Kansas Geological Survey Open-file Report 2003-59, 30 p.
- Gray, D., Anderson, P., Logel, J., Delbecq, F., Schmidt, D., Schmid, R., 2012, Estimation of stress and geomechanical properties using 3D seismic data: *First Break*, v. 30, p. 59-68.
- Hampson, D., Russell, B., and Bankhead, B., 2005, Simultaneous inversion of pre-stack seismic data: Ann. Mtg. Abstracts, Society of Exploration Geophysicists.
- Havskov, J., L. Ottemoller, 1999, SeisAn Earthquake analysis software, *Seismological Research Letters*, **70**.

- Hawkins, K., Leggott, R., Williams, G., Kat, H., 2001, Addressing Anisotropy in 3-D prestack depth migration: A case study from the Southern North Sea: The Leading Edge, May, p528-535.
- K.M. Keranen, M. Weingarten, G.A. Abers, B.A. Bekins, S. Ge, 2014, Sharp increase in central Oklahoma seismicity since 2008 induced by massive wastewater injection. *Science*. **345**. 448-451
- Mazzullo, S. J., B. W. Wilhite, and I. W. Woolsey, 2009, Petroleum reservoirs within a spiculite-dominated depositional sequence: Cowley Formation (Mississippian: Lower Carboniferous), south-central Kansas: AAPG Bulletin, v. 93, no.12, p.1649-1689.
- Misaghi, A., S. Landro, and A. Javaherian, 2010, A comparison of rock physics models for fluid substitution in carbonate rocks: Exploration Geophysics, v. 41, p. 146-154.
- Montgomery, S. L., 1998, Thirtyone formation, Permian Basin, Texas: structural and lithologic heterogeneity in a lower Devonian chert reservoir: AAPG Bulletin, v. 82, no. 1, p. 1-24.
- Lynn, H., 2016, Applied Azimuthal Anisotropy: Geophysical Society of Houston Webinar series.
- Nissen, S. E., T. R. Carr, K. J. Marfurt, and E. C. Sullivan, 2009, Using 3-D seismic volumetric curvature attributes to identify fracture trends in a depleted Mississippian carbonate reservoir: implications for assessing candidates for CO<sub>2</sub> sequestration, *in* M. Grobe, J. C. Pashin, and R. L. Dodge, eds., Carbon dioxide sequestration in geological media—State of the science: AAPG Studies in Geology 59, p. 297–319.
- Rogers, J. P., and M. W. Longman, 2001, An introduction to chert reservoirs of North America, 2001, AAPG Bulletin, v. 85, no.1, p. 1-5.
- Rubinstein, J.L., A.B. Mahani, 2015, Myths and Facts on Wastewater Injection, Hydraulic Fracturing, Enhanced Oil Recovery, and Induced Seismicity. *Seismological Research Letters*. **86**. 1060-1067.
- Ruger, A., 1998, Variation of P-wave reflectivity with offset and azimuth in anisotropic media: Geophysics, v. 63, no. 3, p 935-947.
- Schwab, A., 2016, Characterizing the potential for fault reactivation related to fluid injection through subsurface structural mapping and stress field analysis, Wellington Field, Sumner County, KS: M.S. thesis, University of Kansas.
- Sirazhiev, A., 2012, Seismic Attribute Analysis of the Mississippian Chert at the Wellington Field, south-central Kansas. University of Kansas master's thesis.

- Thomsen, L., 2002, Understanding seismic anisotropy in exploration and exploitation: SEG/EAGE Distinguished instructor short course and text
- Vega, S., K. Berteussen, Y. F. Sun, and A. A. Sultan, 2007, Is Gassmann the best model for fluid substitution in heterogeneous carbonates: 77th Annual International Meeting, SEG, Expanded Abstract, p.1575-1578
- Watney, W. L., W. J. Guy, and A. P. Byrnes, 2001, Characterization of the Mississippian chat in south-central Kansas: AAPG Bulletin, v. 85, no.1, p. 85-113.
- F.R. Walsh, M.D. Zoback, 2015, Oklahoma's recent earthquakes and saltwater disposal. *Science Advances*. **1**. e1500195
- W.L. Yeck, M. Weingarten, H.M. Benz, D.E. McNamara, E.A. Bergman, R.B. Herrman, J.L. Rubinstein, P.S. Earle, 2016, Far-field pressurization likely caused one of the largest injection induced earthquakes by reactivating a large preexisting basement fault structure. *Geophysical Research Letters*. **43**.
- J.C. Zinke, M.D. Zoback, 2000, Structure-related and stress-induced shear-wave velocity anisotropy: observations from microearthquakes near the Calaveras fault in central California. *Bulletin of the Seismological Society of America*. **90**. 1305-1312.

## Appendices

### Appendix A - Relative Permeability Curves in the Arbuckle

#### Introduction

Relative permeability curves play major roles in simulation for the following reasons: 1) Distribution and residual trapping of CO<sub>2</sub> are dependent on drainage relative permeability curves and, in addition, imbibition curves and hysteresis play important roles in calculating the residual CO<sub>2</sub> that can be permanently immobilized in the subsurface (Krevor et al., 2012). 2) Accurate characterization of relative permeability is important to determine the correct injectivity and, therefore, to minimize the number of injectors for more efficient injection rates and injection volume (Krevor et al., 2012).

There have been some studies, including laboratory experiments, of relative permeability in CO<sub>2</sub>-brine systems for different samples in carbonate and sandstone reservoirs (e.g., Bennion and Bachu, 2008; Krevor et al., 2012). However, most and very likely all of the experimental studies do not represent the actual maximum CO<sub>2</sub> relative permeability ( $KrCO_{2max}$ ) and the maximum CO<sub>2</sub> saturation ( $SCO_{2max}$ ) correctly. In Bennion and Bachu (2005, 2008) studies, maximum measured relative permeability ( $KrCO_{2max}$ ) is 0.54 and more often samples with higher absolute permeability have lower  $KrCO_{2max}$  than samples with lower absolute permeability. Often there is no consistency in  $KrCO_{2max}$  measurements achieved in the laboratory experiments and inconsistency in maximum CO<sub>2</sub> saturation ( $SCO_{2max}$ ) and Corey exponents can be seen. Krevor et al. (2012) and Benson et al. (2015) showed that maximum experimental CO<sub>2</sub> saturations ( $SCO_{2max}$ ) and  $KrCO_{2max}$  are limited by the capillary pressure (CO<sub>2</sub> pressures) that can be achieved in the experiment and therefore their values are always lower than the actual. Because of the unattainable high capillary pressure during the experiments when 100% CO<sub>2</sub> is injected, irreducible water saturation cannot be achieved and, therefore, measured  $KrCO_{2max}$ , CO<sub>2</sub> Corey exponents are inferior.

Another issue is that CO<sub>2</sub>-brine relative permeability lab measurements are expensive to run and limited to few samples. Moreover, relative permeability curves vary with different samples and so one set of relative permeability curves cannot represent relative permeability for all rock types in a reservoir. Different sets of relative permeability curves are needed for different samples. In this work, different relative permeabilities were calculated for different Reservoir Quality Index (RQI) ranges, which are more representative and realistic and specific to the Arbuckle reservoir. Drainage and imbibition relative permeability curves were calculated for a CO<sub>2</sub>-brine system based on a water-wet system in the Arbuckle. Nine drainage and nine imbibition curves were calculated for nine rock types based on RQI.

## I. Drainage Relative Permeability Curves

Nine drainage relative permeability curves were calculated using the equations below (previously patented formula: SMH reference No: 1002061-0002):

$$KrCO_2 = krCO_{2max}(1 - Sw_N)^p \quad (\text{Equation 1})$$

$$Krw = krw_{max} * (Sw_N)^q \quad (\text{Equation 2})$$

$$Sw_N = \frac{(Sw - Swir)}{(1 - Swir)} \quad (\text{Equation 3})$$

$$Krw_{max} = 1 \quad (\text{Equation 4})$$

$$KrCO_{2max} = 0.67 RQI^{0.0194} \quad (\text{Equation 5})$$

Where,

KrCO<sub>2</sub> is relative permeability to CO<sub>2</sub>

Krw is relative permeability to water

KrCO<sub>2max</sub> is maximum CO<sub>2</sub> relative permeability

Krw<sub>max</sub> is maximum water relative permeability

Sw<sub>N</sub> is normalized water saturation

P is CO<sub>2</sub> Corey exponent

q is water Corey exponent

Swir is irreducible water saturation

### Irreducible Water Saturation (Swir)

Swir was read at Pc equal 300 psi from the previously calculated drainage Pc curves (fig. 1). Pc curves were derived from NMR log based on CO<sub>2</sub>-brine interfacial tension (IFT). Interfacial tension of 32 dyne/cm was calculated in CO<sub>2</sub>-brine system based on correlations between IFT with salinity, temperature, and pressure (Bennion and Bachu, 2008). There are nine Pc curves, one for each of the nine RQI ranges; therefore, nine Swir values were obtained (fig. 1).

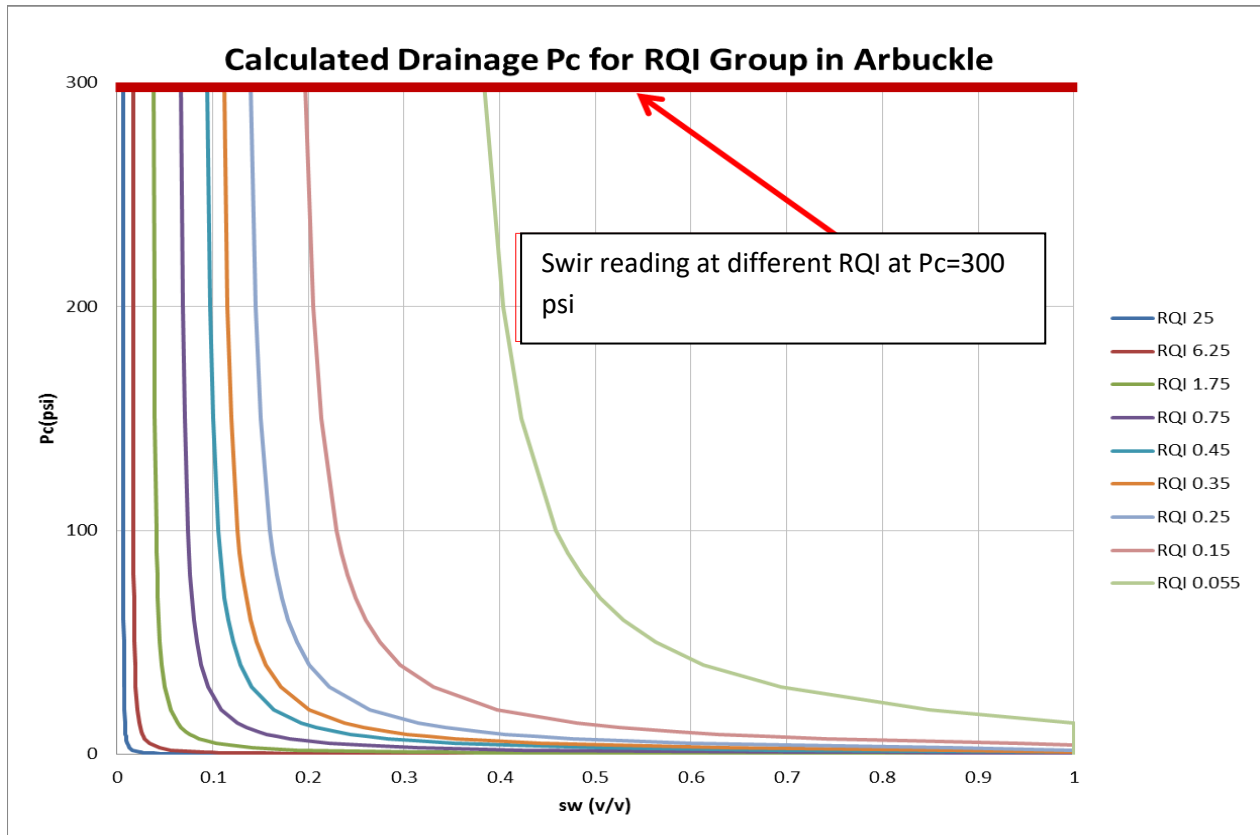


**Figure 1: Drainage capillary pressure curves for CO<sub>2</sub>-brine system in the Arbuckle.**

### **Corey Exponent for CO<sub>2</sub> (p)**

Literature experimental studies, including Bennion and Bachu (2005), were reviewed as discussed in the introduction of this report and, often, results indicated no consistency in Corey exponents for different permeabilities. Higher permeabilities should have higher Corey exponents than lower permeabilities, but often that was not the case. Some results also showed lower permeabilities with higher Corey exponents than the higher permeabilities. For the purpose of this work, highest and lowest Corey exponent values from Bennion and Bachu (2010) were selected for highest and lowest RQI. They were assigned to the nine RQI in descending order as indicated in table 1.

### **Corey Exponent for Brine (p)**

Corey exponents for brine for different permeability do not have great variability and they range from 1.2 to 2.9. Therefore, the average Corey exponent of 1.91 was considered representative for all 9 RQI, Table 1.

Table 1: Values for Drainage Relative Permeability Curves									
RQI	25	6.25	1.75	0.75	0.45	0.35	0.25	0.15	0.055
Swir	0.007	0.017	0.038	0.067	0.095	0.112	0.140	0.197	0.384
CO2 Corey ex	4.5	4.35	4.2	4.05	3.9	3.75	3.6	3.45	3.3
Water Corey ex	1.91	1.91	1.91	1.91	1.91	1.91	1.91	1.91	1.91

## Maximum Relative Permeability of CO2 and Water ( $K_{rCO_2max}$ and $K_{rwmax}$ )

The maximum water relative permeability ( $K_{rwmax}$ ) in the drainage case is always unity. Therefore, a value of 1 was used for  $K_{rwmax}$  in equation 2.

Benson et al. (2015) pointed out that laboratory relative permeability measurements have limitations due to laboratory capillary pressures that can be achieved in the core measurements during experiments. Measured  $K_{rCO_2max}$  values in labs are always lower than actual values. Moreover, the same paper noted that measured  $K_{rCO_2max}$  should be scaled up in the dynamic model. Maximum achieved  $K_{rCO_2max}$  in most and possibly all laboratory studies is 0.54, which is lower than actual values in reservoirs. A formula was designed that can give more reasonable  $K_{rCO_2max}$  for each RQI in the reservoir, equation 5. Calculated  $K_{rCO_2max}$  using equation 4 for maximum RQI (20) is 0.71, which is more realistic than the literature results.

## Drainage Relative Permeability for CO<sub>2</sub>-Brine

Equations 1 and 2 were used to calculate CO<sub>2</sub> and brine relative permeability curves, respectively. All parameters are listed in table 1. Nine drainage relative permeability curves were calculated for nine rock types based on RQI (figs. 2–10).

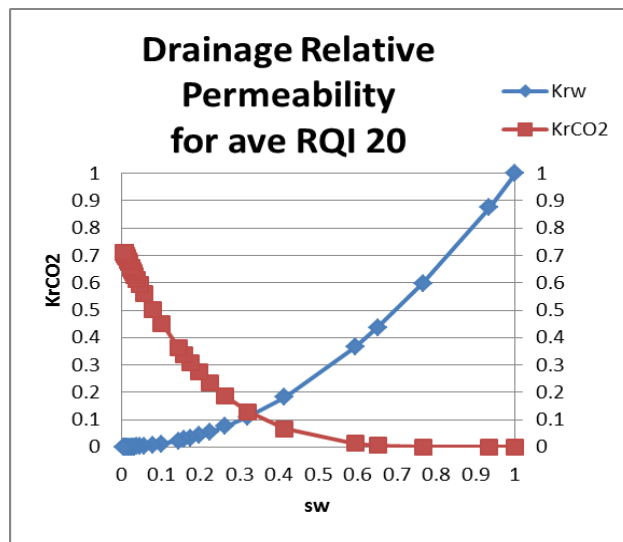


Figure 2: Drainage relative permeability for RQI 20. permeability for RQI 6.25.

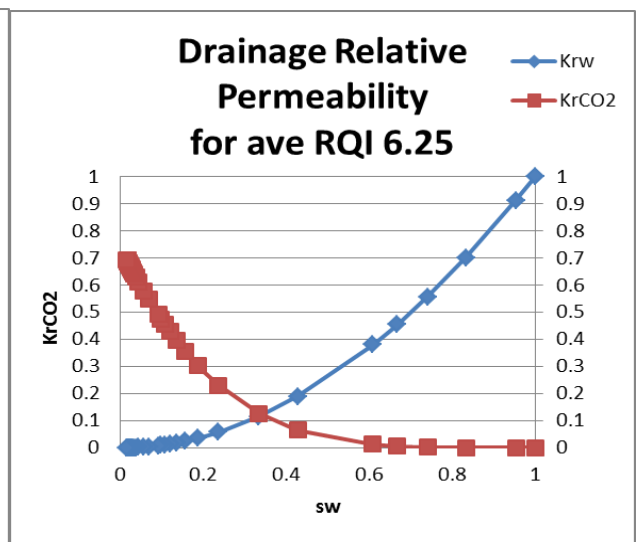


Figure 3: Drainage relative permeability for RQI 6.25.

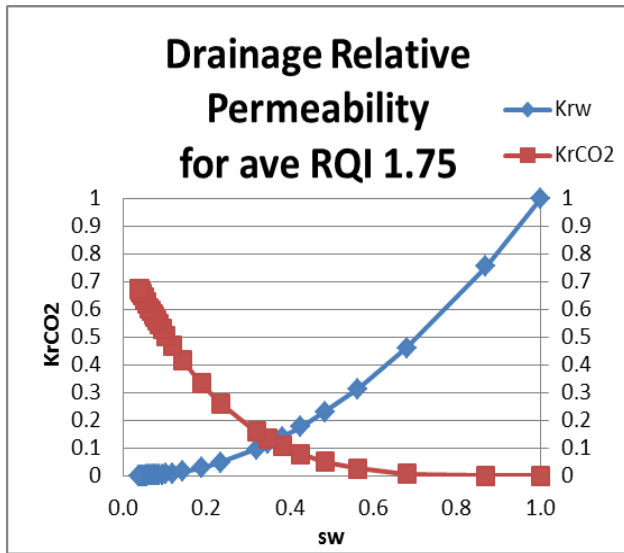


Figure 4: Drainage relative permeability for RQI 1.75.

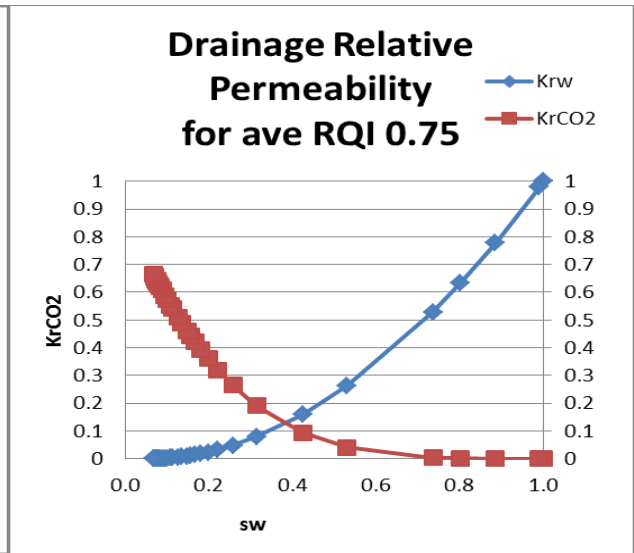


Figure 5: Drainage relative permeability for RQI 0.75.

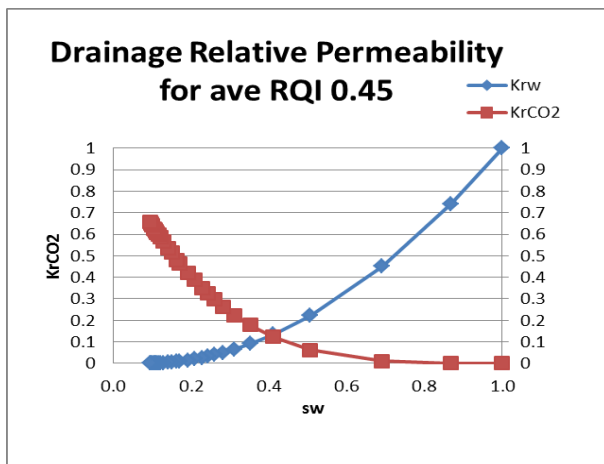


Figure 6: Drainage relative permeability for RQI 0.45.

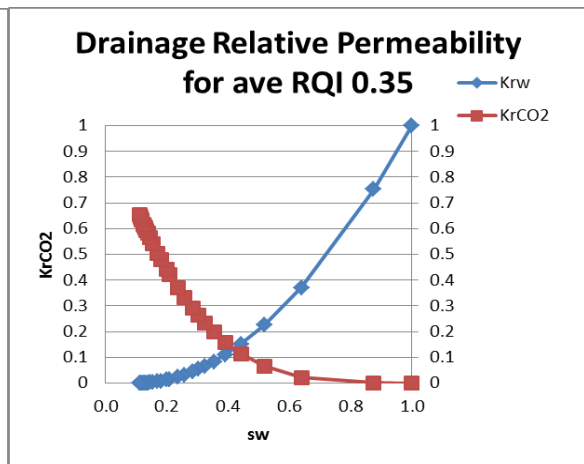


Figure 7: Drainage relative permeability for RQI 0.35.

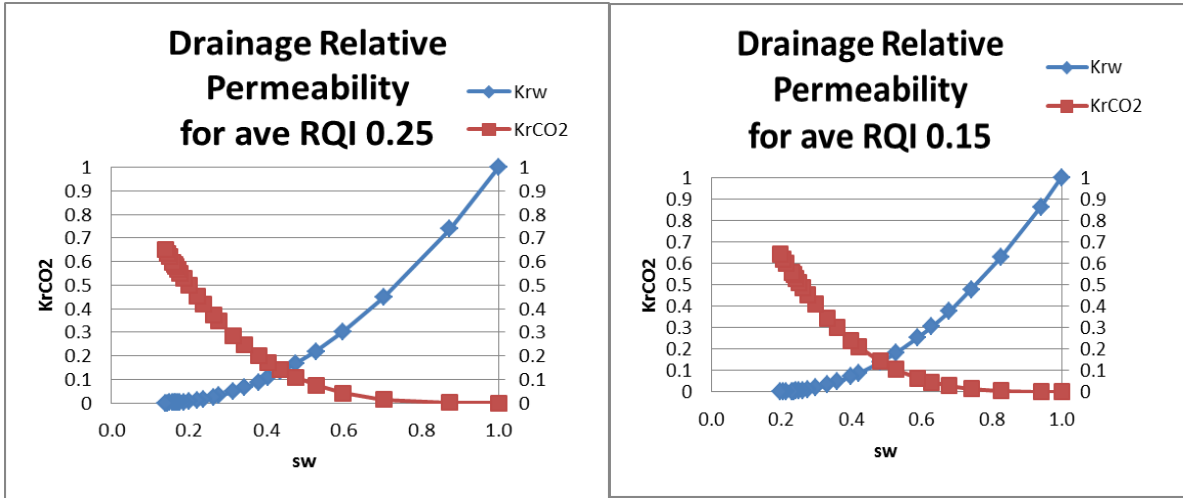


Figure 8: Drainage relative permeability for RQI 0.25.

Figure 9: Drainage relative permeability for RQI 0.15.

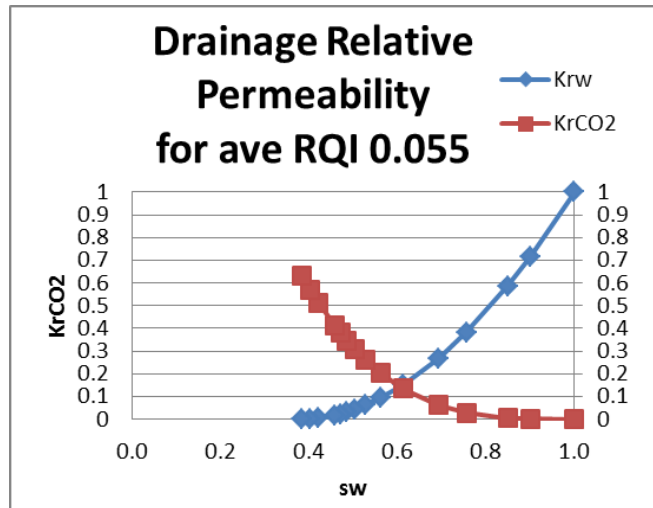


Figure 10: Drainage relative permeability for RQI 0.55.

## II. Imbibition Relative Permeability Curves

After the drainage phase, CO<sub>2</sub> migrates to the top of formation and part of CO<sub>2</sub> is replaced by water in the pore space. In this phase, imbibition relative permeability curves determine fluid flow and the amount of CO<sub>2</sub> that is trapped in the pore space as residual CO<sub>2</sub> saturation. Nine imbibition relative permeability curves were calculated using the equations below (previously patented formula):

$$KrCO_2 = krCO_{2max}(1 - Sw_N)^p \quad \text{(Equation 6)}$$

$$Krw = krw_{max} * (Sw_N)^q \quad \text{(Equation 7)}$$

$$Sw_N = \frac{(Sw - Sw_{ir})}{(1 - SCO_{2r} - Sw_{ir})} \quad \text{(Equation 8)}$$

$$Kr_{w_{max}} = 0.23RQI^{-0.348} \quad (\text{Equation 9})$$

$$Kr_{CO2_{max}} = 0.67 RQI^{0.0194} \quad (\text{Equation 10})$$

Where,

$Kr_{CO_2}$  is relative permeability to  $CO_2$

$Kr_w$  is relative permeability to water

$Kr_{CO_{2max}}$  is maximum  $CO_2$  relative permeability

$Kr_{w_{max}}$  is maximum water relative permeability

$SW_N$  is normalized water saturation

$P$  is  $CO_2$  Corey exponent

$q$  is water Corey exponent

$Sw_{ir}$  is irreducible water saturation

$SCO_r$  is residual  $CO_2$  saturation

### **Irreducible Water Saturation ( $Sw_{ir}$ )**

Irreducible water saturation was read from the plot of previously calculated imbibition  $P_c$  curves at  $P_c$  equal 300 psi. There are nine  $P_c$  curves, one for each of the nine RQI ranges; therefore, nine  $Sw_{ir}$  values were used. The values are listed in table 2.

### **Residual $CO_2$ Saturation ( $SCO_{2r}$ )**

Residual  $CO_2$  saturation ( $SCO_{2r}$ ) was calculated based on a correlation (Burnside and Naylor, 2014) between residual  $CO_2$  saturation ( $SCO_{2r}$ ) and initial  $CO_2$  saturation ( $SCO_{2i}$ ) (fig. 11). This correlation is based on samples from carbonate Nisku formation.  $CO_{2i}$  is one minus  $Sw_{ir}$  (table 2).

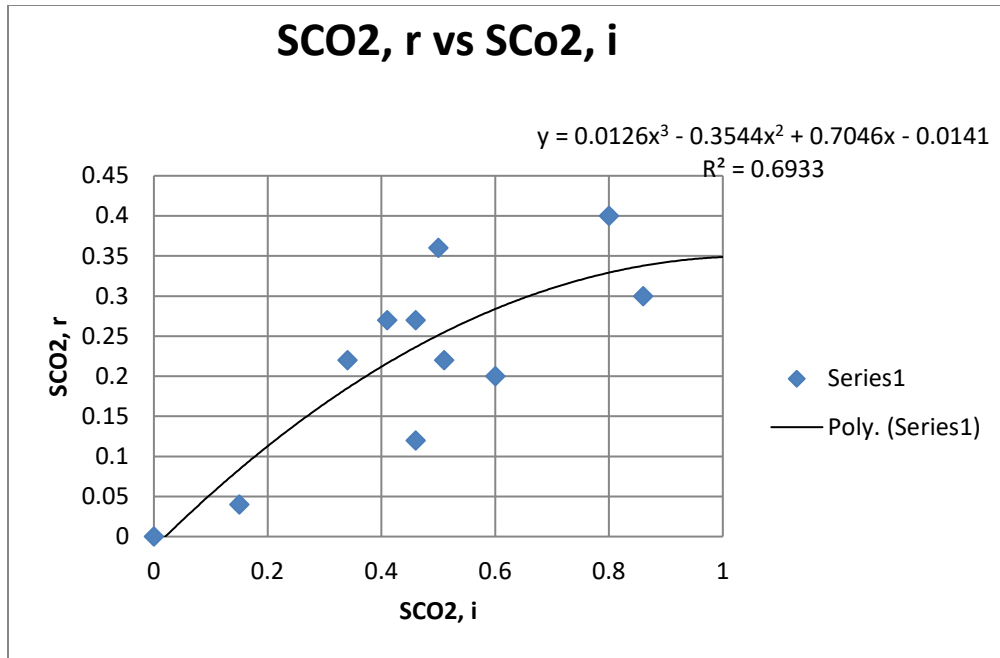


Figure 11: Residual CO<sub>2</sub> saturation versus initial CO<sub>2</sub> saturation.

### Corey Exponent for CO<sub>2</sub> (p) and Corey Exponent for Brine (p)

Corey exponent values for CO<sub>2</sub> from literature (e.g., Bennion and Bachu, 2008, 2010) imbibition curves range from 2.9 to 2.1. Corey exponents were assigned in descending order, with the highest Corey exponent (2.9) assigned to the highest RQI value (20) and the lowest Corey exponent (2.1) assigned to the lowest RQI value (0.055).

Corey exponents for brine for different permeabilities don't have great variations, ranging from 1.2 to 4.5. Therefore, an average Corey exponent of 3 was considered for all nine RQI ranges.

	25	6.25	1.75	0.75	0.45	0.35	0.25	0.15	0.055
RQI	25	6.25	1.75	0.75	0.45	0.35	0.25	0.15	0.055
Swir @ Pc=300 psi	0.007	0.017	0.038	0.066	0.092	0.109	0.136	0.190	0.371
S <sub>co2,i</sub>	0.993	0.983	0.962	0.934	0.908	0.891	0.864	0.810	0.629
S <sub>co2,r</sub>	0.348	0.348	0.347	0.345	0.343	0.341	0.338	0.331	0.292
CO2 Corey ex	2.9	2.8	2.7	2.6	2.5	2.4	2.3	2.2	2.1
Water Corey ex	3	3	3	3	3	3	3	3	3

### Maximum Relative Permeability of CO<sub>2</sub> and Water (KrCO<sub>2max</sub> and Krw<sub>max</sub>)

Maximum water relative permeability (Krw<sub>max</sub>) in the imbibition case was calculated using equation 9. The previous section mentioned that laboratory relative permeability measurements

have limitations due to the low laboratory capillary pressures that can be achieved in the core measurements during experiments. Therefore, measured  $KrCO_{2max}$  values in labs are always lower than actual values in reservoirs. Maximum achieved  $KrCO_2$  in most and possibly all laboratory studies is 0.54, which is lower than the actual maximum value in reservoirs. Equation 10, which is the same formula used in the drainage case, was used to calculate  $KrCO_{2max}$ . Calculated  $KrCO_{2max}$  for maximum RQI (20) is 0.71, which is the same as the drainage case.

### Imbibition Relative Permeability for CO<sub>2</sub>-Brine

Equations 6 and 7 were used to calculate CO<sub>2</sub> and brine relative permeability curves, respectively. All parameters are listed in table 2. Nine sets of imbibition relative permeability curves were calculated for nine rock types based on RQI (figs. 12–20).

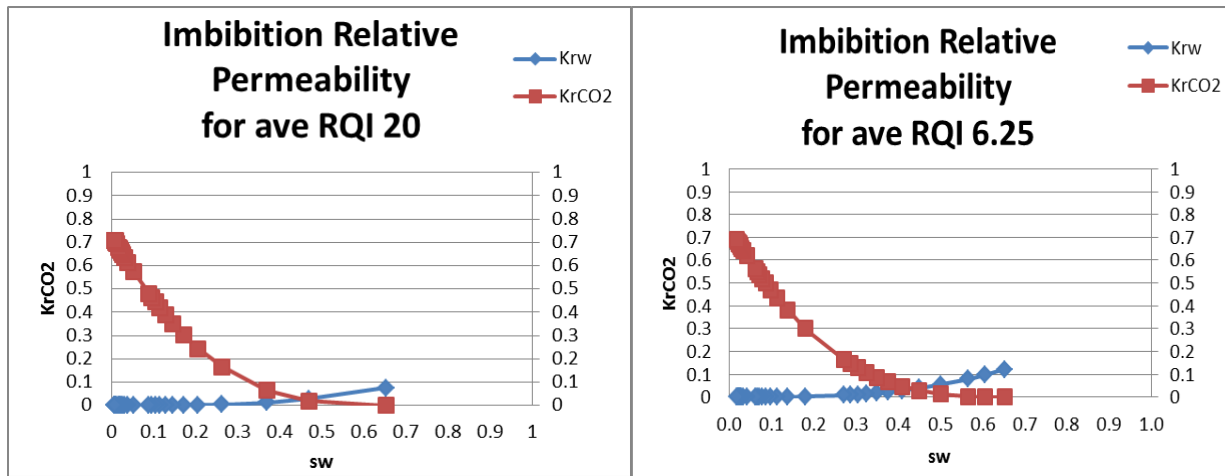


Figure 12: Imbibition relative permeability for RQI 20.

Figure 13: Imbibition relative permeability for RQI 6.25.

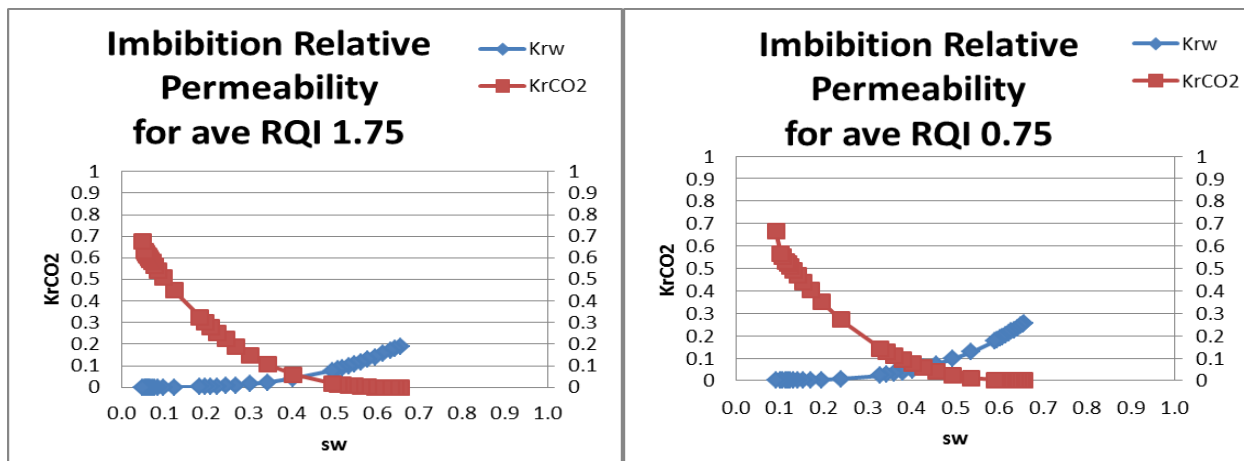


Figure 14: Imbibition relative permeability for RQI 1.75.

Figure 15: Imbibition relative permeability for RQI 0.75.

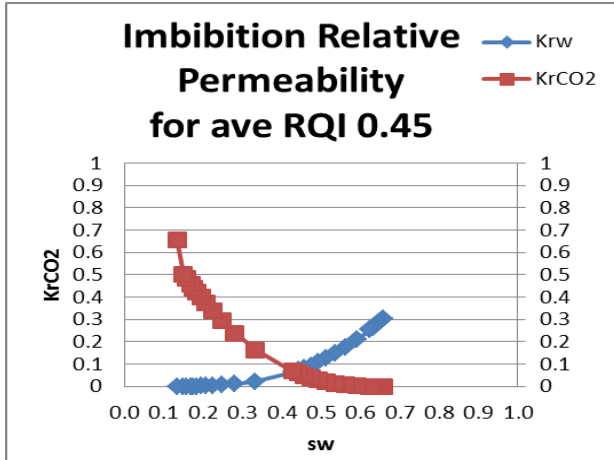


Figure 16: Imbibition relative permeability for RQI 0.45.

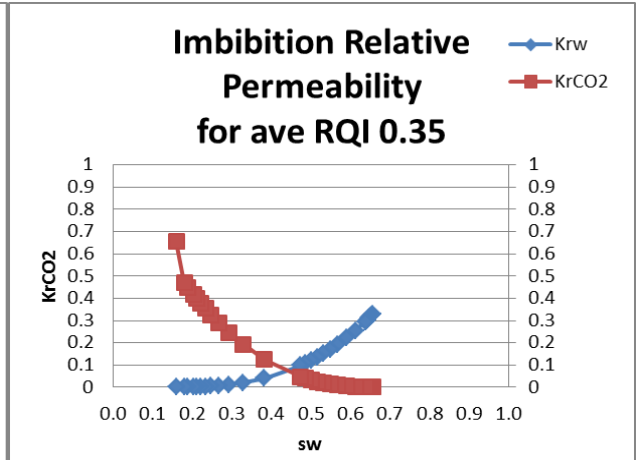


Figure 17: Imbibition relative permeability for RQI 0.35.

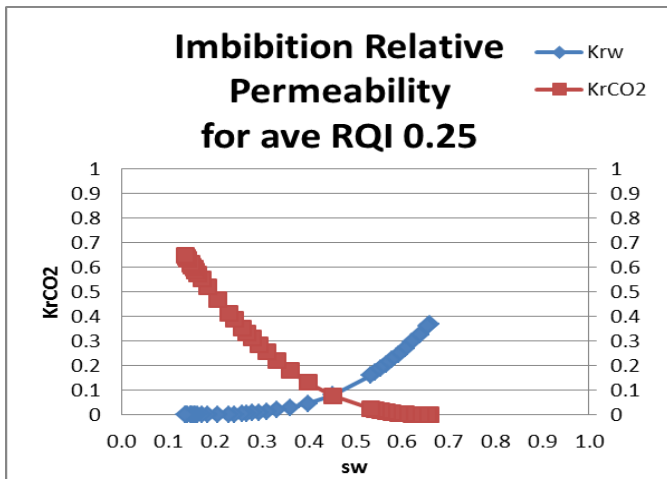


Figure 18: Imbibition relative permeability for RQI 0.25.

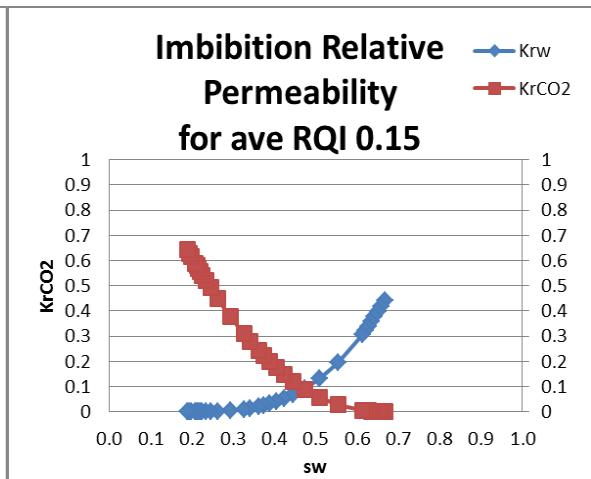
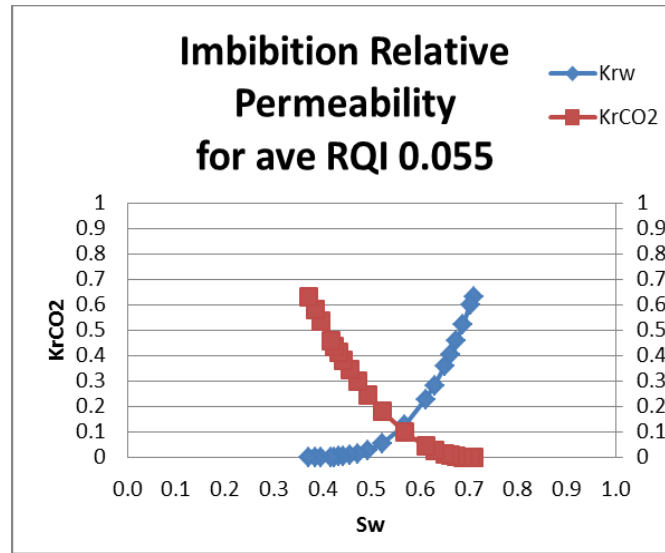


Figure 19: Imbibition relative permeability for RQI 0.15.



**Figure 20: Imbibition relative permeability for RQI 0.055.**

## Conclusion

This work resulted in more realistic relative permeability curves for drainage and imbibition cases in CO<sub>2</sub>-brine systems than the laboratory results from literature. As pointed out, relative permeability results reported in literature do not represent the endpoints of relative permeability curves and need to be scaled up. In this study, Kr max for CO<sub>2</sub> and max CO<sub>2</sub> saturations were increased to reasonable values. These curves will determine CO<sub>2</sub> injection capacity of injection wells more accurately and more realistically than the published curves. In addition, they result in more accurate residual CO<sub>2</sub> that can be trapped as an immobilized phase in the formation. Also, in this work, Corey exponents have consistency with increasing RQIs. Higher RQI values have higher Corey exponents and lower RQIs have lower Corey exponents.

## References

- Bennion, B., and Bachu, S., 2005, Relative permeability characteristics for supercritical CO<sub>2</sub> displacing water in a variety of potential sequestration zones: Society of Petroleum Engineers, doi:10.2118/95547-MS.
- Bennion, B., and Bachu, S., 2008, Drainage and imbibition relative permeability relationships for supercritical CO<sub>2</sub>/brine and H<sub>2</sub>S/brine systems in intergranular sandstone, carbonate, shale, and anhydrite rocks: Society of Petroleum Engineers, doi:10.2118/99326-PA.
- Bennion, D. B., and Bachu, S., 2010, Drainage and imbibition CO<sub>2</sub>/brine relative permeability curves at reservoir conditions for high-permeability carbonate rocks: Society of Petroleum Engineers, doi:10.2118/134028-MS.
- Benson, S. M., Hingerl, F., Zuo, L., Pini, R., Krevor, S., Reynolds, C., Niu, B., Calvo, R., and Niemi, A., 2015, Relative permeability for multi-phase flow in CO<sub>2</sub> storage reservoirs: Global CCS Institute, Stanford University.

Burnside, N. M., and Naylor, M., 2014, Review and implications of relative permeability of CO<sub>2</sub>/brine systems and residual trapping of CO<sub>2</sub>: [International Journal of Greenhouse Gas Control](#), 23, p. 1–11, doi:[10.1016/j.ijggc.2014.01.013](#).

Krevor, S. C. M., Pini, R., Zuo, L., and Benson, S. M., 2012, Relative permeability and trapping of CO<sub>2</sub> and water in sandstone rocks at reservoir conditions: [Water Resources Research](#), 48, W02532, doi:[10.1029/2011WR010859](#).

## APPENDIX A-2. Techlog layouts

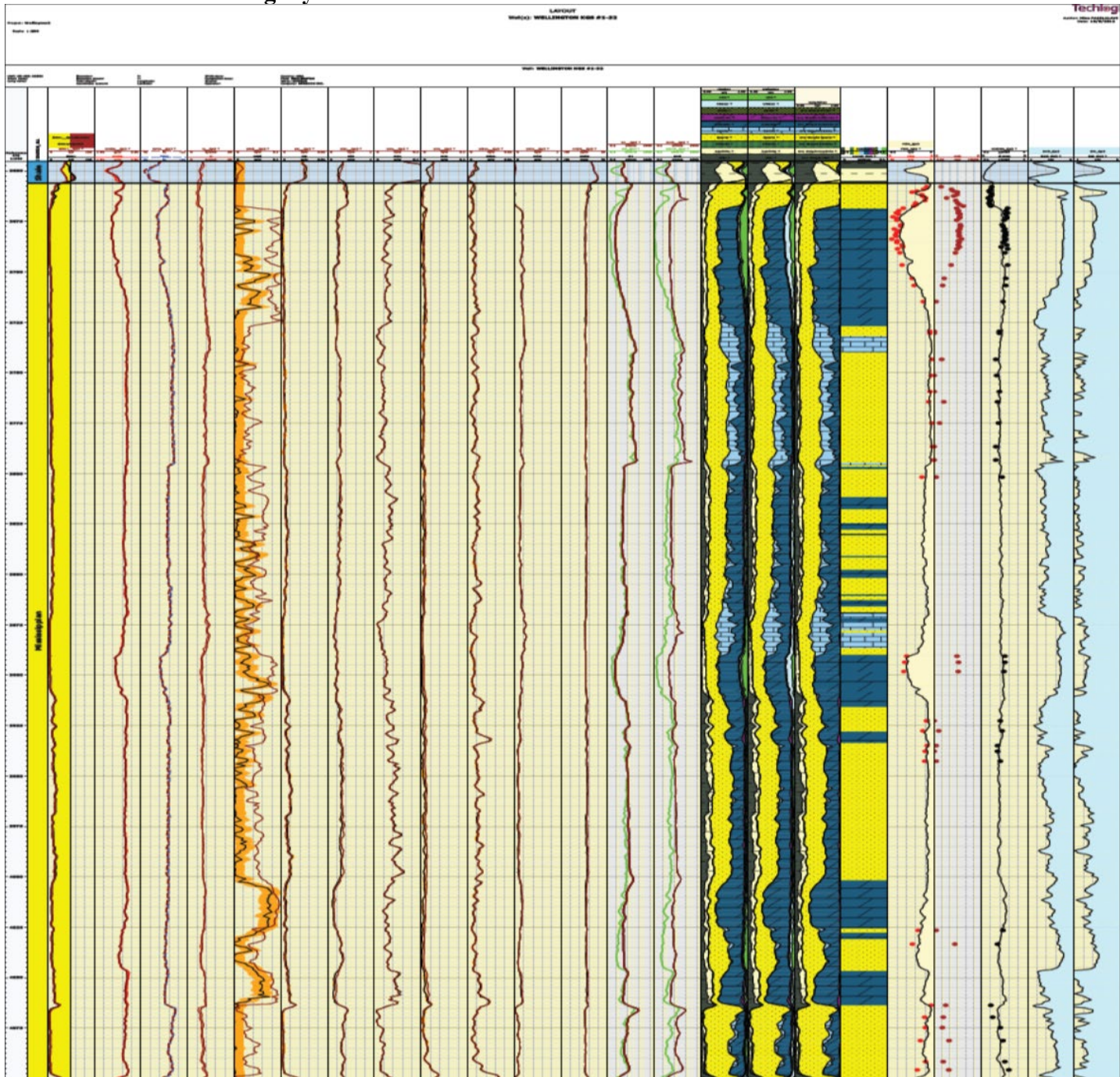


Figure A-1 : Well 1-32 layout—geochemical and conventional log analyzed by Techlog

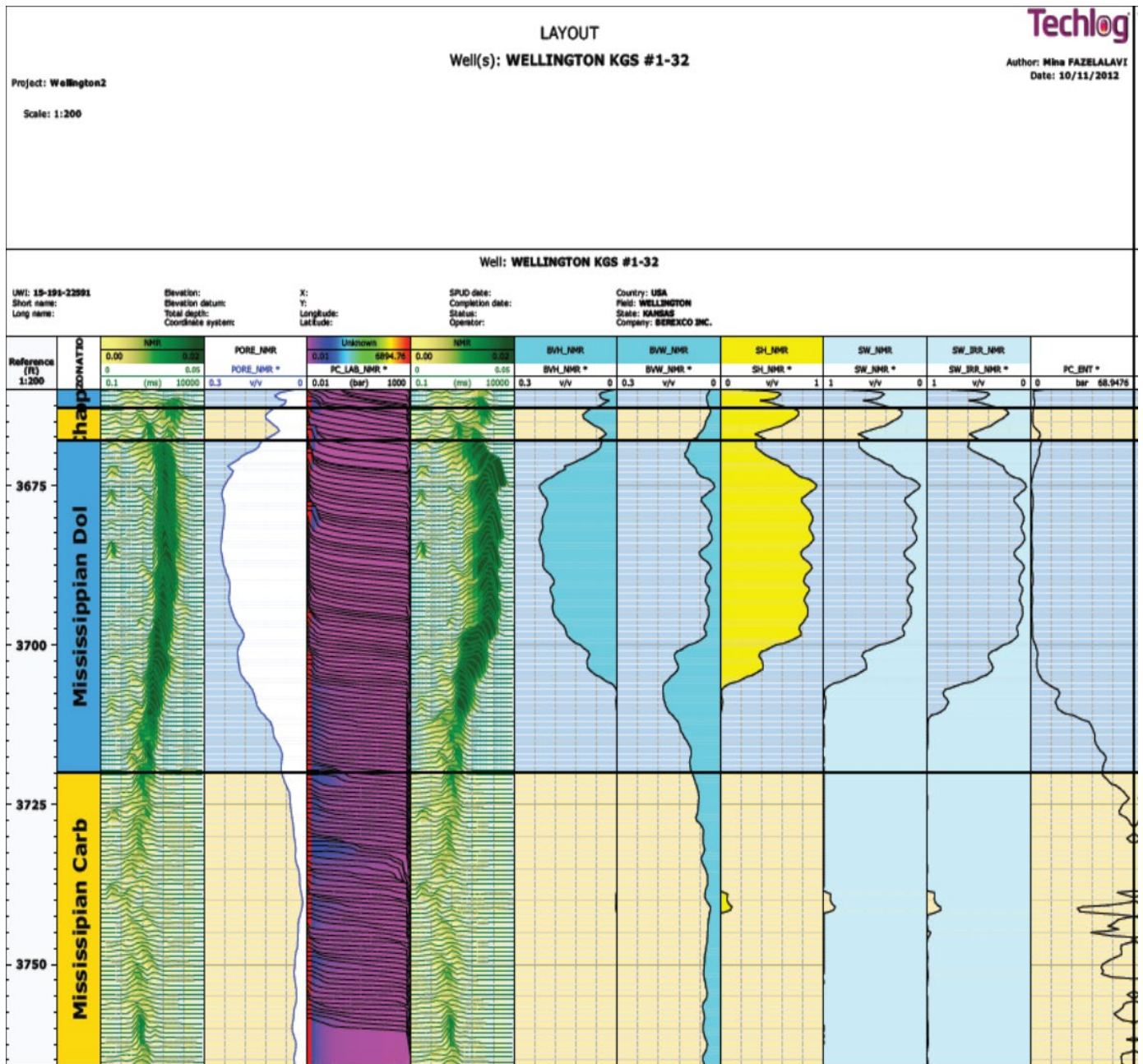
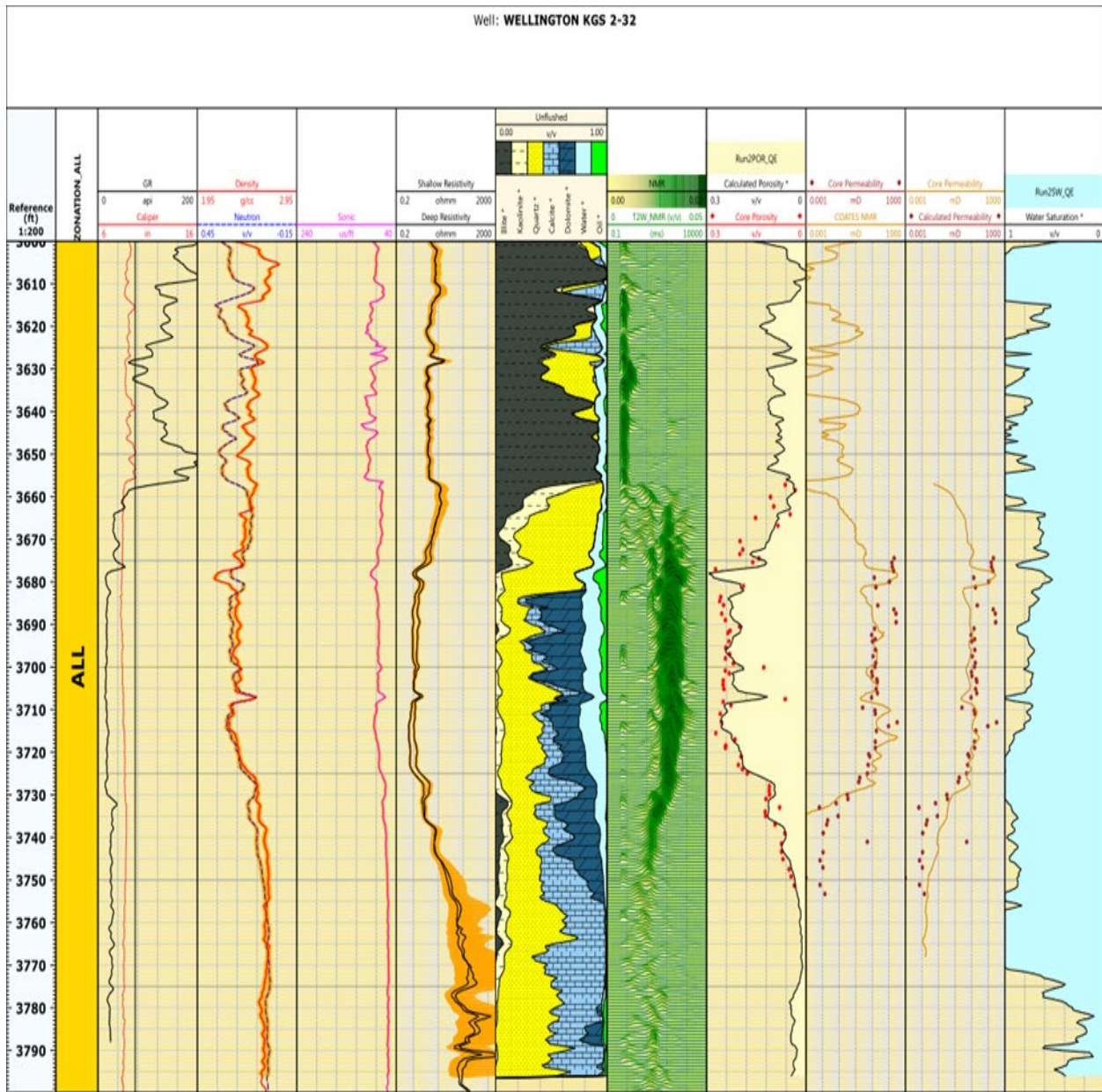


Figure A-2: Well 1-32 layout—Porosity, Pc, Swi and Swirr at Pc\_irr equal 20 bar



**Figure A-3:** Well 2-32 showing permeability by FZI-SWPHI and Coates compared to core. The second column on the right compares permeability by FZI-SWPHI and Coates permeability with core permeability on the third track from right

# LAYOUT

Well(s): **WELLINGTON KGS #1-32** Author: **Mina FAZELALAVI**

Date: **11/7/2012**

Project: **Wellington2**

Scale: **1:100**

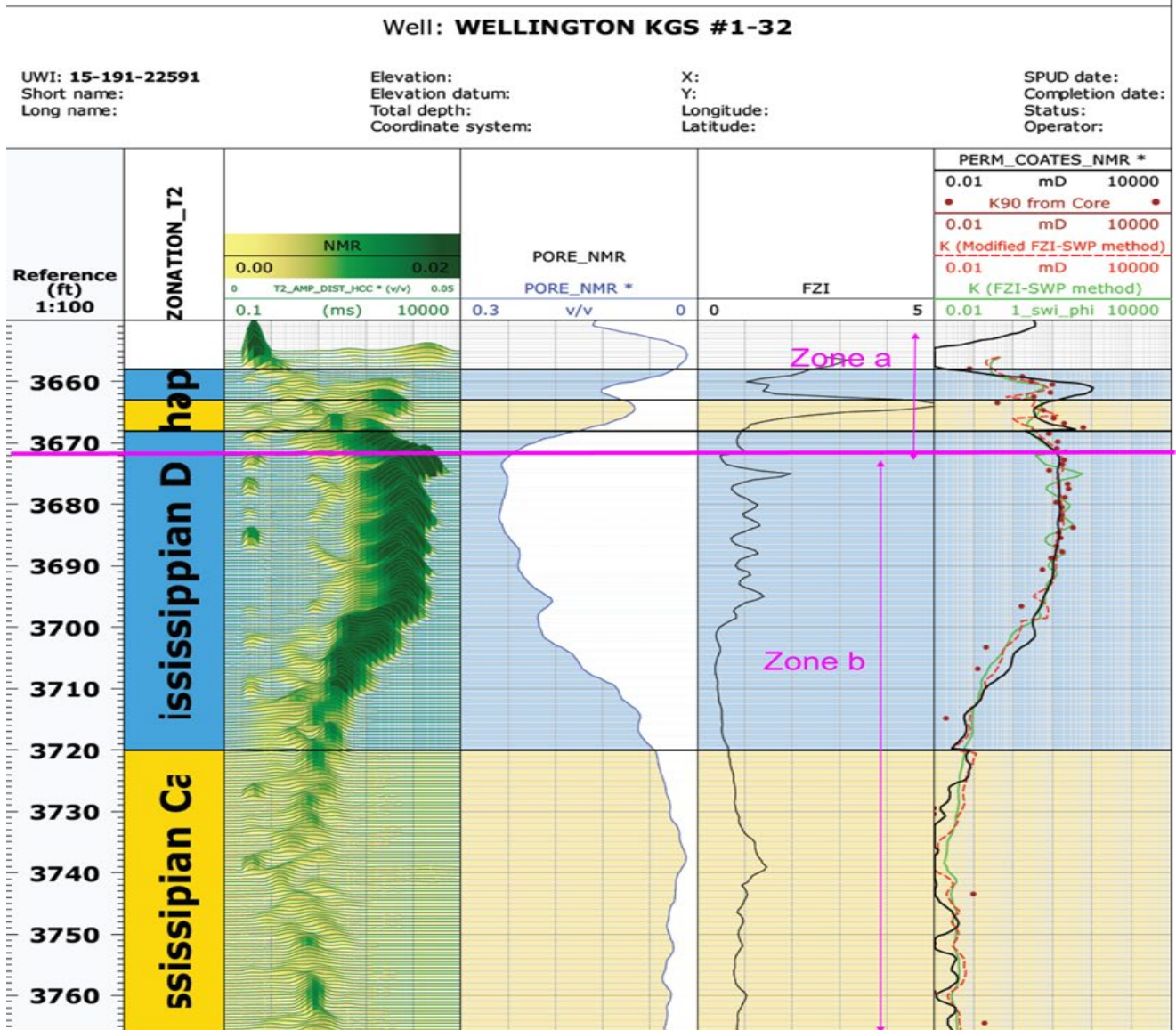


Figure A-4: Well 1-32 showing zone a and b. The first column on the right compares Coates permeability and permeability from FZI-SWP with core permeability

Well: WELLINGTON KGS #1-32

Longitude:  
Latitude:

SPUD date:  
Completion date:  
Status:  
Operator:

Country: USA  
Field: WELLINGTON  
State: KANSAS  
Company: BEREXCO INC.

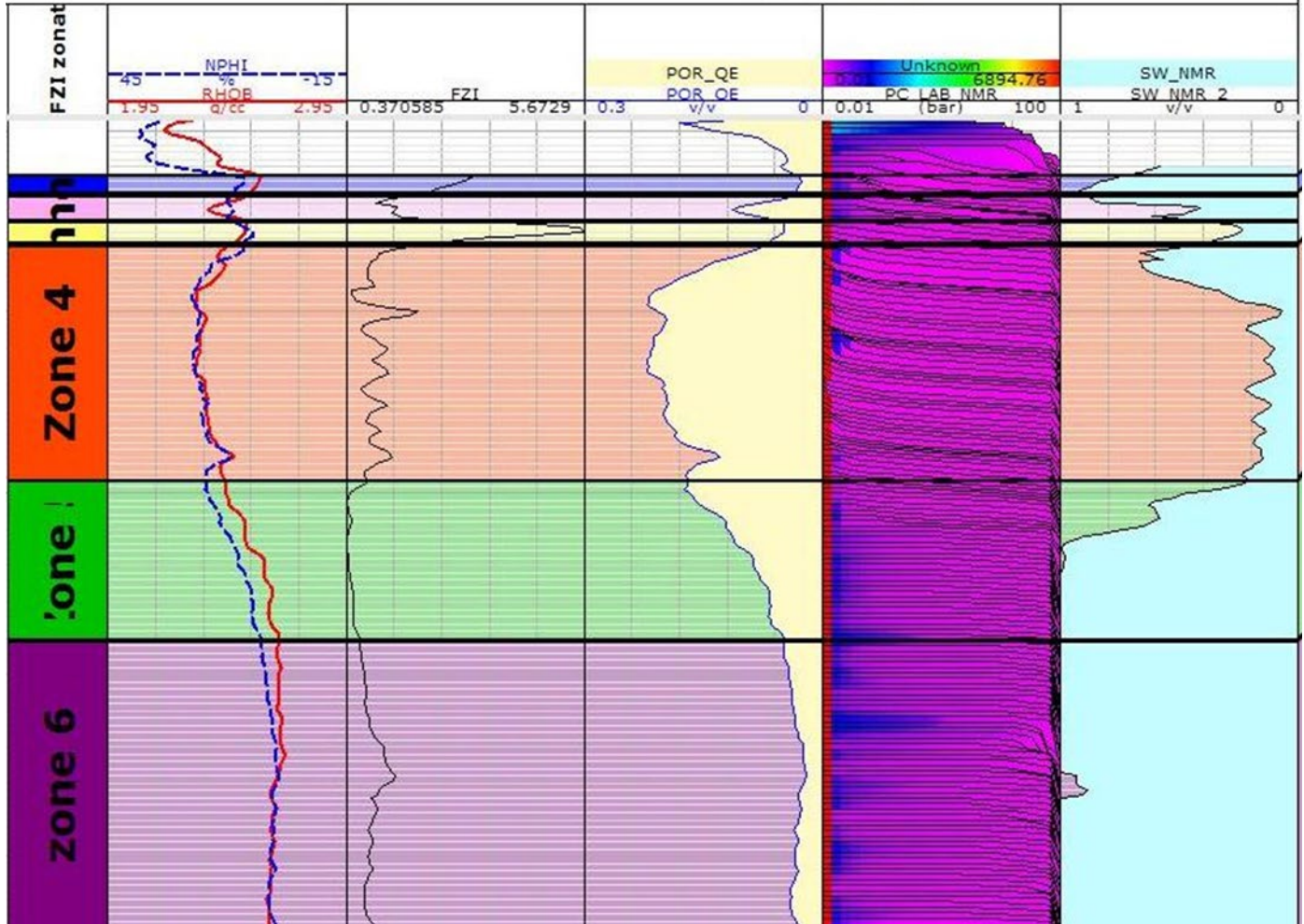


Figure A-5: Well 1-32 layout showing six zones based on similar FZI variation in each zone

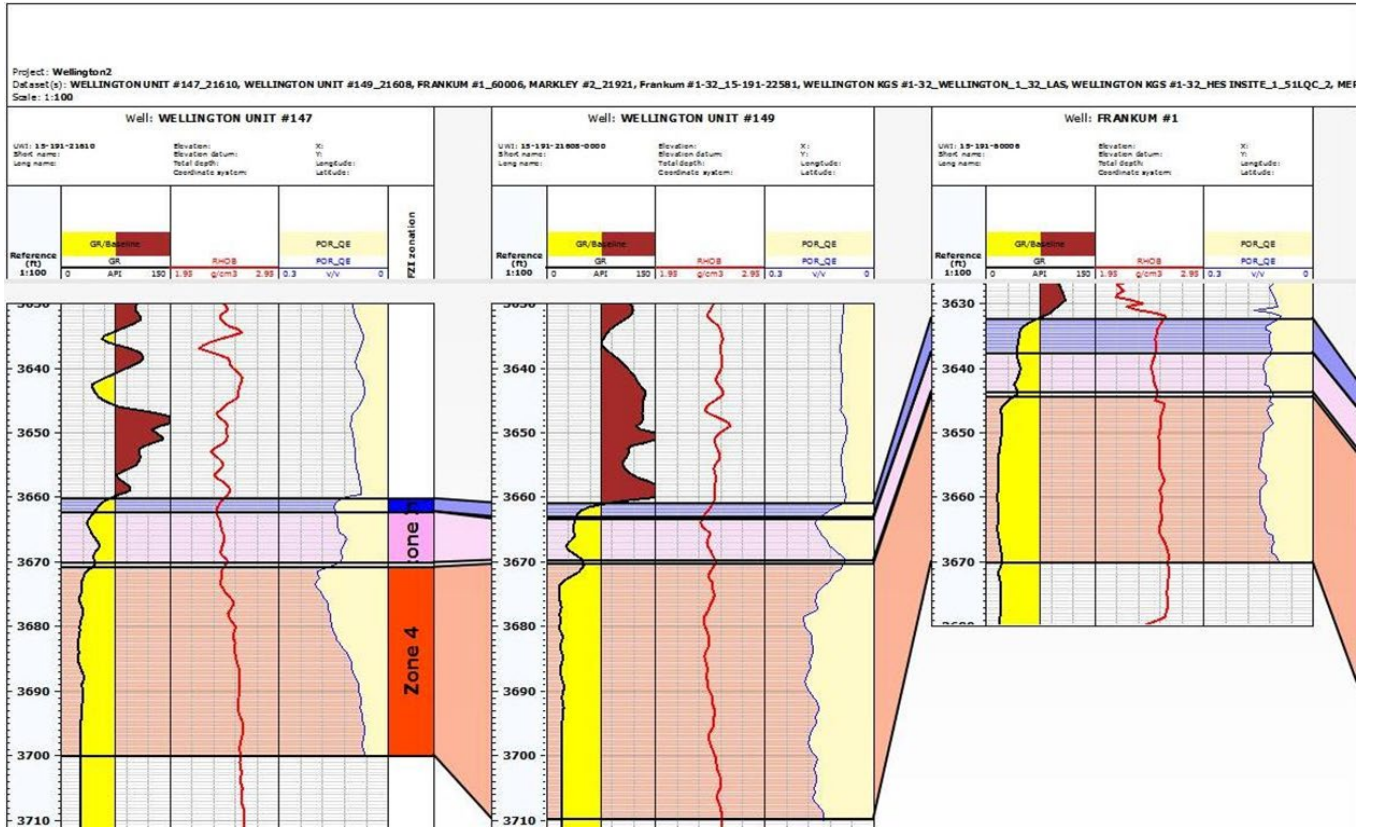


Figure A-6: Equivalent zones in wells 147, 149, and Frankum#1 with equal FZI values corresponding to the six zones of Well 1-32

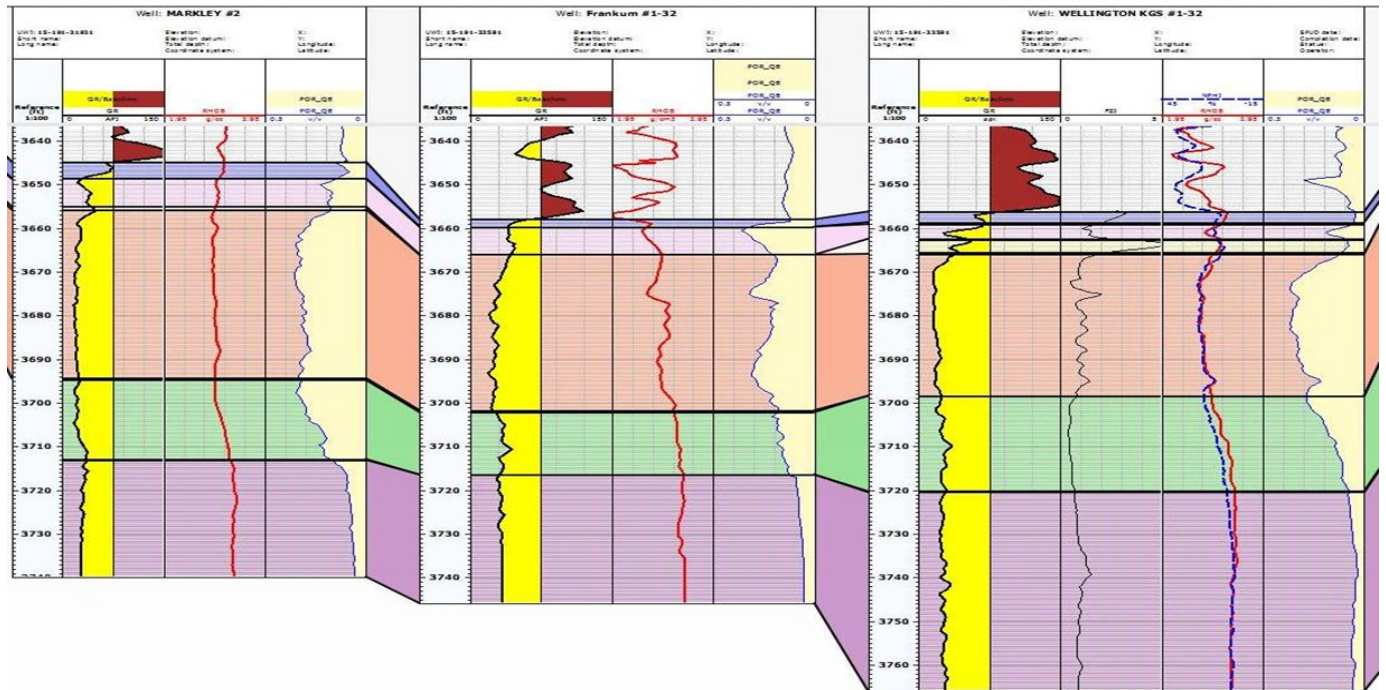


Figure A-7: Equivalent zones in wells Markley#2 and Frankum#1-32 with equal FZI values corresponding to the six zones of Well 1-32

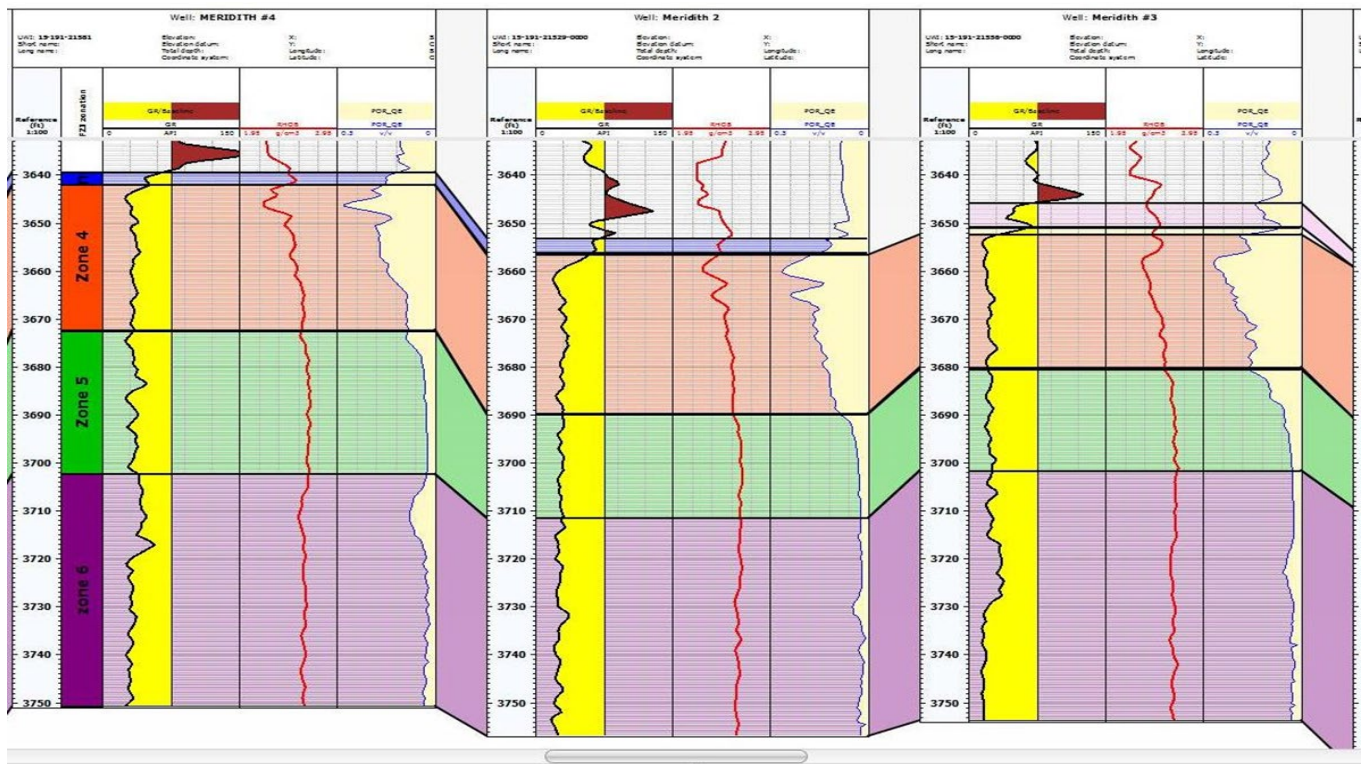


Figure A-8: Figure A 7: Equivalent zones in wells Meridith#4, Meridith2, and Meridith3 with equal FZI values corresponding to the six zones of Well 1-32

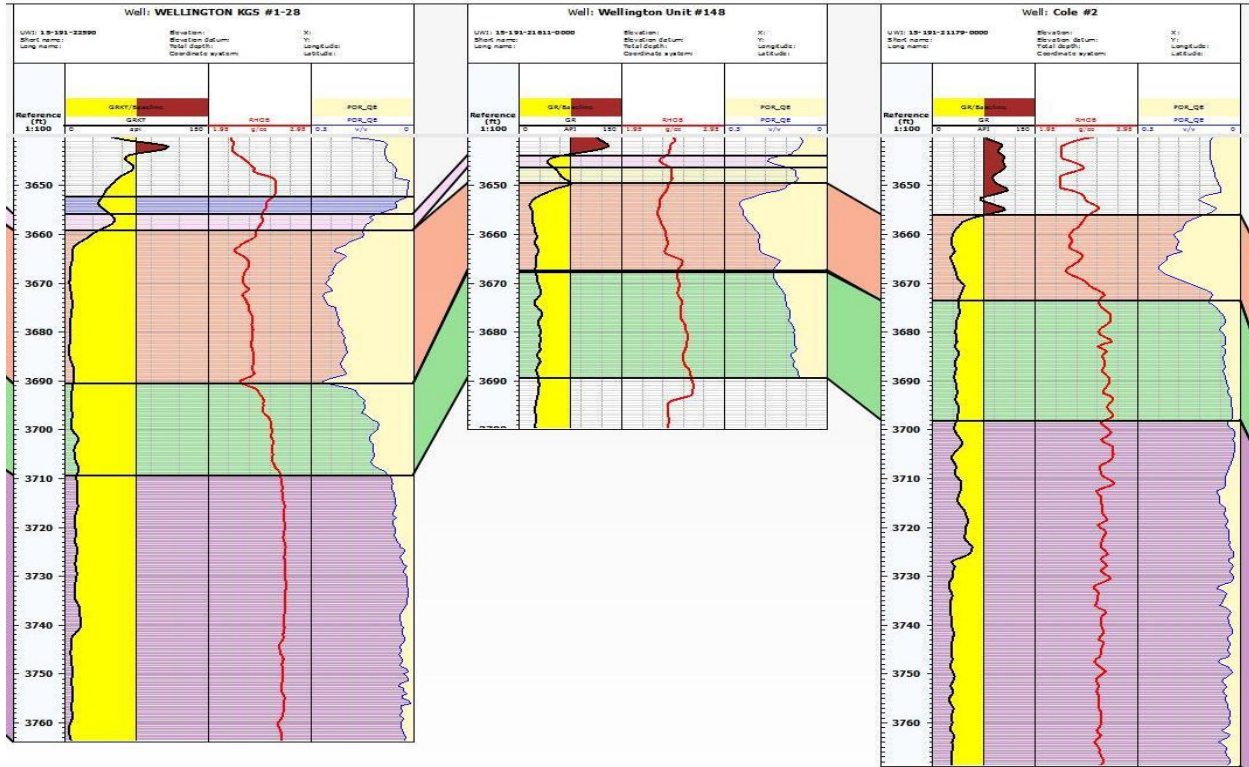


Figure A-9: Equivalent zones in wells 1-28, 148, and Cole #2 with equal FZI values corresponding to the six zones of Well 1-32

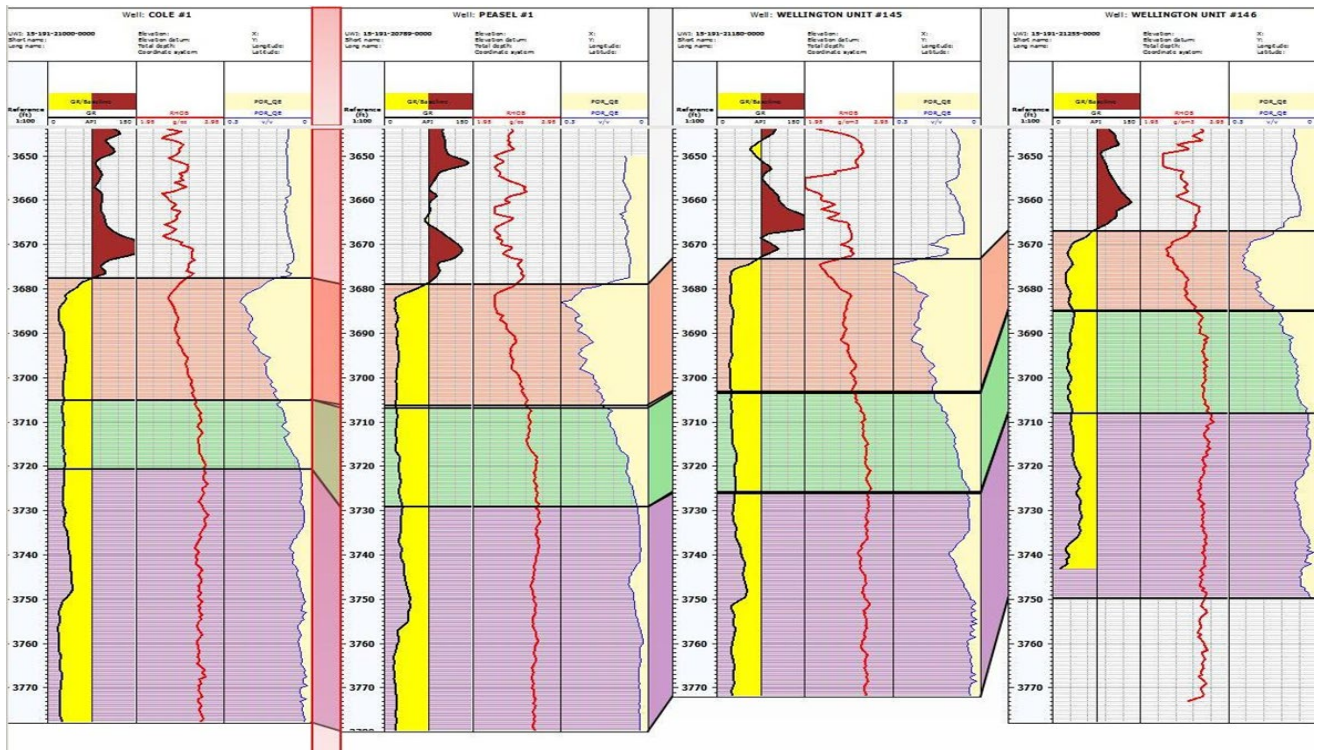


Figure A-10: Equivalent zones in wells Cole #1, Peasel #1, 145, and 146 with equal FZI values corresponding to the six zones of Well 1-32

LAYOUT

Well(s): **WELLINGTON KGS #1-28**



Author: **Mina FAZELALAVI**  
Date: **11/2/2012**

Project: **Wellington2**

Scale: **1:200**

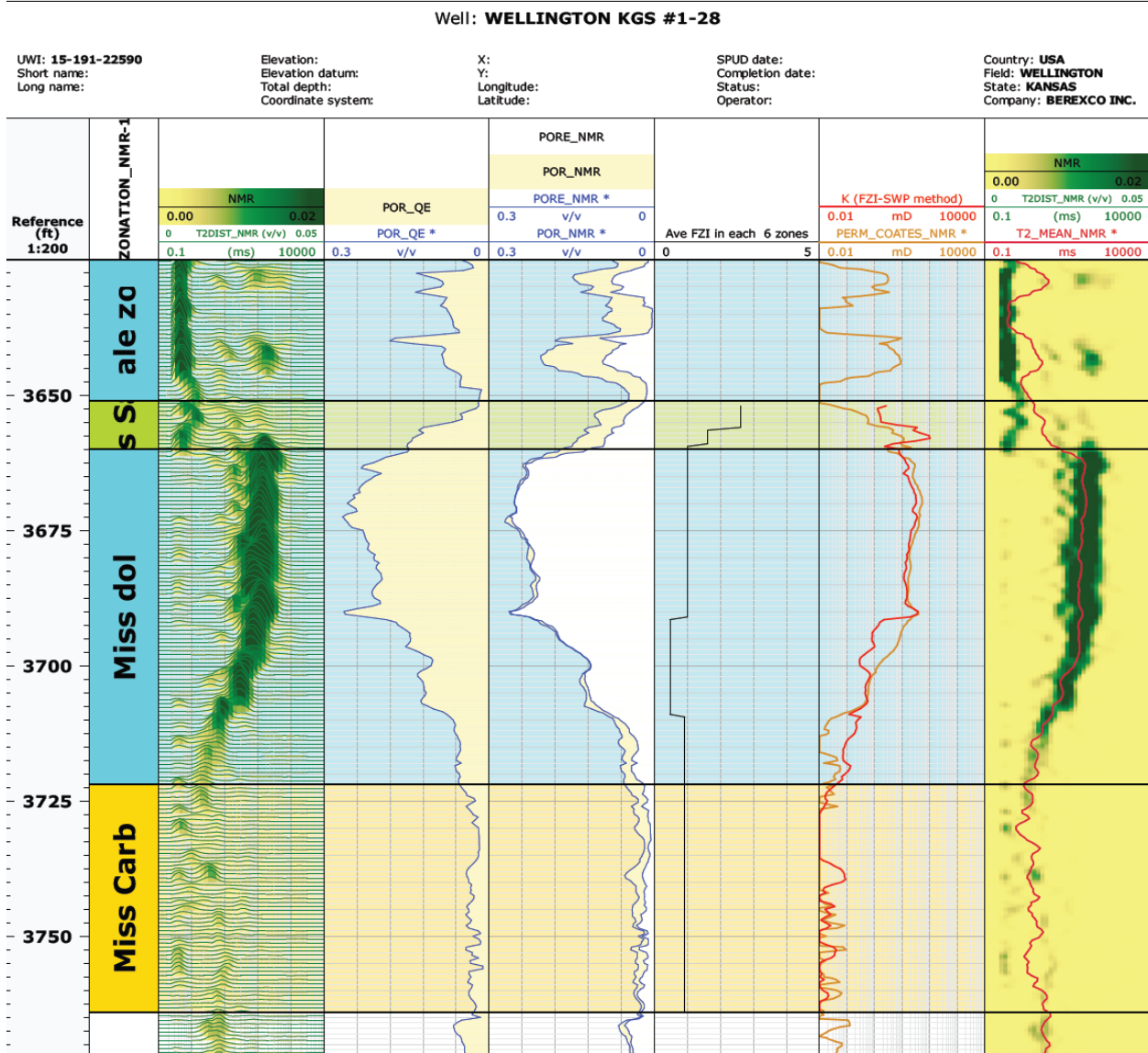
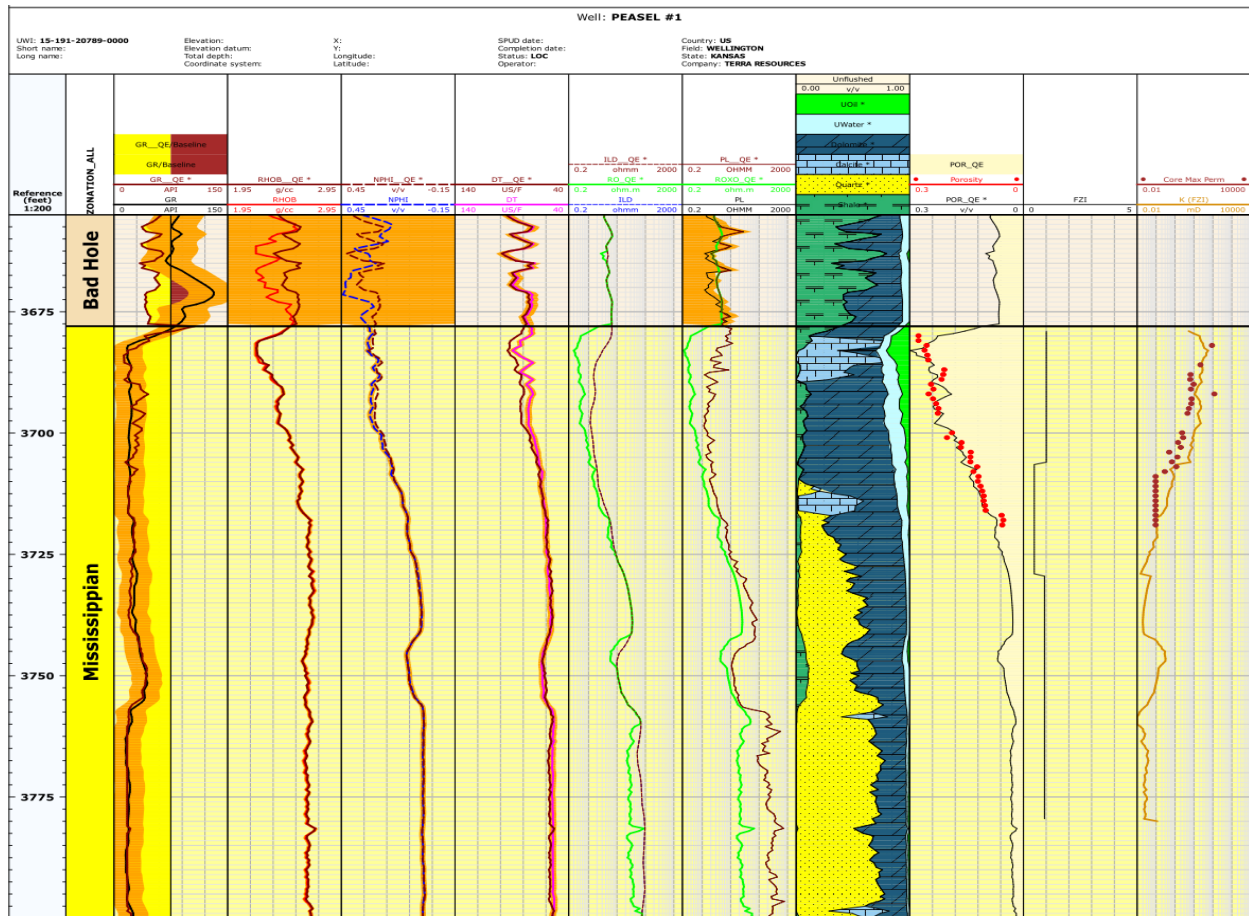


Figure A- 11: Well 1-28 showing average FZI in each of six zones in track 3 from right and comparing permeability from FZI-SWP method to Coates permeability



**Figure A-12: Layout of Peasel #1 comparing permeability from the FZI-SWP method to Coates permeability and showing average FZI in each of the six zones**

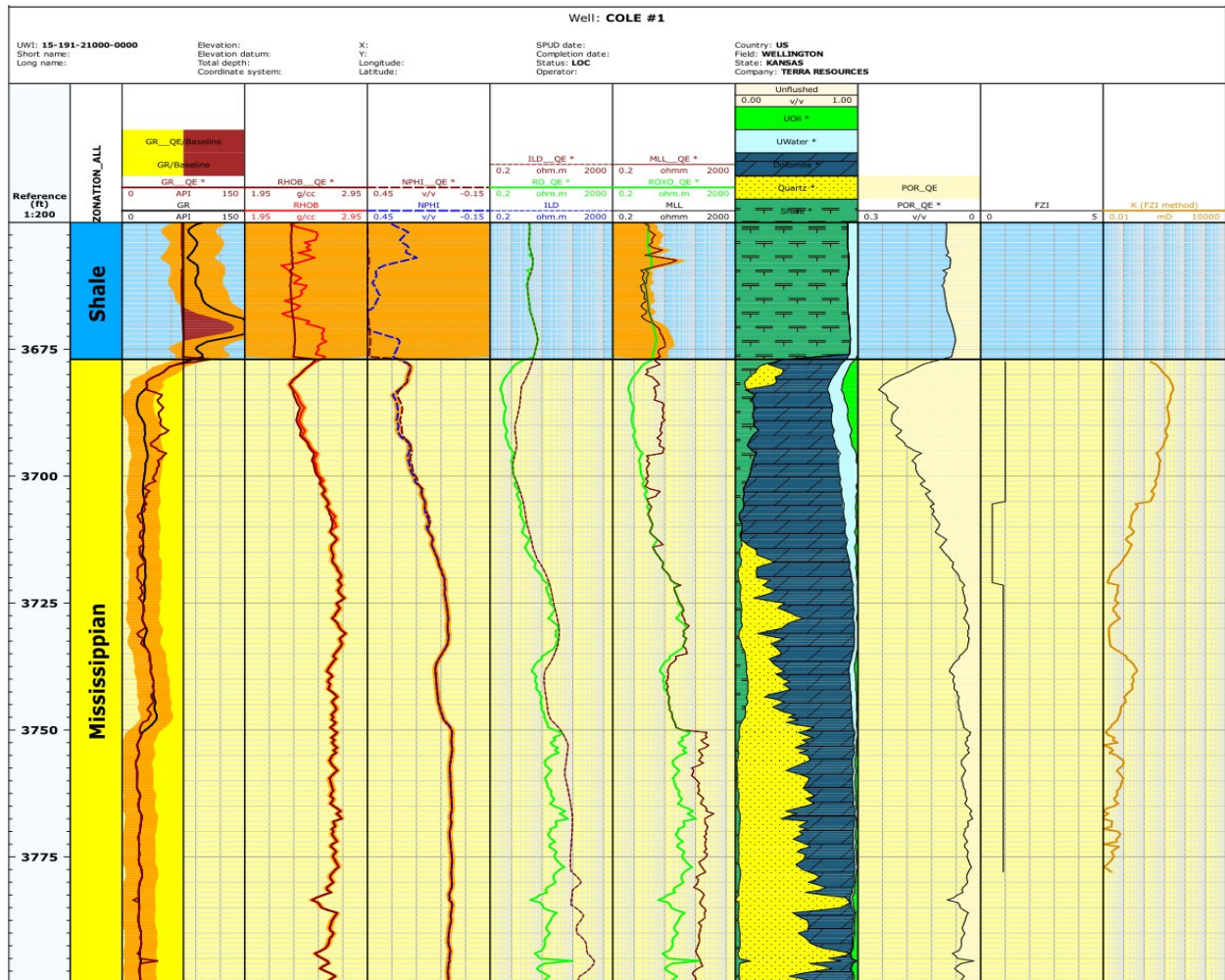


Figure A-13: Layout of Cole #1 showing average FZI in each of six zones and permeability from the FZI-SWP method



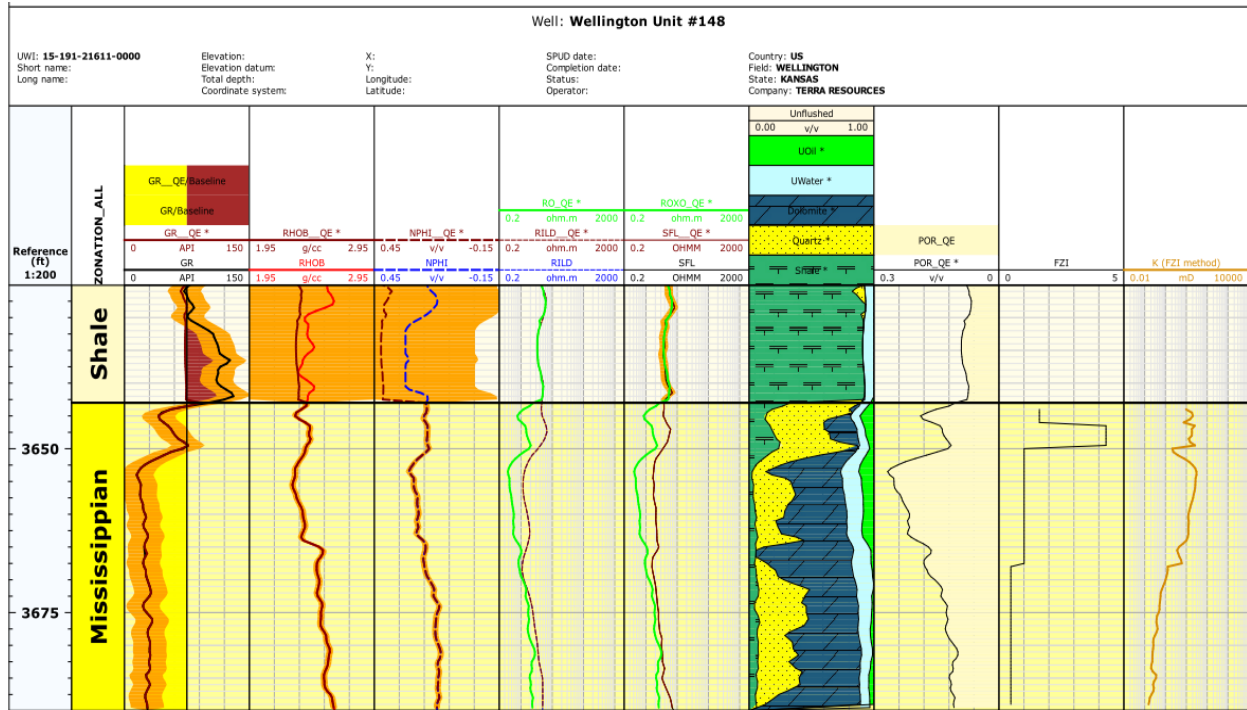


Figure A-15 : Layout of Well 148 showing average FZI in each of six zones and permeability from the FZI-SWP method

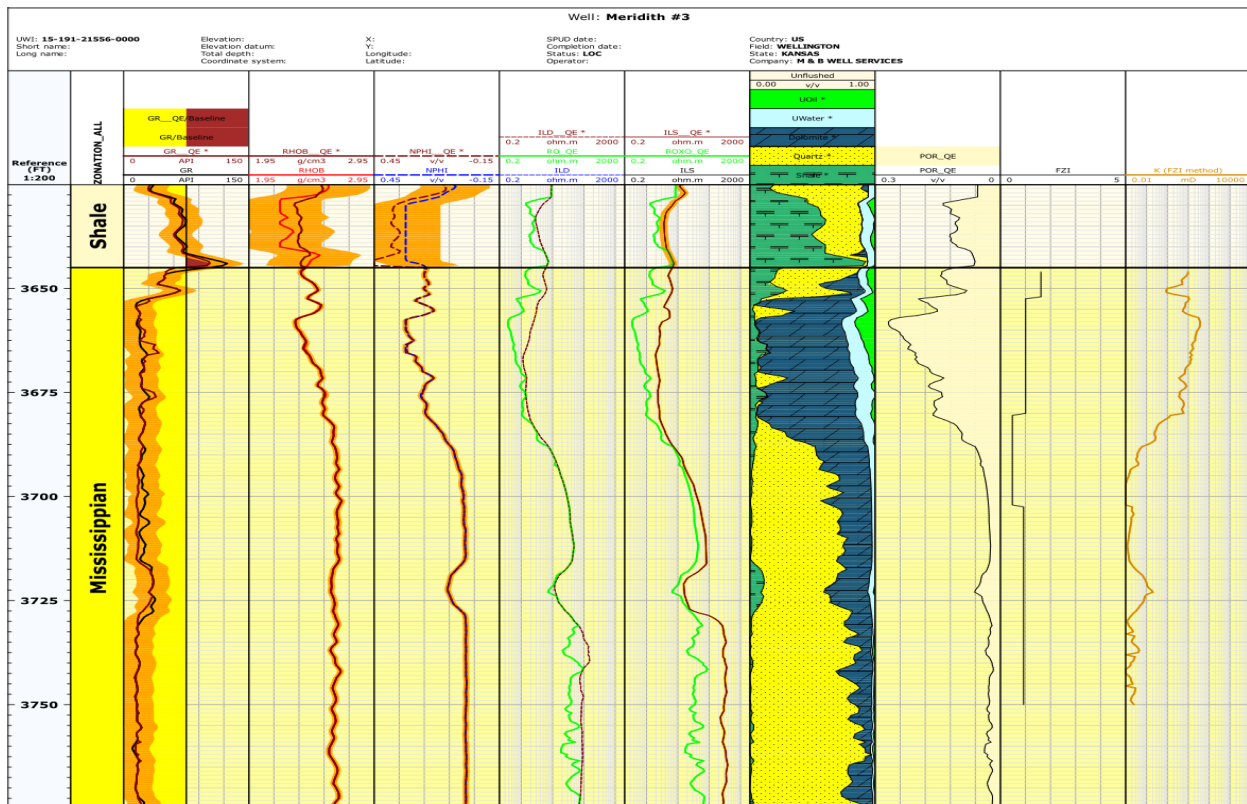


Figure A-16: Figure A-15: Layout of Meridith #3 showing average FZI in each of six zones and permeability from the FZI-SWP method

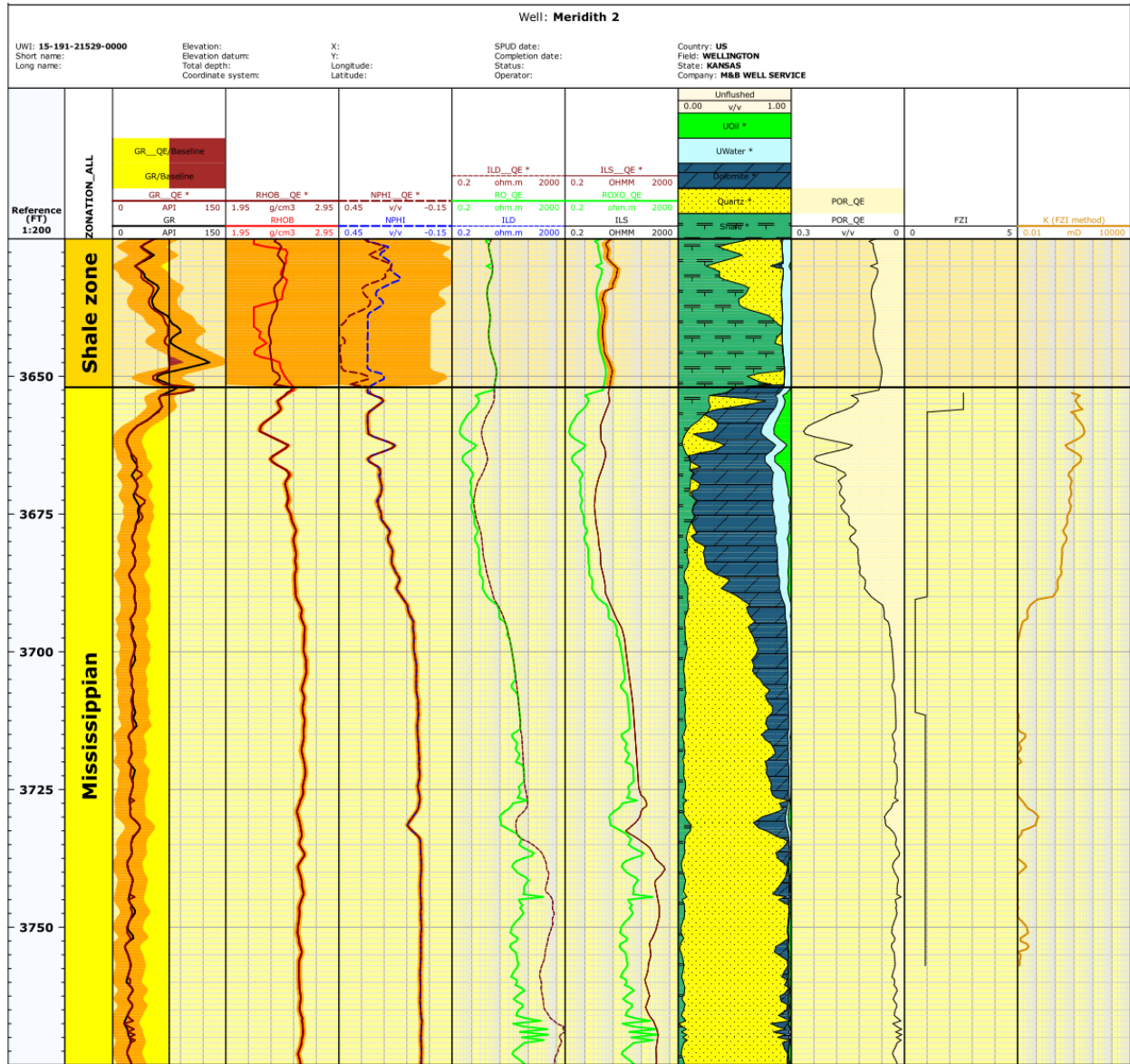


Figure A-17: Layout of Meridith #2 showing average FZI in each of six zones and permeability from the FZI-SWP method

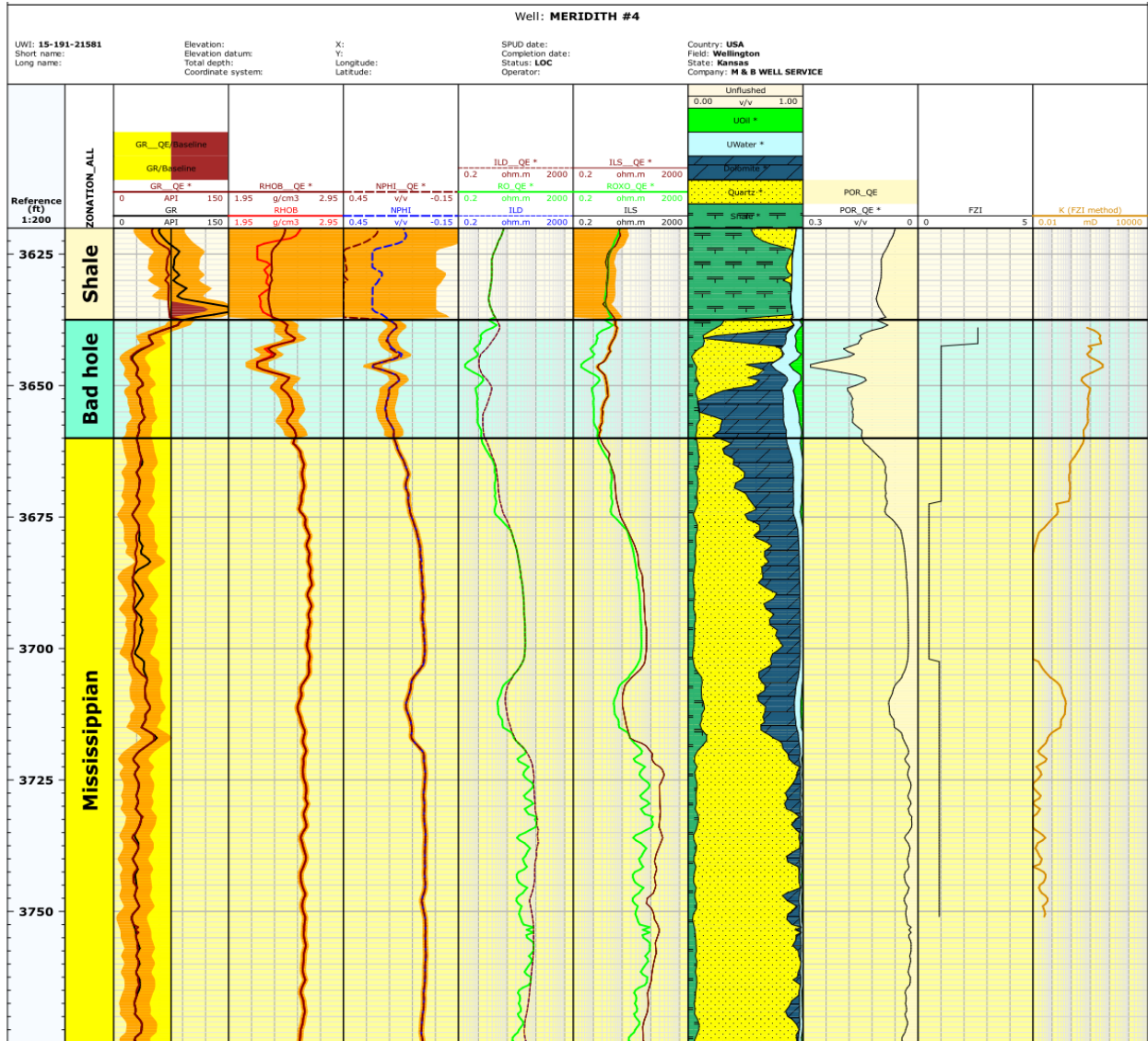


Figure A-18: Layout of Meridith #4 showing average FZI in each of six zones and permeability from the FZI-SWP method

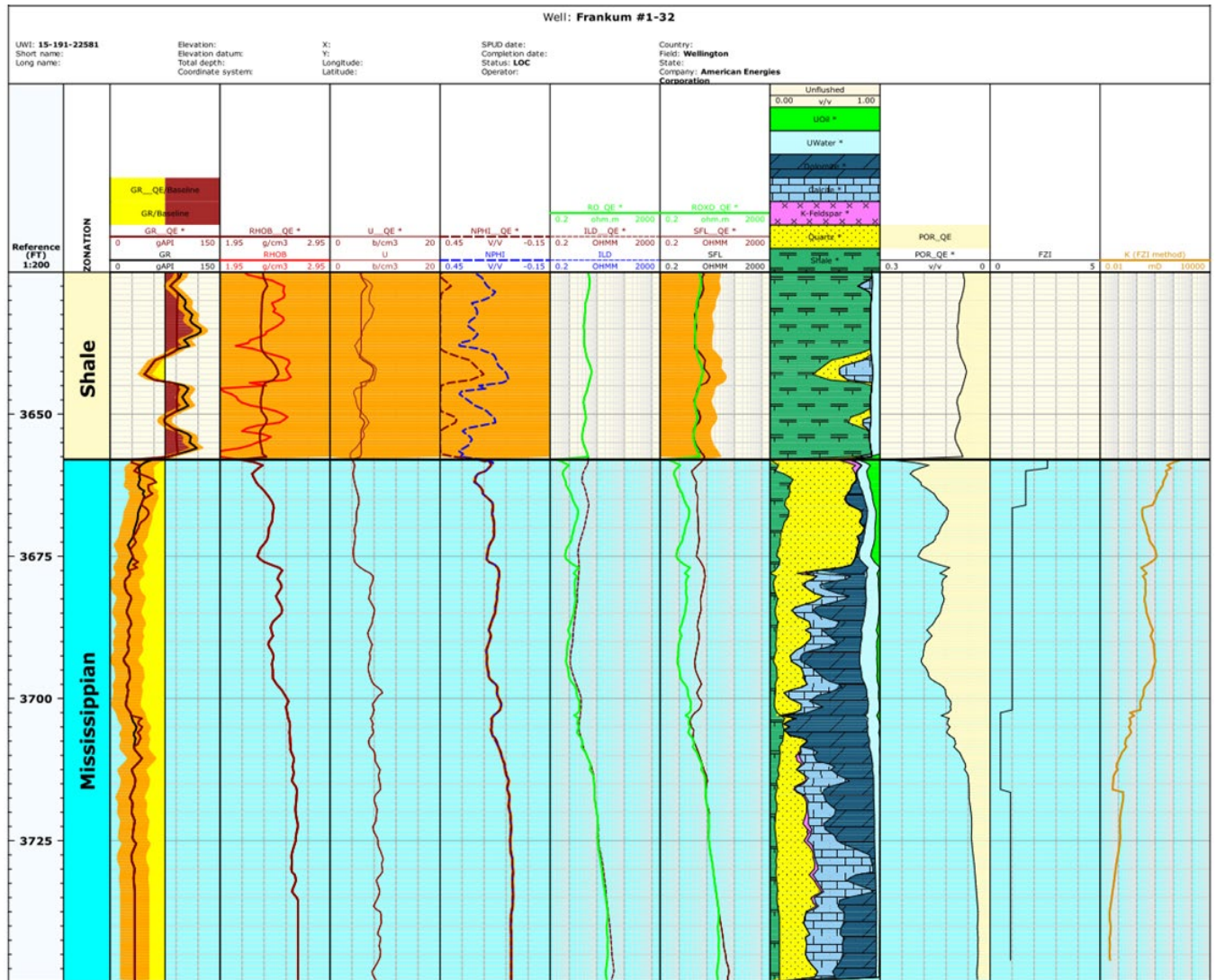


Figure A-19: Layout of Frankum # 1-32 showing average FZI in each of six zones and permeability from the FZI-SWP method

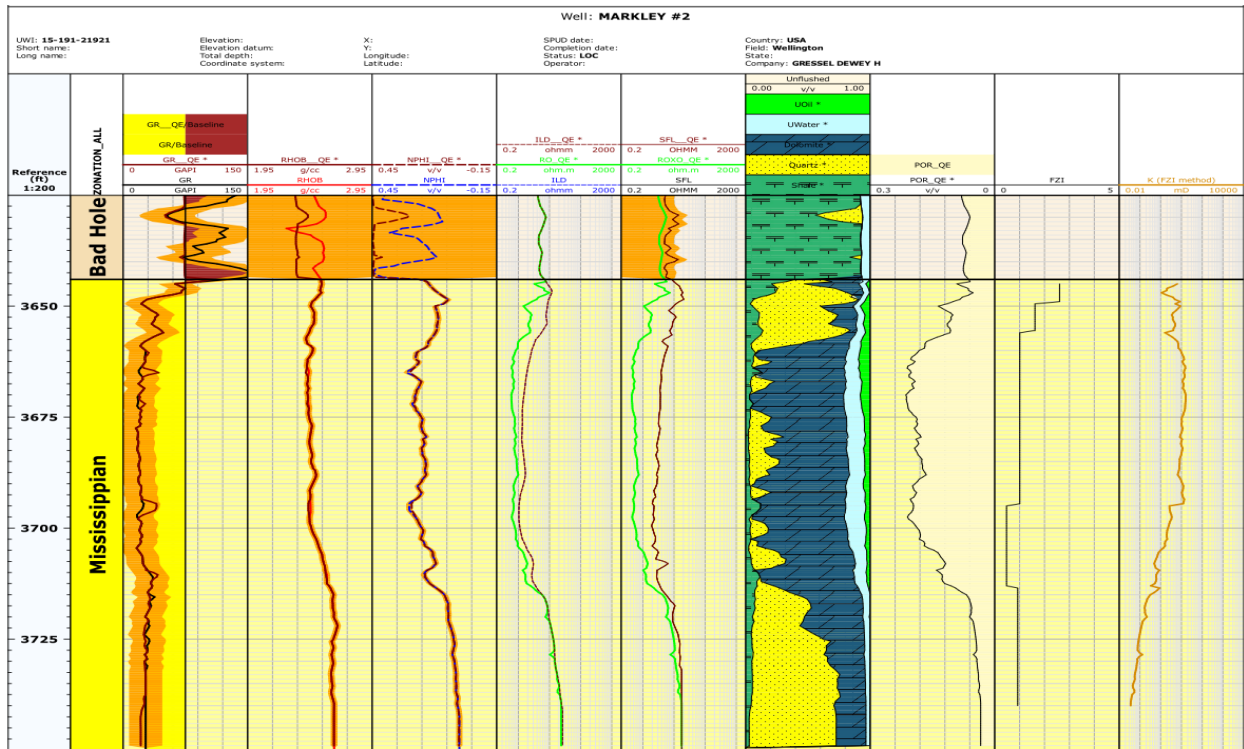


Figure A-20: Layout of Markley #2 showing average FZI in each of six zones and permeability from the FZI-SWP method

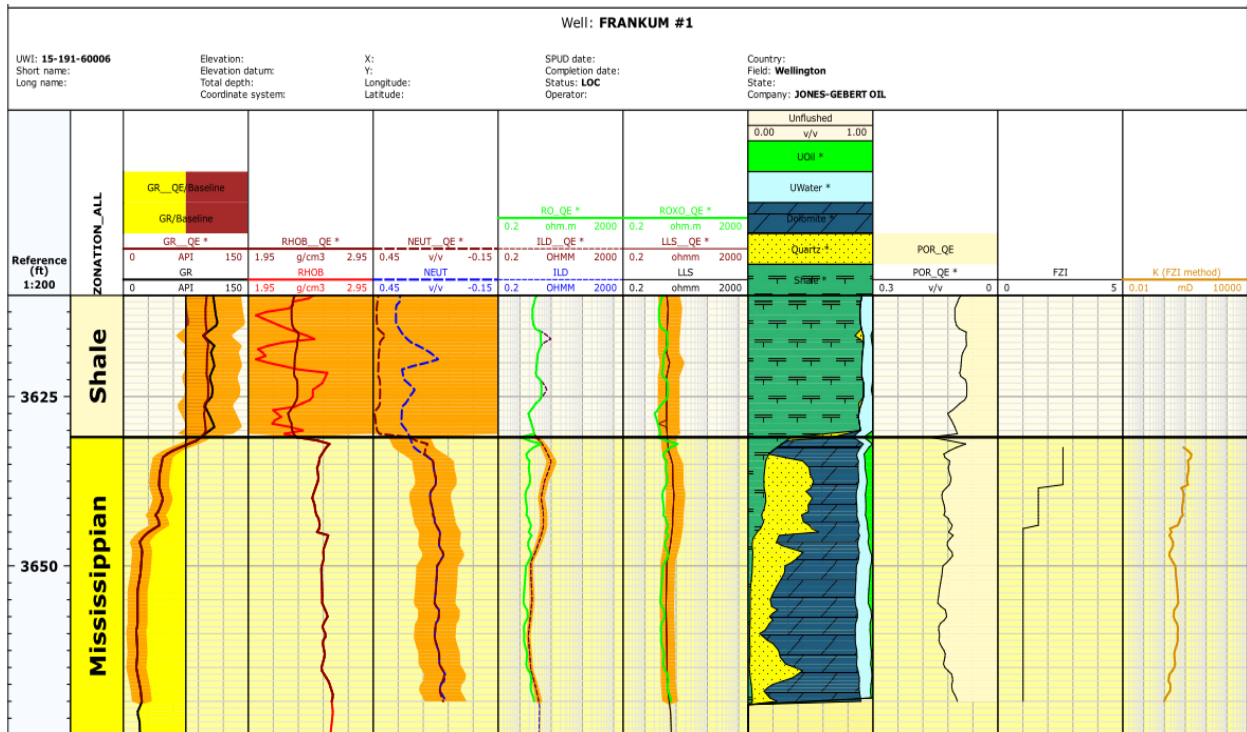


Figure A-21: Layout of Frankum #1 showing average FZI in each of six zones and permeability from the FZI-SWP method

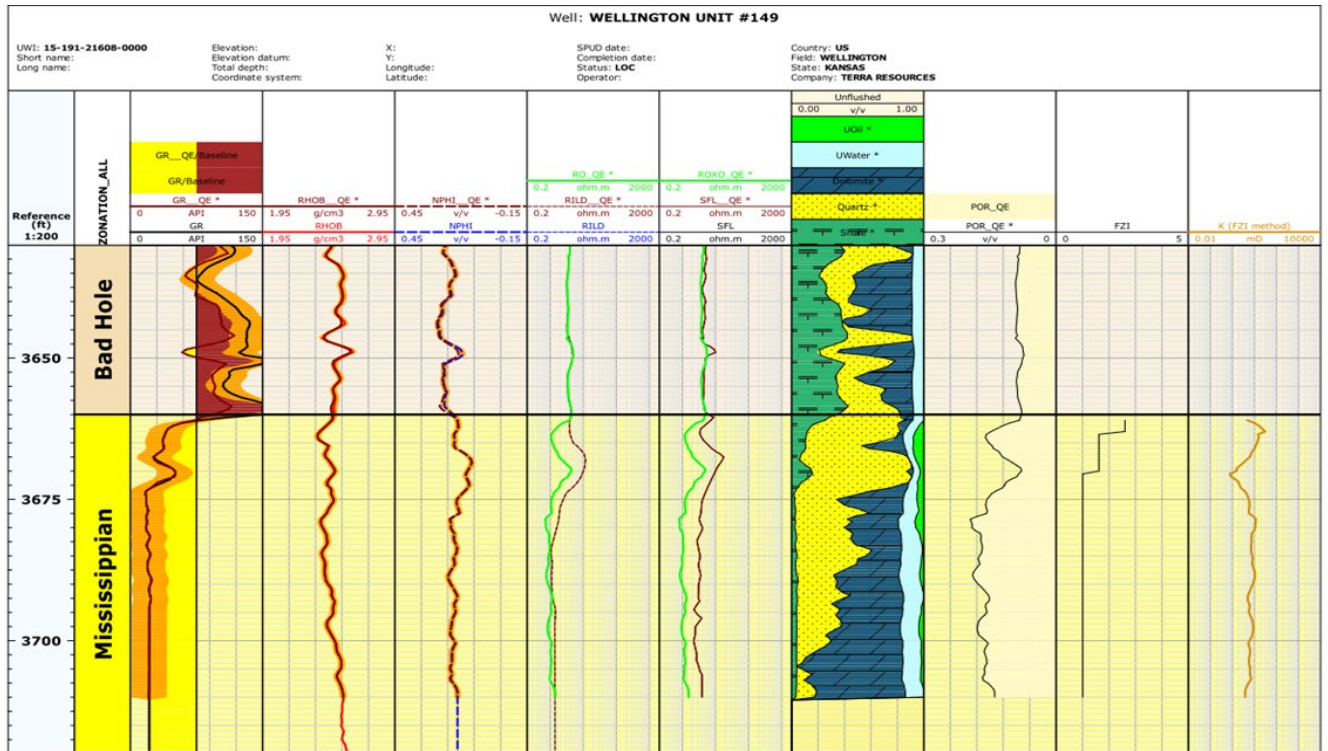


Figure A-22: Layout of Well #149 showing average FZI in each of six zones and permeability from the FZI-SWP method:

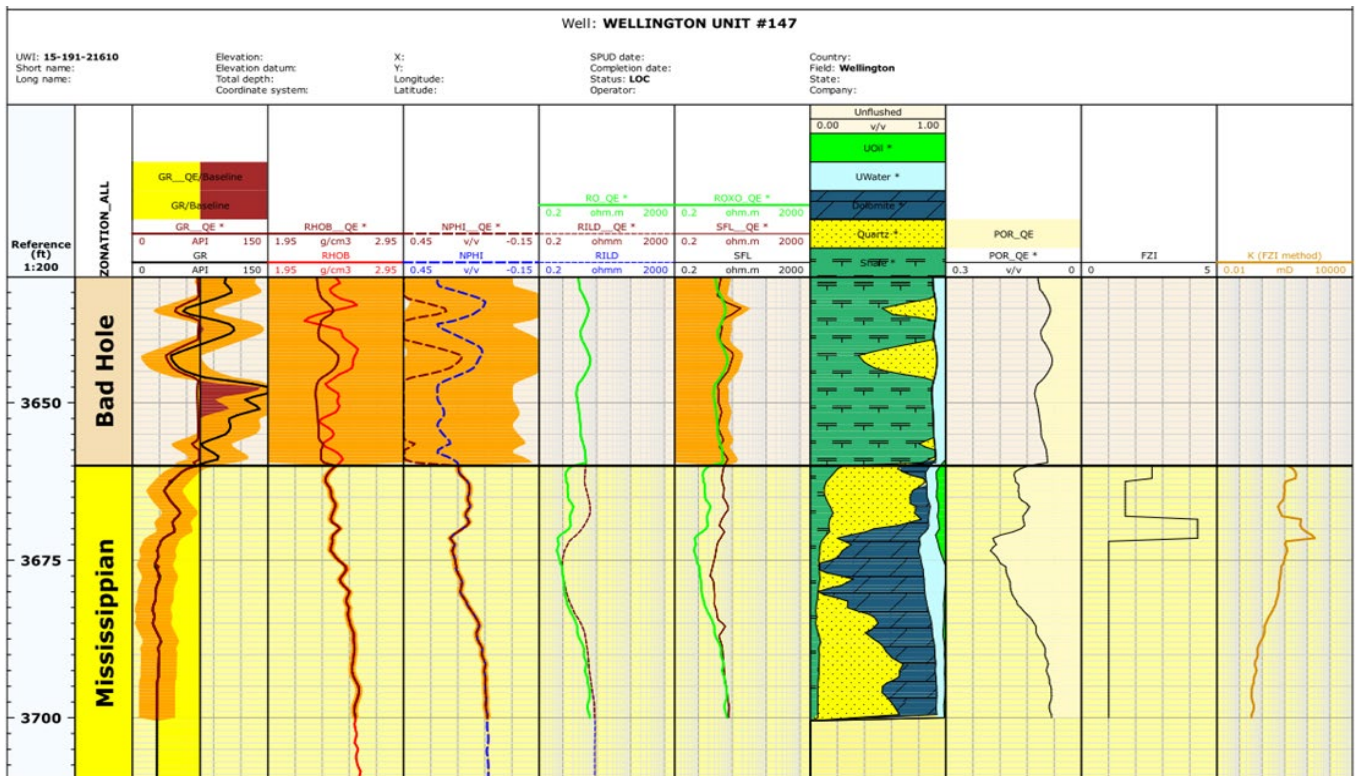


Figure A-23: Layout of Well #147 showing average FZI in each of six zones and permeability from the FZI-SWP method

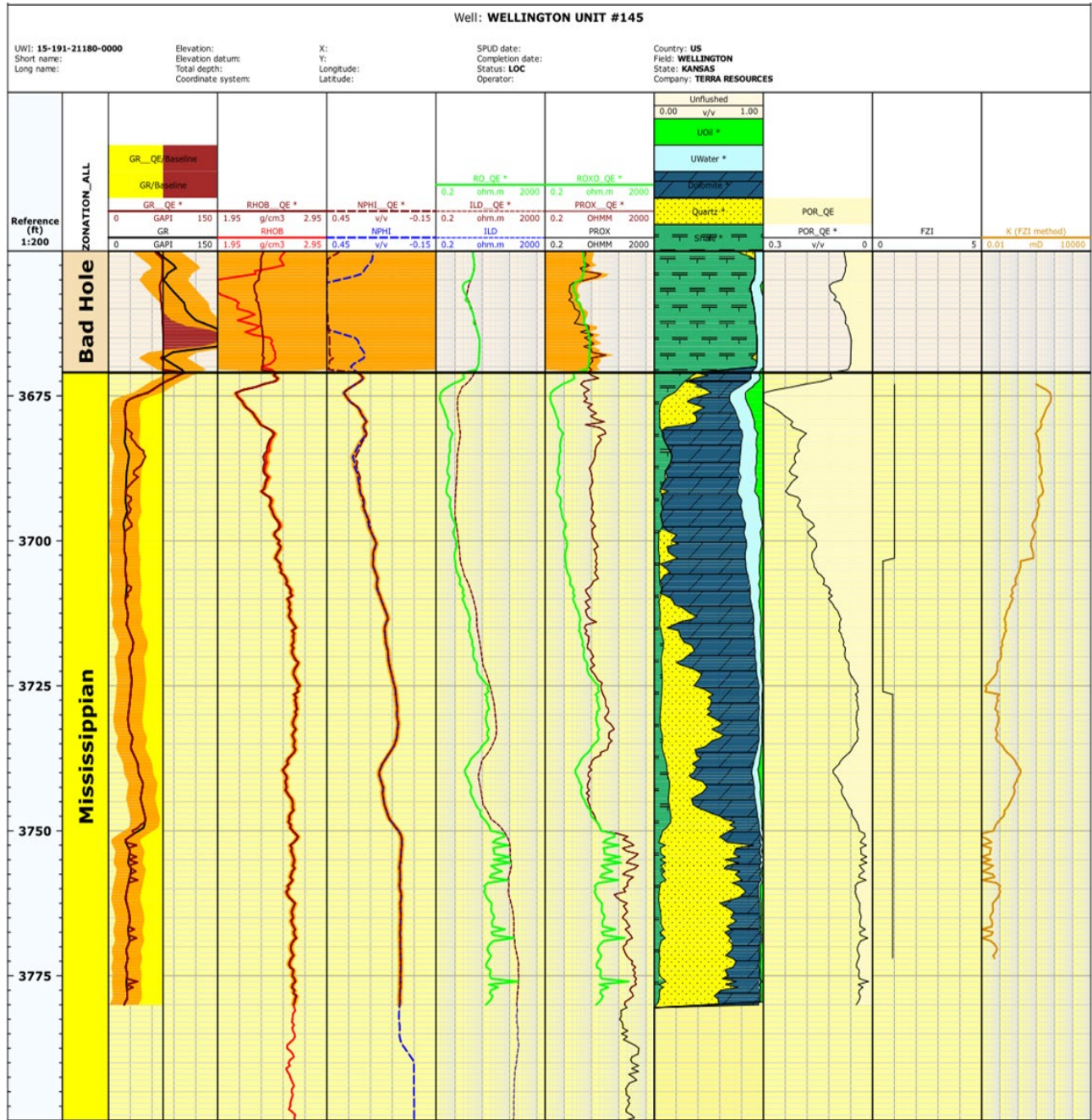


Figure A-24: Layout of Well #145 showing average FZI in each of six zones and permeability from the FZI-SWP method

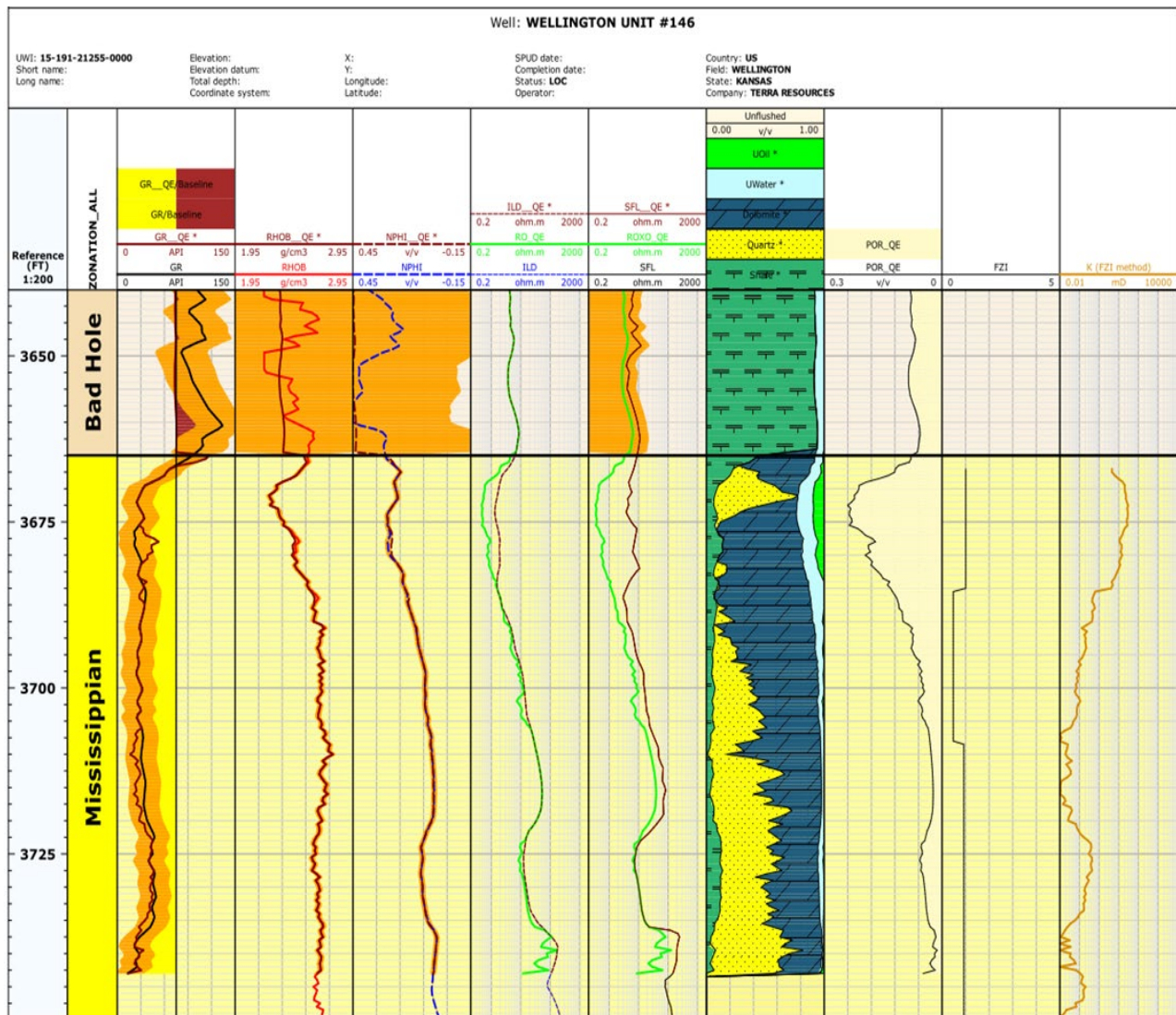


Figure A-25: Layout of Well #146 showing average FZI in each of six zones and permeability from the FZI-SWP method

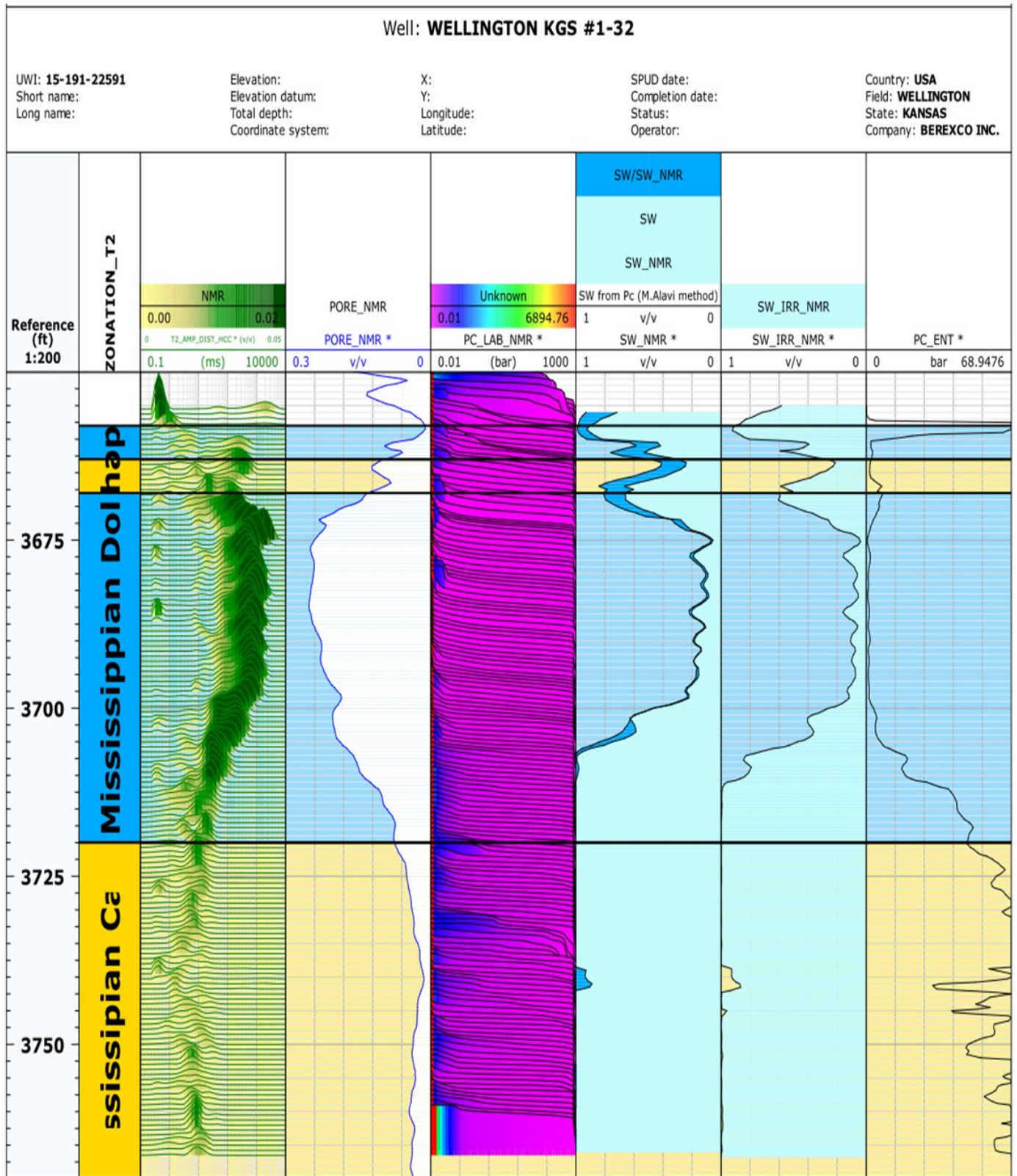


Figure A-26: Calculated initial water saturation using the Pc M.F.Alavi method compared with saturation from the NMR log

**APPENDIX A-3. Relative Permeability Chat Section**

RQI= 0.320				
Sor	Swc	Chat	Krw max	Kro max
0.321	0.45	1	0.204	0.871
q	1.5	p	2.5	
Sw	So	SwD	Krw	kro
0.450	0.550	0.000	0.000	0.871
0.470	0.530	0.087	0.005	0.694
0.490	0.510	0.174	0.015	0.540
0.510	0.490	0.262	0.027	0.408
0.530	0.470	0.349	0.042	0.298
0.550	0.450	0.436	0.059	0.208
0.570	0.430	0.523	0.077	0.137
0.590	0.410	0.610	0.097	0.083
0.610	0.390	0.698	0.119	0.044
0.630	0.370	0.785	0.142	0.019
0.650	0.350	0.872	0.166	0.005
0.670	0.330	0.959	0.191	0.000
0.679	0.321	1.000	0.204	0.000

**Table B1: Relative permeability for the chat section at RQI=0.320**

RQI= 0.280				
Sor	Swc	Chat	Krw max	Kro max
0.300	0.5	2	0.214	0.869
q	1.5	p	2.5	
Sw	So	SwD	Krw	kro
0.500	0.500	0	0	0.869
0.520	0.480	0.1	0.007	0.668
0.540	0.460	0.2	0.019	0.498
0.560	0.440	0.3	0.035	0.356
0.580	0.420	0.4	0.054	0.242
0.600	0.400	0.5	0.075	0.154
0.620	0.380	0.6	0.099	0.088
0.640	0.360	0.7	0.125	0.043
0.660	0.340	0.8	0.153	0.016
0.680	0.320	0.9	0.182	0.003
0.700	0.300	1.0	0.214	0.000

**Table B2: Relative permeability for the chat section at RQI=0.280**

RQI= 0.245				
Sor	Swc	Chat	Krw max	Kro max
0.270	0.56	3	0.224	0.867
q	1.5	p	2.5	
Sw	So	SwD	Krw	kro
0.560	0.440	0.000	0.000	0.867
0.580	0.420	0.118	0.009	0.634
0.600	0.400	0.235	0.026	0.443
0.620	0.380	0.353	0.047	0.292
0.640	0.360	0.471	0.072	0.177
0.660	0.340	0.588	0.101	0.094
0.680	0.320	0.706	0.133	0.041
0.700	0.300	0.824	0.167	0.011
0.720	0.280	0.941	0.204	0.001
0.730	0.270	1.000	0.224	0.000

**Table B3: Relative permeability for the chat section at RQI=0.245**

RQI= 0.220				
Sor	Swc	Chat	Krw max	Kro max
0.240	0.6	4	0.232	0.865
q	1.5	p	2.5	
Sw	So	SwD	Krw	kro
0.600	0.400	0.000	0	0.865
0.620	0.380	0.125	0.010262	0.620
0.640	0.360	0.250	0.029026	0.421
0.660	0.340	0.375	0.053324	0.267
0.680	0.320	0.500	0.082097	0.153
0.700	0.300	0.625	0.114735	0.074
0.720	0.280	0.750	0.150823	0.027
0.740	0.260	0.875	0.190058	0.005
0.760	0.240	1.000	0.232206	0.000

**Table B4: Relative permeability for the chat section at RQI=0.220**

RQI= 0.200				
Sor	Swc	Chat	Krw max	Kro max
0.210	0.66	5	0.240	0.864
q	1.5		p	2.5
Sw	So	SwD	Krw	kro
0.660	0.340	0.000	0.000	0.864
0.680	0.320	0.154	0.014	0.569
0.700	0.300	0.308	0.041	0.344
0.720	0.280	0.462	0.075	0.184
0.740	0.260	0.615	0.116	0.079
0.760	0.240	0.769	0.162	0.022
0.780	0.220	0.923	0.213	0.001
0.790	0.210	1.000	0.240	0.000

Table B5: Relative permeability for the chat section at RQI=0.200

RQI= 0.175				
Sor	Swc	Chat	Krw max	Kro max
0.155	0.75	6	0.251	0.861
q	1.5		p	2.5
Sw	So	SwD	Krw	kro
0.750	0.250	0	0	0.861
0.770	0.230	0.210526316	0.02429	0.477
0.790	0.210	0.421052632	0.068701	0.220
0.810	0.190	0.631578947	0.126212	0.071
0.830	0.170	0.842105263	0.194317	0.009
0.845	0.155	1	0.251455	0.000

Table B6: Relative permeability for the chat section at RQI=0.175

RQI= 0.145				
Sor	Swc	Chat	Krw max	Kro max
0.090	0.83	7	0.268	0.858
q	1.5		p	2.5
Sw	So	SwD	Krw	kro
0.830	0.170	0	0.000	0.858
0.850	0.150	0.25	0.034	0.418
0.870	0.130	0.5	0.095	0.152
0.890	0.110	0.75	0.174	0.027
0.910	0.090	1	0.268	0.000

Table B7: Relative permeability for the chat section at RQI=0.145

RQI= 0.120				
Sor	Swc	Chat	Krw max	Kro max
0.030	0.930	8	0.287	0.855
q	1.5		p	2.5
Sw	So	SwD	Krw	kro
0.930	0.070	0	0.000	0.855
0.950	0.050	0.5	0.101	0.151
0.970	0.030	1	0.287	0.000

Table B8: Relative permeability for the Ccat section at RQI=0.120

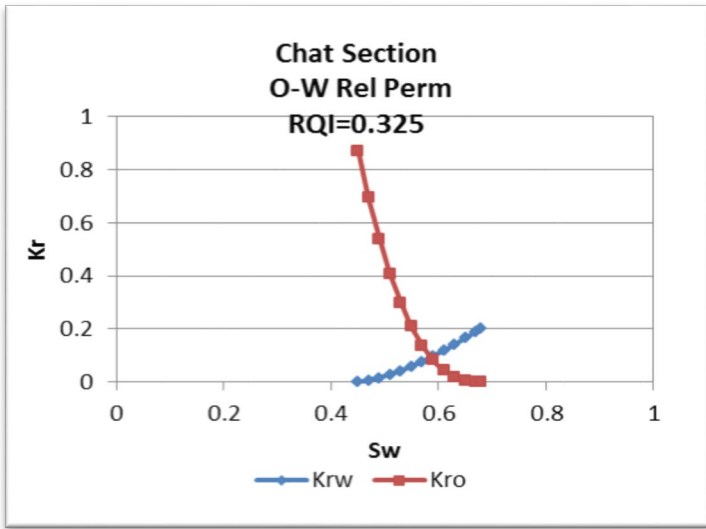


Figure B1: Relative permeability curve for the chat section at RQI=0.325

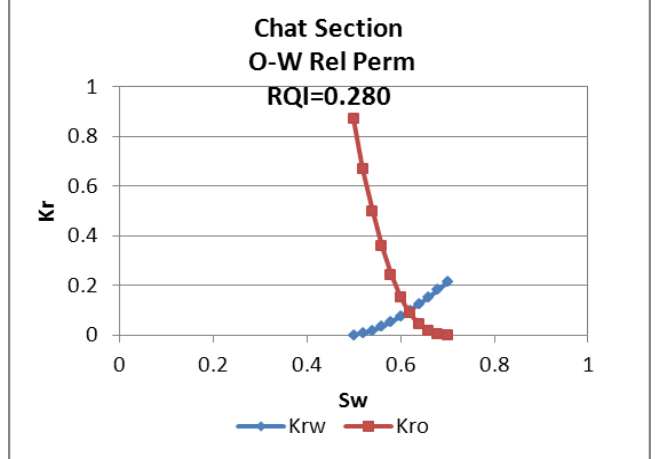


Figure B2: Relative permeability curve for the chat section at RQI=0.280

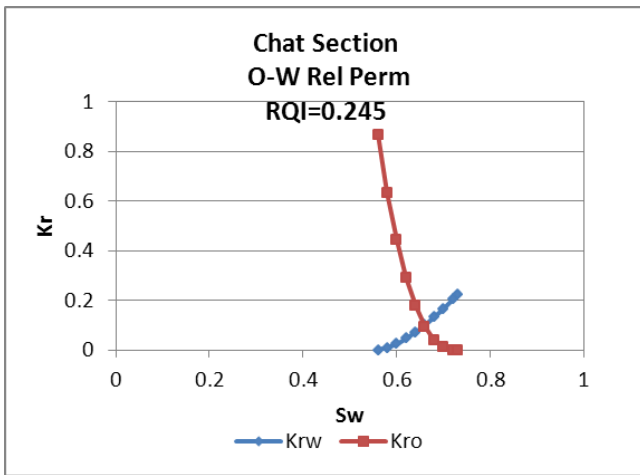


Figure B3: Relative permeability curve for the chat section at RQI=0.245

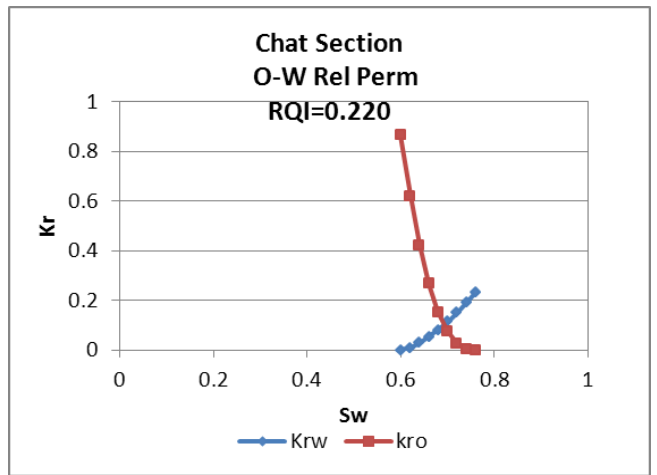


Figure B4: Relative permeability curve for the chat section at RQI=0.220

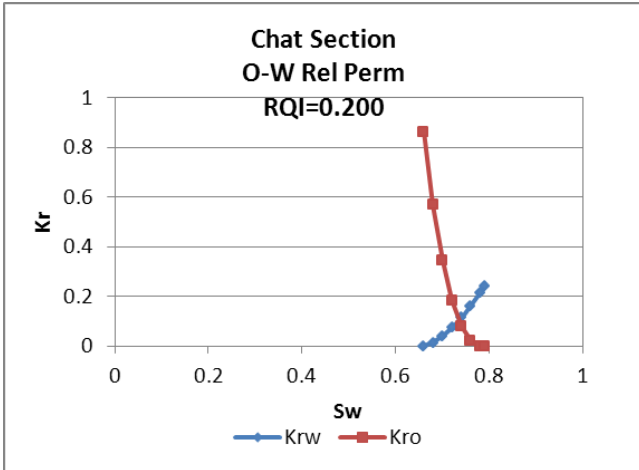


Figure B5: Relative permeability curve for the chat section at RQI=0.200

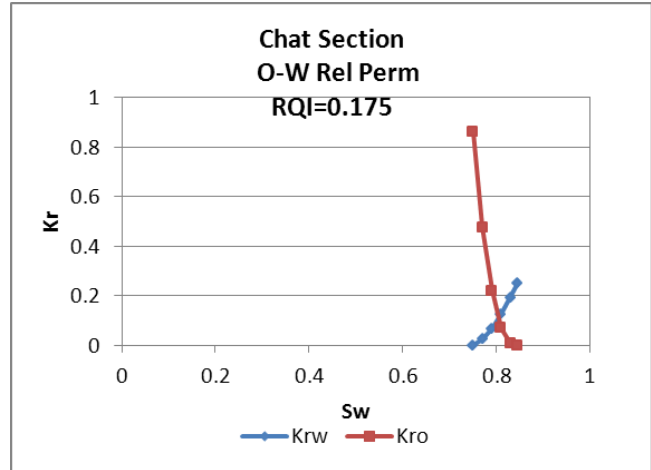


Figure B6: Relative permeability curve for the chat section at RQI=0.175

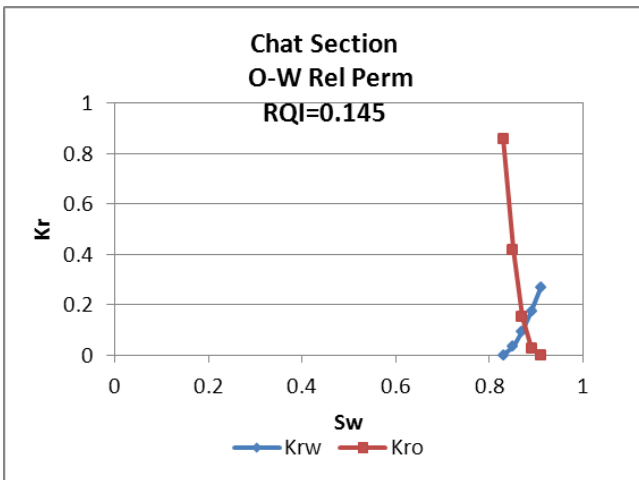


Figure B7: Relative permeability curve for the chat section at RQI=0.145

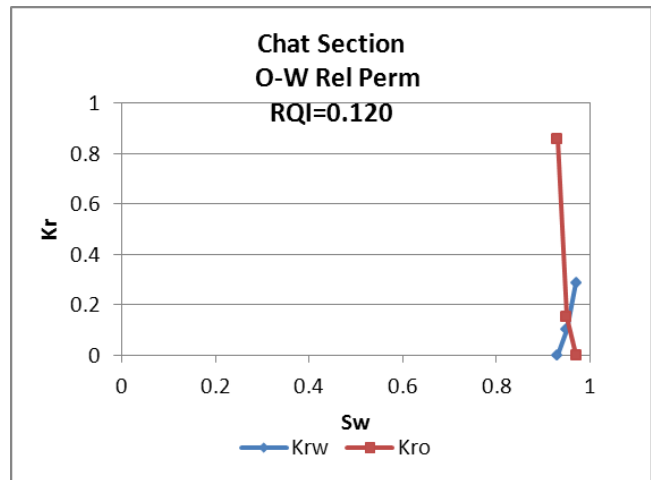


Figure B8: Relative permeability curve for the chat section at RQI=0.120

## APPENDIX A-4. Relative Permeability Carbonate Section

Table C1: Relative permeability table for the carbonate section at RQI=0.520

RQI= 0.520				
Sor	Swc	Carbonate	Krw max	Kro max
0.364	0.08	1	0.172	0.880
q	1.5		p	2.5
Sw	So	SwD	Krw	kro
0.080	0.920	0.000	0	0.880
0.100	0.900	0.036	0.001	0.803
0.120	0.880	0.072	0.003	0.730
0.140	0.860	0.108	0.006	0.661
0.160	0.840	0.144	0.009	0.597
0.180	0.820	0.180	0.013	0.536
0.200	0.800	0.216	0.017	0.479
0.220	0.780	0.252	0.022	0.426
0.240	0.760	0.288	0.027	0.377
0.260	0.740	0.324	0.032	0.331
0.280	0.720	0.359	0.037	0.289
0.300	0.700	0.395	0.043	0.250
0.320	0.680	0.431	0.049	0.215
0.340	0.660	0.467	0.055	0.182
0.360	0.640	0.503	0.061	0.153
0.380	0.620	0.539	0.068	0.127
0.400	0.600	0.575	0.075	0.104
0.420	0.580	0.611	0.082	0.083
0.440	0.560	0.647	0.090	0.065
0.460	0.540	0.683	0.097	0.050
0.480	0.520	0.72	0.105	0.037
0.500	0.500	0.755	0.113	0.026
0.520	0.480	0.791	0.121	0.018
0.540	0.460	0.827	0.129	0.011
0.560	0.440	0.863	0.138	0.006
0.580	0.420	0.899	0.147	0.003
0.600	0.400	0.935	0.156	0.001
0.620	0.380	0.971	0.165	0.0001

Table C2: Relative permeability table for the carbonate section at RQI=0.380

RQI= 0.380				
Sor	Swc	Carbonate	Krw max	Kro max
0.342	0.11	2	0.192	0.874
q	1.5		p	2.5
Sw	So	SwD	Krw	kro
0.110	0.890	0.000	0	0.874
0.130	0.870	0.037	0.001	0.797
0.150	0.850	0.073	0.004	0.723
0.170	0.830	0.110	0.007	0.654
0.190	0.810	0.146	0.011	0.589
0.210	0.790	0.183	0.015	0.528
0.230	0.770	0.219	0.020	0.471
0.250	0.750	0.256	0.025	0.418
0.270	0.730	0.292	0.030	0.369
0.290	0.710	0.329	0.036	0.323
0.310	0.690	0.365	0.042	0.281
0.330	0.670	0.402	0.049	0.242
0.350	0.650	0.438	0.056	0.207
0.370	0.630	0.475	0.063	0.175
0.390	0.610	0.511	0.070	0.146
0.410	0.590	0.548	0.078	0.120
0.430	0.570	0.584	0.086	0.097
0.450	0.550	0.621	0.094	0.077
0.470	0.530	0.657	0.102	0.060
0.490	0.510	0.694	0.111	0.045
0.510	0.490	0.73	0.120	0.033
0.530	0.470	0.767	0.129	0.023
0.550	0.450	0.803	0.138	0.015
0.570	0.430	0.840	0.148	0.009
0.590	0.410	0.876	0.157	0.005
0.610	0.390	0.913	0.167	0.002
0.630	0.370	0.949	0.178	0.001
0.650	0.350	0.986	0.188	0.00002
0.658	0.342	1.000	0.192	0.000

**Table C3: Relative permeability table for the carbonate section at RQI=0.250**

RQI= 0.250				
Sor	Swc	Carbonate	Krw max	Kro max
0.315	0.15	3	0.222	0.867
q	1.5		p	2.5
Sw	So	SwD	Krw	kro
0.150	0.850	0.000	0	0.867
0.170	0.830	0.037	0.002	0.789
0.190	0.810	0.075	0.005	0.714
0.210	0.790	0.112	0.008	0.644
0.230	0.770	0.149	0.013	0.579
0.250	0.750	0.187	0.018	0.517
0.270	0.730	0.224	0.024	0.460
0.290	0.710	0.261	0.030	0.406
0.310	0.690	0.299	0.036	0.357
0.330	0.670	0.336	0.043	0.311
0.350	0.650	0.374	0.051	0.269
0.370	0.630	0.411	0.059	0.231
0.390	0.610	0.448	0.067	0.196
0.410	0.590	0.486	0.075	0.165
0.430	0.570	0.523	0.084	0.136
0.450	0.550	0.560	0.093	0.111
0.470	0.530	0.598	0.103	0.089
0.490	0.510	0.635	0.112	0.070
0.510	0.490	0.672	0.122	0.053
0.530	0.470	0.710	0.133	0.039
0.550	0.450	0.75	0.143	0.028
0.570	0.430	0.784	0.154	0.019
0.590	0.410	0.822	0.165	0.012
0.610	0.390	0.859	0.177	0.006
0.630	0.370	0.897	0.189	0.003
0.650	0.350	0.934	0.200	0.001
0.670	0.330	0.971	0.213	0.0001
0.685	0.315	1.000	0.222	0.0000

**Table C4: Relative permeability table for the carbonate section at RQI=0.160**

RQI= 0.160				
Sor	Swc	Carbonate	Krw max	Kro max
0.278	0.22	4	0.259	0.860
q	1.5		p	2.5
Sw	So	SwD	Krw	kro
0.220	0.780	0.000	0	0.860
0.240	0.760	0.040	0.002	0.777
0.260	0.740	0.080	0.006	0.699
0.280	0.720	0.120	0.011	0.625
0.300	0.700	0.159	0.017	0.557
0.320	0.680	0.199	0.023	0.493
0.340	0.660	0.239	0.030	0.434
0.360	0.640	0.279	0.038	0.380
0.380	0.620	0.319	0.047	0.329
0.400	0.600	0.359	0.056	0.283
0.420	0.580	0.399	0.065	0.241
0.440	0.560	0.438	0.075	0.203
0.460	0.540	0.478	0.086	0.169
0.480	0.520	0.518	0.097	0.139
0.500	0.500	0.558	0.108	0.112
0.520	0.480	0.598	0.120	0.088
0.540	0.460	0.638	0.132	0.068
0.560	0.440	0.677	0.145	0.051
0.580	0.420	0.717	0.158	0.037
0.600	0.400	0.757	0.171	0.025
0.620	0.380	0.80	0.185	0.016
0.640	0.360	0.837	0.199	0.009
0.660	0.340	0.877	0.213	0.005
0.680	0.320	0.917	0.228	0.002
0.700	0.300	0.956	0.243	0.00034
0.720	0.280	0.996	0.258	0.00000
0.722	0.278	1.000	0.259	0.000





**Figure C1: Relative permeability curve for the carbonate section at RQI=0.520**

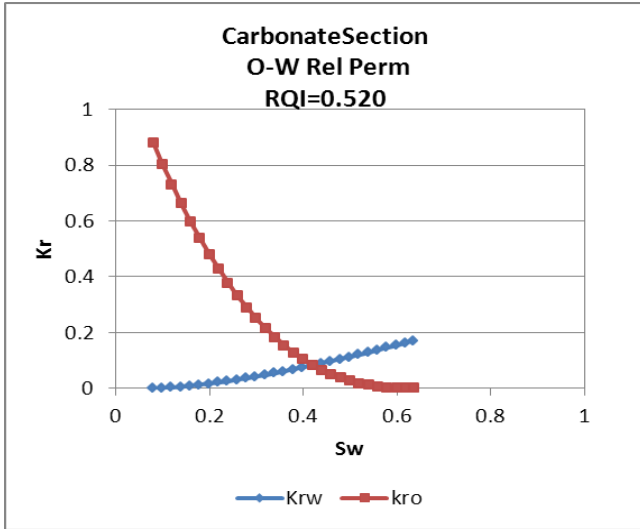


**Figure C2: Relative permeability curve for the carbonate section at RQI=0.380**

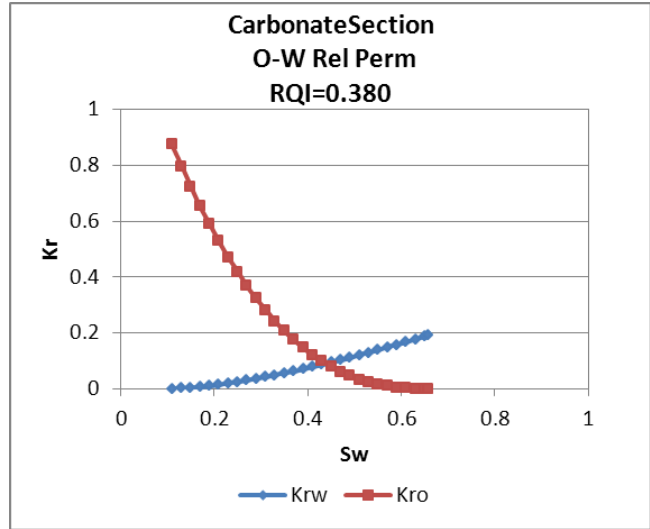


**Figure C3: Relative permeability curve for the carbonate section at RQI=0.25**

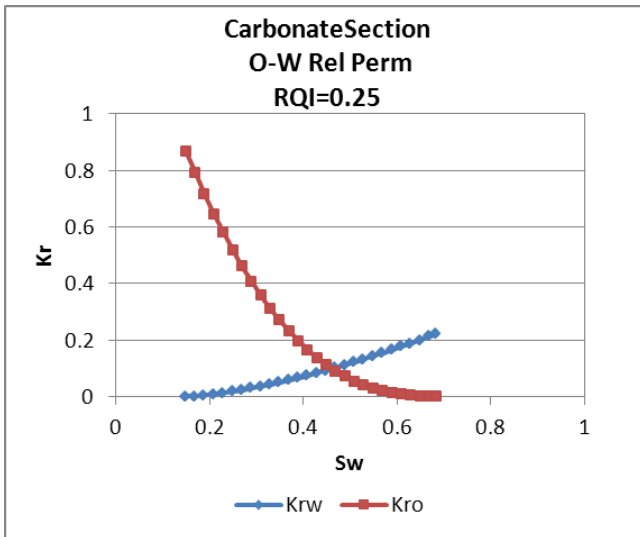


**Figure C4: Relative permeability curve for the carbonate section at RQI=0.16**

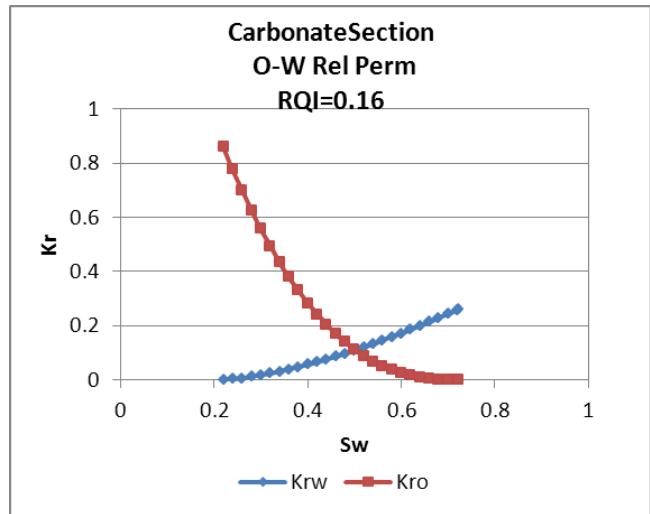


**Figure C5: Relative permeability curve for the carbonate section at RQI=0.100**

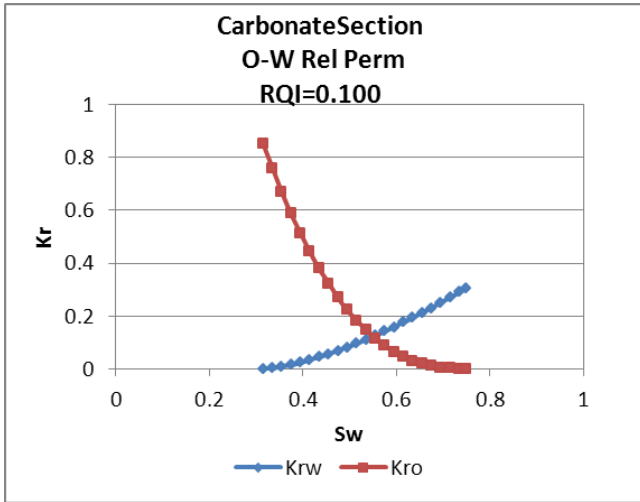


**Figure C6: Relative permeability curve for the carbonate section at RQI=0.08**

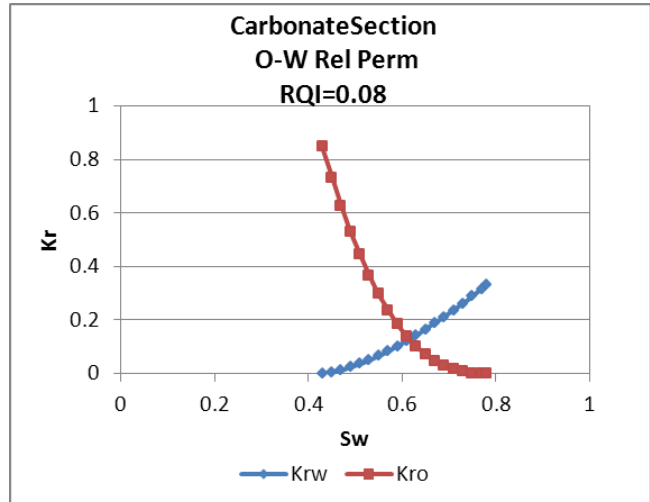


**Figure C7: Relative permeability curve for the carbonate section at RQI=0.06**

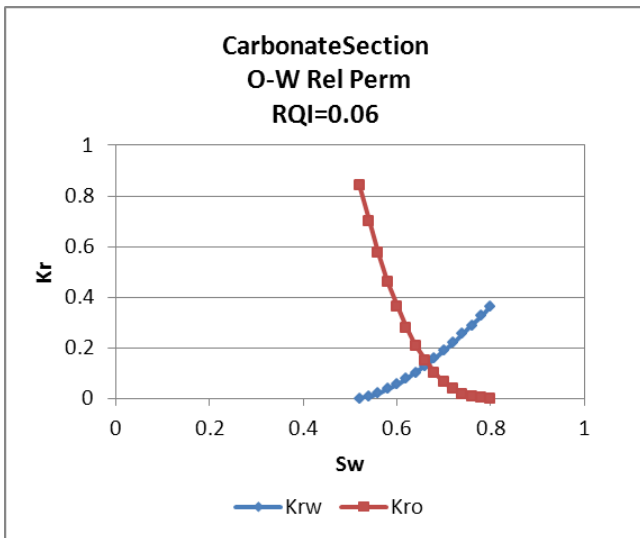
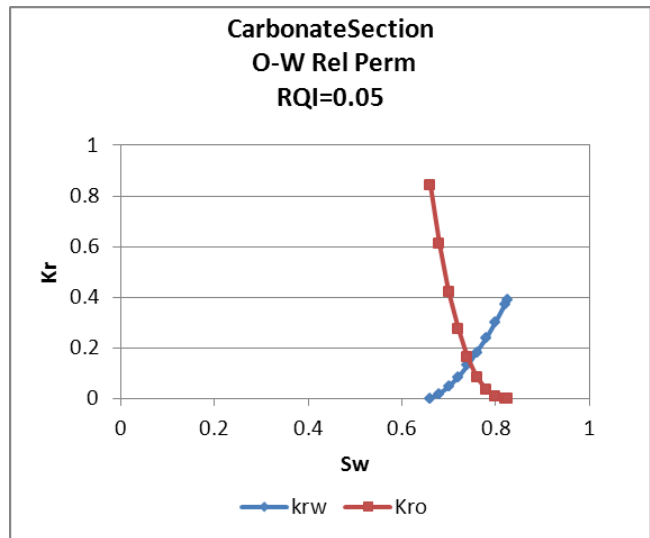


**Figure C8: Relative permeability curve for the carbonate section at RQI=0.05**





## Appendix B

### Pressure Transient Analysis in the Arbuckle (Step-Rate Test, Interference Test, and DST Analysis)

#### Description of the Step-Rate Test

A step-rate test was performed in August 2011 in well 1-32 at gauge depth of 5,025 ft using the pump schedule described below. Pressure responses were measured at observation well 1-28.

- A) Pump at 2 bpm for 20 minutes, then shut down for 15 minutes.
- B) Pump at 5 bpm for 20 minutes, then shut down for 15 minutes.
- C) Pump at 7.5 bpm for 20 minutes, then shut down for 15 minutes.
- D) Pump at 10 bpm for 20 minutes, then shut down for 15 minutes.
- E) Pump at 12.5 bpm for 20 minutes, then shut down for 15 minutes.
- F) Pump at 13.4 bpm for 20 minutes, then shut down for 23 minutes.
- G) Pump at 13.4 bpm for 1 hour 5 minutes, then shut down for 16 minutes
- H) Pump at 9.4 bpm for 35 minutes, then shut down. End of pumping.

#### Step-Rate Test Analysis

The step-rate test consisted of eight injection periods and eight fall-offs (fig. 1). All eight injection periods were selected and modeled (simulated) by Fekete WellTest commercial software. Because all injection periods were selected in this model, the model tries to match the pressures in all periods at the same time with a single skin. Measured pressures were simulated, and permeability and skin were calculated. Measured pressures are in good agreement with calculated pressures (fig. 1). However, an accurate match between the calculated and measured pressures with a single skin is not possible because each injection period has a different skin. An induced fracture occurred at injection period 5; fracture pressure and closure pressure were calculated and are discussed in following sections.

#### Results

Calculated permeability from the step-rate test is 113 mD for a 30 ft interval that is in vertical communication based on vertical permeability and Lorenz plot (fig. 11) ;where, results of flow units and flow capacity( $\Sigma kh\%$ ) are shown in figure 12. Calculated permeability from the analysis is close to the log-derived average permeability (74 mD) for the same interval. There are vertical barriers above and below this interval, and 25 ft of the interval is perforated. The calculated skin for injection period 7 is -7.6. This skin was used in the analysis for all injection periods.

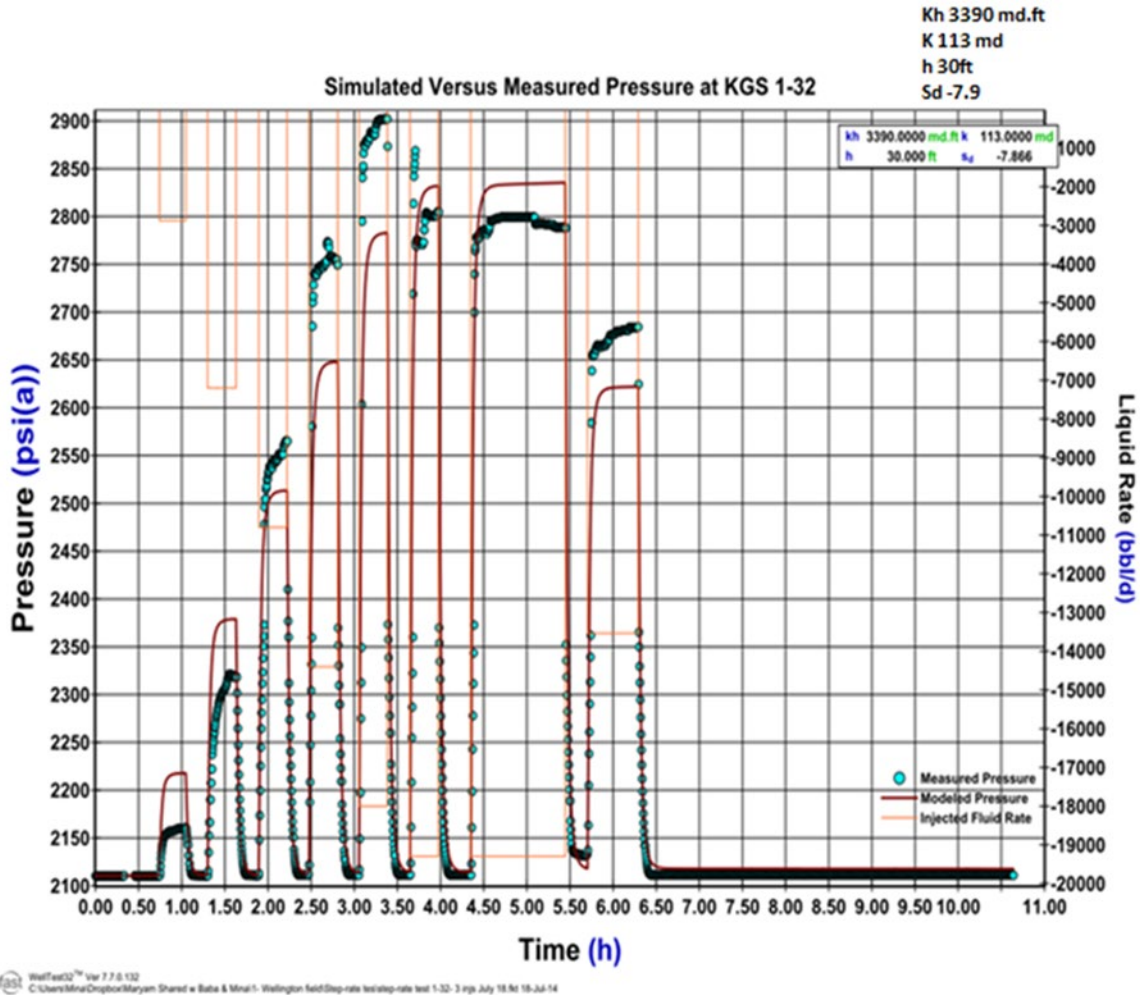


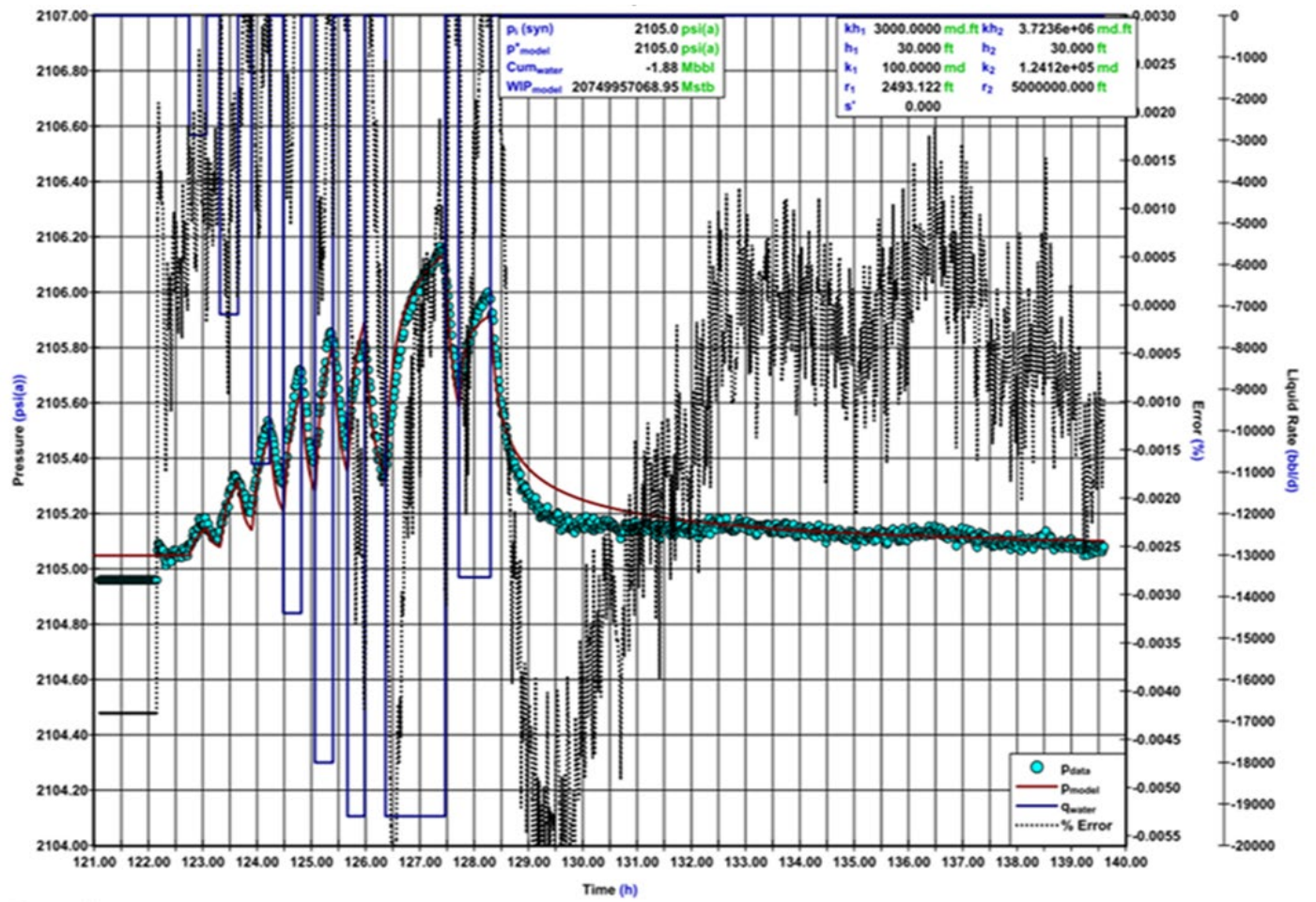
Figure 21. Simulated pressures in red versus measured pressures.

## Interference Test Analysis

Well 1-32 was the injection well, and pressure responses were measured at observation well 1-28. The distance between wells 1-32 and 1-28 is 3,500 ft.

### Results of the Interference Test Analysis

Pressure transient data of well 1-28 were modeled using a composite dual porosity-permeability model (zone/region 1 and 2). The composite model resulted in a better match between modeled pressures and measured pressures (fig. 2). Based on this model, permeability in the vicinity of well 1-32 to a radius of 2,493 ft (region 1) has a lower value (100 mD) for the 30 ft interval that is in vertical communication than permeability from a radius of 2,493 ft to the vicinity of 1-28 (region 2), where the value increased to 124 D (fig.3). Permeability for region 1 is close to the log-derived average permeability (74 mD). Greater permeability for the farther radius is associated with a fracture or runs from 1-32 toward 1-28. Figure 4 shows results of the dual porosity-permeability model with its associated parameters and calculated permeability and skin.



WellTest02™ Ver 7.7.0.132  
 C:\Users\MinalDrozbox\Marvam Shared w Baba & Minal-1-Wellington field\Step-rate test\Step-rate test 1-28-Mina-MFA-2 (2).ft 15-Jul-14

Figure 22. Interference analysis results (modeled pressures in red and measured pressures in blue).

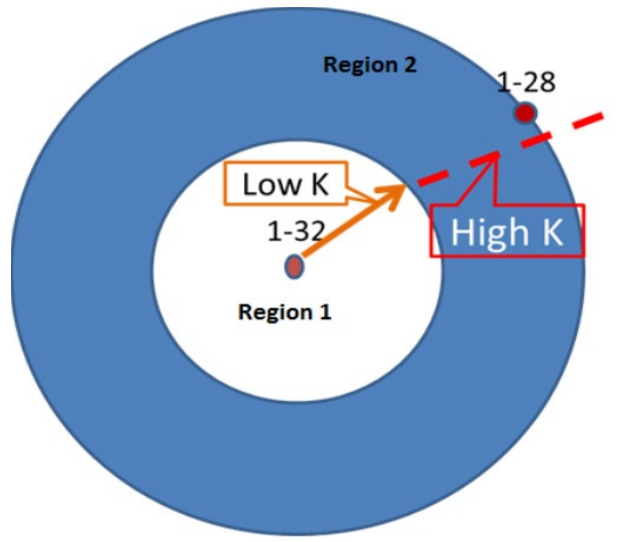


Figure 23. Diagram of Interference analysis showing regions 1 and 2 associated with two permeabilities.

Reservoir	Zone 1	Zone 2
$s_D$ -7.800	$k_1$ 100.0000 md	$k_2$ 1.2412e+05 md
$D$ 0.000 1/MMscfd	$h_1$ 30.000 ft	$h_2$ 30.000 ft
<input checked="" type="checkbox"/> Changing Wellbore Storage	$\mu_1$ 0.7011 cP	$\mu_2$ 0.7011 cP
$C_{wD}$ 640000.000	$\phi_{t1}$ 5.00 %	$\phi_{t2}$ 5.00 %
$V_w$ 250.481 bbl	$S_{g1}$ 0.00 %	$S_{g2}$ 0.00 %
$C_D$ 800.000	$S_{o1}$ 0.00 %	$S_{o2}$ 0.00 %
$C_{pD}$ 100.000	$S_{w1}$ 100.00 %	$S_{w2}$ 100.00 %
Parameters	$c_{r1}$ 3.0000e-06 1/psi	$c_{r2}$ 3.0000e-06 1/psi
$r_w$ 0.300 ft	$c_{t1}$ 4.7707e-06 1/psi	$c_{t2}$ 4.7707e-06 1/psi
<input checked="" type="checkbox"/> Observation Well	Boundary	Boundary
$r_o$ 3500.000 ft	$r_{s1}$ 2493.122 ft	$r_{s2}$ 5000000.000 ft
Extrapolated Pres. ( $p^*$ )	<input checked="" type="checkbox"/> Dual Porosity	<input checked="" type="checkbox"/> Dual Porosity
$t_{sh}$ 12.00 month	$\omega_1$ 0.001	$\omega_2$ 0.001
Forecast Rate Calcs.	$\lambda_1$ 5.2285e-10	$\lambda_2$ 1.3292e-07
$t_{row}$ 12.00 month		
$p_{row}$ 349.8 psi(a)		

Figure 24. Results of the interference analysis showing the dual porosity-permeability model and its associated calculated permeability and skin.

## Fracture/Breakdown Pressure Calculation

Fracture occurred at injection period 5, where injection pressure exceeded formation fracture pressure. Fracture (breakdown) pressure is about 2,900 psi (figs. 5 and 6). The fracture gradient is 0.58 psi/ft in the Arbuckle at the gauge depth of 5,025 ft.

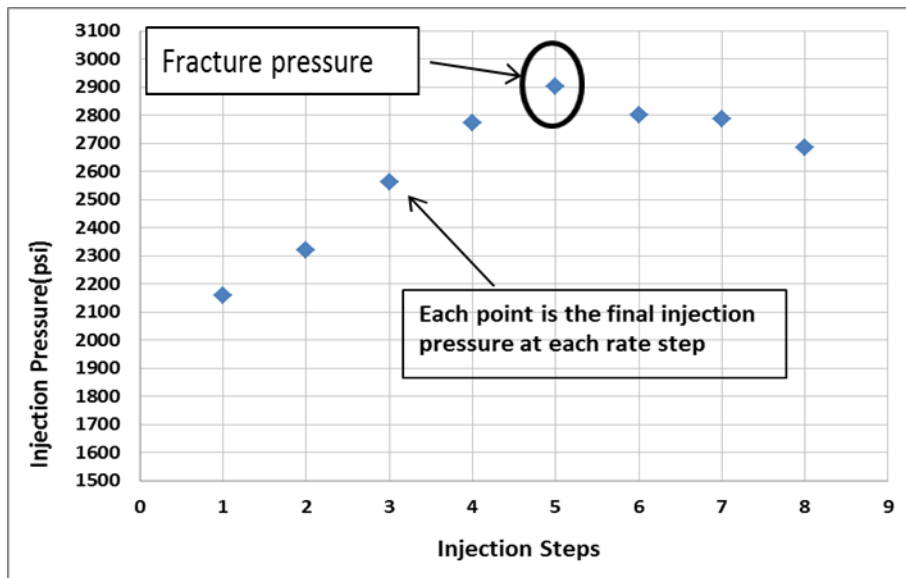


Figure 25. Injection pressure versus injection step showing that fracture occurred at injection step 5.

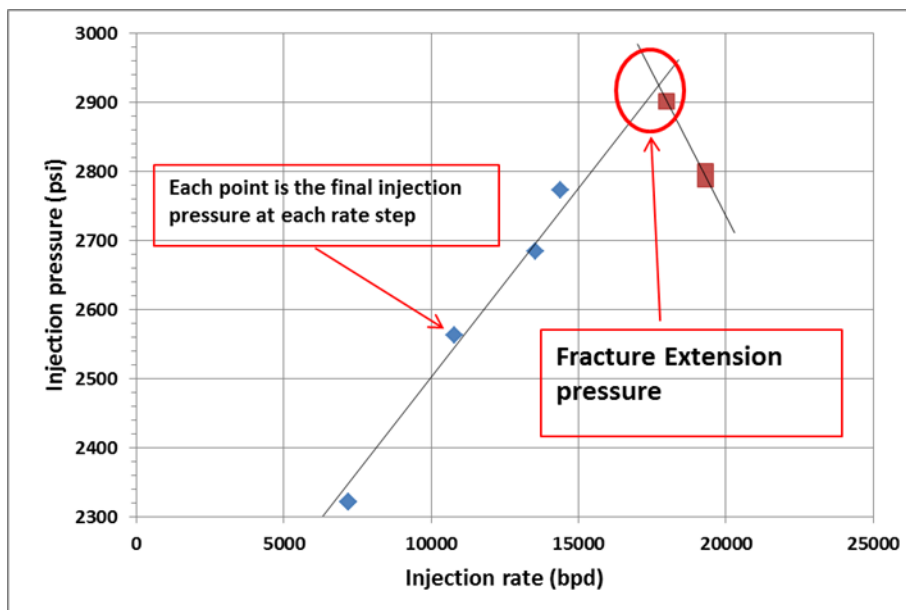


Figure 26. Injection pressure versus injection rate (bbl/D) where the intersection is the fracture pressure.

### Determination of Closure Pressure/Minimum Stress

Fracture occurred on rate step 5, and the fracture remained open during injection periods 5 and 6 until the injectivity index started to drop (fig. 7). The fracture closes at the point where the injectivity index returns

to its value before initiation of fracture. Closure pressure or minimum stress is slightly less than 2,666 psi, and its gradient is 0.53 psi/ft (fig. 8). One or two more rate steps at lower rates were needed to give a more accurate closure pressure.

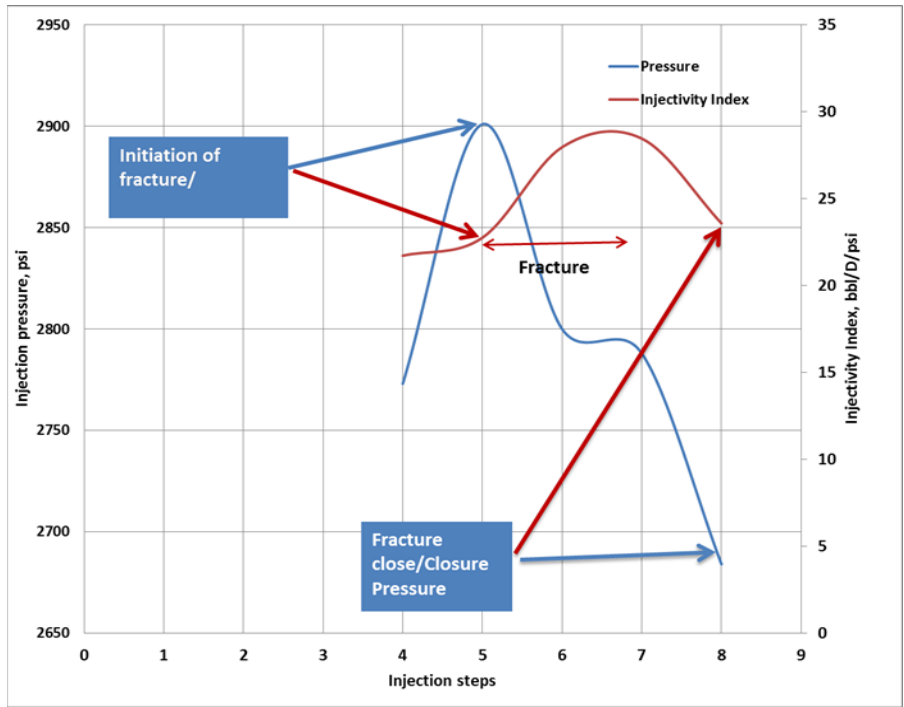


Figure 27. Injection pressure versus injection steps.

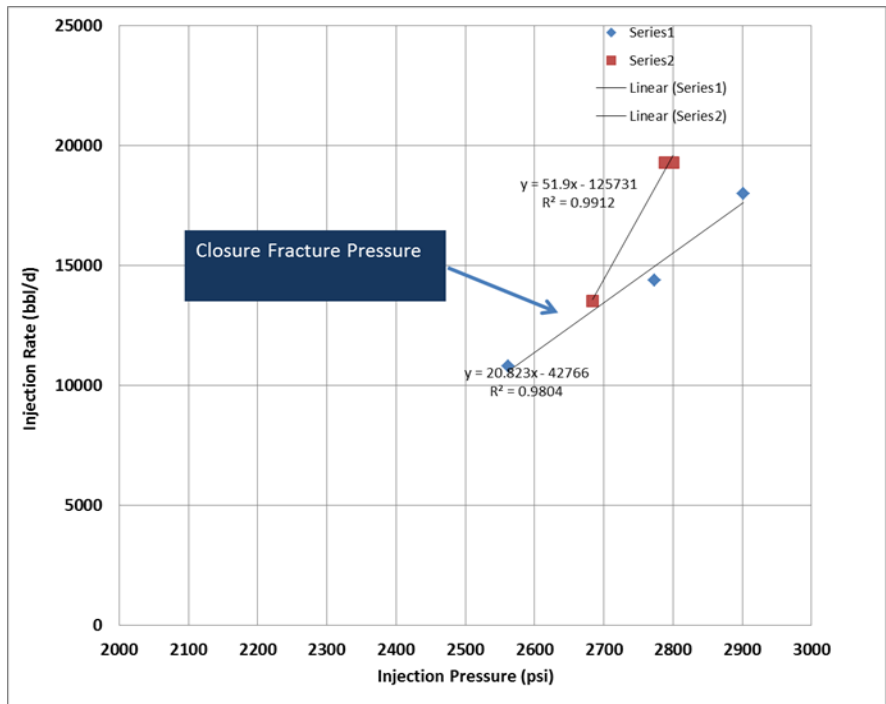


Figure 28. Injection rate versus injection pressure.

## DST Analysis in Well 1-32 and 1-28

### DST Validity in Well 1-32

Only DST 1 and 4 are valid for analysis. DST 2 and 3 are not suitable for analysis, and they would give inferior results if they were analyzed. Flowing pressure of DST 2 is equal to shut-in pressure; therefore, there is no build up to be analyzed. Only temperature and reservoir pressure are valid in DST 2. The same issues apply to DST 3.

### DST Results

DST 4 was analyzed by the FEKETE WellTest build up module, and permeability and skin were calculated (fig. 9). The test interval was 4,175–4,190 ft.

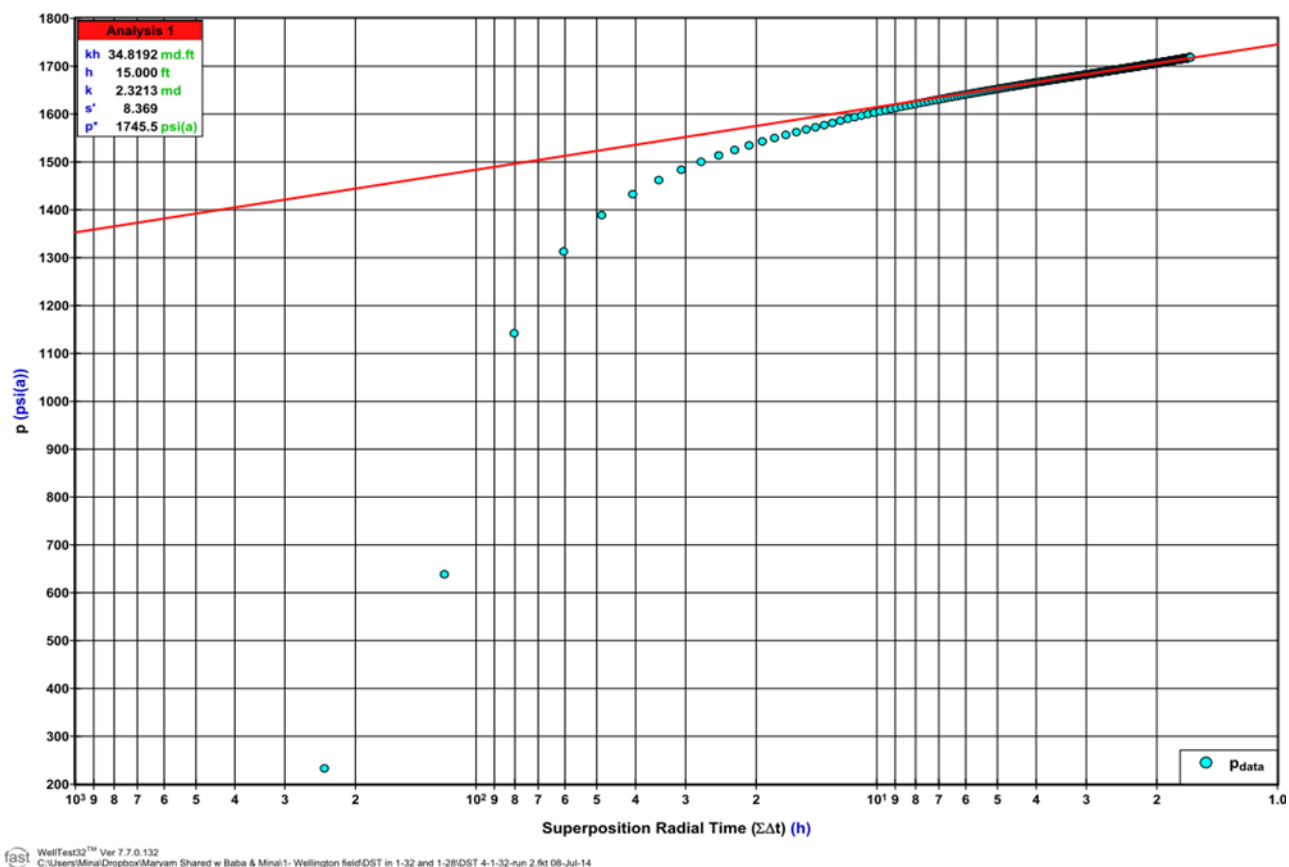


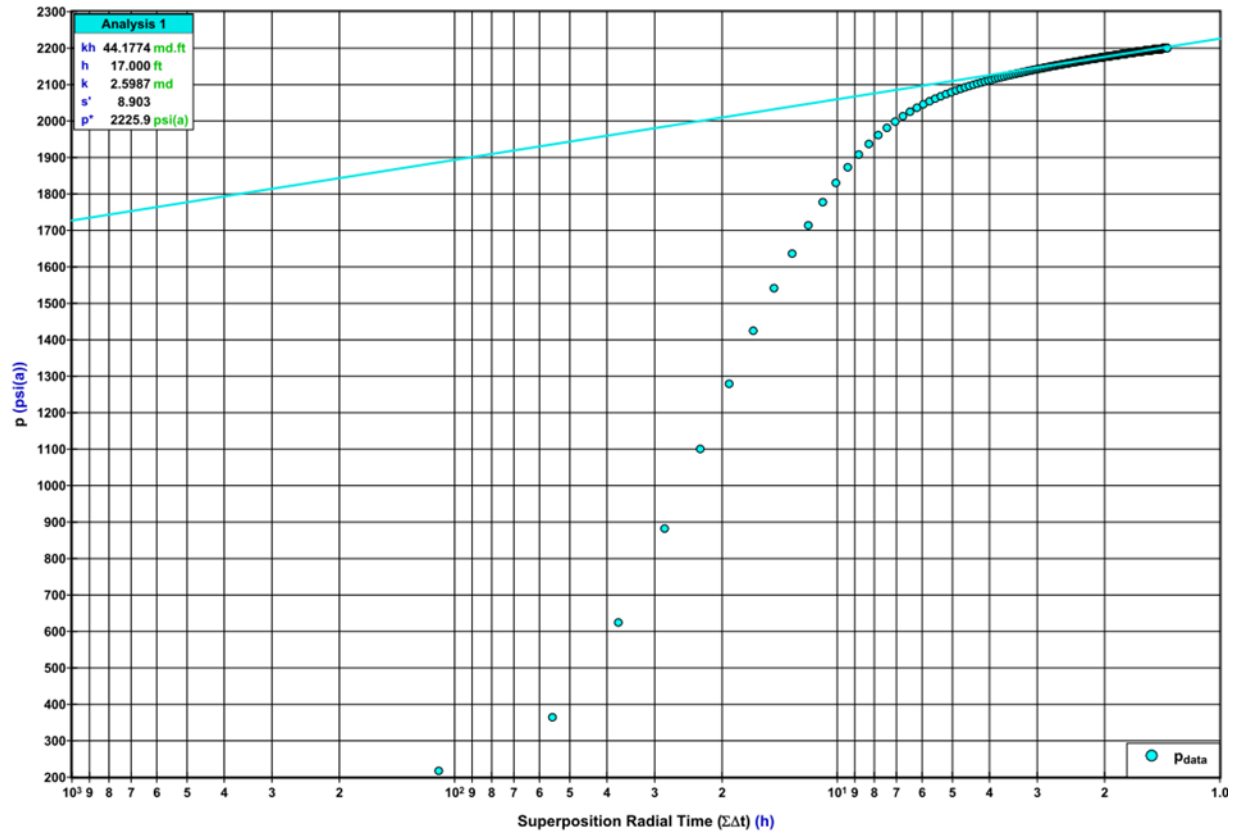
Figure 29. DST 4 radial flow analysis results.

### DST Validity in Well 1-28

Only DST 1 is valid for analysis. DST 2 has a short flow period and does not have a transient period. Only reservoir pressure measurements during shut-in periods from DST 2 are valid. DST 3 and 4, like DST 2, have short transient times and are not valid for analysis.

## Results of DST 1

DST 1 was analyzed by the FEKETE WellTest build up module, and permeability and skin were calculated for test interval 5,133–5,250 ft.



WellTest32™ Ver 7.7.0.132  
C:\Users\Minat\Dropbox\Marvian Shared w Baba & Minat\1-Wellington field\DST in 1-32 and 1-28\DST-1-28-5.9t 09-Jul-14

Figure 30. DST 1 radial flow analysis results.

## Results of Calculated Permeability from Pressure Transient Analysis (Step-Rate, Interference, and DSTs) Compared to Log-Derived Permeability and Core Permeability 90 Degree (If Available)

Well 1-32				
DST Interval	K from DST	Log connectivity	Average Log Derived K90	Average Core K90
ft	mD	ft	mD	mD
4175-4190	2.32	4175-4090	4.61	4.59

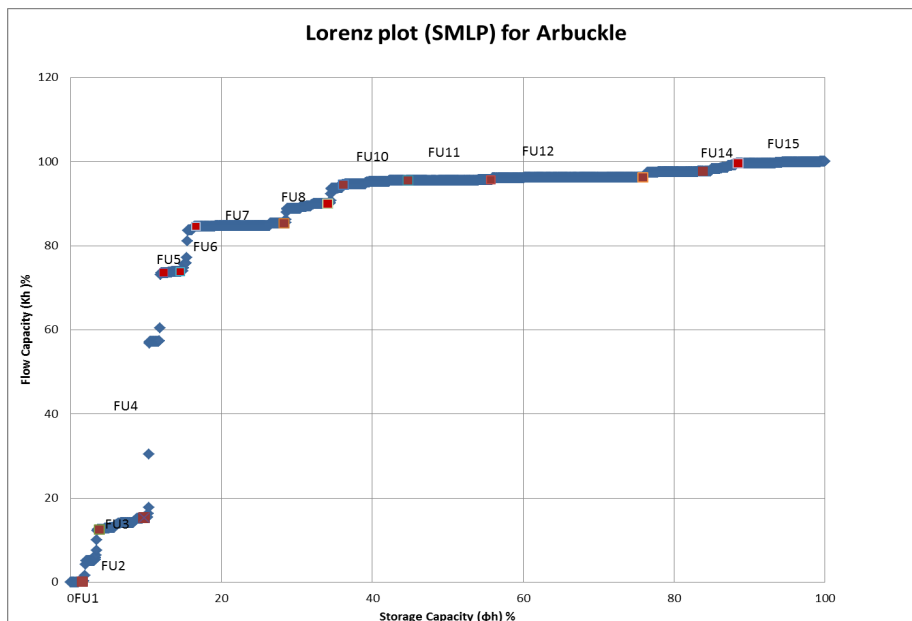
Well 1-28				
DST Interval	K from DST	Log Connectivity	Average Log Derived K90	Average Core K90
ft	mD	ft	mD	mD
5133-5250	2.60 mD	5133-5160	2.17 (5133-5160)	NA

Step-Rate Test results				
Interval	Gauge Depth@	K from Step-Rate Test	Average Log Derived K90	Average Core K90
ft	ft	mD	mD	mD
30	4869	113	74	NA

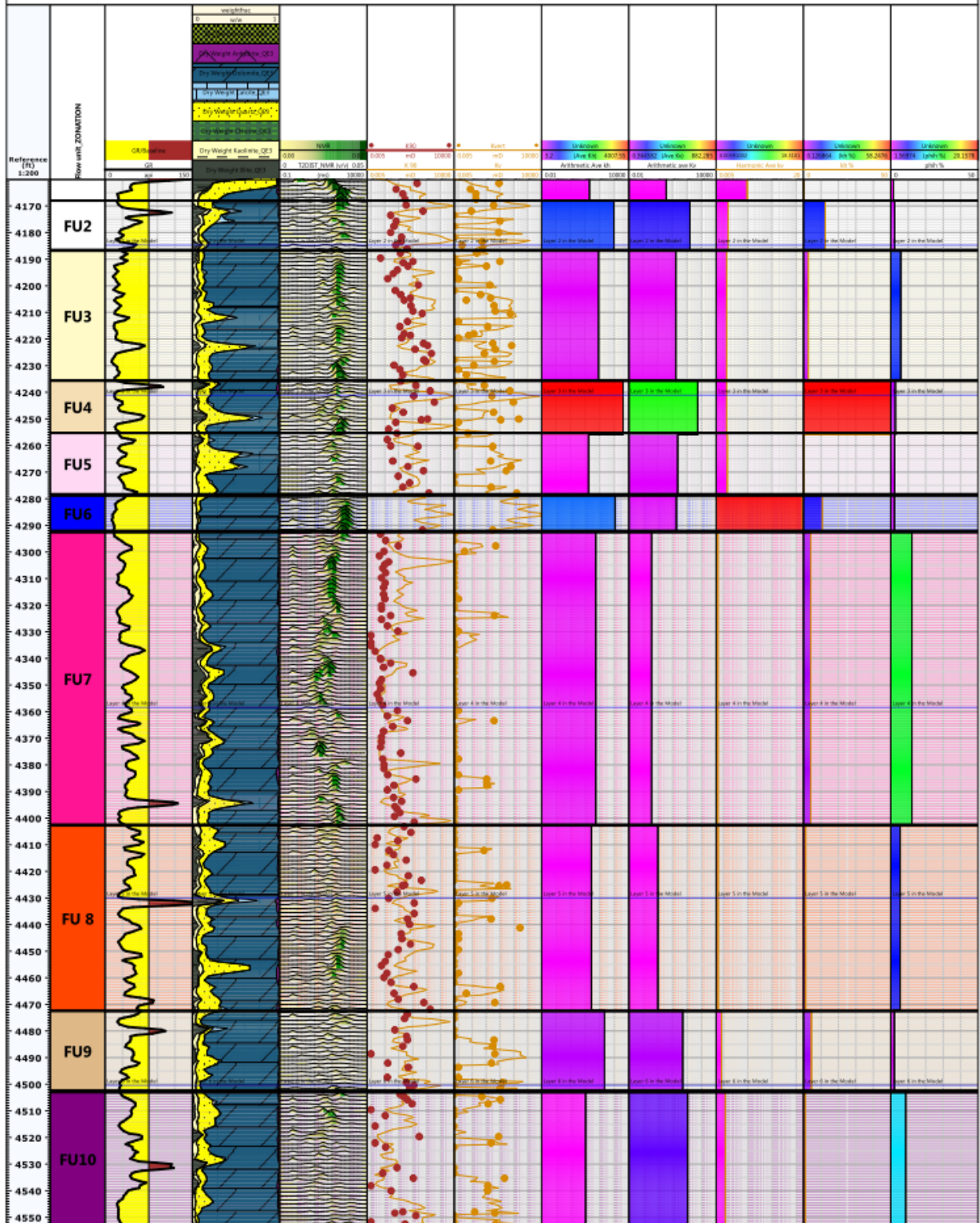
  

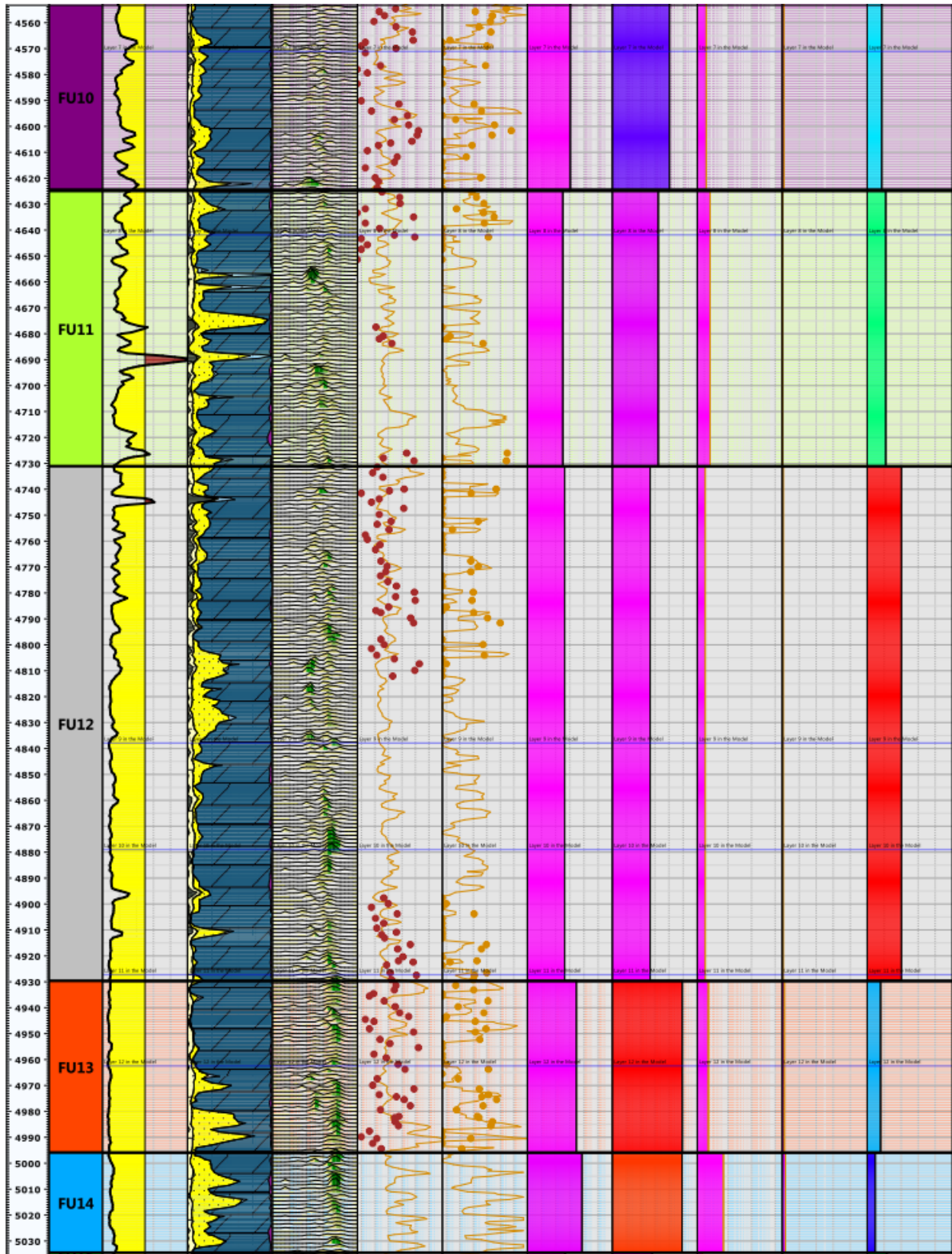
Interference test result				
Interval	K for Zone 1	K for Zone 2	Ave K90 from Log for Zone1	Average Core K90
ft	mD	D	mD	mD
30	100	124	74	NA



**Figure 31. Lorenz plot (SMLP) and flow units FU1 to FU15.**

Well: WELLINGTON KGS #1-32





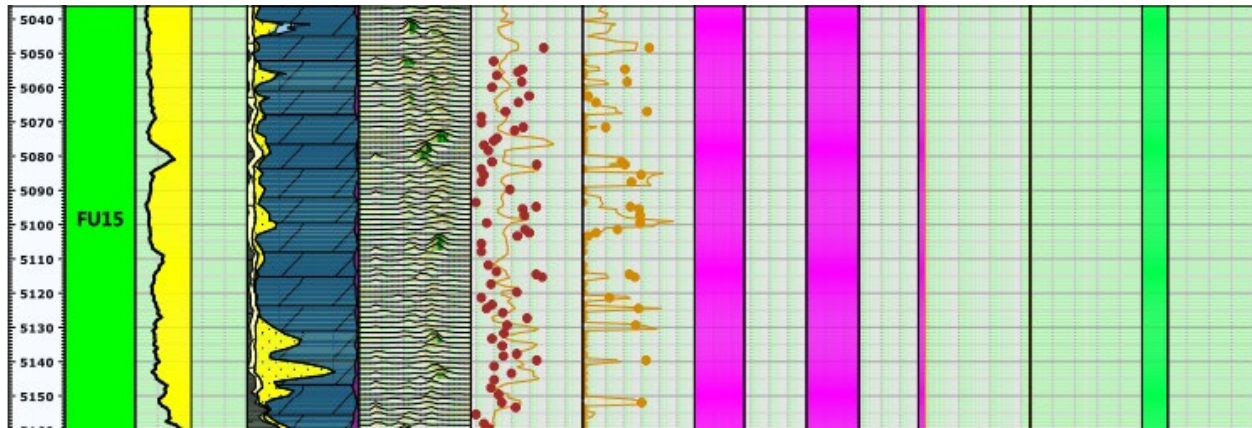


**Figure 32. Layout of 1-32 showing flow units from Lorenz plot and flow capacity ( $\Sigma Kh\%$ ).**

### **Conclusion**

- Permeability values calculated from step-rate and interference tests are close to log-derived permeability values.
- The lower permeability value (74 mD) from the interference analysis is matrix permeability and is in agreement with log-derived permeability (100 mD).
- Greater permeability (124 D) in zone/region 2 from the interference test analysis is associated with a radius farther from the 1-32 wellbore to the vicinity of well 1-28. This greater permeability, which is not matrix permeability, is associated with fault or fracture.
- Composite dual porosity-permeability model resulted in accurate permeability estimations in the two regions.
- Permeability values calculated from DSTs in wells 1-32 and 1-28 are in agreement with log-derived permeability and core data, when present.

## Appendix C

### Mississippian Reservoir

#### I- Introduction

There are 17 wells with complete suites of porosity and resistivity logs available in sections 28, 29, 32, 33, and 2-32 drilled from 1956 to 2016. Also, there were five older wells with older completion dates from 1936 to 1948. These wells had one porosity log, usually neutron logs with no scale or counts/API units. Resistivity logs were not recorded in these wells. The neutron logs of the five older wells were normalized with the neutron logs of the key well (1-32) and then converted to the equivalent formation porosity using Well 1-32. The 17 newer wells were quality controlled and analyzed by Techlog in terms of porosity, water, oil saturation, and minerals. Three of these 16 wells (1-32, 1-28 and 2-32) had NMR logs. The NMR logs were analyzed by Techlog to derive effective porosity, Coates permeability and Pc curves. Only Well 1-32, 2-32 and Peasel 1 had core data. These core data had porosity, permeability (90 degree and maximum), and matrix density. Based on the production history of the field, the field production started in 1929 without any significant water production prior to 1943. Newer wells were drilled after this date and must be invaded by formation water or water flood. Therefore, water saturation derived from Techlog using resistivity logs is not representative of initial water saturation of the reservoir. Moreover, the older wells didn't have any resistivity logs; therefore, initial water saturation couldn't be derived from resistivity logs.

Well 1-32 has the most complete set of data and was used as the key well. Routine core data of this well was analyzed by FZI method, and FZI was correlated with log-derived porosity and water saturation of this well (NMR irreducible water saturation). Based on irreducible water saturation and porosity, permeability in Well 1-32 was estimated, which matched very well with core data. Since initial water saturation was not available in other wells to be converted to irreducible water saturation to find permeability, permeability of these wells were estimated by another technique. The reservoir was divided into six zones based on log signatures and FZI, and then the permeability of each zone was estimated.

#### II. Permeability Determination

##### a. Permeability of Well 1-32

Permeability of this well can be obtained by different methods and different sources of data. The basic permeability data source is routine core analysis, which was discussed above. Another method is Coates equation (equation 3), which relates permeability to porosity, FFI, and BWT:

$$K_{\text{Coates}} = A * (10 * \phi)^B * \left(\frac{\text{FFI}}{\text{BWT}}\right)^C \quad (\text{Equation 3})$$

Coates permeability was calculated using FFI and BWT from NMR; however, different A pre-factors in the above equation were used in different intervals of the reservoir to match Coates permeability with core permeability.

The reservoir was divided into three intervals and the following pre-factors were applied.

- Zone 1: from 3,658 to 3,668 ft, A= 4.5
- Zone 2: from 3,668 to 3,720 ft, A=0.8
- Zone 3: from 3,720 to 4,100 ft, A=3

Coates permeability is compared with core data in fig. A3 (Appendix A). The match between Coates permeability and core data is acceptable but not perfect. In addition to Coates, permeability of this well was obtained according to “*Determination of Reservoir Permeability based on Irreducible Water Saturation and Porosity from Log Data and Flow Zone Indicator (FZI) from Core*, IPTC-17429.” Equation 4 was used to calculate permeability.

$$K = 1014 \left[ \frac{a}{S_{wir}\phi_e} + b \right]^2 \frac{\phi_e^3}{(1-\phi_e)^2} \quad (\text{Equation 4 or FZI-SWIPHI})$$

Constants **a** and **b** in the above equation can be found by relating FZI to  $\frac{1}{S_{wir}\phi_e}$  as follow:

$$FZI = \frac{a}{S_{wir}\phi_e} + b \quad (\text{Equation 5})$$

For this purpose, FZI from core was statistically related to the reciprocal of porosity and irreducible water saturation from NMR. To find the right constants, the reservoir interval had to be divided into two zones, A and B. Zone A is mainly the chat conglomerate sequence, which has bimodal T2 distributions; the dolomite and limestone sections below the chat conglomerate, generally, have single modal pore size distribution (fig. A3—Appendix A2) (zone A and B). Due to changes in T2 distribution shape, two correlations were necessary. The first correlation is derived for zone A (chat conglomerate), which is shown in fig. 1 and equation 6.

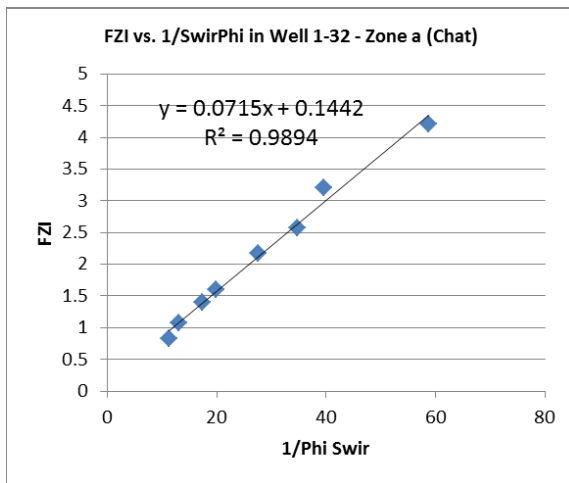


Figure 1: FZI vs. 1/PhiSwir for zone A (chat)

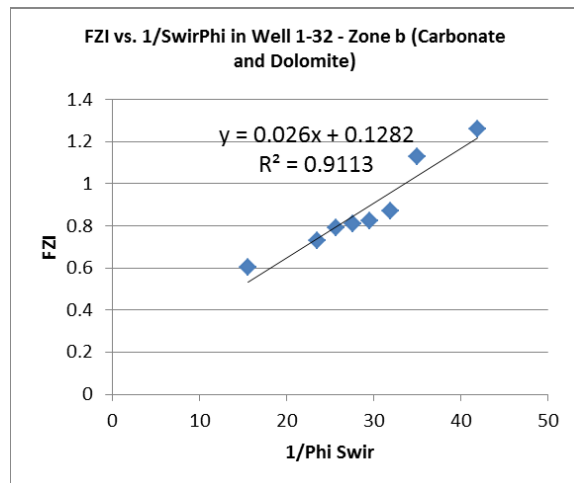


Figure 2: FZI vs. 1/PhiSwir for zone B (dolomite and carbonate)

The permeability equation for zone A is given in equation 7.

$$FZI_{ZoneA} = \frac{0.0715}{S_{wir}\phi_e} + 0.1442 \quad (\text{Equation 6})$$

$$K = 1014 \left[ \frac{0.0715}{S_{wir}\phi_e} + 0.1442 \right]^2 \frac{\phi_e^3}{(1-\phi_e)^2} \quad (\text{Equation 7})$$

For zone B, the correlation between FZI and  $\frac{1}{S_{wir}\phi_e}$  is obtained and illustrated in fig. 2. Substituting FZI in the Tiab equation by this correlation, the following permeability equation (equation 9) for zone B is obtained.

$$FZI_{ZoneB} = \frac{0.026}{S_{wir}\phi_e} + 0.1282 \quad (\text{Equation 8})$$

$$K = 1014 \left[ \frac{0.026}{S_{wir}\phi_e} + 0.1282 \right]^2 \frac{\phi_e^3}{(1-\phi_e)^2} \quad (\text{Equation 9})$$

Equations 7 and 9 were applied respectively to zones A and B of Well 1-32 and permeability versus depth was generated. Permeability by this method matches better with core data as shown in fig. A3 (Appendix A) (FZI-SWPHI). This method could, easily, be applied to all of the wells in the field if initial water saturation and porosity existed. Initial water saturation data can be converted to irreducible water saturation by a method that was discussed in the paper. However, in the Wellington Field, application of this method to other wells is not practical due to lack of initial water saturation due to logging after a long period of water flooding in the Mississippian reservoir.

#### **b. Permeability in Well 2-32**

Well 2-32 has NMR log data, and two methods can be used to determine its permeability. 1) Coates permeability in this well was obtained using the same **A** factors that were used in Well 1-32. 2) Permeability was calculated for this well using equation 4.

Coates permeability is compared to permeability by equation 4 in fig. 3 (Appendix A) where there is a better match between permeability by equation 4 with core data.

#### **c. Permeability in Well 1-28**

Well 1-28 has NMR log data, and two methods were used to determine permeability in this well. 1) Coates permeability in this well was obtained using the same **A** factors that were used in Well 1-32.

2) Permeability was calculated for this well based on assigned FZI values to different zones of the reservoir and calculation of permeability by the Tiab equation (Equation 10). The method of assigning FZI will be discussed in the next section.

Coates permeability is compared with the second approach in fig. A10 (Appendix A), where there is a better match between permeability by the second approach with core data.

#### **d. Equivalent FZI Zones in Other Wells Corresponding to Well 1-32 FZI**

Equations 7 and 9 could be used for permeability determination in all of the wells, if reliable initial water saturation existed in these wells (initial water saturation can be converted to irreducible water saturation by Pc equations). This method could not be used effectively in this case because log-based water saturations are generally affected by oil production from the reservoir and water injection in the reservoir. Another

method, which has often been used and is described in the literature, is relating FZI from core in the key well with log signatures through regression or Neural Network and subsequent application of the resulting correlation to other wells with similar logs. It is doubtful that this process gives accurate results in the Mississippian formation because, generally, wells are old and do not have high-quality logs. In addition, the method works better if a deep resistivity log is included in regression analysis for correlation determination. However, in this field, deep resistivity in Well 1-32 and other wells is affected by production or water injection.

Another method is proposed, which is not ideal and is not theoretically correct but which might provide the best possible permeability model for predicting permeability based on the existing data.

Comparison of T2 distribution, before hydrocarbon correction, in Well 1-32 and Well 1-28, shows that there are intervals with similar shape and size of pore in both of the wells. It is concluded that tortuosity, shape factor of grains and surface area per grain volume are similar in both wells in co-relatable intervals. Therefore, it can be said that zones of equal FZI exist in both of the wells.

FZI values of Well 1-32 are plotted versus depth in fig. A3 (Appendix A). Study of FZI variation with depth indicates that the reservoir can be divided into six zones (3 zones in chat and 3 zones in the carbonate interval), each zone with a distinct average FZI. These zones are shown in fig. A4 (Appendix A) and table 1:

**Table 1: Average FZI in six zones of Well 1-32**

<b>Zone</b>	<b>from (ft)</b>	<b>to (ft)</b>	<b>FZI (<math>\mu\text{m}</math>)</b>
1	3,656	3,659	2.605
2	3,659	3,662.5	1.618
3	3,662.5	3,665.5	4.285
4	3,665.5	3,698.5	1.007
5	3,698.5	3,720	0.476
6	3,720	3,766	0.925

It is assumed that equivalent zones with equal FZI value exist in other wells, which can be defined by log correlation. Porosity, density, and GR logs of the wells were used to find equivalent zones in other wells corresponding to six zones of Well 1-32. Well cross sections of figs. A5–A9 (Appendix A) show boundaries of the zones in other wells. FZI values in table 1 were assigned to respective zones in other wells and a permeability log was generated, as will be discussed below.

#### **e. Permeability in Well Peasel 1**

Well Peasel 1 had core data, which are plotted in fig. A11 (Appendix A). Average FZI values from Well 1-32 were assigned to equivalent zones in well Peasel 1, and permeability of this well was calculated based on assigned FZI values using the Tiab Equation (equation 10). The calculated permeability is also plotted in fig. A11 (Appendix A) and is compared with core permeability. There is a good match between the derived permeability using FZI and core data.

#### f. Permeability in Other Wells

It was assumed that each zone in figs. A5–A9 (Appendix A) had a specific FZI value; these are listed in table 1. This assumption is approximately but not theoretically correct and may give a good estimate of permeability in other wells, where no other viable and more accurate method exists. Based on FZI of each zone and effective porosity of the wells, the permeability of all zones in all wells was calculated using the Tiab equation (equation 10).

$$K = 1014 \text{ FZI}^2 \frac{\phi_e^3}{(1-\phi_e)^2} \quad (\text{Equation 10})$$

Although there was a good match between calculated permeability by this method in well Peasel 1 with core permeability, it is admitted that the predicted permeability in other wells, except for Well 1-32 and Well 1-28, are not ideal. However, considering the available data, it is believed it is the best that could be estimated. Calculated permeability data of wells are shown in Figs. A10 to A24 (Appendix A).

The obtained permeability data can be used in the construction of the dynamic model of the reservoir. During history matching of the dynamic model, when there is mismatch, permeability of the well can be multiplied by a factor to obtain the desired match between actual production data and simulation results. By this procedure, model permeability could be improved.

### III. Calculation of Capillary Pressure Curves Prior to Receiving SCAL Data

Available data for determination of Pc curves are generalized Pc curves for the Mississippian formation, NMR data of Well 1-32 and Well 1-28. Data used to generate Pc curves for both chat and carbonate sequences of this reservoir were drawn mainly from key well (Well 1-32). The shape of the generalized Pc curves was also used in the process.

Often Pc curves are related to the permeability of the rock or the FZI in the literature, while in geological sedimentary environments, different Pc curves could exist for a single permeability or a specific FZI. In this work, endpoints of Pc curves (entry pressure, irreducible water saturation) and therefore the Pc curve of a rock are related to its Reservoir Quality Index (RQI). In this section, using data of the key well and generalized data, Pc curves are defined for different RQI values in the Mississippian formation. Since permeability in all wells against depth is found according to Section I of this report, RQI at each depth can be determined and Pc curves based on RQI can be applied to all wells to find initial water saturation. Often the grid of the dynamic or static model of the reservoir is divided into several saturation regions, each with a specific RQI. Pc curves and relative permeability tables are prepared for each region.

Both drainage and imbibition Pc curves were calculated for the reservoir. Depending on the path of oil migration into the Mississippian formation, either drainage or imbibition Pc curves could be applied to the model and wells to represent the initial condition of the reservoir.

Drainage and imbibition capillary pressure curves were calculated according to “A Novel Technique for Generation of Accurate Capillary Pressure (Pc) Curves from Conventional Logs and Routine Core Data and New Pc Endpoint Functions after Considering the Sedimentary Environment and Pore Throat size Distribution Shape (PTSDS).”

Eight capillary pressure curves were calculated for drainage and imbibition for nine average RQI values according to the paper cited above. The formula constitutes a function for the shape of Pc curves and functions for the end-points that are entry pressure ( $P_{\text{entry}}$ ) and Irreducible water saturation ( $S_{\text{wir}}$ ). The end-points are correlated to RQI.  $P_{\text{entry}}$  was calculated from entry radius (R15) and Winland R35 (R35). There is a relationship between R35 and R15 and a relationship between  $P_{\text{entry}}$  and R15; therefore,  $P_{\text{entry}}$  can be calculated from R15 derived from R35.  $S_{\text{wir}}$  was calculated from the NMR log at a Pc equal to 20 bars (290 psi). For calculating the imbibition curves, another term which is the residual oil saturation ( $SO_r$ ) was needed.  $SO_r$  was calculated based on a correlation that was derived based on SCAL data of other reservoirs and modified for this field.

#### a. Irreducible Water Saturation ( $S_{\text{wir}}$ )

Based on the paper mentioned above, there is a good correlation between irreducible water saturation of reservoir rocks and RQI. In the Mississippian reservoir, initial water saturation was not available from logs due to production of the field. However, NMR data from three of the wells can provide irreducible water saturation in these wells.

NMR data of Well 1-32 was used to determine the irreducible water saturation at a Pc of 20 bars (290 psi). Also interfacial tension between oil and water was entered in the TechLog Module to find  $S_{\text{wir}}$  versus depth for this well. Previously, permeability for the Mississippian in Well 1-32 was determined by equation 7 and equation 9. Based on porosity and calculated permeability of Well 1-32, RQI in this well was determined. Figure 5 plots the irreducible water saturation in Well 1-32 in the chat conglomerate against RQI.

Equation 15 was determined from Figure 5 that is the relationship between  $S_{\text{wir}}$  and RQI, where R2 is equal to 0.99, indicating good correlation.

$$S_{\text{wir}} = 0.0685RQI^{-1.082} \quad \text{Equation 15}$$

The same procedure was repeated for the carbonate section of the Mississippian formation. Figure 6 is the plot of  $S_{\text{wir}}$  vs. RQI for this section:

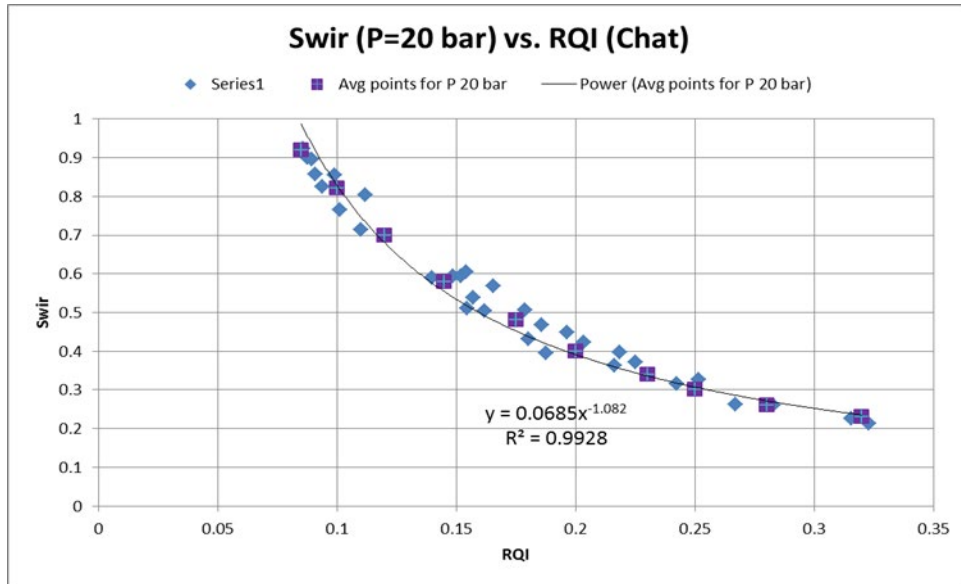


Figure 5: Swir vs. RQI for Zone zone A (chat)

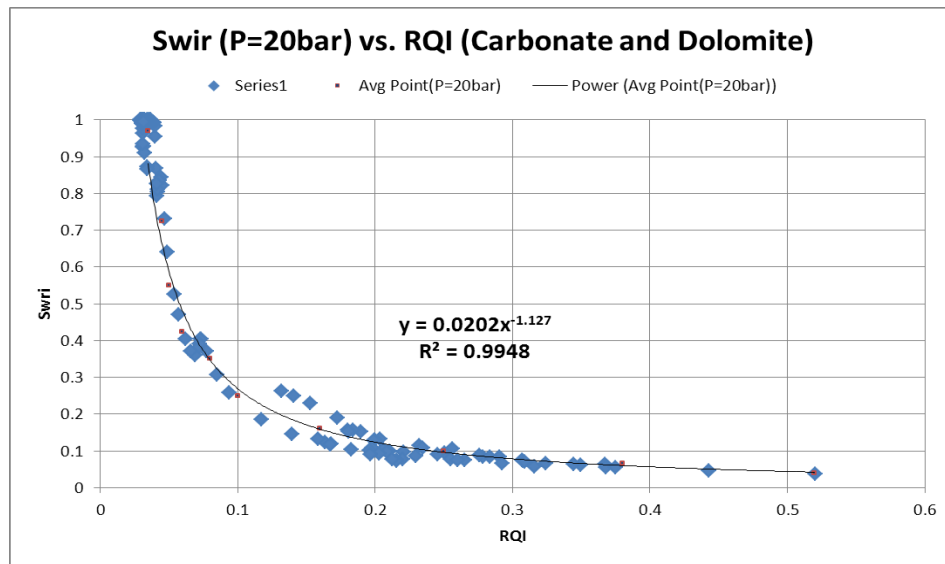


Figure 6: Swir vs. RQI for Zone zone B (carbonate and dolomite)

Equation 16 can be used to determine Swir for the carbonate section.

$$S_{wir} = 0.0202RQI^{-1.127} \quad \text{Equation 16}$$

### b. Entry Pressure (Pe)

There is a good correlation between capillary entry pressure and RQI. Entry pressure in Well 1-32 was determined from NMR data using oil and water interfacial tension. In the Mississippian formation, two correlations were obtained: one for the chat conglomerate and another for the carbonate section of this formation. Figure 7 plots entry pressure from the NMR against RQI in the chat conglomerate.

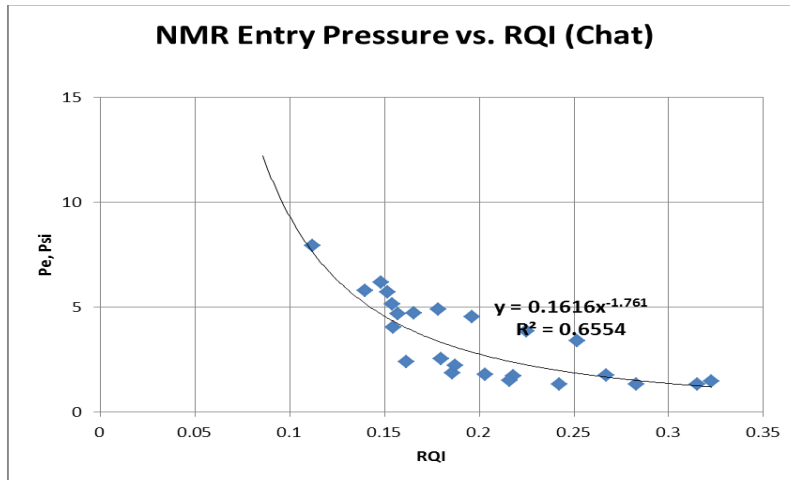


**Figure 7: Entry pressure vs. RQI in zone A (chat)**

The following equation shows that entry pressure is a function of RQI in the chat conglomerate.

$$P_e = 0.1616RQI^{-1.761} \quad \text{(Equation 17)}$$

Also, fig. 8 plots entry pressure versus RQI in the carbonate section. This plot results in equation 18, which relates entry pressure in this section with RQI.

$$P_e = 0.1467RQI^{-1.312} \quad \text{(Equation 18)}$$

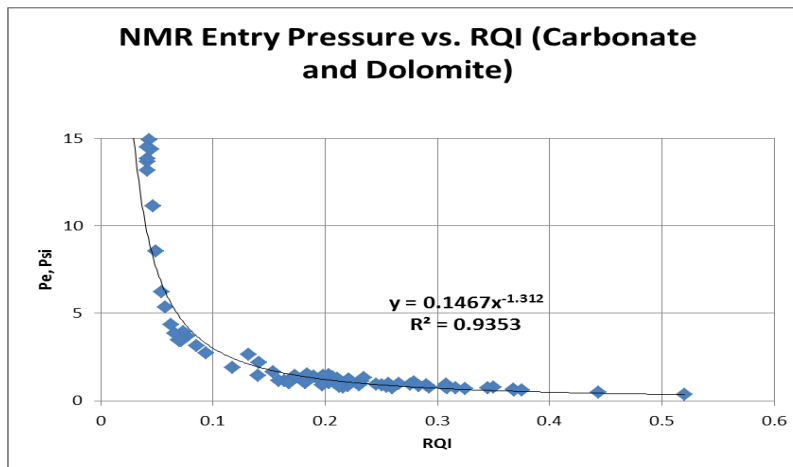


**Figure 8: Entry pressure vs. RQI in zone B (carbonate and dolomite)**

### c. Residual Oil Saturation

A correlation between residual oil saturation and RQI is necessary for derivation of imbibition capillary pressure curves. Reliable SCAL data for the Mississippian formation are not available at the present time to drive this correlation. In the absence of such data, the following correlation was used for the carbonate section. The correlation has been derived based on SCAL data of other reservoirs and modified for this field.

$$1 - S_{or} = 0.5811RQI^{-0.139} \quad (\text{Equation 19})$$

For the chat section of the Mississippian formation, the equation for the residual oil saturation has been adjusted to the following:

$$1 - S_{or} = 0.427RQI^{-0.407} \quad (\text{Equation 20})$$

#### d. Shape of Pc curves

A function between normalized non-wetting phase saturation ( $S_{nwn}$ ) and equivalent radius (EQR) is needed.  $S_{nwn}$  is defined according to equation 21.

$$S_{nwn} = \frac{1 - S_{wi}}{1 - S_{wir}} \quad (\text{Equation 21})$$

$S_{nwn}$  is a function of equivalent radius (EQR) (equation 22). Constants  $a$  and  $b$  in this equation will be found from the shape of generalized Pc curves later.

$$S_{nwn} = (1 - aEQR)(1 - EQR^b) \quad (\text{Equation 22})$$

EQR depends on entry pressure and capillary pressure (equation 23), where entry pressure is a function of RQI, which will be derived from the NMR log of Well 1-32.

$$EQR = \frac{P_e}{P_c} \quad (\text{Equation 23})$$

$S_{nwn}$  correlations were obtained for Chat and Carbonate individually.  $S_{nwn}$  was calculated for several water saturations along the curves for Chat and plotted against respective EQR, fig. 9.

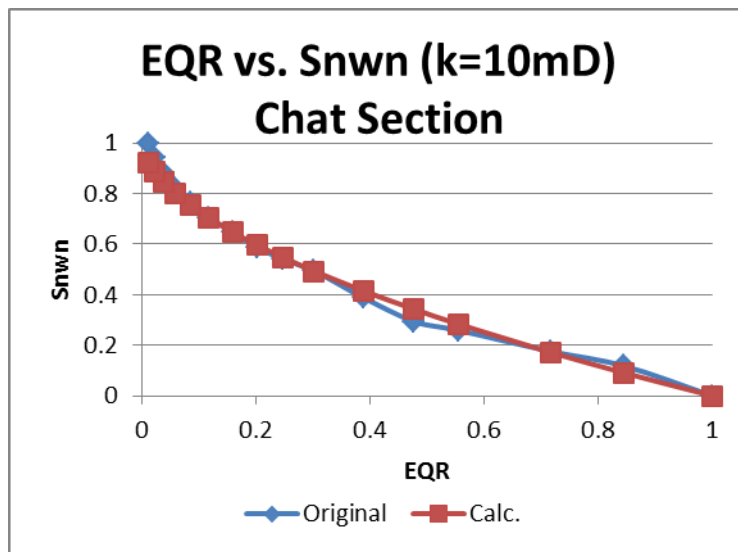
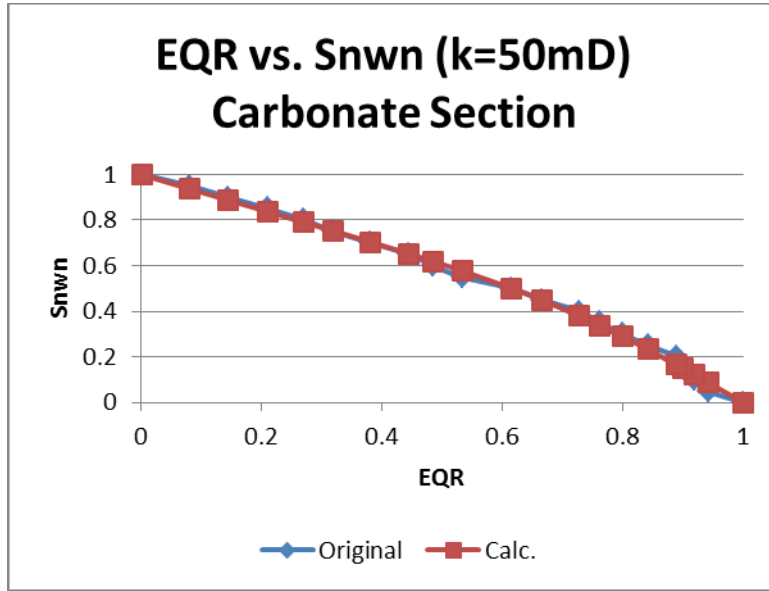


Figure 9:  $S_{nwn}$  vs. EQR for chat section at  $K=10\text{mD}$

Constants  $a$  and  $b$  of equation 22 were derived by regression and resulted in the following equation for the chat conglomerate of this reservoir.

$$S_{nwn} = (1 - 0.00155EQR)(1 - EQR^{0.5697}) \quad (\text{Equation 24})$$

$S_{nwn}$  was calculated for several water saturations along the curves for Carbonate and plotted against respective EQR, fig. 10.



**Figure 330:  $S_{nwn}$  vs. EQR for the carbonate section at  $K=50mD$**

Constants  $a$  and  $b$  of equation 22 were derived by regression and resulted in the following equation for the Carbonate zone of this reservoir.

$$S_{nwn} = (1 - 0.5245EQR)(1 - EQR^{3.1249}) \quad (\text{Equation 25})$$

#### e. Calculation of Drainage Capillary Pressure Curves

Equation 25 is proposed for drainage water saturation. According to equation 26, initial water saturation ( $S_{wi}$ ) is a function of  $S_{wir}$  and  $S_{nwn}$ . It was shown that irreducible water saturation is a function of RQI (equations 15 and 16) and  $S_{nwn}$  is a function of RQI and  $P_c$  (equations 22 and 23).  $S_{wir}$  and  $S_{nwn}$  in equation 26 can be replaced by respective functions and an equation can be obtained that expresses  $S_{wi}$  in terms of RQI and  $P_c$ .

$$S_{wi} = 1 - S_{nwn}(1 - S_{wir}) \quad (\text{Equation 26})$$

For the chat conglomerate, equations 15 and 22 were incorporated into equation 26 to obtain equation 27, which gives water saturation for every  $P_c$  and RQI.

$$S_{wi} = 1 - \left(1 - 0.0015 \frac{0.1616RQI^{-1.761}}{P_c}\right) \left(1 - \left(\frac{0.1616RQI^{-1.761}}{P_c}\right)^{0.569}\right) (1 - 12.885RQI^2 + 8.031RQI - 1.4924) \quad (\text{Equation 27})$$

It was decided to calculate eight capillary pressure curves for the chat conglomerate to be used in the reservoir model. RQI in chat ranges from 0.108 to 0.340. This range was divided into eight subdivisions (table 2).

**Table 2: Subdivisions of RQI range in chat section**

<b>RT</b>	<b>From</b>	<b>To</b>	<b>Avg RQI</b>
1	0.300	0.340	0.320
2	0.265	0.300	0.280
3	0.240	0.265	0.250
4	0.215	0.240	0.230
5	0.188	0.215	0.200
6	0.160	0.188	0.175
7	0.133	0.160	0.145
8	0.108	0.133	0.120

The mid-range of each subdivision was used to calculate eight Pc curves (equation 27, table 3). The generated Pc curves are shown in fig. 11. These curves are in agreement with generalized curves, when the right permeability and RQI are considered and compared.

**Table 3: Drainage Pc table for different RQI groups in the Mississippian chat**

a 0.0016	b 0.570	Drainage Table in Mississippian Chat						
RQI	0.32	0.28	0.245	0.22	0.2	0.175	0.145	0.12
Pe	1.20	1.52	1.92	2.33	2.75	3.48	4.84	6.76
Swir	0.23	0.26	0.3	0.34	0.4	0.48	0.58	0.7
Pc	Swi							
0	1.00	1.00	1.00	1.00	1.00	1.00	1.00	1.00
0.1	1.00	1.00	1.00	1.00	1.00	1.00	1.00	1.00
0.2	1.00	1.00	1.00	1.00	1.00	1.00	1.00	1.00
0.3	1.00	1.00	1.00	1.00	1.00	1.00	1.00	1.00
0.4	1.00	1.00	1.00	1.00	1.00	1.00	1.00	1.00
0.5	1.00	1.00	1.00	1.00	1.00	1.00	1.00	1.00
0.6	1.00	1.00	1.00	1.00	1.00	1.00	1.00	1.00
0.7	1.00	1.00	1.00	1.00	1.00	1.00	1.00	1.00
0.8	1.00	1.00	1.00	1.00	1.00	1.00	1.00	1.00
0.9	1.00	1.00	1.00	1.00	1.00	1.00	1.00	1.00
1	1.00	1.00	1.00	1.00	1.00	1.00	1.00	1.00
2	0.806	0.893	0.985	1.00	1.00	1.00	1.00	1.00
3	0.687	0.763	0.844	0.911	0.971	1.00	1.00	1.00
4	0.618	0.687	0.761	0.825	0.885	0.960	1.00	1.00
5	0.572	0.636	0.706	0.767	0.827	0.903	0.993	1.00
6	0.538	0.599	0.666	0.725	0.785	0.861	0.952	1.00
8	0.492	0.547	0.611	0.667	0.727	0.804	0.896	0.973
10	0.460	0.513	0.574	0.628	0.688	0.765	0.858	0.940
12	0.438	0.488	0.547	0.599	0.659	0.737	0.831	0.916
14	0.420	0.469	0.526	0.577	0.637	0.715	0.810	0.898
20	0.385	0.431	0.484	0.534	0.594	0.672	0.767	0.862
30	0.353	0.395	0.446	0.494	0.554	0.632	0.729	0.828
40	0.335	0.375	0.424	0.471	0.531	0.609	0.706	0.809
50	0.322	0.361	0.409	0.455	0.515	0.594	0.691	0.796

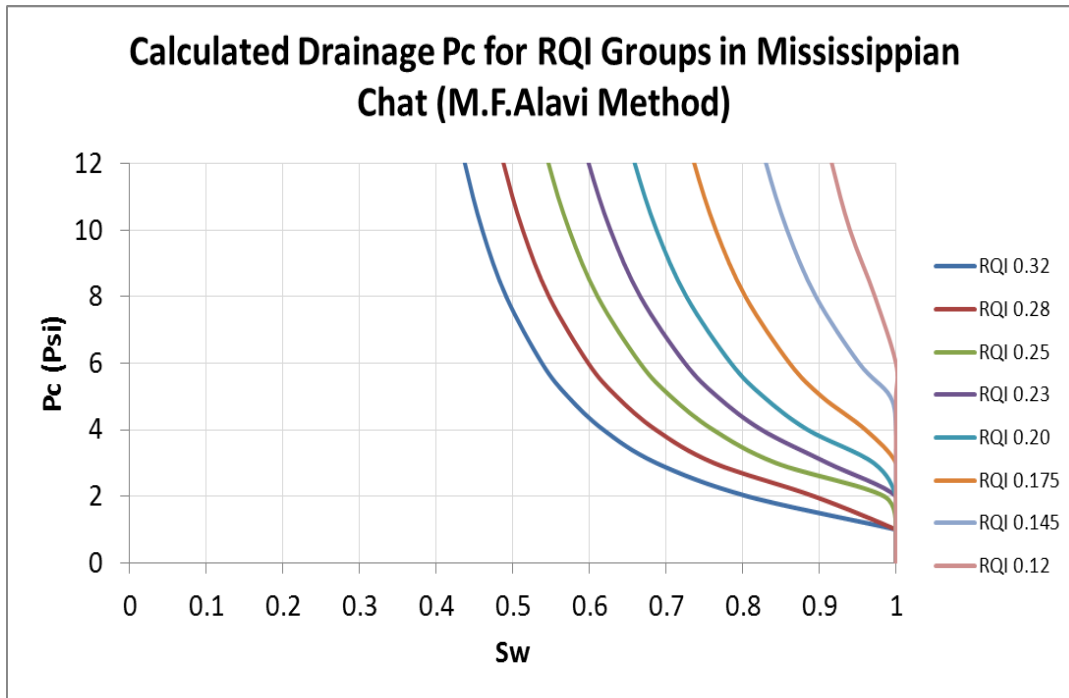


**Figure 11: Calculated drainage Pc curves for the Mississippian chat**

For the carbonate section of the reservoir, equations 16 and 25 were integrated into equation 26 to obtain an equation expressing  $S_{wi}$  in terms of RQI and  $P_c$  (equation 28).

$$S_{wi} = 1 - \left(1 - 0.5245 \frac{0.1467RQI^{-1.312}}{P_c}\right) \left(1 - \left(\frac{0.1467RQI^{-1.312}}{P_c}\right)^{3.125}\right) (1 - 0.0202RQI^{-1.127}) \quad (\text{Equation 28})$$

The RQI in the carbonate section ranges from 0.045 to 0.590. The range was divided into eight smaller intervals (table 4). The midpoint of each range was found and, based on these RQI values, eight  $P_c$  curves were calculated for the carbonate section of the reservoir (table 5 and fig. 12).

**Table 4: RQI subdivisions in the Mississippian carbonate**

RT	From	To	Avg RQI
1	0.450	0.590	0.520
2	0.315	0.450	0.380
3	0.205	0.315	0.250
4	0.130	0.205	0.160
5	0.090	0.130	0.100
6	0.070	0.090	0.080
7	0.055	0.070	0.060
8	0.045	0.055	0.050

**Table 5: Drainage Pc table for different RQI groups in the Mississippian carbonate**

<b>a</b> 0.524	<b>b</b> 3.125	<b>Drainage Table in Mississippian Carbonate</b>						
<b>RQI</b>	0.52	0.38	0.25	0.16	0.1	0.08	0.06	0.05
<b>Pe</b>	0.346	0.522	0.904	1.624	3.009	4.033	5.882	7.471
<b>Swir</b>	0.04	0.065	0.1	0.16	0.25	0.35	0.425	0.55
<b>Pc</b>	<b>Swi</b>							
0	1	1	1	1	1	1	1	1
0.1	1	1	1	1	1	1	1	1
0.2	1	1	1	1	1	1	1	1
0.3	1	1	1	1	1	1	1	1
0.4	0.809	1	1	1	1	1	1	1
0.5	0.582	1	1	1	1	1	1	1
0.6	0.450	0.821	1	1	1	1	1	1
0.7	0.367	0.658	1	1	1	1	1	1
0.8	0.312	0.547	1	1	1	1	1	1
0.9	0.272	0.468	1	1	1	1	1	1
1	0.243	0.410	0.872	1	1	1	1	1
2	0.131	0.205	0.371	0.769	1	1	1	1
3	0.099	0.154	0.260	0.487	1	1	1	1
4	0.084	0.131	0.214	0.378	0.732	1	1	1
5	0.075	0.117	0.189	0.324	0.592	0.816	1	1
6	0.069	0.108	0.173	0.291	0.511	0.701	0.983	1
8	0.062	0.097	0.154	0.255	0.426	0.578	0.782	0.956
10	0.057	0.091	0.143	0.234	0.383	0.517	0.678	0.836
12	0.055	0.086	0.136	0.221	0.357	0.482	0.619	0.766
14	0.052	0.083	0.131	0.212	0.340	0.459	0.582	0.721
20	0.049	0.078	0.121	0.196	0.311	0.423	0.524	0.655
30	0.046	0.074	0.114	0.184	0.290	0.397	0.487	0.614
40	0.044	0.071	0.111	0.178	0.280	0.385	0.471	0.596
50	0.043	0.070	0.109	0.174	0.274	0.378	0.461	0.586

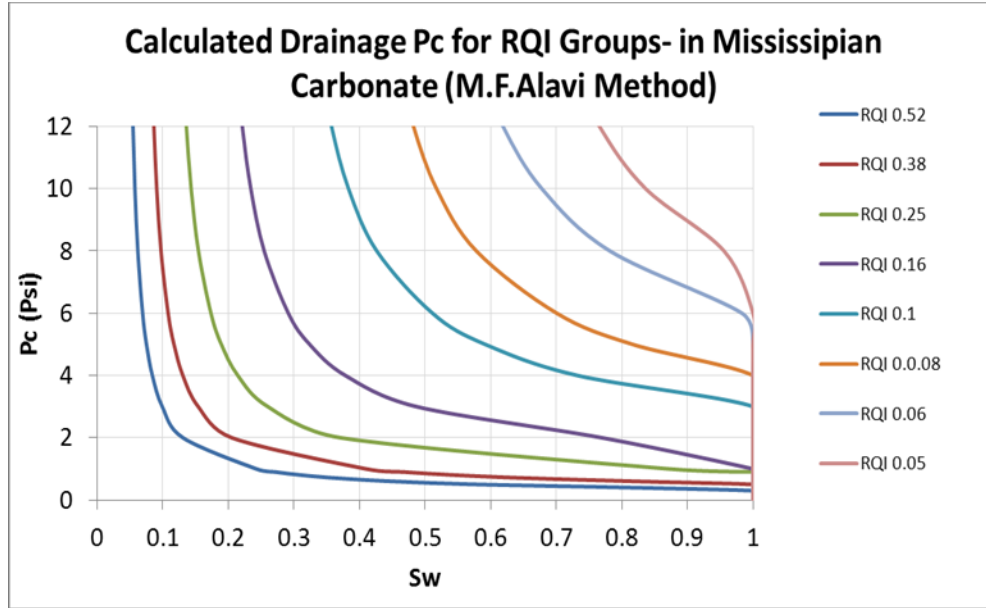


Figure 12: Calculated drainage Pc curve for the Mississippian carbonate

#### f. Calculation of Imbibition Capillary Pressure Curves

Normalized non-wetting phase water saturation is defined according to equation 29 for imbibition.

$$S_{nwn} = \frac{1 - S_{wi} - S_{or}}{1 - S_{wir} - S_{or}} \quad (\text{Equation 29})$$

$S_{nwn}$  is equal to 0 when  $P_c$  is 0; therefore, EQR in terms of entry pressure and  $P_c$  should be expressed by the following equation:

$$EQR = \frac{P_e}{P_c + P_e} \quad (\text{Equation 30})$$

Equation 31 is proposed for derivation of initial water saturation for imbibition in terms of  $S_{wir}$ ,  $S_{or}$ , and  $S_{nwn}$ . Correlations for  $S_{wir}$ ,  $S_{or}$ , and  $S_{nwn}$  were proposed. Substituting these correlations in equation 31 result in two equations that give initial water saturation based on RQI and  $P_c$ : the first (equation 32) is for the chat conglomerate and the second (equation 33) was derived for the carbonate section of the Mississippian formation.

$$S_{wi} = 1 - S_{or} - S_{nwn}(1 - S_{wir} - S_{or}) \quad (\text{Equation 31})$$

$$S_{wi} = 0.427RQI^{-0.407} - \left(1 - 0.00155 \frac{0.1616RQI^{-1.761}}{P_c + 0.1616RQI^{-1.761}}\right) \left(1 - \left(\frac{0.1616RQI^{-1.761}}{P_c + 0.1616RQI^{-1.761}}\right)^{0.569}\right) (-12.885RQI^2 + 8.031RQI - 1.4924 + 0.427RQI^{-0.407}) \quad (\text{Equation 32})$$

$$S_{wi} = 0.5811RQI^{-0.139} - \left(1 - 0.5245 \frac{0.1467RQI^{-1.312}}{P_c + 0.1467RQI^{-1.312}}\right) \left(1 - \left(\frac{0.1467RQI^{-1.312}}{P_c + 0.1467RQI^{-1.312}}\right)^{3.125}\right) (-0.0202RQI^{-1.127} + 0.5811RQI^{-0.139}) \quad (\text{Equation 33})$$

Based on equation 32 for imbibition, eight capillary pressure curves were generated for the chat conglomerate (table 6 and fig. 13).

**Table 6: Imbibition Pc table for different RQI groups in the Mississippian chat**

a 0.001553		b 0.570		Imbibition Table in Mississippian Chat				
RQI	0.32	0.28	0.245	0.22	0.2	0.175	0.145	0.12
Pe	1.20	1.52	1.92	2.33	2.75	3.48	4.84	6.76
Sor	0.32	0.3	0.27	0.24	0.21	0.155	0.09	0.03
Swir	0.23	0.26	0.3	0.34	0.4	0.48	0.58	0.7
Pc	Swi							
0	0.679	0.700	0.730	0.760	0.790	0.845	0.910	0.970
0.1	0.659	0.684	0.718	0.750	0.782	0.839	0.906	0.968
0.2	0.642	0.670	0.706	0.741	0.775	0.834	0.902	0.966
0.3	0.626	0.657	0.696	0.732	0.768	0.828	0.899	0.963
0.4	0.612	0.645	0.686	0.724	0.761	0.823	0.895	0.961
0.5	0.599	0.634	0.677	0.716	0.755	0.818	0.892	0.959
0.6	0.587	0.624	0.668	0.709	0.749	0.813	0.889	0.957
0.7	0.576	0.615	0.660	0.702	0.743	0.809	0.886	0.955
0.8	0.566	0.606	0.653	0.695	0.737	0.804	0.883	0.953
0.9	0.557	0.598	0.646	0.689	0.732	0.800	0.880	0.951
1	0.548	0.590	0.639	0.683	0.727	0.796	0.877	0.950
2	0.487	0.533	0.587	0.635	0.686	0.762	0.851	0.933
3	0.450	0.497	0.552	0.602	0.656	0.736	0.831	0.919
4	0.425	0.471	0.527	0.578	0.634	0.716	0.814	0.907
5	0.406	0.452	0.507	0.559	0.616	0.700	0.800	0.897
6	0.392	0.437	0.492	0.543	0.602	0.686	0.789	0.888
8	0.371	0.415	0.469	0.520	0.579	0.665	0.769	0.873
10	0.356	0.399	0.452	0.502	0.563	0.649	0.754	0.861
12	0.345	0.387	0.439	0.489	0.550	0.636	0.742	0.851
14	0.336	0.377	0.429	0.478	0.539	0.626	0.732	0.843
20	0.318	0.357	0.408	0.456	0.517	0.603	0.710	0.823
30	0.300	0.338	0.387	0.434	0.495	0.581	0.687	0.803
40	0.290	0.327	0.374	0.420	0.482	0.567	0.673	0.790
50	0.283	0.319	0.366	0.411	0.472	0.557	0.663	0.780

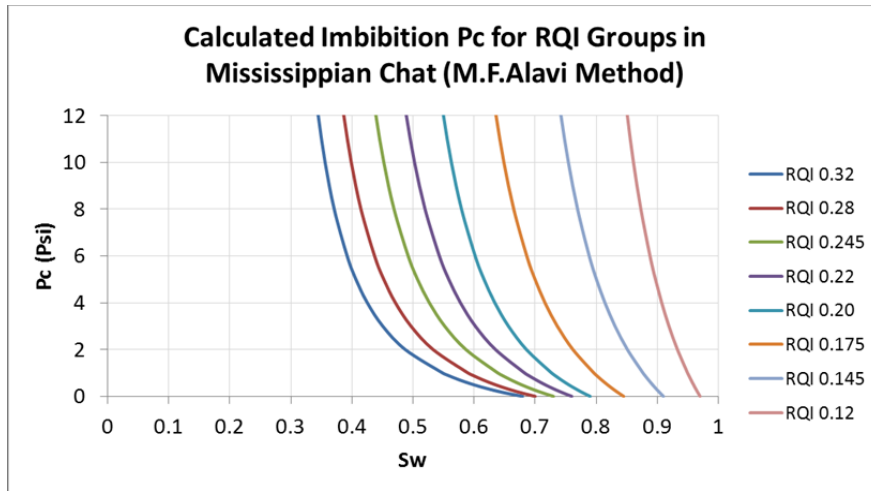


**Figure 13: Calculated imbibition Pc curve for the Mississippian chat**

For the carbonate section, equation 33 was used to calculate eight capillary pressure curves (table 7 and fig. 15).

Table 7: Imbibition Pc table for different RQI groups in the Mississippian carbonate

a 0.52	b 3.12	Imbibition Table in Mississippian Carbonate						
RQI	0.52	0.38	0.25	0.16	0.1	0.08	0.06	0.05
Pe	0.35	0.52	0.90	1.62	3.01	4.03	5.88	7.47
Sor	0.36	0.34	0.31	0.28	0.25	0.22	0.20	0.17
Swir	0.04	0.065	0.1	0.16	0.25	0.35	0.425	0.55
Pc	Swi							
0	0.636	0.658	0.685	0.722	0.750	0.780	0.800	0.826
0.1	0.443	0.518	0.599	0.673	0.726	0.765	0.791	0.820
0.2	0.334	0.423	0.530	0.631	0.703	0.750	0.782	0.815
0.3	0.268	0.358	0.475	0.593	0.683	0.736	0.773	0.810
0.4	0.226	0.311	0.431	0.560	0.663	0.723	0.765	0.805
0.5	0.197	0.277	0.396	0.531	0.645	0.710	0.757	0.800
0.6	0.175	0.251	0.366	0.505	0.628	0.698	0.749	0.795
0.7	0.159	0.230	0.342	0.482	0.612	0.687	0.741	0.791
0.8	0.146	0.214	0.321	0.462	0.597	0.676	0.734	0.786
0.9	0.136	0.200	0.304	0.443	0.583	0.665	0.727	0.782
1	0.128	0.189	0.289	0.427	0.570	0.656	0.720	0.777
2	0.088	0.133	0.208	0.327	0.477	0.580	0.663	0.741
3	0.073	0.112	0.176	0.281	0.424	0.532	0.623	0.713
4	0.065	0.102	0.159	0.255	0.390	0.500	0.593	0.692
5	0.060	0.095	0.149	0.238	0.367	0.477	0.571	0.675
6	0.057	0.090	0.141	0.227	0.351	0.460	0.553	0.661
8	0.053	0.084	0.132	0.212	0.329	0.437	0.528	0.641
10	0.050	0.080	0.126	0.202	0.315	0.422	0.511	0.627
12	0.049	0.078	0.122	0.196	0.305	0.412	0.499	0.616
14	0.048	0.076	0.119	0.191	0.298	0.404	0.490	0.609
20	0.045	0.073	0.113	0.182	0.285	0.389	0.473	0.593
30	0.044	0.070	0.109	0.175	0.274	0.377	0.458	0.580
40	0.043	0.069	0.107	0.172	0.268	0.371	0.451	0.574
50	0.042	0.068	0.105	0.169	0.265	0.367	0.446	0.569

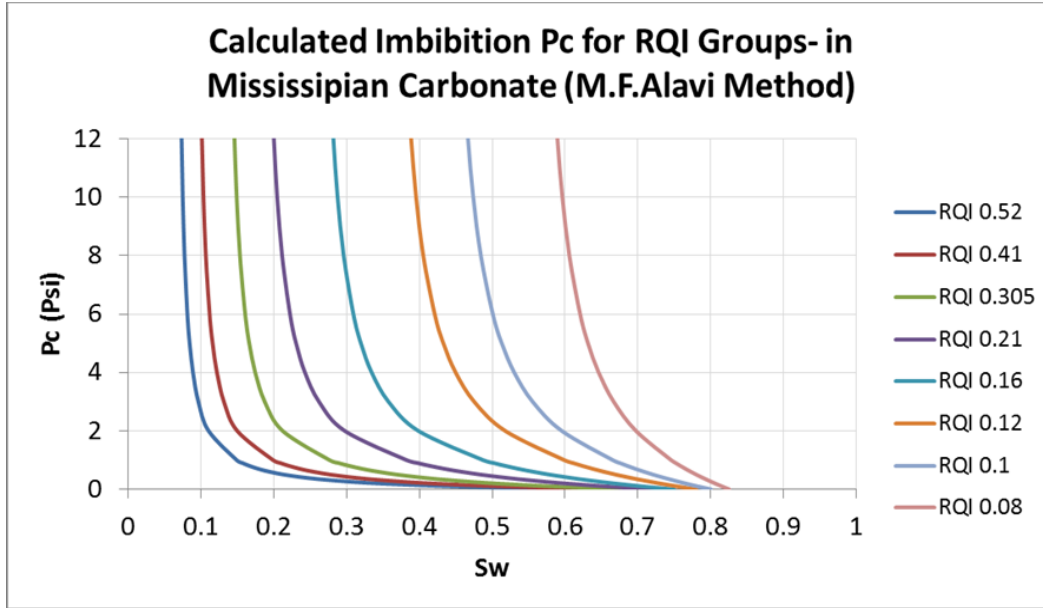


Figure 15: Calculated imbibition Pc curve for the Mississippian carbonate

#### IV. Calculation of Imbibition Relative Permeability Curves prior to receiving SCAL data

Relative permeability tables are critical data in reservoir simulation. It was proposed before to define eight saturation regions in the chat conglomerate model and eight in the carbonate section, based on the RQI of grid cells. Assuming that the reservoir is under saturated and that its pressure will always remain above bubble point pressure, only oil and water relative permeability tables are estimated for eight saturation regions each in the chat conglomerate and carbonate section of the Mississippian reservoir. To estimate relative permeability for these regions, the following modified Corey equations were used.

$$K_{ro} = k_{ro_{Swi}}(1 - S_{wD})^p \quad \text{(Equation 34)}$$

$$K_{rw} = k_{rw_{Sorw}} * (S_{wD})^q \quad \text{(Equation 35)}$$

$$S_{wD} = \frac{(S_w - S_{wc})}{(1 - S_{orw} - S_{wc})} \quad \text{(Equation 36)}$$

Corey exponent  $p$  (Oil Corey Exponent) and  $q$  (Water Corey Exponent) were assumed at 2.5 and 1.5, respectively, based on experience from SCAL in other fields. Critical water saturation ( $S_{wc}$ ) was taken from Pc curves where capillary pressure is 10 psi. Residual oil saturation ( $S_{or}$ ) was previously estimated by equations 19 and 20 based on SCAL data of several fields.

Oil relative permeability at  $S_{wc}$  and max water permeability at  $S_{or}$  was derived from equations 37 and 38, which are correlations obtained from SCAL data in other fields.

$$K_{rw_{Sorw}} = 0.1371RQI^{-0.348} \quad \text{(Equation 37)}$$

$$Kro_{Swi} = 0.8909RQI^{0.0194} \quad \text{(Equation 38)}$$

Tables B1 to B8 (Appendix B) present the parameters that were used to calculate the relative permeability of the chat conglomerate. Tables C1 to C8 (Appendix C) present the same parameters for the carbonate section of the Mississippian reservoir.

Eight sets of relative permeability tables were generated for the chat conglomerate (fig. 16), and eight sets of these curves were calculated for the carbonate section (fig. 17). All eight relative permeability curves for each chat and carbonate section can be found in Appendix B (figs. B1 to B8) and Appendix C (figs. C1 to C8).

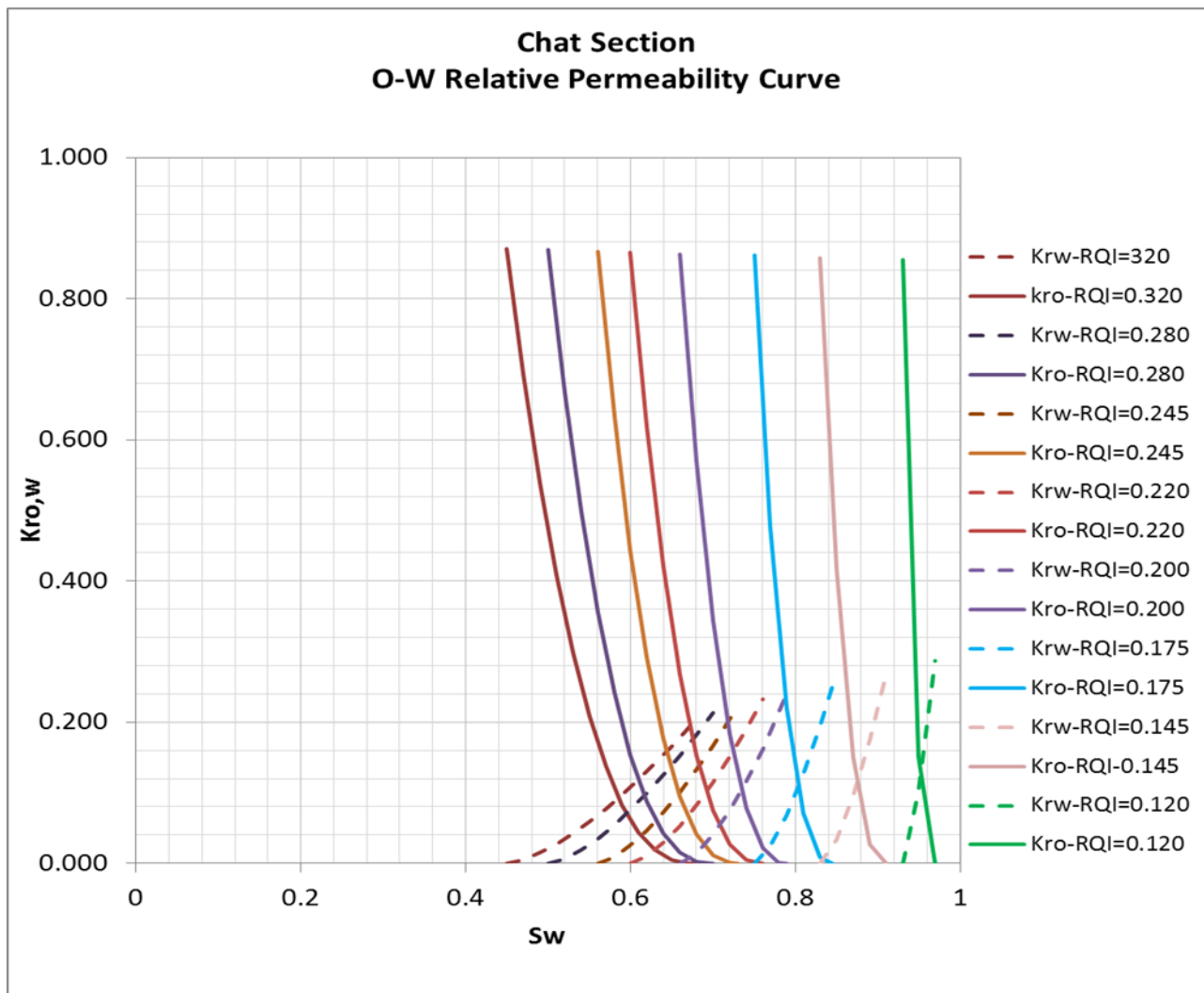


**Figure 16: Relative permeability curves for the chat section at different RQI groups:**

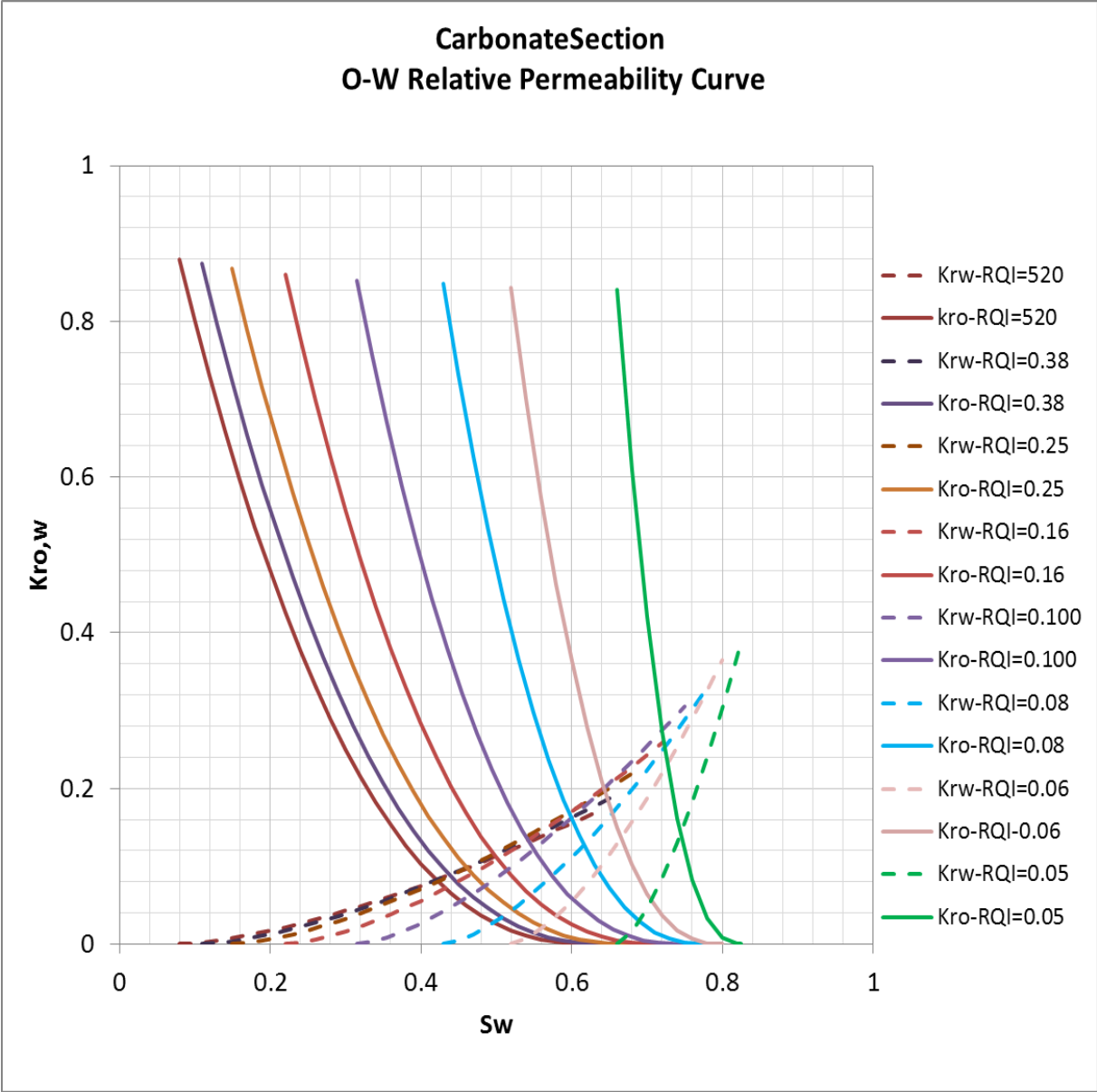


**Figure 1 7: Relative permeability curves for the carbonate section at different RQI groups**

## V. Calibration of Previously Calculated Capillary Pressure and Relative Permeability Curves using Special Core Analysis (SCAL)

The relative permeability and capillary pressure curves were calculated twice in the Mississippian. The first time was prior to the receipt of receiving the laboratory Pc and relative permeability core measurements and the second time was after receiving the core measurements and this time they were calibrated using the core measured endpoints. Two core plug samples with similar RQI were sent to the Core lab for Pc and relative permeability measurements. The initial estimation of Pc curves was based on the endpoints that were calculated from NMR log. As shown in figure 5, there is a slight difference between calculated Pc and measured Pc before calibration. However, there is an excellent match between the calculated Pc and measured Pc after calibration, figure 5. Moreover, there is a slight difference between the initial calculated relative permeability and measured relative permeability. However, the match between them is excellent after calibration, figure 11.

Previously, the Mississippian was divided into two zones, chert (upper part) and carbonate (Lower part). The chert zone is not present in all wells in the Mississippian. Chert is about 20ft thick in Well 2-32 and about 13ft thick in Well 1-32, figure A3 and A1. Due to the variability in pore size shape from chert to carbonate zone, distinct sets of capillary pressure (Pc) and relative permeability curves were derived in each zone. Chert zone was neither implemented in the Geo-model nor the simulation due to its complexity; therefore, only the Pc and relative permeability curves for the carbonate zone were calibrated. Relative permeability and Pc curves were measured by Core Lab in two core-plugs in the carbonate zone of well 2-32. The 2 samples had identical reservoir quality index (RQI) that results in identical Pc and relative permeability curves. The two samples were used to calibrate the previously calculated Pc and relative permeability curves. First part of this report (A) is calibration of the Pc curves and second part (B) is calibration of the relative permeability curves.

### A. Calibrating Capillary Pressure Curves

#### I. Irreducible Water Saturation (Swir)

Previously, Irreducible water saturation (Swir) was calculated for all depths from NMR T2 distribution and capillary pressure module in Techlog. The two Swir from the Pc core measurements were plotted on the previously plotted Swir from NMR against RQI, figure 1. Swir from Pc core measurements (in green) for RQI of 0.2 and 0.17 were lower in values than the calculated Swir from NMR module (in blue); therefore, the fitted curve was adjusted to pass through the Swir from the two Pc core measurements. The adjusted power equation of the curve will be used to calculate Pc curves for each RQI.

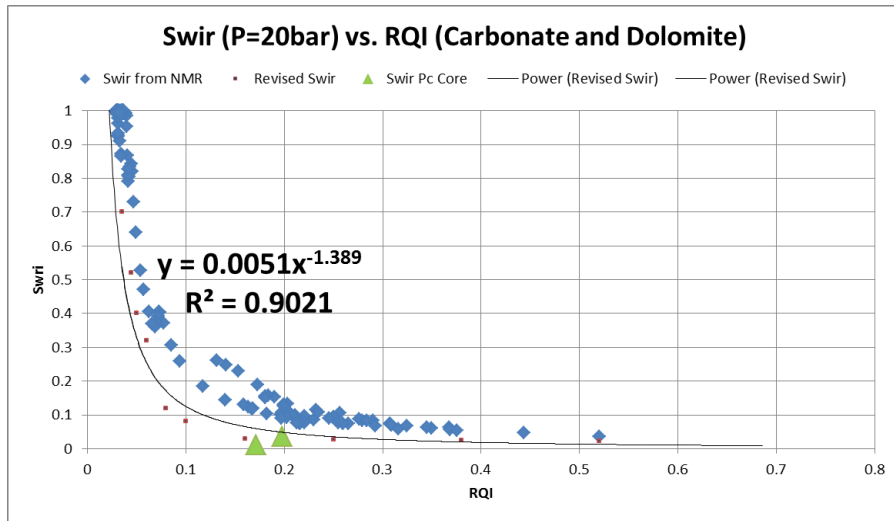


Figure 34: Irreducible water saturation (Swir) versus reservoir quality index (RQI)

## II. Entry Pressure (P<sub>e</sub>)

Previously calculated P<sub>e</sub> from NMR did not match very well with the P<sub>e</sub> from the Pc core measurements for RQI of 0.2 and 0.17, figure 2. Therefore, an alternative method that is entry pressure derivation from Winland R35 was attempted.

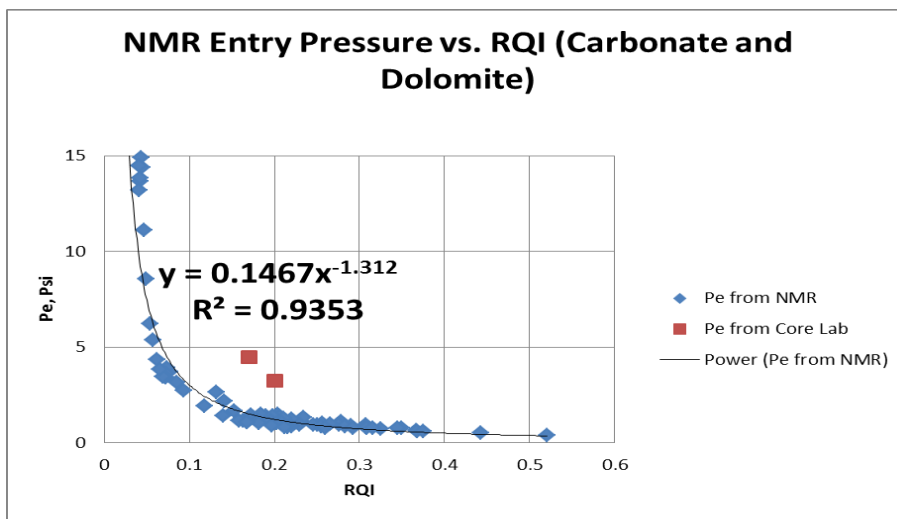
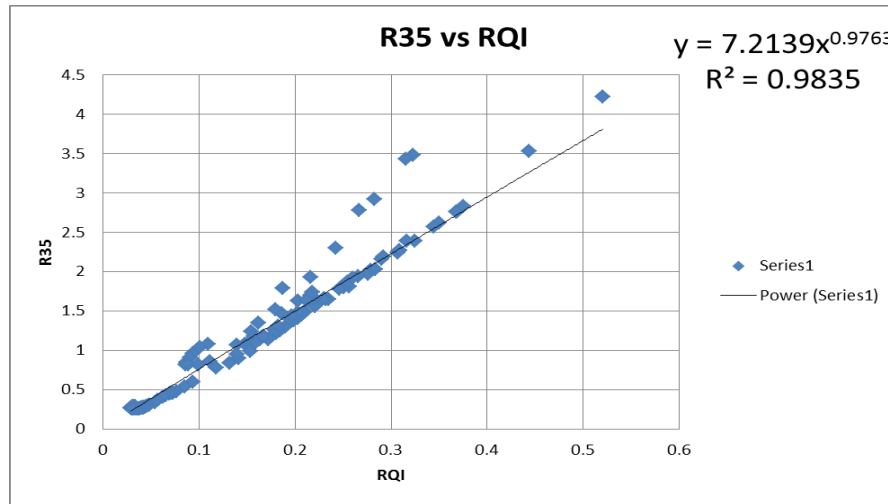


Figure 35: Entry pressure from NMR versus RQI

P<sub>e</sub> was calculated for all depths from entry pore throat radius (R<sub>entry</sub>) in which R<sub>entry</sub> is calculated from Winland R35. It was noted previously that entry pressure (P<sub>e</sub>) has a strong relationship with RQI. Also, there is a strong power correlation between R35 and RQI. On the other hand, there is a linear relationship between Winland 35 and R<sub>entry</sub>; therefore, both R<sub>entry</sub> and P<sub>e</sub> can be correlated to RQI. R35 was calculated using equation 1:

$$\log R35 = 0.732 + 0.588 \log K - 0.864 \log \phi \quad \text{Equation 1}$$

Previously calculated porosity and permeability in the Mississippian formation were used in equation 1 to calculate R35. Winland R35 was plotted against RQI (figure 3) and the power equation was used for determination of  $R_{entry}$ .



**Figure 3: R35 Winland versus Reservoir Quality Index (RQI)**

Figure 3 results in equation 2 which relates R35 to RQI. This relationship is

$$R35 = 7.21RQI^{0.98} \quad (\text{Equation 2})$$

$R_{entry}$  is related to the relationship between R35 and RQI (figure 2) multiplied by a pre-factor, equation 3:

$$R_{entry} = c * (a * RQI^b) \quad \text{Equation 3}$$

Where:

C is a pre-factor,  $a=7.21$  and  $b=0.98$  from equation 2

Pre-factor c in equation 3 depends on the size of pores, degree of sorting and T2 distribution. This factor was determined by try and error so that the entry pressures ( $P_e$ ) from laboratory for the two RQI match with the  $P_e$  calculated by equation 4, figure 4:

$$P_e = \frac{2 * \sigma * \cos\theta * 0.147}{c * (a * RQI^b)} \quad \text{Equation 4}$$

Where,

$\sigma$  is interfacial tension

$\theta$  is contact angle in oil-brine system

Pre-factor c was determined by try and error by equation 4 which resulted in a value of 1.05. Interfacial tension of 20 dyne/cm and contact angle of 30 were used for oil-brine system.  $P_e$  was plotted against RQI

to derive an equation to relate  $P_e$  to RQI which will be later used to calculate the  $P_c$  curves for each RQI in the Mississippian.

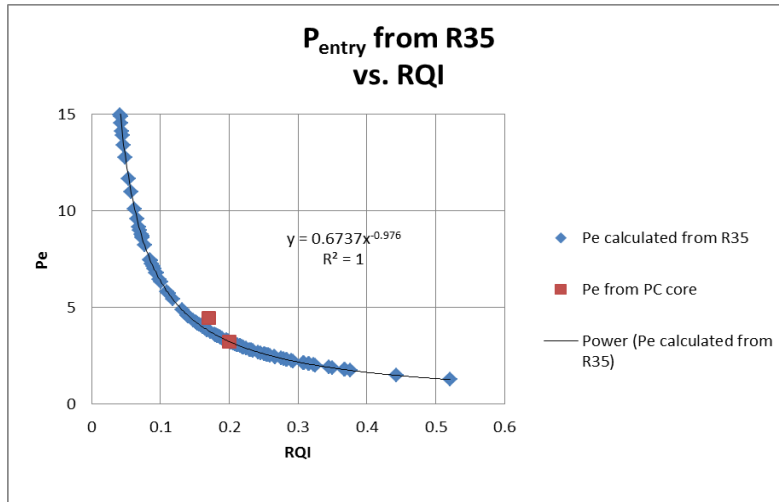


Figure 36: Entry pressure from R35 Winland

## II. Shape of $P_c$ curves

The previously calculated function between Normalized Non-wetting phase saturation ( $S_{nwn}$ ) and Equivalent radius (EQR) was revised. This function was previously derived from the generalized  $P_c$  curves from (Bhattacharya et al., 2003). This function was re-calculated using one of the  $P_c$  core samples that had RQI of 0.17. To calibrate the shape of  $P_c$  curves for all RQI, equivalent radius (EQR) which is  $P_e/pc$  and Normalized Non-wetting phase saturation ( $S_{nwn}$ ) which is  $(1-sw)/(1-sw_{ir})$  were calculated for all Lab water saturations.  $S_{nwn}$  was plotted against EQR (figure 4) and constants  $a$  and  $b$  of the curve were calculated by regression.

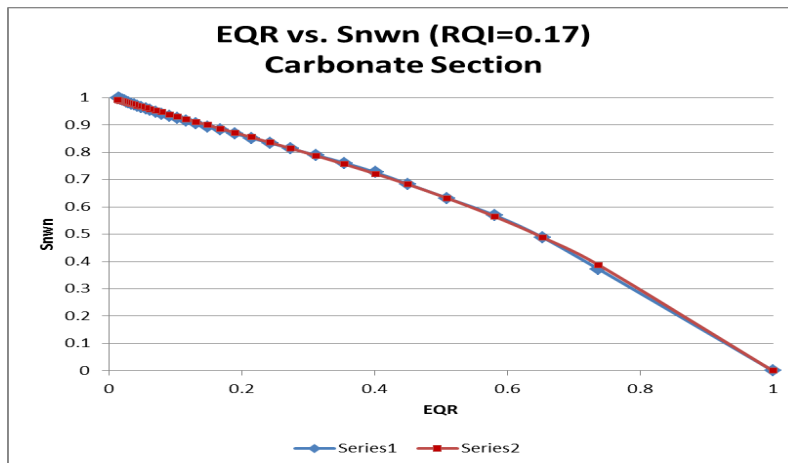


Figure 37: Non-wetting phase saturation ( $S_{nwn}$ ) versus reservoir quality index (RQI)

Figure 4 results in constants a and b equal to 0.67 and 4.79 respectively. The two constants, a and b, define the shape of Pc curves.

### Drainage Capillary Pressure Curves

Drainage capillary pressure curves were re-calculated by incorporating equations from sections I, II and III into equation 5:

$$S_{wi} = 1 - \left( 1 - 0.671 \frac{0.707 RQI^{0.976}}{P_c} \right) \left( 1 - \left( \frac{0.707 RQI^{0.976}}{P_c} \right)^{4.79} \right) (1 - 0.0051 RQI^{-1.39})$$

Calculated Pc after calibration is compared with the calculated Pc before calibration and measured Pc from the core plug for the respective RQI of 0.2, figure 5. There is a good match between calculated Pc and measured Pc after calibration.

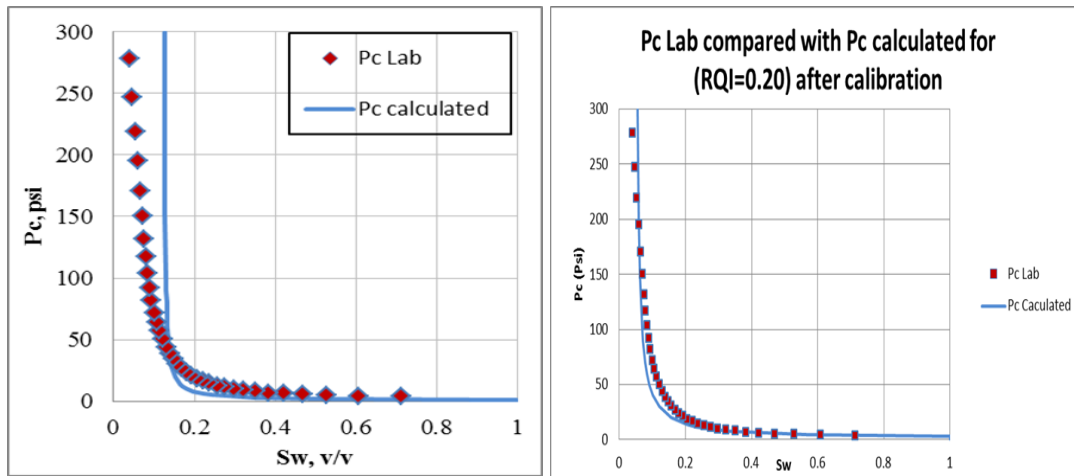


**Figure 38: Capillary pressure curves for RQI 0.2 before calibration (left) and after calibration (right)**

Since there is a good match between the calculated and measured Pc in figure 5; therefore, drainage Pc curves were calculated for eight RQI average that was sub-divided previously, figure 6:

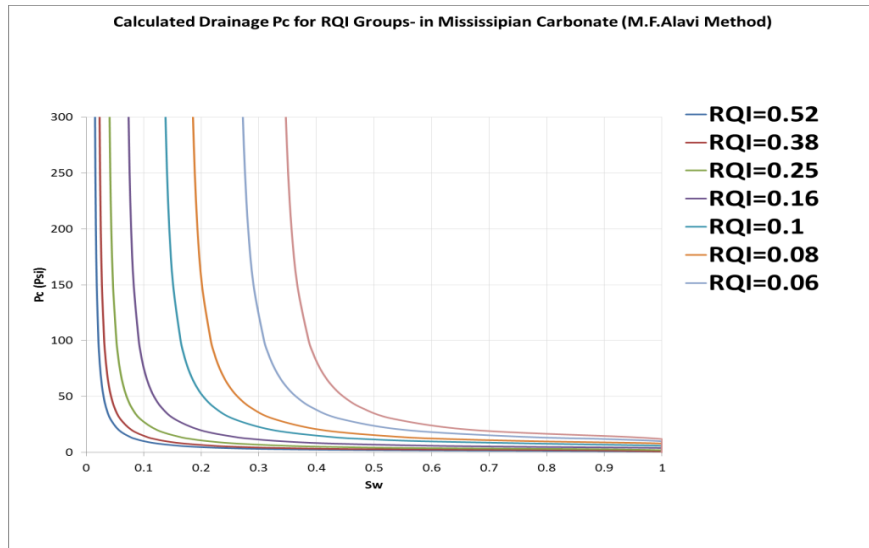


Figure 39: Drainage Pc curves for all RQI

### Imbibition Capillary Pressure Curves

For revising the imbibition Pc curves, the same correlations as drainage curves were used; except, an additional term of residual oil saturation was incorporated. A relationship between Initial oil saturation (Soi) and residual oil saturation (Sor) was obtained from literature and the curve was adjusted slightly to lie on the residual oil measured from the relative permeability core measurements, figure 7.

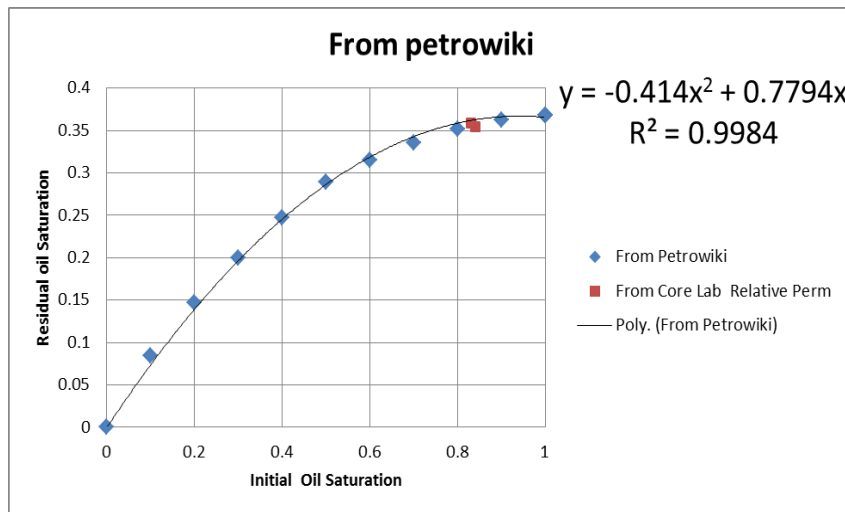


Figure 7: Relationship between residual oil saturation (Sor) and Initial oil saturation (Soi)

## B. Calibrating Imbibition Relative Permeability Curves

### I. Corey Exponents for Water and Oil

Relative permeability curves were measured in two core plug samples by Core Lab for RQI of 0.15 and 0.18 respectively. The laboratory relative permeability curves to water and oil were normalized for determination of Corey exponents for water and oil using equation 1.

$$K_{riN} = \frac{K_{ri}}{K_{rimax}} \quad \text{Equation 1}$$

Where,

i represent fluid (oil, water etc)

$K_{riN}$ : Normalized relative permeability for that fluid

$K_{rimax}$ : Maximum relative permeability for that fluid

To find Corey exponents for water and oil, Corey relative permeability correlations in equation 2 and 3 were used to curve fit the normalized relative permeabilities ( $K_{roN}$  and  $K_{rwN}$ ). Normalized water saturation ( $S_{wN}$ ) in equation 2 and 3 was calculated by equation 4. Corey exponents for water and oil (b and a) are the fit parameters that were determined by least square regression.

$$K_{rwN} = S_{wN}^b \quad \text{Equation 2}$$

$$K_{roN} = (1 - S_{wN})^a \quad \text{Equation 3}$$

$$S_{wN} = \frac{S_w - S_{wi}}{1 - S_{wi} - S_{or}} \quad \text{Equation 4}$$

Where,

$K_{rwN}$  : Normalized relative permeability to water

$S_{wN}$  : normalized water saturation.

b: Corey exponent for water

$K_{roN}$ : Normalized relative permeability to oil

a: Corey exponents for oil

Figure 8 shows the fitted Normalized relative permeability for oil and water and the best-fit values for b and a are 0.88 and 2.12 respectively.

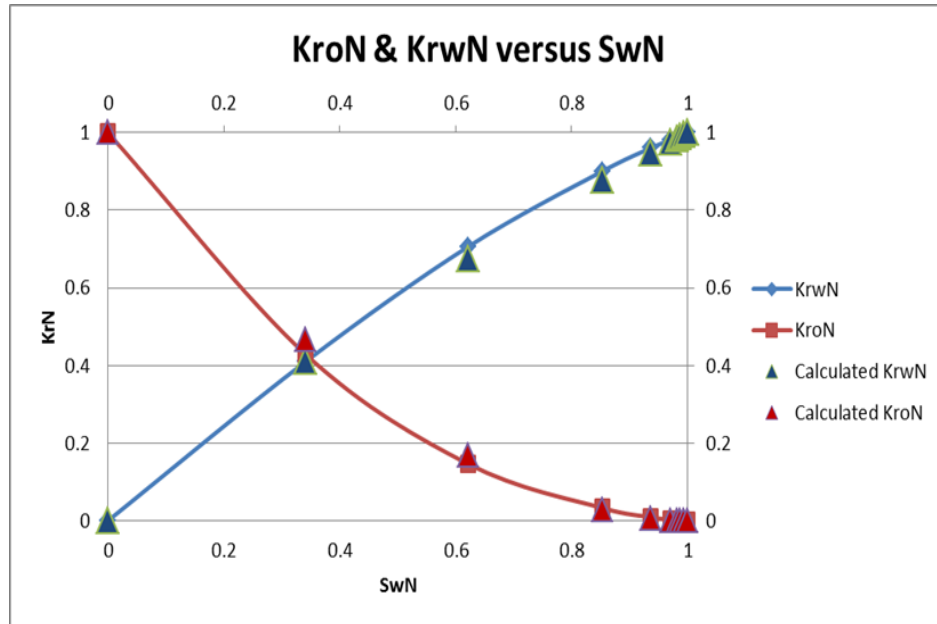


**Figure 8: Normalized relative permeability (KroN) versus normalized water saturation (SwN) and best fit for a and b**

The calculated Corey exponents for water and oil (b and a) from the two samples were averaged and will be used in the previously proposed relative permeability formula. The Corey exponents for each core sample and the average of the two are listed in table 1:

Table 1: Calculated Corey exponents for each sample individually and average values

Sample No	RQI	a	b
1	0.18	2.4	0.93
2	0.15	1.84	0.83
<b>Average</b>	<b>0.165</b>	<b>2.12</b>	<b>0.88</b>

## II. Connate Water Saturation (Swc) and Residual Oil Saturation (Sor)

Previously connate water saturation (Swc) was taken from Pc curves where capillary pressure is 10 psi , figure 9. The average Swc of the two samples from Lab is slightly less than the previously plotted connate water for the same RQI; therefore, the curve was adjusted to match the Swc from Lab, figure 10.

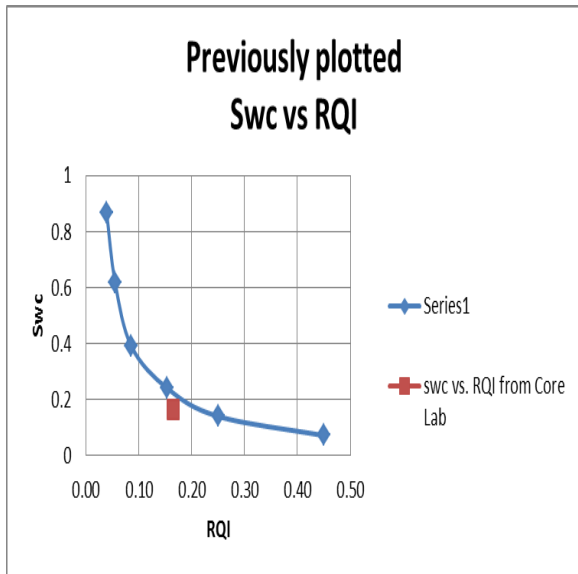


Figure 9: Previously Swc versus RQI with Swc form Lab

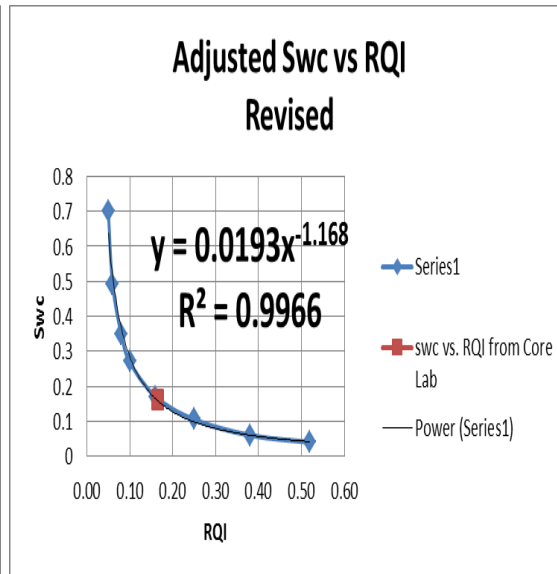


Figure 10: Adjusted Swc to match with Swc form Lab

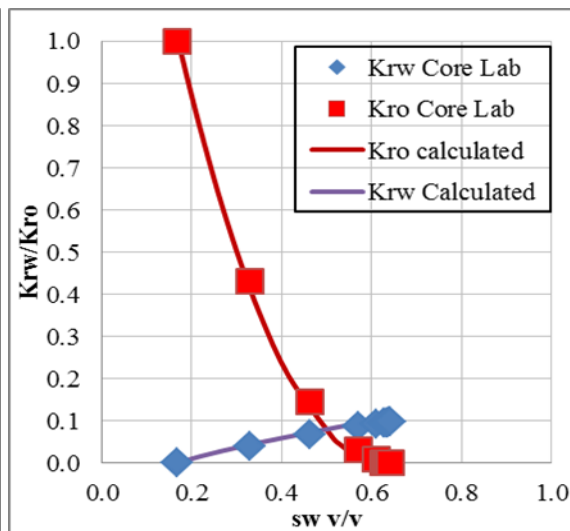
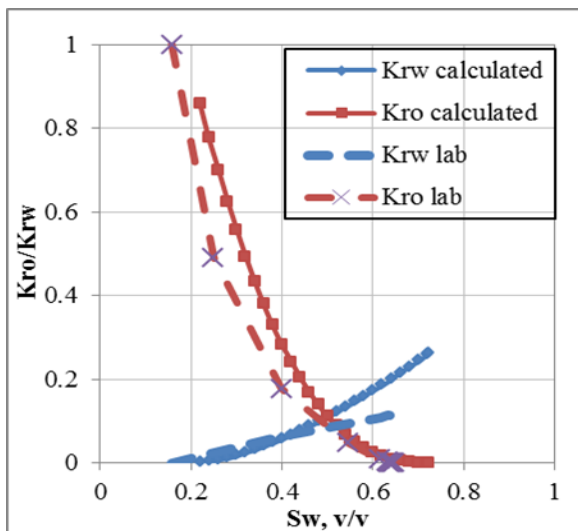


Figure 1 1: Relative permeability curves for RQI 0.16 before calibration (left) and after calibration (right)

## Appendix D

### Calculation of Horizontal and Vertical Permeability in the Arbuckle

#### A. Calculation of Permeability from NMR log of Well 1-32

First it was attempted to calculate NMR permeability using Coates and SDR equations. However, a reasonable match between calculated and core permeability could not be obtained using these equations, although several pre-factors of the equations were tried. It was decided to calculate permeability by relating core FZI to  $1/(Swir*\Phi)$  and using the new technique. Predicted permeability was first calculated based on FZI from 90-degree core permeability and the same process was repeated for max permeability of core samples.

Pore structure in the Arbuckle is very complex and there are a lot of variations in pore size distribution (unimodal, bimodal, and trimodal) versus depth in very short intervals. Due to this complexity and non-homogeneity in pore size distribution, Arbuckle permeability was calculated based on pore size classification (micro, meso, and mega pores). FZI in each pore size class was correlated to  $1/(Swir*\Phi)$  of the same class.

To obtain a better match between calculated permeability and core permeability, the Arbuckle was divided into two zones. Zone 1 was considered to be from 4,160 to 4,700 ft and zone 2 from 4,700 to 5,200 ft.

#### Part 1: Determination of Permeability Using Permeability at 90 degree from Core

##### Permeability in Zone 1 (4,160 – 4,700 ft)

Permeability in zone 1 was calculated based on correlations between FZI from core and  $1/(Swir*\phi)$  from log. FZI from core data was calculated using permeability at 90 degree, and  $1/(swir*\phi)$  was calculated using effective porosity and irreducible water saturation from the NMR log. FZI and  $1/(swir*\phi)$  were sorted from low to high values. All FZI values less than 2 and  $1/(swir*\phi)$  values less than 48 were considered for micro pore sizes, which correspond to permeability values less than about 0.5 mD. Similarly, FZI from 2 to 11 and  $1/(swir*\phi)$  from 48 to 106 were considered for meso pore sizes, which correspond to permeability from about 0.5 to 25 mD. Finally, FZI from 11 to 150 and  $1/(swir*\phi)$  from 106 to 851 were considered for mega pore sizes, which correspond to permeability greater than about 25 mD. Table 1 lists the ranges.

**Table 1: Ranges of FZI and  $1/(Swir*\Phi)$**

	Approx k	FZI	Excel Row	$1/(Swir*\Phi)$	Excel Row
<b>Micro</b>	<0.5	<2.02	4–82	<48.62	4–430
<b>Meso</b>	0.5-25	2.02-10.97	83–170	48.62-106	431–937
<b>Mega</b>	>25	10.97-150	170–246	106-851	938–1,083

Percentiles (5, 10, 20... 90) of FZI population in each class were correlated with respective percentiles of  $1/(Swir*\phi)$  population (figs. 1, 2, and 3). Four different correlations between FZI and

1/(swir\*phi) were derived for micro, meso, and mega pore sizes. Figures 1, 2, and 3 show these correlations. Two of the equations are for micro pore sizes.

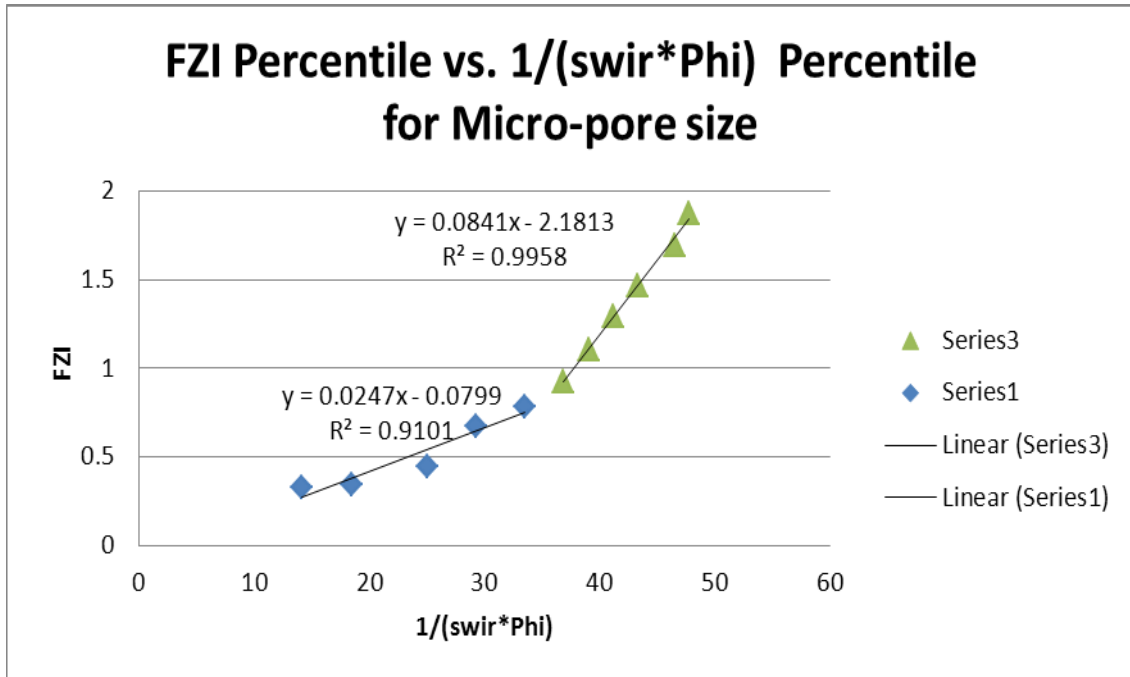


Figure 40: Plot of FZI vs 1/(swir\*phi) for micro pore sizes

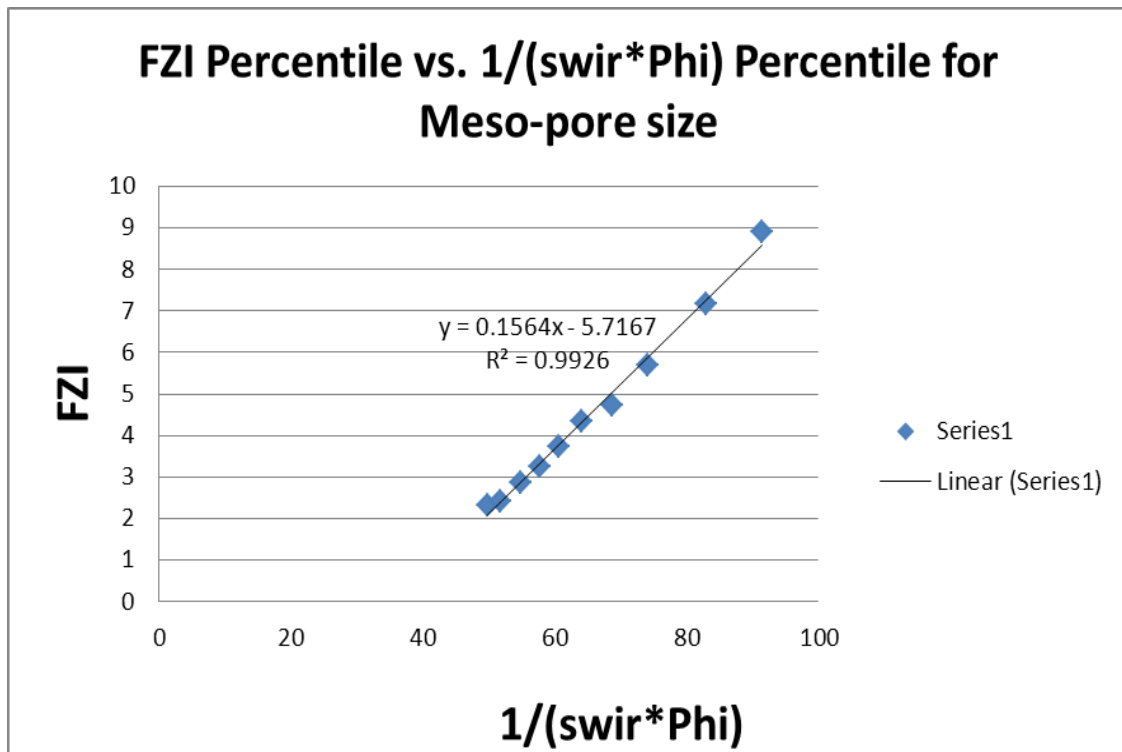


Figure 2: Plot of FZI vs 1/(swir\*phi) for meso pore sizes

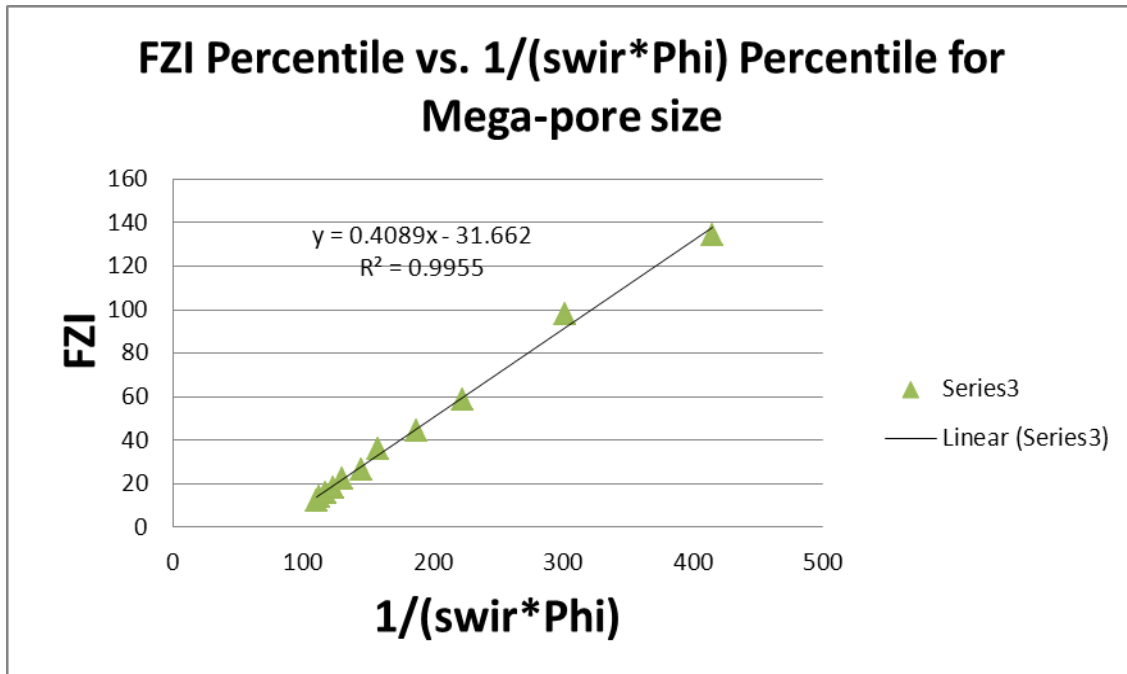


Figure 3: Plot of FZI vs 1/(swir\*phi) for mega pore sizes

Permeability in Zone 1 was calculated using Equation 3 and coefficients  $a$  and  $b$ , which were derived from the correlations.

$$\text{Eq. 1: } K = 1014[FZI]^2 \frac{\phi_e^3}{(1-\phi_e)^2}$$

$$\text{Eq. 2: } FZI = \frac{a}{S_{wir}\phi_e} + b$$

$$\text{Eq. 3: } K = 1014 \left[ \frac{a}{S_{wir}\phi_e} + b \right]^2 \frac{\phi_e^3}{(1-\phi_e)^2}$$

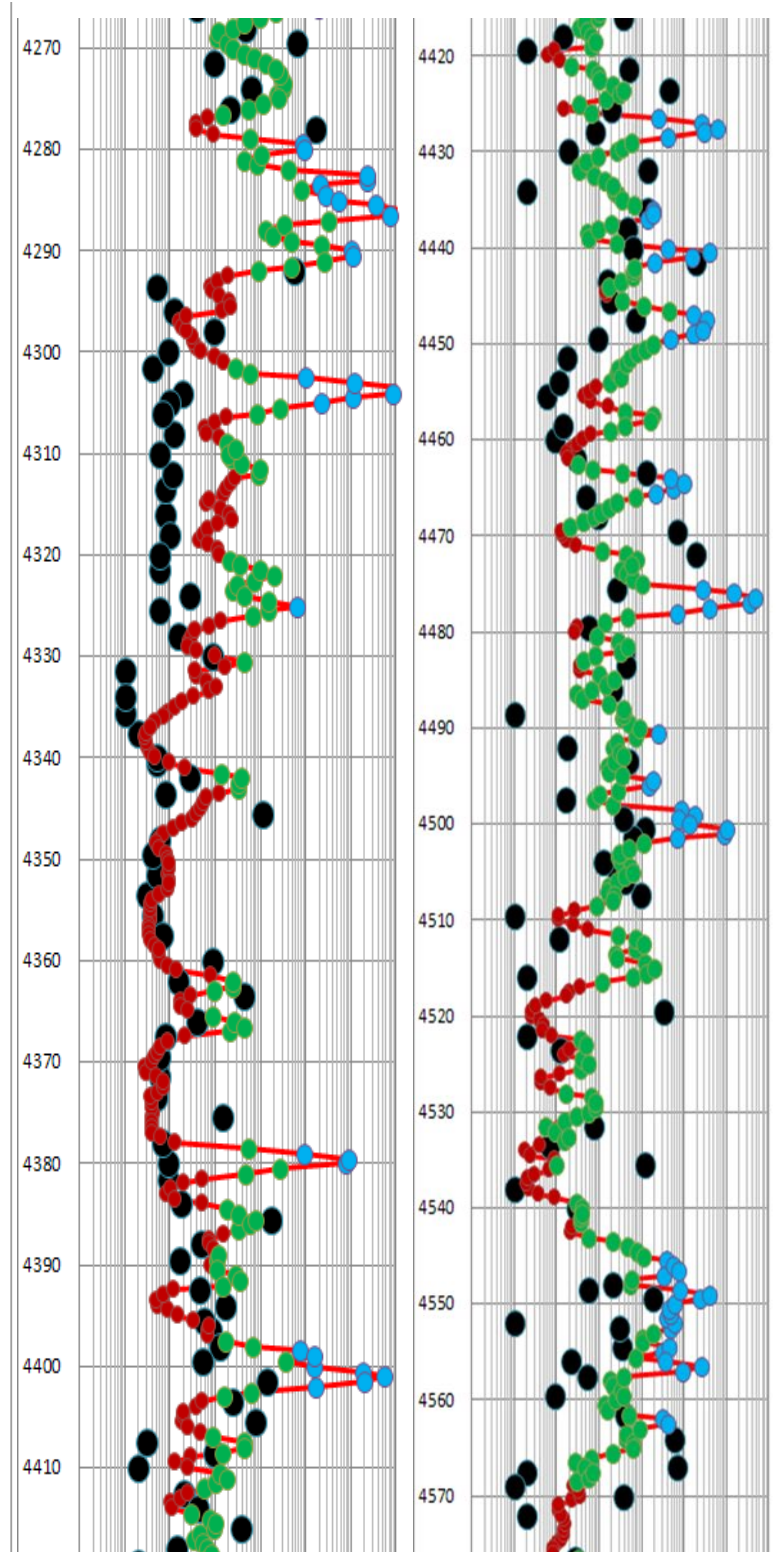
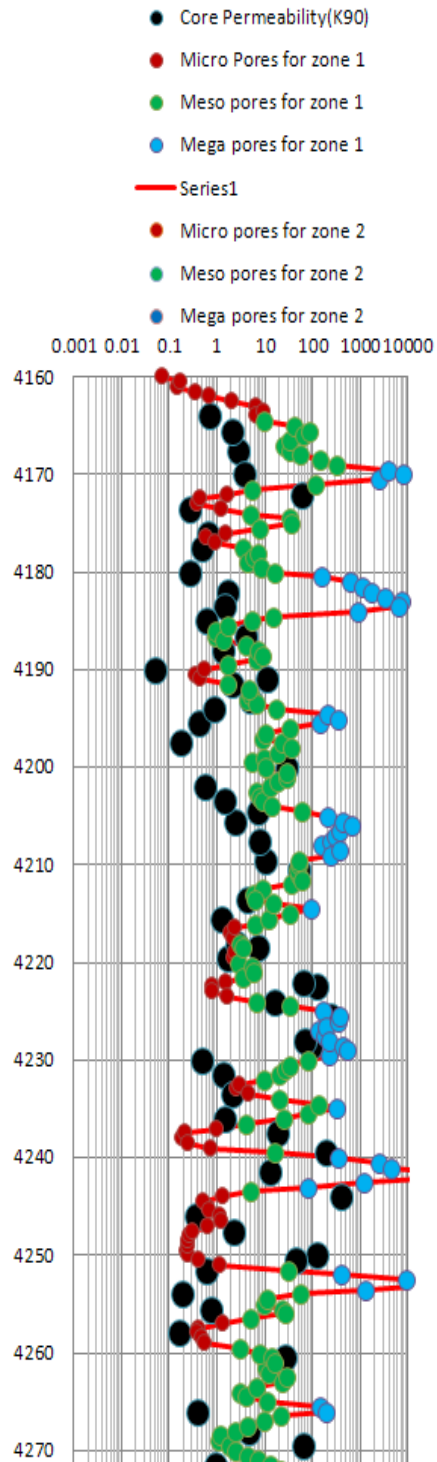
Table 2 lists coefficients  $a$  and  $b$ , which were obtained by the correlations and their 1/(Swir\*Phi) range of application. The table also gives the approximate T2 distribution range for each pore size class.

**Table 2: Coefficients  $a$  and  $b$  of Equation 3**

	$a$	$b$	R2	1/(Swir*Phi)	Approx T2
<b>Micro</b>	<b>0.0247</b>	<b>-0.0779</b>	<b>0.9101</b>	<b>&lt;36</b>	<b>&lt;50</b>
<b>Micro</b>	<b>0.0841</b>	<b>-2.1813</b>	<b>0.996</b>	<b>&lt;48</b>	<b>&lt;50</b>
<b>Meso</b>	<b>0.1564</b>	<b>-5.7167</b>	<b>0.9926</b>	<b>48–106</b>	<b>50–1,100</b>
<b>Mega</b>	<b>0.4089</b>	<b>-31.662</b>	<b>0.9955</b>	<b>&gt;106</b>	<b>50–10,000</b>

Figure 4 plots calculated permeability versus depth where they are compared with core permeability. Calculated micro pore permeability is shown by brown dots in this plot, while meso and mega pore permeability values are shown by green and blue dots, respectively. Although T2 distribution curves were very complex, it is believed that calculated permeability matches very well with core data.

## Permeability vs. Depth



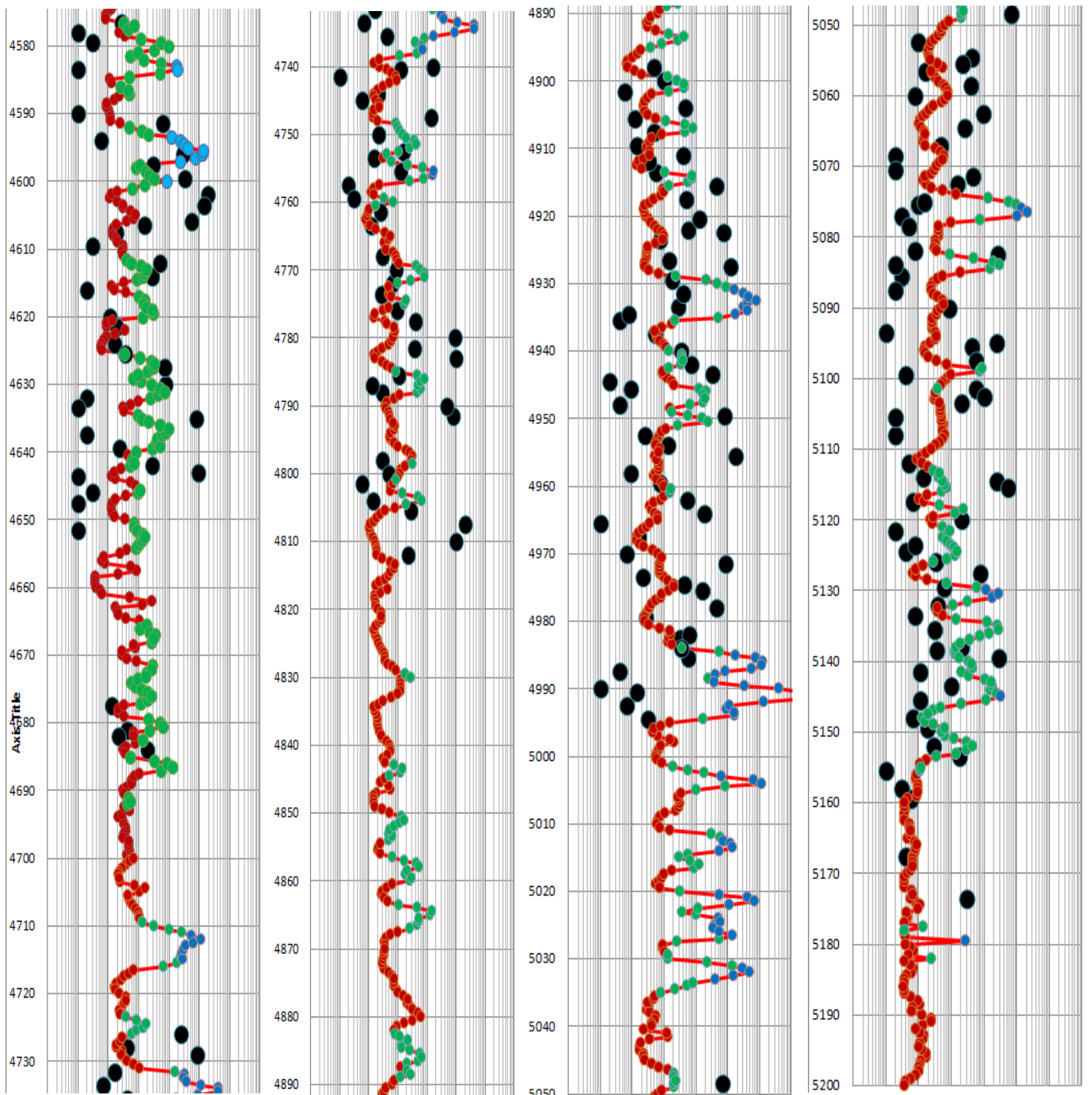


**Figure 4: Permeability vs. depth (micro, meso, and mega pore permeability values)**

**Permeability in Zone 2 (4,700 – 5,200)**

The same ranges of FZI and  $1/(swir*\phi)$  were considered for micro, meso, and mega pore size classifications in Zone 2, which correspond to approximate permeability ranges of less than 0.5mD, from 0.5 to 25mD, and greater than 25mD, respectively. Table 3 lists the ranges.

**Table 3: Ranges of FZI and 1/(Swir\*Phi)**

	Approx k	FZI	Excel Row	1/SwPhi	Excel Row
<b>Micro</b>	0–0.5	0–2.02	247–297	0–48.62	1,084–1,750
<b>Meso</b>	0.5–25	2.02–10.97	298–366	48.62–106	1,751–2,011
<b>Mega</b>	>25	10.97–150	367–404	106–851	2,012–2,080

Percentiles (5, 10, 20 ... 90) of FZI population were correlated with respective percentiles of 1/(Swir\*phi) population for each pore size category (figs. 5, 6, and 7). Four different correlations between FZI and 1/(swir\*phi) were derived for micro, meso, and mega pore sizes. Figures 5, 6, and 7 show these correlations. Two of the equations are for micro pore sizes.

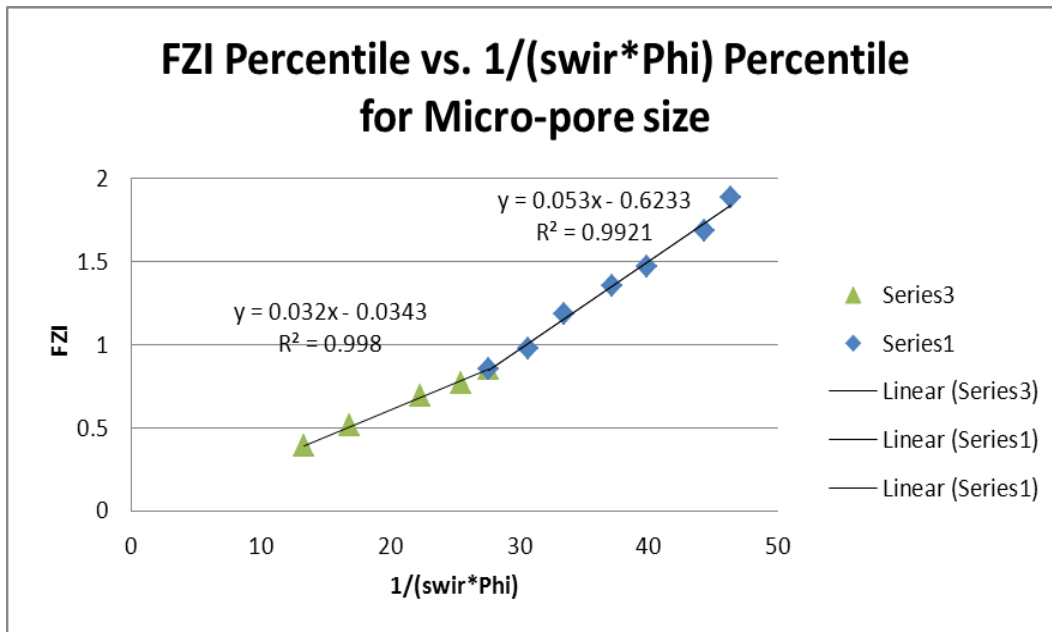


Figure 5: Plot of FZI vs 1/(swir\*phi) for micro pore sizes

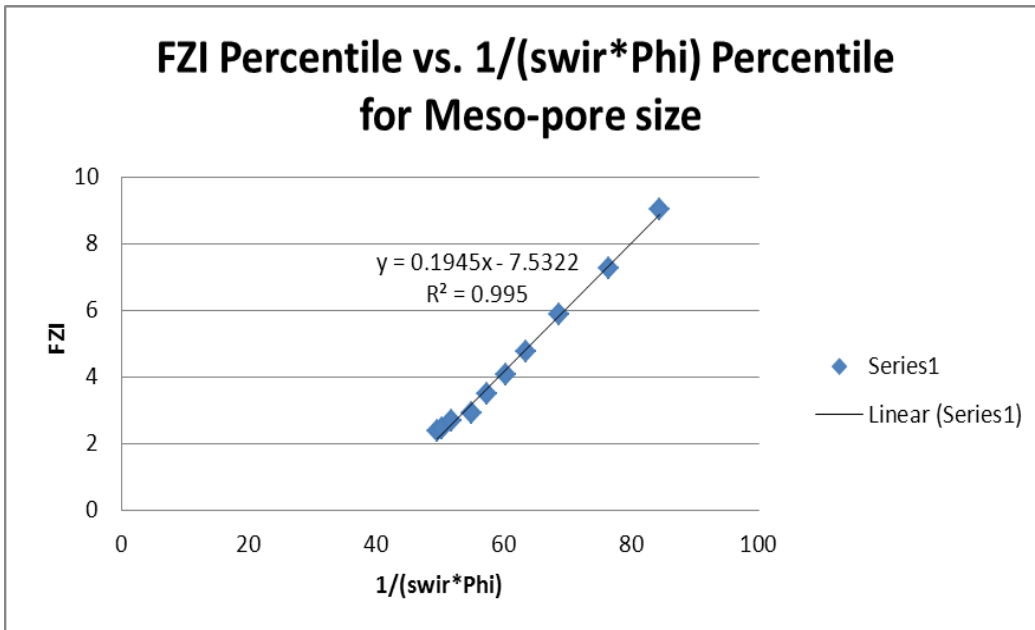


Figure 6: Plot of FZI vs 1/(swir\*phi) for meso pore sizes

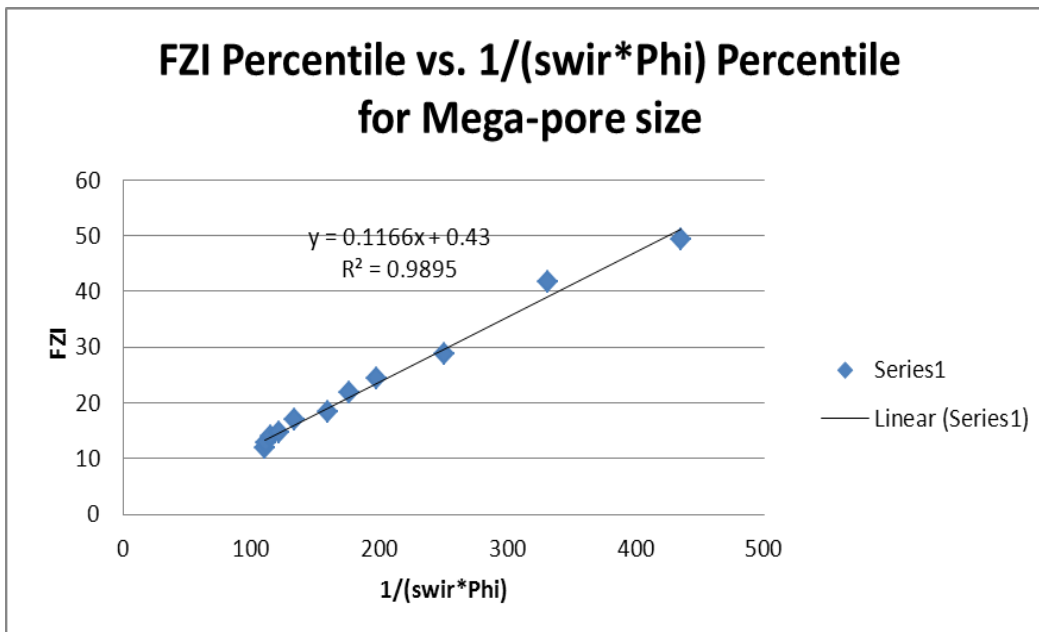


Figure 7: Plot of FZI vs 1/(swir\*phi) for mega pore sizes

Permeability in zone 2 was calculated using Equation 3. Table 4 lists coefficients  $a$  and  $b$ , which were obtained by the correlations, and their 1/(Swir\*Phi) range of application. The table also gives the approximate T2 ranges.

**Table 4: Coefficients *a* and *b* of Equation 3**

	<i>a</i>	<i>b</i>	R2	1/(Swir*Phi)	Approx T2
<b>Micro</b>	<b>0.032</b>	<b>-0.034</b>	<b>0.998</b>	<b>&lt;28</b>	<b>&lt; 50</b>
<b>Micro</b>	<b>0.053</b>	<b>-0.623</b>	<b>0.992</b>	<b>28–48</b>	<b>&lt; 50</b>
<b>Meso</b>	<b>0.195</b>	<b>-7.532</b>	<b>0.995</b>	<b>48–106</b>	<b>50–1,100</b>
<b>Mega</b>	<b>0.1166</b>	<b>0.43</b>	<b>0.990</b>	<b>&gt;106</b>	<b>50–10,000</b>

Figure 4 plots the calculated permeability in Zone 2 versus depth and compared with core measurements. Details of calculations are in an Excel Workbook called calculated permeability based on  $K_{90}$  from the NMR log of well 1-32, which is available upon request, and a layout of calculated permeability with log derived lithology, GR, NMR T2 distribution can be seen in Sheet 2 (Graphs) of this Excel Workbook.

## Part 2: Determination of Permeability using Maximum Permeability from Core

### Permeability Based on $K_{Max}$ in Zone 1 (4,160–4,700 ft)

Correlations between FZI from core using  $K_{max}$  and  $1/(Swir*\phi)$  from log were used to derive permeability. Maximum permeability and porosity from routine core analysis were used to calculate FZI. Irreducible water saturation and effective porosity from the NMR log were used to calculate  $1/(Swir*\phi)$ . The same ranges of FZI and  $1/(Swir*\phi)$  as mentioned in the first part of the report were used for micro, meso, and mega pore size classification. These ranges correspond to permeability ranges of less than 0.5, from 0.5 to 25 mD, and greater than 25 mD respectively. Table 5 lists the ranges.

**Table 5: Ranges of FZI and  $1/(Swir*\phi)$** 

	Approx k	FZI	Excel Row	$1/(Swir*\phi)$	Excel Row
<b>Micro</b>	<b>&lt;0.5</b>	<b>&lt;2.02</b>	<b>4–114</b>	<b>&lt;48.62</b>	<b>4–430</b>
<b>Meso</b>	<b>0.5–25</b>	<b>2.02–10.97</b>	<b>115–218</b>	<b>48.62–106</b>	<b>431–937</b>
<b>Mega</b>	<b>&gt;25</b>	<b>10.97–150</b>	<b>219–318</b>	<b>106–851</b>	<b>938–1,083</b>

Four different correlations were derived for micro, meso, and mega pore size based on max permeability of whole cores. Figures 8, 9, and 10 show these correlations.

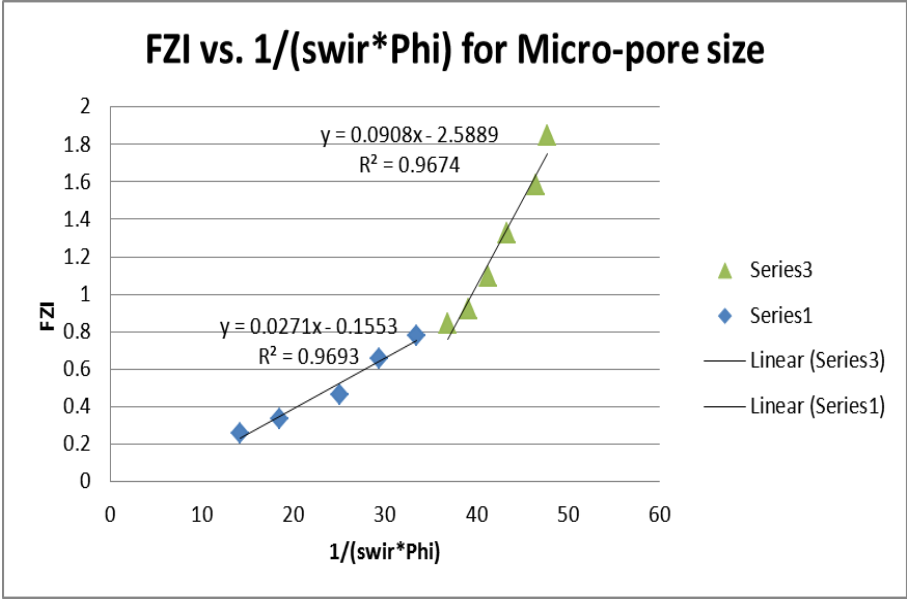


Figure 8: Plot of FZI vs 1/(swir\*phi) for micro pore sizes

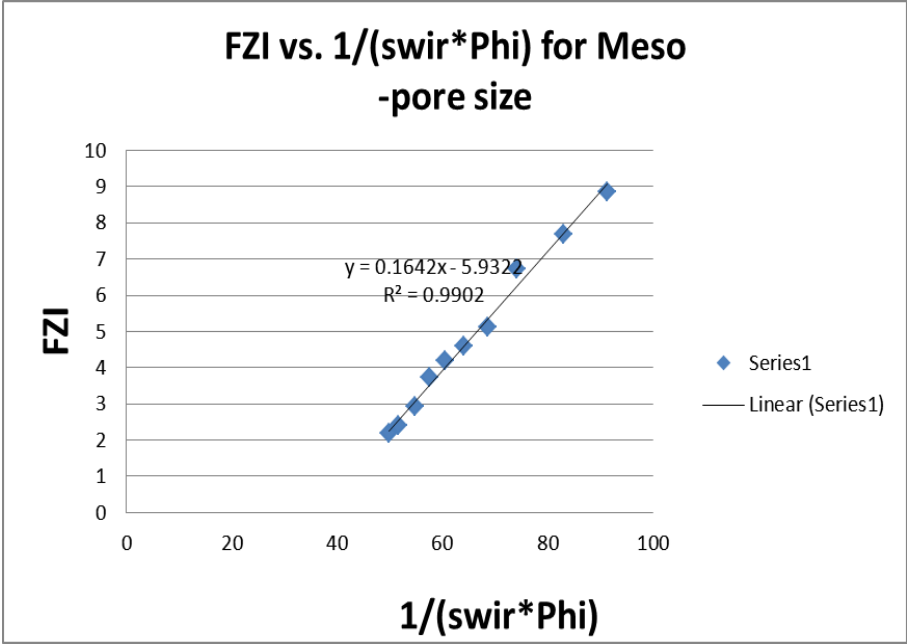


Figure 9: Plot of FZI vs 1/(swir\*phi) for meso pore sizes

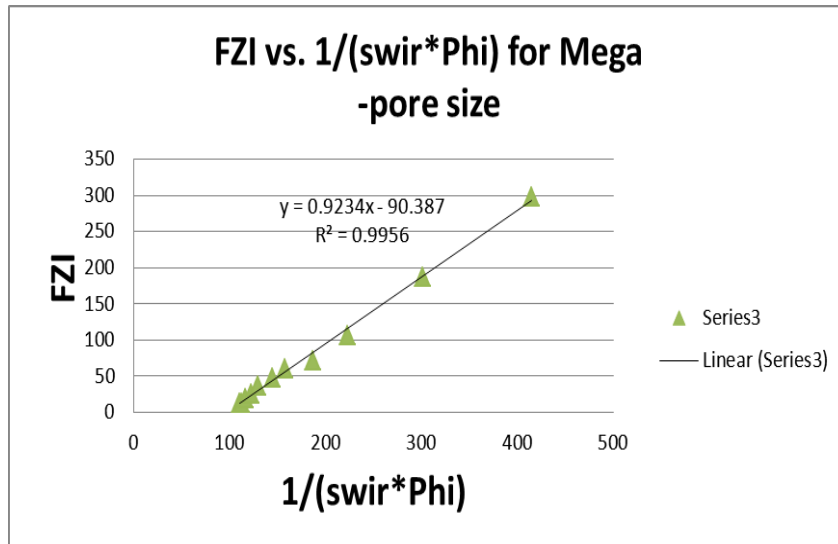


Figure 10: Plot of FZI vs  $1/(swir*\phi)$  for mega pore sizes

Permeability was calculated in zone 1 using Equation 3, and coefficients  $a$  and  $b$  were derived from figs. 1, 2, and 3. Table 6 lists the coefficients and applied ranges.

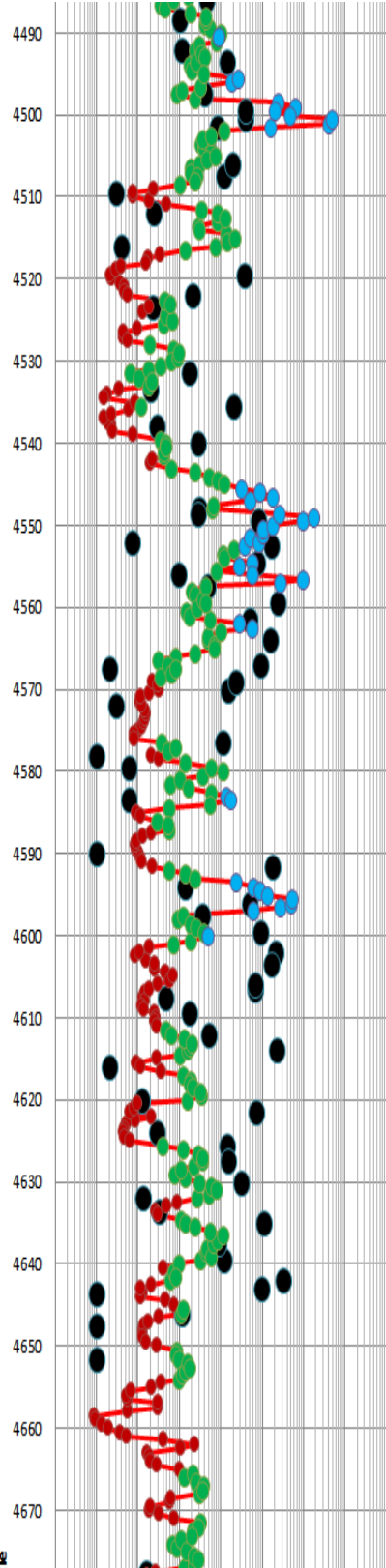
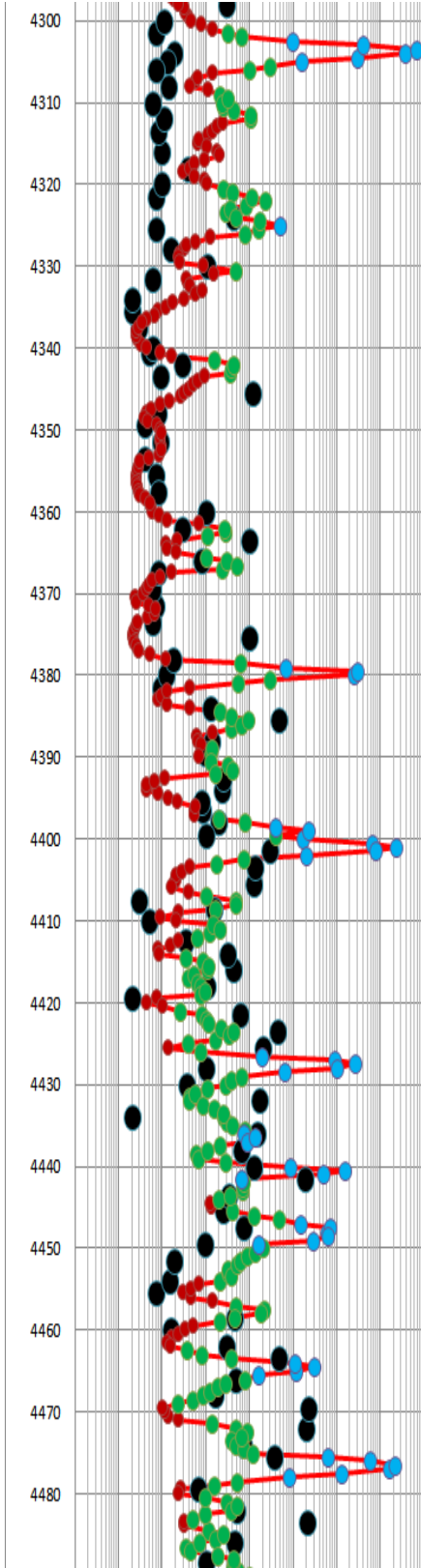
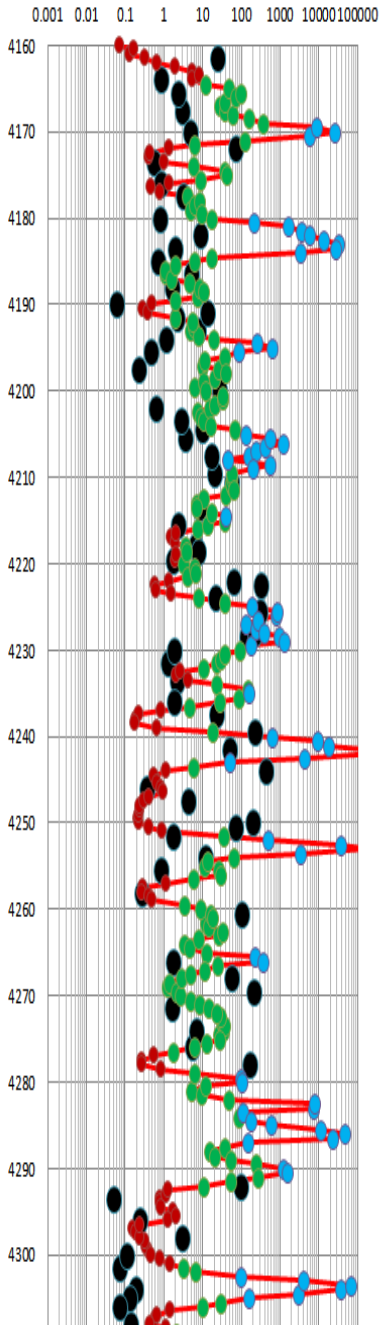
**Table 6: Coefficients  $a$  and  $b$  of Equation 3**

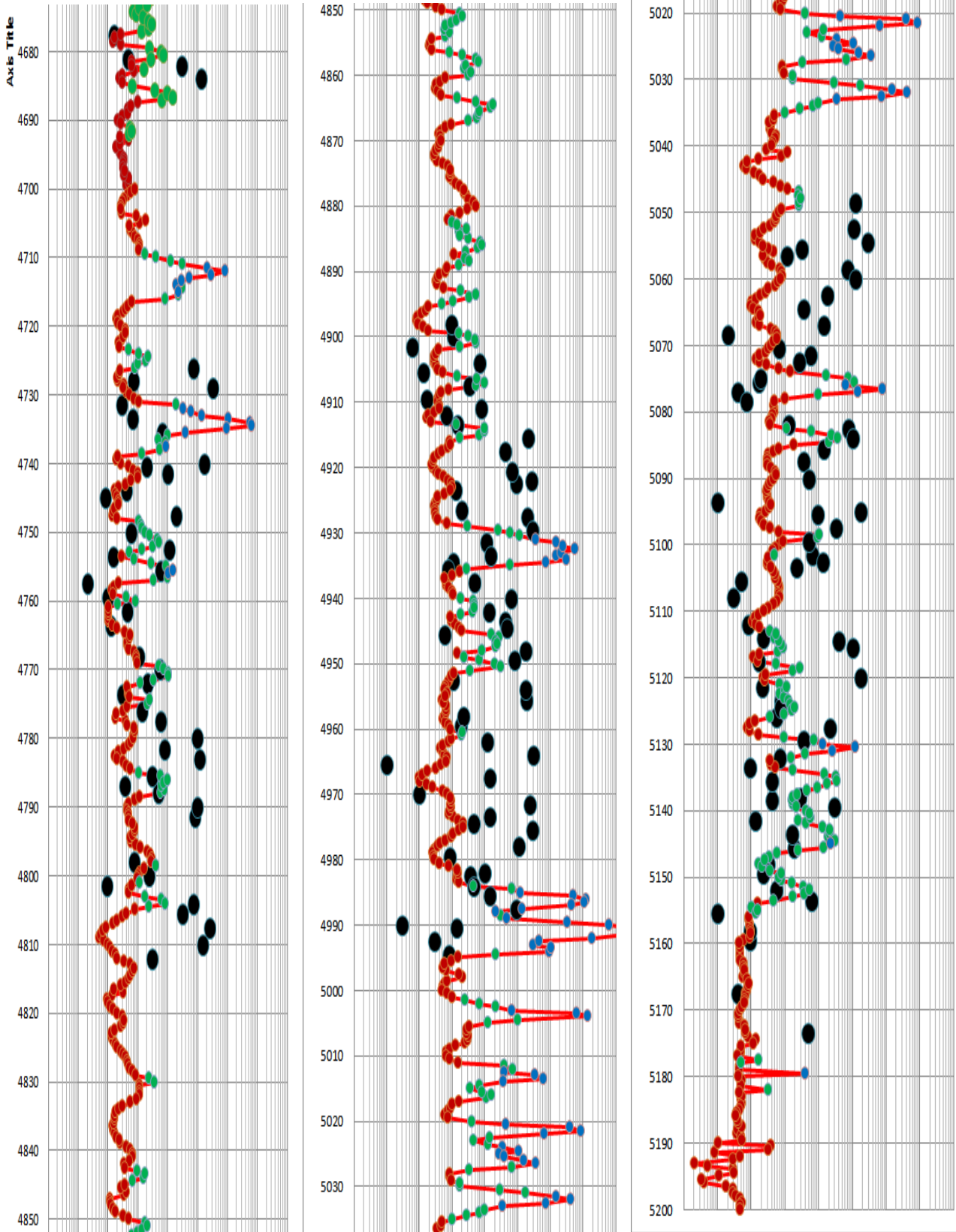
	$a$	$b$	R2	$1/(Swir*\Phi)$	Approx T2
<b>Micro</b>	<b>0.0271</b>	<b>-0.1553</b>	<b>0.9693</b>	<b>&lt;36</b>	<b>&lt;50</b>
<b>Micro</b>	<b>0.0908</b>	<b>-2.5889</b>	<b>0.9674</b>	<b>&lt;48</b>	<b>&lt;50</b>
<b>Meso</b>	<b>0.1642</b>	<b>-5.9322</b>	<b>0.9902</b>	<b>48–106</b>	<b>50–1,100</b>
<b>Mega</b>	<b>0.9234</b>	<b>-90.387</b>	<b>0.9956</b>	<b>&gt;106</b>	<b>50–10,000</b>

Figure 11 plots calculated permeability versus depth where they are compared with core max permeability. Calculated micro pore permeability is shown by brown dots in this plot, and meso and mega pore permeability values are shown by green and blue dots, respectively.

# Permeability vs. Depth

- Core Permeability(K90)
- Micro-zone 1
- Meso for zone 1
- Mega for zone 1
- Series1
- Micro for zone 1





**Fig. 11: Permeability vs. depth (micro, meso, and mega pore permeability values)**

**Permeability Based on  $K_{Max}$  in Zone 2 (4,700 – 5,200)**

The same ranges of FZI and  $1/(swir*\phi)$  were considered for micro, meso, and mega pore size classifications in Zone 2, which correspond to approximate permeability range of less than 0.5, from 0.5 to 25 mD, and greater than 25 mD respectively. Table 7 lists the ranges:

**Table 7: Ranges of FZI and  $1/(Swir*\Phi)$**

	Approx k	FZI	Excel Row	$1/(Swir*\Phi)$	Excel Row
<b>Micro</b>	<0.5	<2.02	319-348	<48.62	4-430
<b>Meso</b>	0.5-25	2.02-10.97	348-404	48.62-106	431-937
<b>Mega</b>	>25	10.97-150	405-480	106-851	938-1083

Three correlations between FZI and  $1/(swir*\phi)$  were derived in zone 2. Figures 12, 13, and 14 show these correlations.

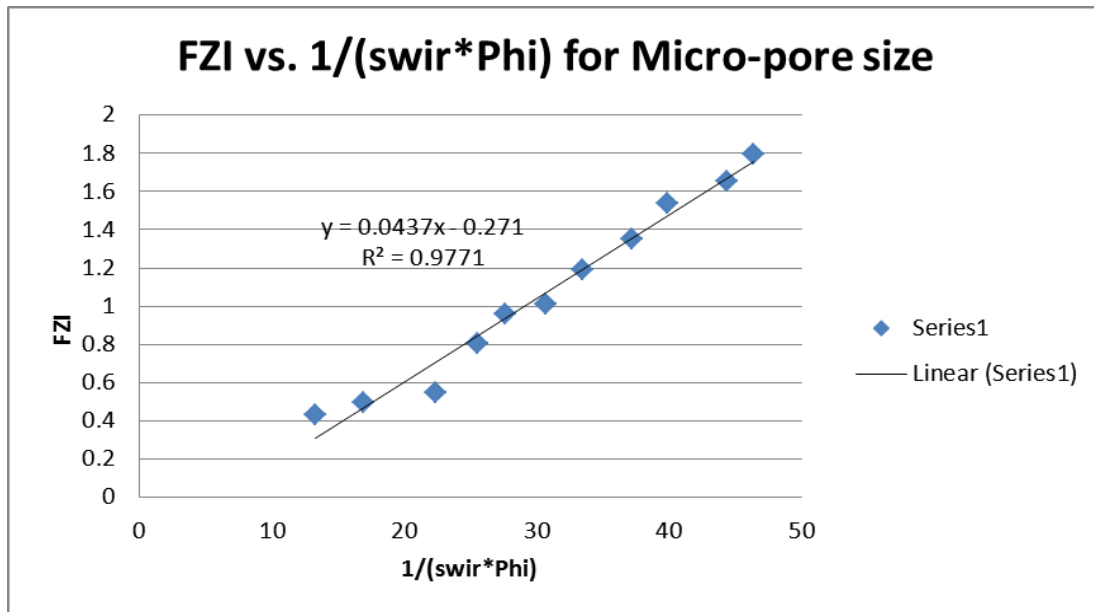


Figure 12: Plot of FZI vs  $1/(swir*\phi)$  for micro pore sizes

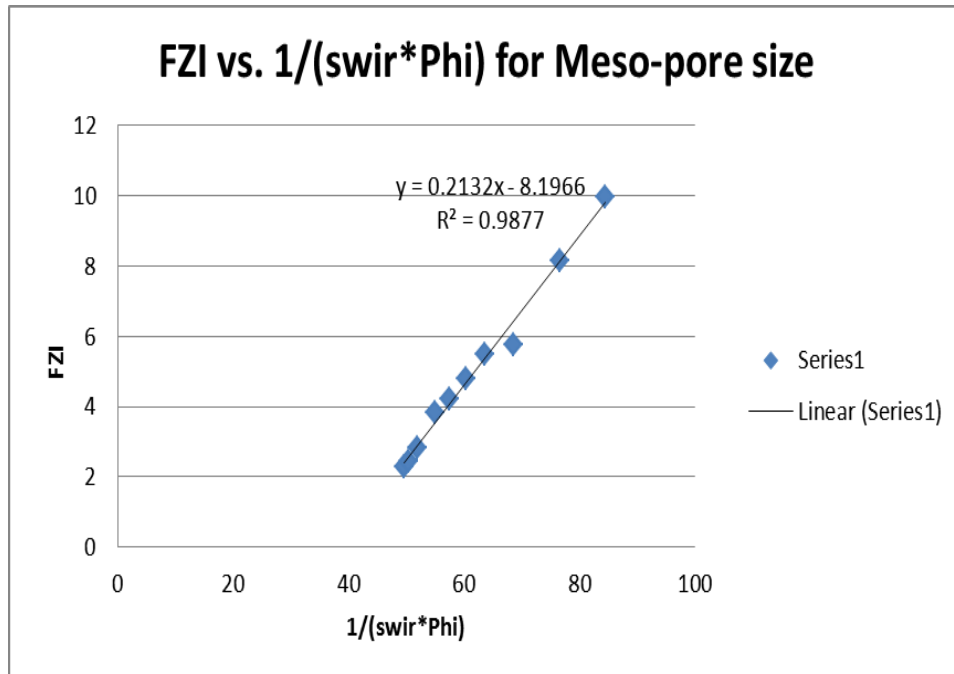


Figure 13: Plot of FZI vs 1/(swir\*phi) for meso pore sizes

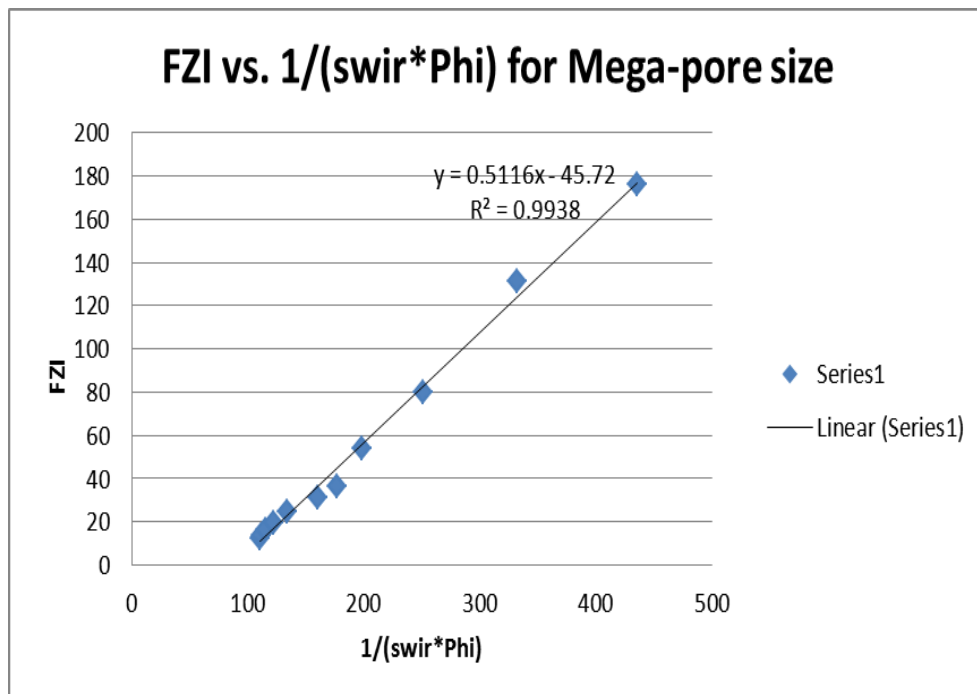


Figure 14: Plot of FZI vs 1/(swir\*phi) for mega pore sizes

Permeability was calculated in zone 2 using Equation 3, and coefficients  $a$  and  $b$  were derived from figs. 12, 13, and 14. Details of calculations are in an Excel Workbook called calculated permeability based on  $K_{Max}$  from the NMR log of well 1-32, which is available upon request, and a layout of calculated permeability with log-derived lithology, GR, NMR T2 distribution can be seen in Sheet 2 (Graphs) of this Excel Workbook. Table 8 lists the coefficients and applied ranges of  $1/(Swir*Phi)$ .

**Table 8: Coefficients  $a$  and  $b$  of Equation 3**

	$a$	$b$	R2	$1/(Swir*Phi)$	Approx T2
<b>Micro</b>	<b>0.0437</b>	<b>-0.271</b>	<b>0.9771</b>	<b>&lt;48</b>	<b>&lt;50</b>
<b>Meso</b>	<b>0.2132</b>	<b>-8.1966</b>	<b>0.9877</b>	<b>48–106</b>	<b>50–1,100</b>
<b>Mega</b>	<b>0.5116</b>	<b>-45.72</b>	<b>0.9938</b>	<b>&gt;106</b>	<b>50–10,000</b>

### Comparison of Predicted Permeability Based on Core Permeability at 90 Degree and Maximum Permeability

Predicted permeability based on max core permeability is almost equal to predicted permeability based on 90-degree core permeability for micro and meso pore intervals. However, higher permeability is predicted for mega pore intervals when core sample max permeability is used. This difference is attributed to differences between max core permeability and 90-degree core permeability for the same porosity when core samples have mega pores. The difference between max core permeability and 90-degree permeability is small when the core samples are micro and meso pore type.

Since 90-degree core sample permeability is more representative of reservoir average permeability, it is suggested to base predicted permeability of the Arbuckle on 90-degree core sample permeability data.

### Calculation of Vertical Permeability in the Arbuckle

Based on routine core analysis data, a single relationship does not exist between vertical ( $K_v$ ) and horizontal ( $K_h$ ) permeability in the Arbuckle formation. However, rock samples can be divided into five groups, and a specific relationship can be defined for each group. The Arbuckle is a layered formation, and vertical permeability of each layer is quite different from the surrounding layers. Therefore, it should be divided into layers based on  $K_v/K_h$  relationships.

#### Group 1

This group contains 15 samples; both vertical and horizontal permeability in these samples is less than 0.01 mD. Since actual vertical and horizontal permeability could not be measured in the lab and  $K_v/K_h$  could not be found, it is suggested to assume the following relationship (Eq. 1; derived for Group 3) be applied to this group. Vertical fractures may not exist in this group.

$$\text{Eq. 1} \dots K_v = 0.1871K_h$$

$$R^2 = 0.5367$$

#### Group 2

Group 2 consists of 216 core samples. Vertical permeability of these samples is less than 0.01 md but horizontal permeability ranges from 0.02 mD to 210 mD. A vertical permeability of less than 0.01 mD (suggested 0.005 mD) could be assigned to layers of the reservoir with this type of rock. Vertical fractures may not exist in this group.

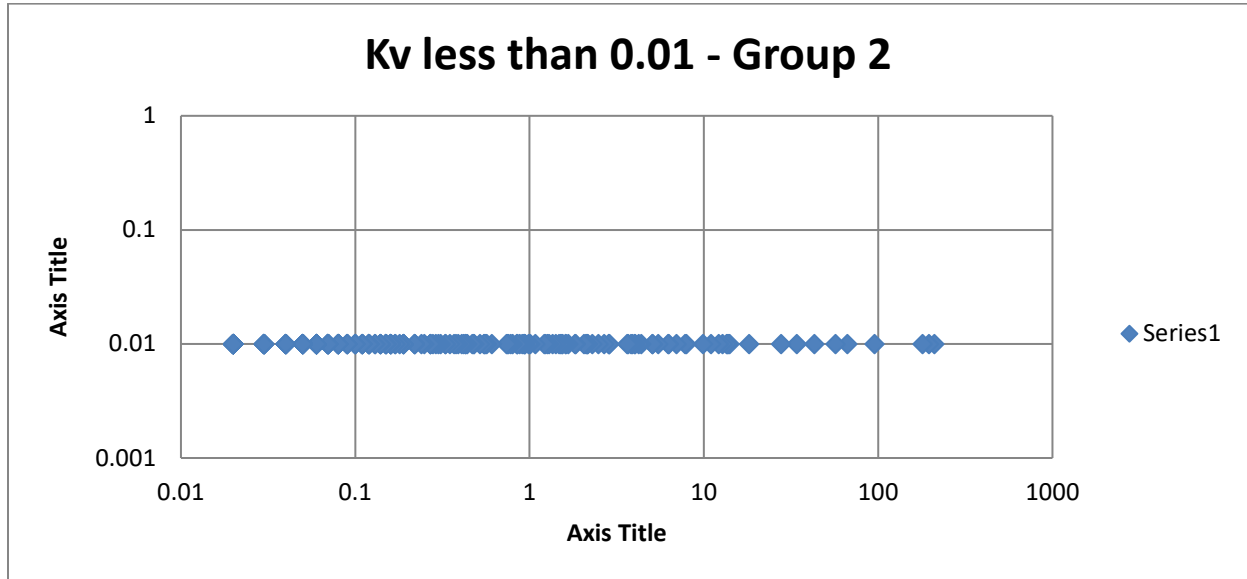


**Figure 1 – Kv vs. Kh for Group 2 core samples**

**Group 3**

This group has 97 core samples. As shown in fig. 2, vertical permeability of these samples is less than horizontal permeability and the following relationship is proposed for determination of Kv. Vertical fractures may not exist in this group.

$$\text{Eq. 1 ..... } K_v = 0.1871K_x$$

$$R^2 = 0.5367$$

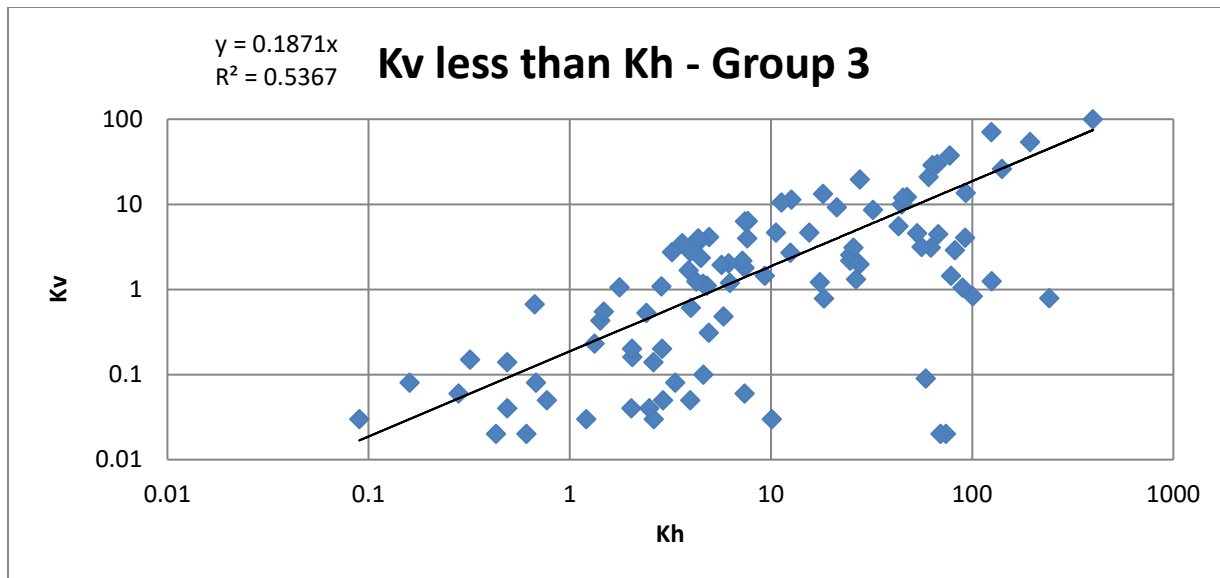


**Figure 2 – Relationship between Kv and Kh for Group 3 core samples**

**Group 4**

There are 60 core samples in Group 4. Vertical permeability of these samples is more than horizontal permeability, as shown in fig. 3. Equation 2 describes the average relationship between Kv and Kh.

$$\text{Eq. 2 ..... } K_v = 2.4484K_x$$

$$R^2 = 0.6916$$

This relationship indicates that the rocks include vertical fractures that increase vertical permeability by several times.

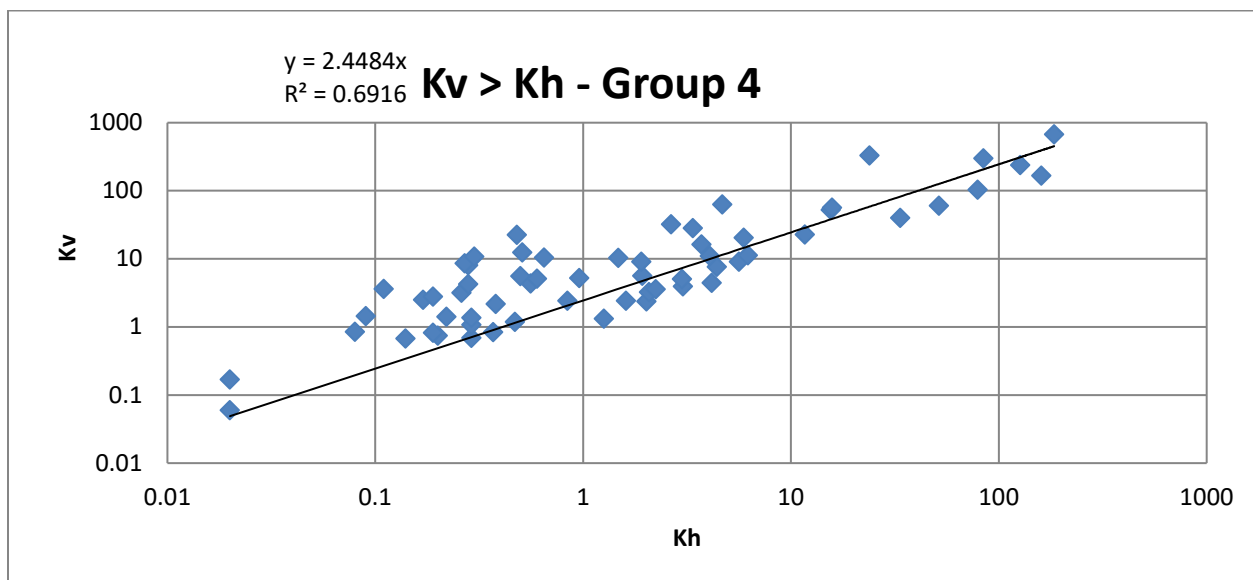


**Figure 3 – Relationship between Kv and Kh for Group 4 core samples**

### Group 5

This group has 18 core samples. Vertical permeability is much bigger than horizontal permeability, which shows that the rocks in this group are extensively fractured in a vertical direction. Figure 4 is a plot of  $K_v$  versus  $K_h$ , and the following relationship is proposed for layers with this type of rock.

$$\text{Eq. 3 ... } K_v = 82.624K_h$$
$$R^2 = 0.9906$$

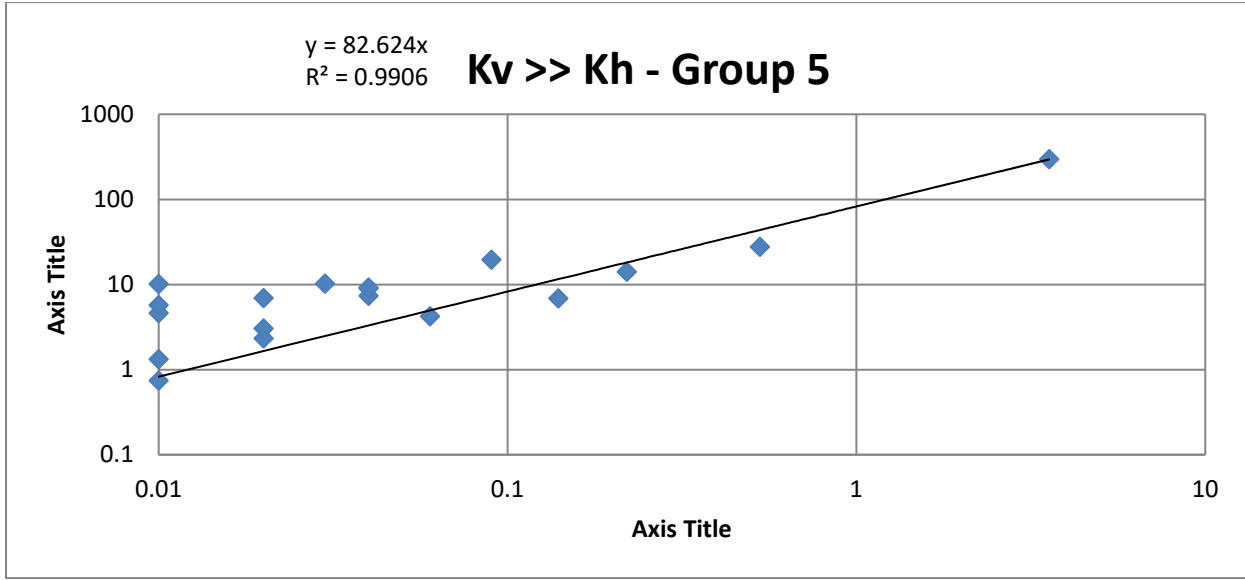


**Figure 4 – Relationship between  $K_v$  and  $K_h$  for Group 5 core samples**

## Appendix E

### Drainage Capillary Pressure Curves in Arbuckle

The Pc curves were derived based on a theoretical method (M.F.Alavi) that relates endpoints of capillary pressure curves to Reservoir Quality Index (RQI). Based on this investigation, there are good correlations between endpoints of capillary pressure curves (entry pressure and irreducible water saturation) and RQI.

The key well (well 1-32) was used to calculate Pc curves for the Arbuckle. Generated Pc curves from the NMR log of well 1-32 were used to find correlations between endpoints and RQI for determination of Pc curves. Pc curves from NMR were in mercury-air system and then converted to a CO<sub>2</sub>-brine system (Fig. 1).

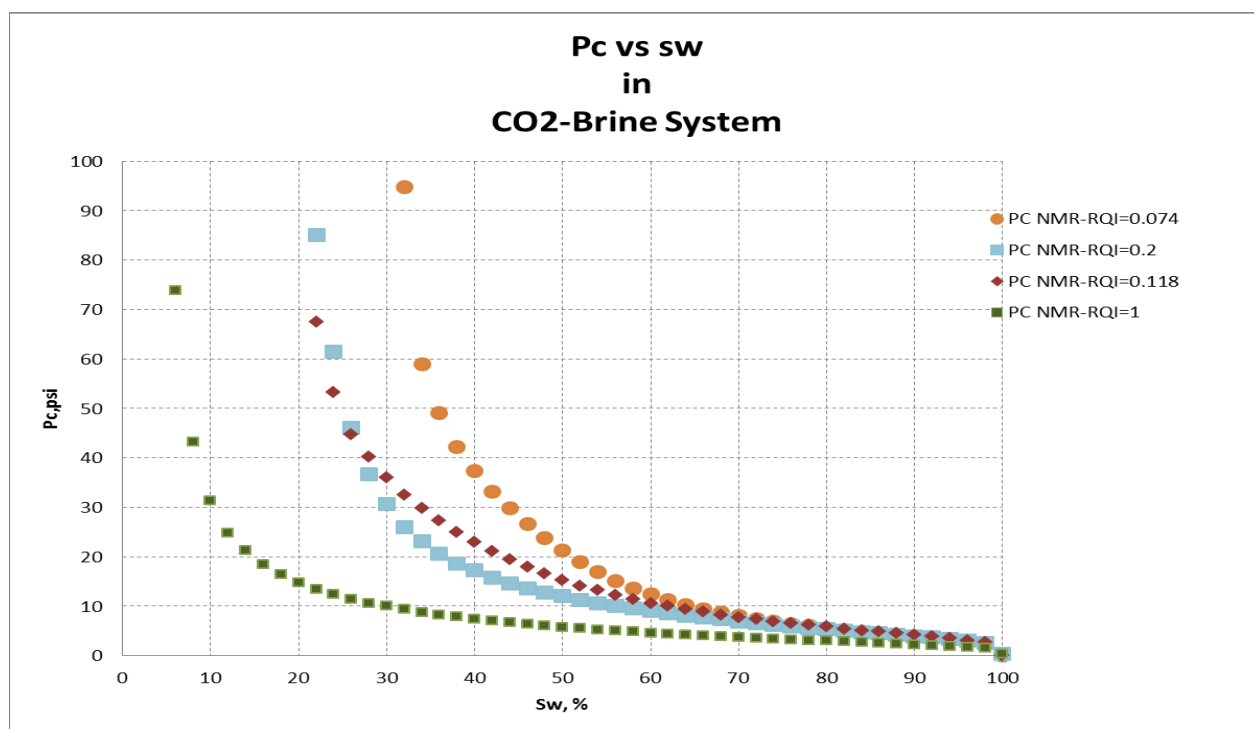


**Figure 41: Pc curves generated from NMR**

#### a. Entry Pressure

Based on SCAL data of other fields, a good correlation can be found between capillary entry pressure and RQI. Pore throat at entry pressure in well 1-32 was determined from Winland R35, and entry pressure was calculated from pore throat radius. Winland R35 was calculated using Equation 1:

$$\log R35 = 0.732 + 0.588 \log K - 0.864 \log \phi \quad \text{Eq. 1}$$

Previously, the permeability of the Arbuckle in Well 1-32 was determined. Based on porosity and the calculated permeability of Well 1-32, RQI in this well was obtained. R35 was plotted against RQI in fig. 1 to find an equation in terms of RQI:

$$R35 = 12.885 RQI^{-1.178} \quad \text{Eq. 2}$$

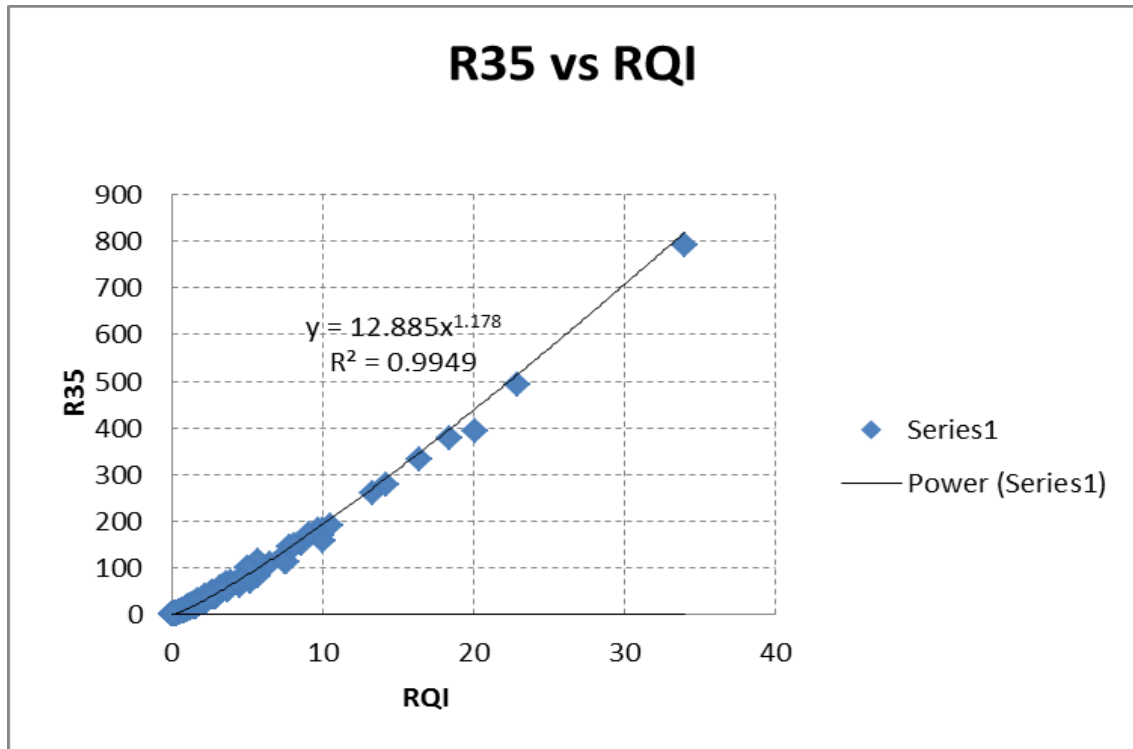


**Figure 42: R35 versus RQI**

Equation 2 was multiplied by a factor (1.35) to calculate the entry pore throat radius (Equation 3). The factor, 1.35, was determined based on studies of other carbonate reservoirs.

$$R_{\text{entry}} = 1.39 * (a * RQI^b) \quad \text{Eq. 3}$$

Entry pressure was calculated using Equation 3 and interfacial tension between CO<sub>2</sub> and brine, Equation 4:

$$P_e = \frac{2 * \sigma \cos\theta * 0.147}{1.39 * (a * RQI^b)} \quad \text{Eq. 4}$$

A function between entry pressure and RQI was found by calculating Equation 4 for  $P_{\text{entry}}$  in terms of RQI. Interfacial tension of 30 dyne/cm was calculated using an equation from an article, “*Interfacial Tension Data and Correlations of Brine/CO<sub>2</sub> Systems under Reservoir Conditions, (Chalbaud et al. 2006).*” A contact angle of zero was used for the CO<sub>2</sub>-brine system. After simplifying, Equation 4 becomes:

$$P_e = 0.49 * RQI^{-1.178} \quad \text{Eq.5}$$

### **b. Irreducible Water Saturation**

Irreducible water saturation is needed to calculate normalized non-wetting phase saturation ( $S_{nw}$ ). Based on irreducible water saturation of SCAL data, mainly carbonate reservoirs, irreducible water saturation at certain capillary pressure can be correlated very well to the RQI of the rock. There is a good correlation between irreducible water saturation of reservoir rocks and RQI. NMR data of Well 1-32 were used to determine irreducible water saturation at a  $P_c$  of 20 bars (290 psi). Also interfacial tension between CO<sub>2</sub>

and water was given to the Tech-Log Module to find Swir versus depth for this well. Irreducible water saturation in Well 1-32 in the Arbuckle is plotted against RQI in fig. 3.

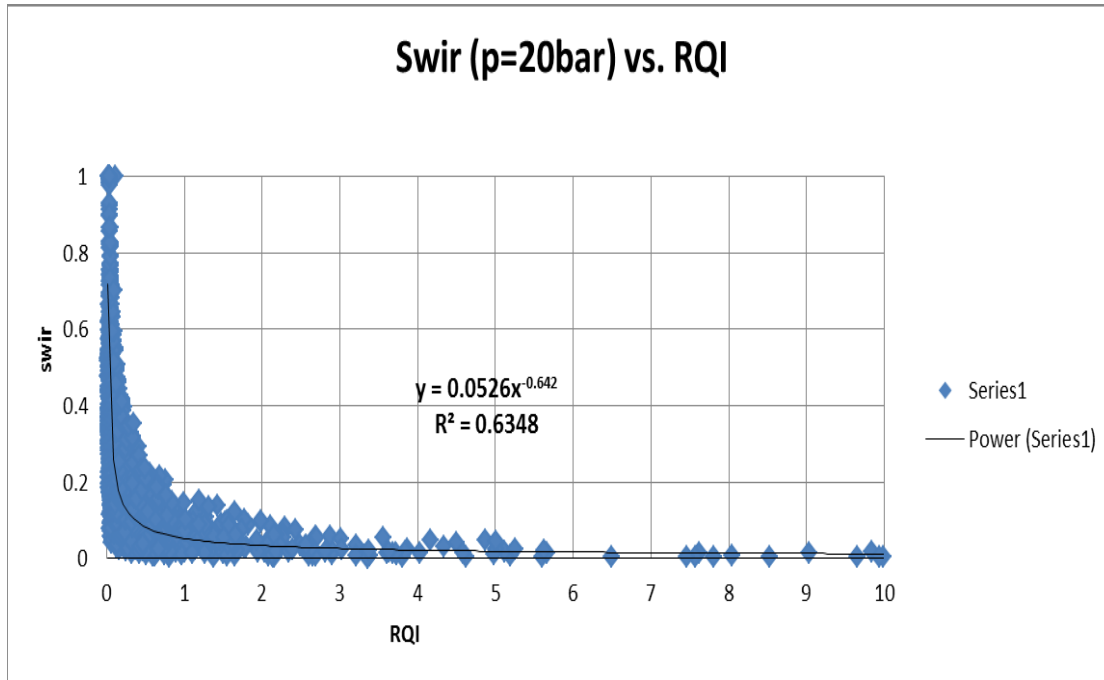


**Figure 43: Irreducible water saturation vs. RQI**

The relation between swir and RQI was obtained from Figure 3, Eq. 6::

$$\text{Swir} = 0.0526 * \text{RQI}^{-0.642} \quad \text{Eq. 6}$$

### c. Shape of Normalized Pc curve

The Pc curves that were obtained from NMR (fig. 1) were normalized by plotting SnWn (Normalized Non-Wetting Phase Saturation, Equation 9) versus EQR (Equivalent Radius, Equation 7). The shape of normalized Pc curves appears in fig 4. To find EQR at any Pc, entry pressure of the Pc curve was used. A function in the form of Equation 7 was fit through the normalized data points in fig. 4 and constants a and b of this equation were found.

$$S_{nwn} = (1 - aEQR)(1 - EQR^b) \quad \text{Eq. 7}$$

$$a = 1 * 10^{-6}$$

$$b = 0.898$$

Equivalent radius is a function of entry pressure and capillary pressure (Equation 8), where entry pressure is a function of RQI, which is given by Equation 5.

$$EQR = \frac{P_e}{P_c} \quad \text{Eq. 8}$$

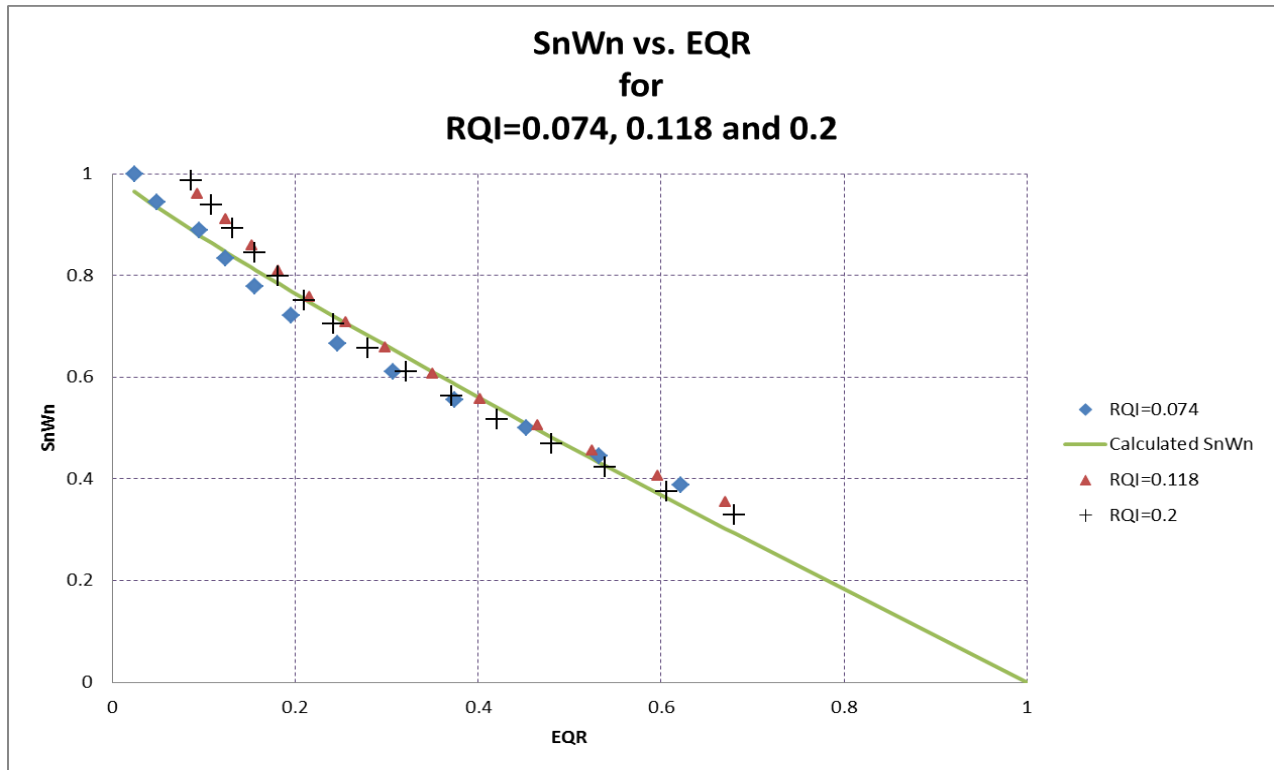


**Figure 44: SnWn vs. EQI for RQI 1, 5.19 and 20**

Equation 9 defines SnWn (normalized non-wetting phase saturation). Irreducible water saturation was calculated using equation 6 and initial water saturation is known at every Pc.

$$S_{nwn} = \frac{1-S_{wi}}{1-S_{wir}} \quad \text{Eq. 9}$$

Values of constants a and b of Equation 7, which were derived by regression before, were replaced in Equation 7 to get Equation 10. This equation will be used to calculate drainage capillary pressure curves.

$$S_{nwn} = (1 - 1 * 10^{-6} \frac{P_e}{P_c}) (1 - \frac{P_e^{0.898}}{P_c}) \quad \text{Eq. 10}$$

#### d. Calculation of Drainage Capillary Pressure Curves

Equation 11 is obtained from Equation 9 and will be used for calculating drainage water saturation:

$$S_{wi} = 1 - S_{nwn}(1 - S_{wir}) \quad \text{Eq. 11}$$

According to Equation 11, initial water saturation (Swi) is a function of Snwn . It was shown that Snwn is a function of Pe and Pc (Equation 10), where Pe is a function of RQI. Snwn in Equation 11 can be replaced by respective functions and an equation can be obtained that expresses Swi in terms of RQI and Pc:

$$S_{wi} = 1 - \left(1 - a \frac{0.507RQI^{-1.178}}{P_c}\right) \left(1 - \left(\frac{0.507RQI^{-1.178}}{P_c}\right)^b\right) (1 - 0.0526RQI^{-0.642}) \quad \text{Eq.12}$$

Constants (a and b) were previously found (Equation 7). They were incorporated into Equation 12, which gives water saturation for every Pc and RQI. Nine Pc curves were calculated for nine rock types. RQI in the Arbuckle changes from 0.017 to 34. This range was divided into nine subdivisions (table 1):

Table 1: Subdivisions of RQI range

RT	RQI from	RQI To	Ave RQI
1	40	10	25
2	10	2.5	6.25
3	2.5	1	1.75
4	1	0.5	0.75
5	0.5	0.4	0.45
6	0.4	0.3	0.35
7	0.3	0.2	0.25
8	0.2	0.1	0.15
9	0.1	0.01	0.055

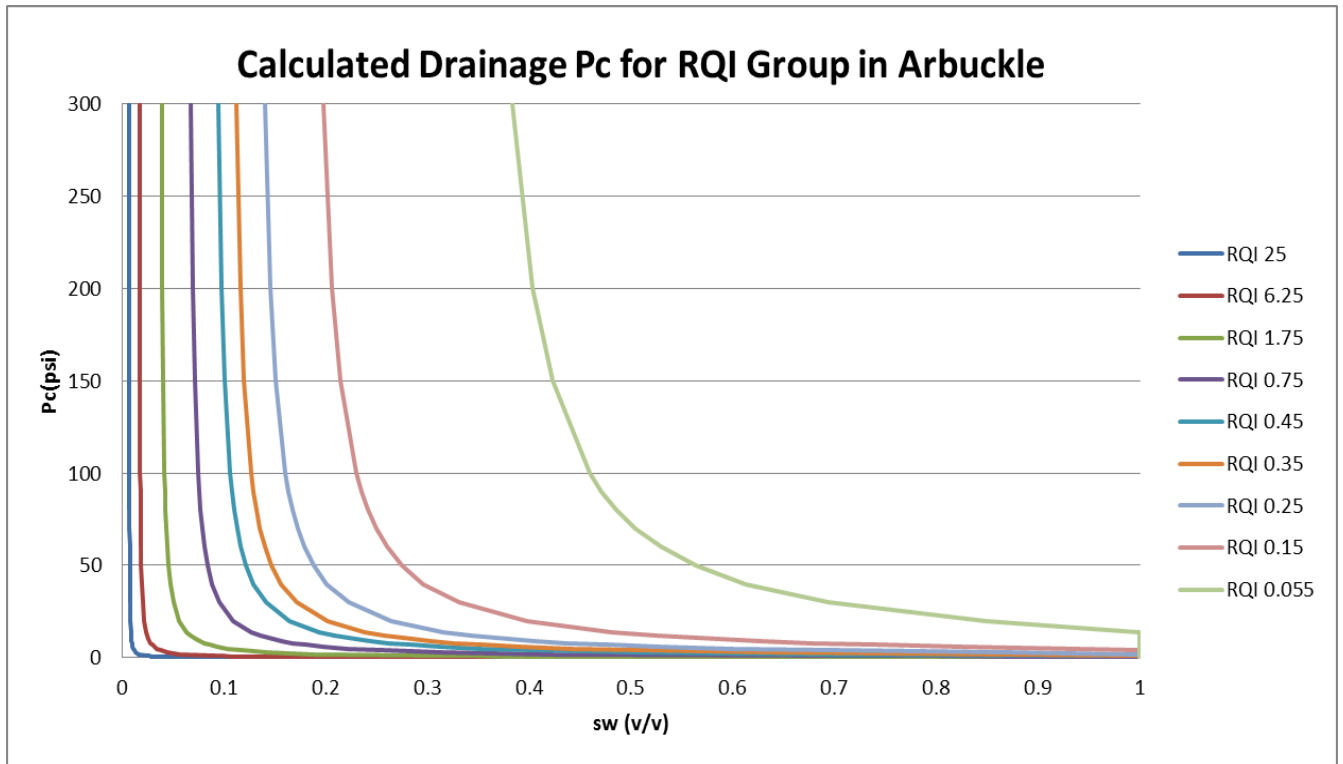
The mid-range of each subdivision was used to calculate 9 Pc curves using Equation 12, Table 2. The generated Pc curves are shown in fig. 5. These curves are in agreement with NMR Pc curves, when the right permeability and RQI are considered and compared (fig. 6). [Figure 7](#) shows water saturation by Equation 12 compared to water saturation from NMR capillary pressure module. The two water saturations are in good agreements which indicate the accuracy of the generated water saturation by equation 12.

**Nomenclature**

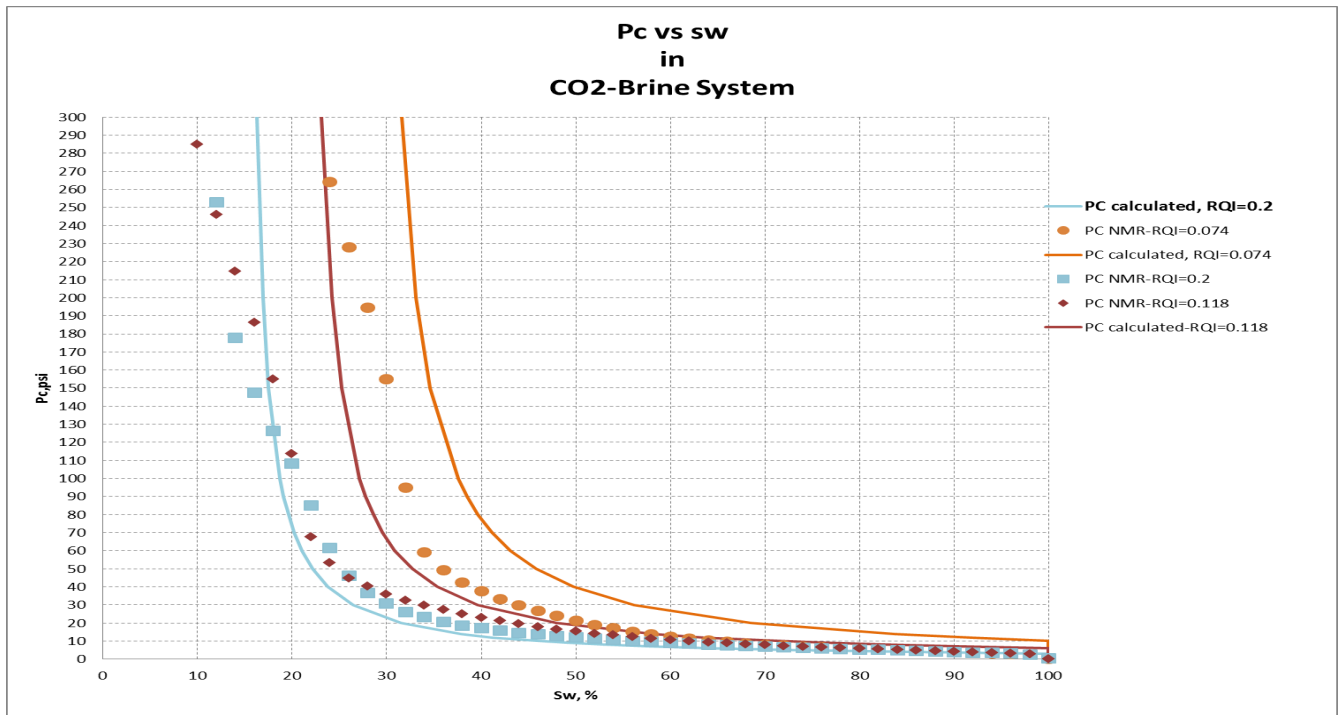
- $a$  = constant
- $b$  = constant
- $EQR$  = Equivalent Radius
- $NMR$  = Nuclear magnetic resonance
- $P_e$  = Entry Pressure
- $PC$  = capillary pressure
- $RQI$  = Reservoir Quality Index ( $\mu m$ )
- $R35$  = Winland R35
- $R_{entry}$  = pore throat radius at entry pressure
- $Snwn$  = Normalized non-wetting phase saturation
- $Swi$  = Initial water saturation
- $Swir$  = Irreducible water saturation (fractional pore volume)

Table 2: Nine Pc curves for nine RQI

a		b		Drainage PcTable in Arbuckle						
0.000001		0.89773								
RQI	25	6.25	1.75	0.75	0.45	0.35	0.25	0.15	0.055	
Pe	0.011107	0.056862	0.254725	0.691113	1.261498	1.696129	2.521144	4.601882	15.00457548	
swir	0.006661	0.016219	0.036724	0.06327	0.087826	0.103203	0.128088	0.177801	0.338589041	
Pc	swi									
0	1	1	1	1	1	1	1	1	1	
0.1	0.145	0.609	1	1	1	1	1	1	1	
0.2	0.081	0.334	1	1	1	1	1	1	1	
0.3	0.058	0.237	0.868	1	1	1	1	1	1	
0.4	0.046	0.187	0.679	1	1	1	1	1	1	
0.5	0.039	0.156	0.563	1	1	1	1	1	1	
0.6	0.034	0.135	0.483	1.000	1	1	1	1	1	
0.7	0.031	0.120	0.425	0.989	1	1	1	1	1	
0.8	0.028	0.108	0.382	0.885	1	1	1	1	1	
0.9	0.026	0.099	0.347	0.802	1	1	1	1	1	
1	0.024	0.091	0.319	0.736	1	1	1	1	1	
2	0.016	0.056	0.188	0.424	0.691	0.877	1	1	1	
3	0.013	0.044	0.142	0.314	0.507	0.641	0.874	1	1	
4	0.012	0.038	0.118	0.257	0.412	0.518	0.704	1.000	1	
5	0.011	0.034	0.103	0.222	0.353	0.443	0.600	0.941	1	
6	0.010	0.031	0.093	0.198	0.313	0.392	0.528	0.826	1	
7	0.010	0.029	0.086	0.180	0.284	0.354	0.477	0.742	1	
8	0.009	0.028	0.080	0.167	0.262	0.326	0.437	0.678	1	
9	0.009	0.027	0.076	0.157	0.244	0.304	0.406	0.628	1	
10	0.009	0.026	0.072	0.148	0.230	0.286	0.381	0.587	1	
12	0.009	0.024	0.067	0.136	0.209	0.258	0.343	0.526	1	
14	0.008	0.023	0.063	0.126	0.193	0.238	0.315	0.481	1.00	
20	0.008	0.021	0.056	0.109	0.164	0.201	0.264	0.398	0.850	
30	0.007	0.020	0.050	0.095	0.141	0.171	0.222	0.331	0.694	
40	0.007	0.019	0.047	0.088	0.129	0.156	0.201	0.296	0.613	
50	0.007	0.018	0.045	0.083	0.121	0.146	0.188	0.274	0.563	
60	0.007	0.018	0.044	0.080	0.116	0.140	0.179	0.260	0.529	
70	0.007	0.018	0.043	0.078	0.113	0.135	0.172	0.249	0.505	
80	0.007	0.018	0.042	0.076	0.110	0.131	0.167	0.241	0.486	
90	0.007	0.018	0.042	0.075	0.108	0.129	0.163	0.235	0.471	
100	0.007	0.017	0.041	0.074	0.106	0.126	0.160	0.230	0.459	
150	0.007	0.017	0.040	0.071	0.100	0.119	0.150	0.214	0.422	
200	0.007	0.017	0.039	0.069	0.097	0.116	0.145	0.206	0.403	
300	0.007	0.017	0.038	0.067	0.095	0.112	0.140	0.197	0.384	

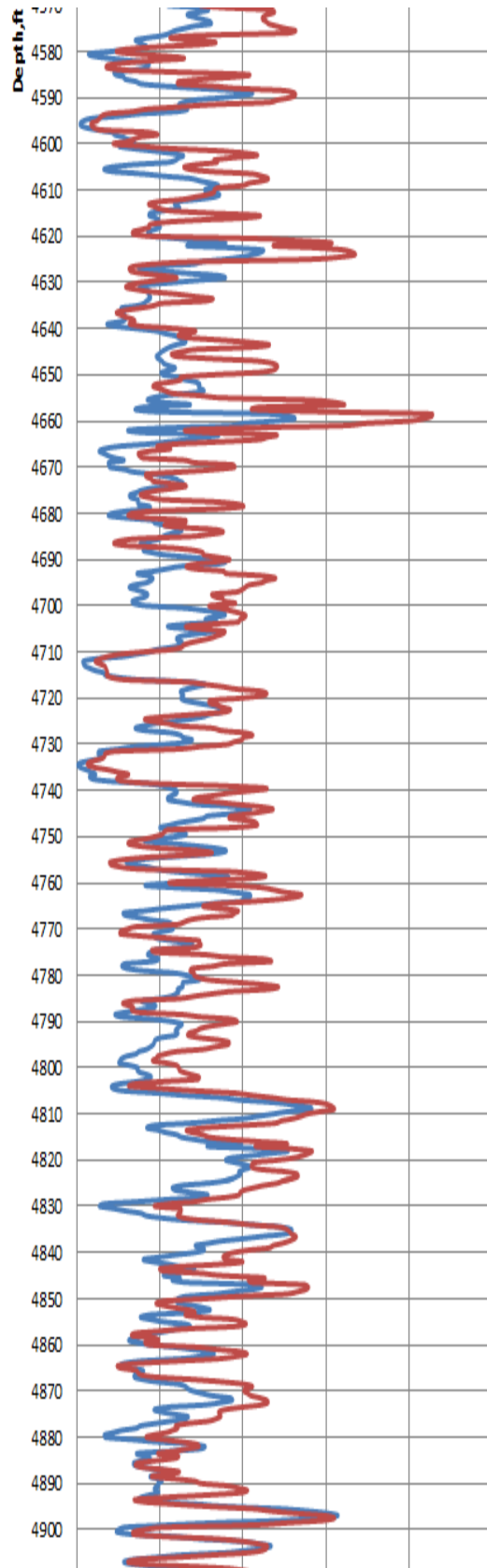
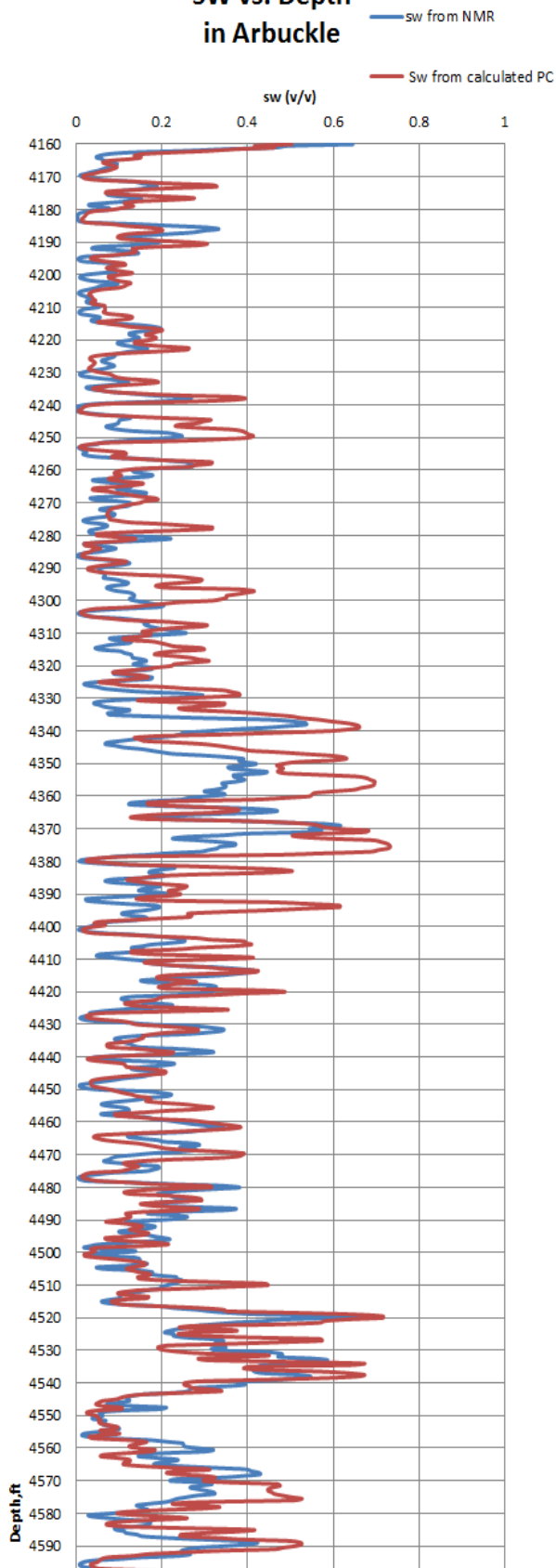


**Figure 45: Nine Pc curves for nine rock types for the specified RQI**



**Figure 46: Calculated Pc compared with generated Pc from NMR**

### SW vs. Depth in Arbuckle



## Appendix S-A

### Seismic Publications & Presentations

(\* indicates student advisees; \*\* invited presentation)

- Nolte K.A.\*, Tsoflias G.P., Bidgoli T.S. and L.W. Watney (2017), Shear-Wave Anisotropy Reveals Pore Fluid Pressure-Induced Seismicity in the US Midcontinent, *Science Advances*, 3, e1700443 (2017).
- Tsoflias G. P., Graham B.\*, Haga L.\* and W. Lynn Watney (2017) Seismic Reservoir Characterization for Assessment of CO<sub>2</sub> EOR at the Mississippian Reservoir in South-Central Kansas, Abstract NS33A-0054, Fall AGU Meeting, New Orleans, LA, December 11-15, 2017.
- Nolte K. A\*, G. P. Tsoflias, Bidgoli T. and W. L. Watney (2017) A new earthquake monitoring method? Change in shear-wave anisotropy as a tool to monitor induced seismicity in Kansas and Oklahoma, Abstract S13D-06, Fall AGU Meeting, New Orleans, LA, December 11-15, 2017.
- Nolte K. A\*, G. P. Tsoflias, Bidgoli T. and W. L. Watney (2017) Understanding induced seismicity: Temporal link between pore pressure increase and shear-wave anisotropy, Society of Exploration Geophysicists, Injection Induced Seismicity Workshop, Dallas, TX., USA, November 6-8, 2017.
- Molina Z.\*, Nolte K.\* and G. Tsoflias (2017), An Overview of Injection Induced Seismicity in Kansas and Oklahoma, SACNAS National Conference, Salt Lake City, UT., USA, October 19 - 21, 2017.
- Nolte K. A.\*, Tsoflias G. P., Bidgoli T. S., and W. L. Watney (2017), Monitoring Seismicity Near an Active CO<sub>2</sub> EOR Injection, in DOE NETL Mastering the Subsurface Through Technology Innovation, Partnerships and Collaboration: Carbon Storage and Oil and Natural Gas Technologies Review Meeting, Pittsburgh, PA, August 1-3, 2017.
- Graham, B. L. \*, Haga, L. N. \*, Nolte, K. A. \*, Tsoflias, G. P., and W. L. Watney (2017), Fracture Mapping and Feasibility of Monitoring CO<sub>2</sub> *in situ* From Seismic Data at the Mississippian Carbonate Reservoir, Wellington Oil Field, South-Central Kansas, in DOE NETL Mastering the Subsurface Through Technology Innovation, Partnerships and Collaboration: Carbon Storage and Oil and Natural Gas Technologies Review Meeting, Pittsburgh, PA, August 1-3, 2017.
- Molina Z.\*, Nolte K.\* and G. Tsoflias (2017), Injection Induced Seismicity in Sumner County, Kansas, KU Undergraduate Research Symposium, Lawrence, Kansas, July 28, 2017.
- Molina Z.\*, Nolte K.\* and G. Tsoflias (2017), Monitoring Induced Seismicity in Sumner County, Kansas, KU Undergraduate Research Symposium, Lawrence, Kansas, April 22, 2017. Awarded “*Outstanding Student Presentation*”.
- Nolte A.\*, Tsoflias G. P., Bidgoli T. S. and W. L. Watney (2017), Understanding the Temporal-Spatial Relationship of Induced Seismicity in Southern Kansas, KU Graduate Research Symposium, Lawrence, Kansas, April 6, 2017.

- Nolte A.\*, Tsoflias G. P., Bidgoli T. S. and W. L. Watney (2017), Direct Evidence of Pore Fluid Pressure Increases Inducing Seismicity in the US Midcontinent Through Analysis of Shear-Wave Anisotropy, 2017 Annual Meeting of the Kansas Interdisciplinary Carbonate Consortium, Lawrence, Kansas, March 5-7, 2017 (4 pages).
- Nolte A.\*, Tsoflias G. P. and W. L. Watney (2017), Monitoring the Northward Advance of Injection Induced Seismicity in Southern Kansas, 2017 Annual Meeting of the Kansas Interdisciplinary Carbonate Consortium, Lawrence, Kansas, March 5-7, 2017 (2 pages).
- Graham B.\*, Tsoflias G. P. and W. L. Watney (2017), Seismic Determination of Azimuthal Anisotropy in the Mississippian Chert and Arbuckle from 3D P-P Reflection Data in Wellington Field, South-Central Kansas, 2017 Annual Meeting of the Kansas Interdisciplinary Carbonate Consortium, Lawrence, Kansas, March 5-7, 2017 (4 pages).
- Graham B.\*, Tsoflias G. P. and W. L. Watney (2017), Re-processing of 3D Seismic for Enhanced Imaging of the Mississippian and Arbuckle at Wellington Field, South-Central Kansas, 2017 Annual Meeting of the Kansas Interdisciplinary Carbonate Consortium, Lawrence, Kansas, March 5-7, 2017 (4 pages).
- Haga L.\*, Tsoflias G. P. and W. L. Watney (2017), Time-Lapse Imaging of CO<sub>2</sub> Injection at the Mississippian Reservoir, Wellington Field, South-central Kansas, 2017 Annual Meeting of the Kansas Interdisciplinary Carbonate Consortium, Lawrence, Kansas, March 5-7, 2017 (4 pages).
- Tsoflias G. P. and M. Becker (2016), GPR Phase Response to Fracture Saline Tracers, Abstract GP51B-1388, Fall AGU Meeting, San Francisco, Calif., December 12-16, 2016.
- Nolte K.\*, Tsoflias G. P. and L. W. Watney (2016), Monitoring the Increase in Seismicity in South-Central Kansas, Abstract S43C-2871, Fall AGU Meeting, San Francisco, Calif., December 12-16, 2016.
- Nolte A.\*, Tsoflias G. P. and W. L. Watney (2016), Monitoring the Increase in Seismicity in South-Central Kansas, G-Hawk Annual Symposium, Lawrence, Kansas, September 16, 2016 (3<sup>rd</sup> place award).
- Sodré B.\*, Nolte K\* and G. Tsoflias (2016), Analysis of Earthquakes in Sumner County, South Central Kansas, KU Summer Undergraduate Research Poster Session, Lawrence, Kansas, July 29, 2016.
- Nolte K.\*, Graham B.\*, Tsoflias G. P. and W. L. Watney (2016), Monitoring Induced Seismicity Near the Wellington Oil Field CO<sub>2</sub> Injection in the Mississippian and Arbuckle reservoirs, 2016 Annual Meeting of the Kansas Interdisciplinary Carbonate Consortium, Lawrence, Kansas, April 25-27, 2016 (4 pages).
- Graham B.\*, Tsoflias G. P. and W. L. Watney (2016), Seismic Modeling of CO<sub>2</sub> Fluid Substitution in the Mississippian Cherty Dolomite and Arbuckle Group Dolomite Reservoirs, Wellington Field, South-Central Kansas, 2016 Annual Meeting of the Kansas Interdisciplinary Carbonate Consortium, Lawrence, Kansas, April 25-27, 2016 (4 pages).
- Tsoflias G. P.\*\*\*, Fadolkarem Y. and W. L. Watney (2015), Seismic Characterization of the Mississippian in South-central Kansas, AAPG Workshop on Revitalizing Reservoirs, San Antonio, TX, December 1-2, 2015.

- Fadolalkarem Y.\*, Tsoflias G. P. † and W. L. Watney (2015), Seismic AVO Analysis of the Mississippian Chert and Arbuckle Group at Wellington Field, South-central Kansas, 2015 Annual Meeting of the Kansas Interdisciplinary Carbonate Consortium, Lawrence, Kansas, April 12-14, 2015 (4 pages).
- Fadolalkarem Y.\*, Tsoflias G. P. † and W. L. Watney (2015), Use of Seismic Multiattribute Regression Analysis for Porosity Prediction in the Mississippian Chert and Arbuckle Group at Wellington Field, 2015 Annual Meeting of the Kansas Interdisciplinary Carbonate Consortium, Lawrence, Kansas, April 12-14, 2015 (4 pages).
- Fadolalkarem Y.\*, Tsoflias G. P. and W. L. Watney (2014), Pre-stack Seismic Attribute Analysis of the Mississippian Chert and Arbuckle at Wellington Field, South-central Kansas, 2014 Annual Meeting of the Kansas Interdisciplinary Carbonate Consortium, Lawrence, Kansas, April 27-30, 2014 (4 pages).
- Sirazhiev A.\*, Tsoflias G. P. and L. Watney (2013), Seismic Attribute Analysis of the Mississippian Chert at the Wellington Field in South-Central Kansas, AAPG Mid-Continent Section Meeting, Wichita, Kansas, October 12-15, 2013.
- Sirazhiev A.\*, Tsoflias G. P. and W. L. Watney (2012), Relating seismic amplitude and frequency response to porosity variability at the top of the Mississippian Chert, South-Central KS, 2012 Annual Meeting of the Kansas Interdisciplinary Carbonate Consortium, Lawrence, Kansas, April 2-6, 2012 (4 pages).

